MULTILAYER OPTICAL STRUCTURES FOR TIME-RESOLVED MESO-SCALE SENSING OF SHOCK-COMPRESSION IN HETEROGENEOUS MATERIALS

A Thesis
Presented to
The Academic Faculty

By

David Scripka

In Partial Fulfillment
of the Requirements for the Degree
Doctor of Philosopy in the
School of Materials Science and Engineering

Georgia Institute of Technology

May 2018

MULTILAYER OPTICAL STRUCTURES FOR TIME-RESOLVED MESO-SCALE SENSING OF SHOCK-COMPRESSION IN HETEROGENEOUS MATERIALS

Approved by:

Dr. Naresh Thadhani
School of Materials Science and Engineering
Georgia Institute of Technology

Dr. Christopher J. Summers
School of Materials Science and Engineering
Georgia Institute of Technology

Dr. Seung Soon Jang
School of Materials Science and Engineering
Georgia Institute of Technology

Dr. Zhitao Kang
School of Materials Science and Engineering
Georgia Institute of Technology

Dr. Keo Springer
Materials Science Division
Lawrence Livermore National Laboratory

Date Approved: April 3, 2018

ACKNOWLEDGEMENTS

I have spent the better part of the last decade at Georgia Tech, and my time here has been both enjoyable and deeply transformative. There are many people have who have been an integral part of this experience, and I am indebted to them for their support, encouragement, and friendship throughout the years. First, I want to thank my Advisor, Dr. Naresh Thadhani for all of his guidance throughout both my undergraduate and graduate careers. He has truly been an advocate for me both academically and professionally, and I owe much of my growth as a scientist to him. Second, Dr. Christopher Summers and Dr. Zhitao Kang provided essential expertise on the optical aspects of my research, and I am grateful for their guidance. Third, many others provided invaluable support to me as I conducted my research: Gyuhyon (Eric) Lee as my collaborator on this project who performed much of the design and all of the fabrication work, Dr. Greg Kennedy with his vast knowledge of shock physics and seemingly every item in the HSR lab here at Tech, Dr. Manny Gonzales with his rigorous application of statistics and uncertainty propagation, Dr. Jennifer Breidenich with her broad experimental expertise and assistance with many of the more difficult aspects of the experimental setup, and Dr. Nick Glumac for his advice and suggestions on high-efficieny spectrograph design. I am also grateful to Dr. Stefany Holguin, Sukanya Sharma, Travis Voorhees, and Andrew Boddorf for their friendship and support, and especially Dr. Rene Diaz and Dr. Alex Bryant for countless insightful comments, suggestions, and a surprising amount of fun in our shared office of four years.

I am also exceedingly grateful to my family. To my parents Hal and Cheryl, thank you for your unceasing support and the deep curiosity that you instilled in me. To my sister Amy, thank you for your superb writing advice and copy-editing expertise, a deep technical skill that I greatly admire. To my sister Ashley, thank you for your thought-provoking perspective and counsel on academia, career pathways, and the importance of maintaining true work-life balance. To my brother Will, thank you for challenging my view

of the world and for showing me what true resilience is. And to my wife Carlee, thank you for your patience and unconditional support throughout these last five years. I could not have done it without you.

Finally, I am indebted to the research agencies and academic fellowships that funded this work: the Defense Threat Reduction Agency (DTRA) through Grant HDTRA-1-12-1-0052, the Air Force Office of Scientific Research (AFOSR) through Grant 9550-15-10499, the National Defense Science and Engineering Graduate Fellowship (NDSEG), and the Georgia Tech President's Fellowship. Scientific research is an important long-term investment, and I am honored that I was entrusted with a small part of it.

TABLE OF CONTENTS

LIST OF TABLES

LIST OF FIGURES

SUMMARY

Heterogeneous materials play important roles in many different applications across a wide range of industries. Examples include engineered composites, particulate systems, and energetic materials, which all display complex meso-scale features and behaviors. This complexity leads to significant gaps in the understanding of heterogeneous materials, especially under extreme conditions such as shock-compression. A fundamental challenge in this area of research is a lack of experimental diagnostics that can provide spatially-resolved information under the demanding temporal and environmental conditions of shock loading. Multilayer optical structures, due to their unique spectral responses that can be correlated to externally induced loads, have the potential to serve as a new class of sensor for these complex materials and conditions.

This work presents the theory, development, and evaluation of novel multilayer optical structures as time-resolved pressure sensors with meso-scale spatial sensitivity. Time-resolved spectroscopy of laser-driven shock-compression experiments on the multilayers demonstrated spectral shifts of the characteristic spectral peaks to shorter wavelengths (blueshifts), and simultaneous velocimetry established that these spectral shifts are unambiguously correlated to the laser-driven shock pressure. An optomechanical model was developed and used to predict the spectral response of the multilayers as a function of pressure, and when informed with quality empirical data, quantitatively matches the experimentally observed blueshift. Experiments and simulations of spatially heterogeneous shock loading demonstrate the ability of the multilayers to resolve not only multiple pressures but also to capture the subtle features present in shock-compressed heterogeneous materials, all while maintaining nano-second level temporal resolution. Overall, multilayer-based sensing is a fundamentally new time-resolved diagnostic method in the fields of high-strain-rate material behavior and shock physics. This work has provided the theoretical and empirical foundation for broad classes of different multilayer structures, and demonstrated their

unique potential utility for capturing the complex meso-scale pressure histories needed to enable new insights into the dynamic response of heterogeneous materials.

CHAPTER 1
INTRODUCTION AND OBJECTIVES

Heterogeneous materials are frequently observed in a wide variety of environments and engineering applications. For example, geologic materials such as soil, sand, and rock have a strong heterogeneous character. Engineered composite materials, such as bonded particulate materials and laminates, also possess an intrinsically heterogeneous nature. Broadly, heterogeneous materials are defined by a departure from microstructural homogeneity, with the scale of such departure ranging from the microscopic to the macroscopic.

It is well known that such materials have complex mechanical behavior that can be difficult to predict. The multi-scale mechanisms that drive the macroscopic response of heterogeneous materials must be understood in order to form predictive and descriptive models. For a large number of materials, it is the meso-scale that plays the dominant role in controlling many features of bulk material behavior [1]. The meso-scale has a range of definitions depending on the nature and scale of the heterogeneity in the system, although it can be generally defined as the length scale at which the dominant heterogeneity is discretely observable. For example, in a geologic material such as sand, the meso-scale is the length at which individual grains of sand and grain-grain interactions can be clearly defined. This illustrates the difficulty in rigorously testing and observing meso-scale behavior in complex heterogeneous materials as the pertinent length scale is often on the order of microns requiring high spatial-resolution diagnostics.

This requirement is particularly difficult for materials under the high-magnitude dynamic loads often encountered in applications where many heterogeneous materials are designed to operate, such as blast loading and impact events. Under such conditions of shock-compression, not only are there spatial resolution difficulties introduced by varying length scales, but often the meso-scale features and interactions that drive the material's

bulk response have short time-scales ranging from microseconds to nanoseconds. While there are many existing time-resolved experimental diagnostics used in the study of dynamic material behavior, very few have the requisite spatial sensitivity to resolve essential meso-scale features. And while computational methods can certainly provide significant insight into dynamic meso-scale behavior, without high quality experimental data for validation it is impossible to verify the accuracy of such models. The net result for many important heterogeneous material systems is that knowledge of their shock-compression behavior is poorly understood. In order to address this significant knowledge gap, two specific advances are required. First, new experimental diagnostics that possess high spatial *and* temporal sensitivity must be developed. Second, rigorous computational models that fully incorporate relevant meso-scale features must be validated against the experimental data generated from such meso-scale time-resolved diagnostics.

The aim of this dissertation is to contribute to closing this knowledge gap by investigating and testing novel optical devices for use as advanced time-resolved meso-scale diagnostics. The investigation focuses on multilayer optical structures, a relatively easily produced type of 1-dimensional photonic crystal. These multilayer structures have unique spectral characteristics, which are intrinsically related to the mechanical and thermodynamic state of the materials in the multilayer. Externally induced changes in these conditions produce a corresponding change in the spectral response of the multilayer, resulting in an optically-based sensor by monitoring the temporal evolution of the spectral response. Further, if the external loading is spatially localized, the corresponding spectral alteration is similarly spatially localized. This spatially resolved behavior, combined with the inherently fast response time of optical operation, is a strong indicator that multilayer optical structures can have significant potential to be leveraged as meso-scale time-resolved diagnostics.

Due to the novel nature of this work, it was essential that the structure and behavior of multilayer optical structures under shock-compression be well characterized, including under both uniform and heterogeneous loading conditions. In order to meet these goals,

the objectives of this dissertation are as follows:

1. Develop multilayer structures with physical and spectral features well-suited for time-resolved meso-scale sensing of dynamic shock-compression effects, leveraging different materials, multilayer designs, and fabrication methods.

2. Develop theoretical models describing the mechanisms that control the mechanical and spectral response of the multilayer designs under shock-compression, and compare and validate these models to experimental data.

3. Develop computational methods that can accurately predict both the mechanical and optical response of the multilayer designs under shock-compression, incorporating theoretical models, non-uniform multilayer deformation and compression, and different temporal and spatial loading scales.

4. Determine the mechanical and spectral response of multilayer designs under both uniform and heterogeneous shock-compression with simulations and experiments, and evaluate the potential and practical application of using the multilayers as time-resolved meso-scale diagnostics for probing shock-compression in heterogeneous materials.

This dissertation will address these and other relevant topics across the following chapters. Chapter 2 addresses the history and current knowledge of the shock-compression of heterogeneous materials, the history and development of other time-resolved diagnostics, and the basic principles of operation and design for the multilayer optical structures studied in this dissertation. Chapter 3 describes the development of an experimental setup for laser-driven shock-compression of the multilayer structures with simultaneous time-resolved spectroscopy and velocimetry, and also presents a custom computational framework that can produce time-resolved spectra for the multilayers under arbitrary spatial and temporal loading conditions. Chapter 4 details the focused development of multilayer structures

with materials and spectral features specifically designed for capturing shock-compression effects on nanosecond to microsecond time-scales as well as the definition of theoretical models that can predict the mechanical and optical responses of the multilayers under such loads. Chapter 5 presents experimental results of 1-dimensional shock-compression experiments compared with predictions of the theoretical models, and Chapter 6 describes the experimental and simulated response of the multilayers to spatially heterogeneous, multi-pressure shock loads. Chapter 7 discusses the practical aspects of experimental implementation and data extraction/analysis when using the multilayer structures in time-resolved meso-scale sensing of shock-compression in heterogeneous materials. Finally, Chapter 8 concludes the dissertation with a discussion and summary of the results, as well as identifying directions for future work.

CHAPTER 2

BACKGROUND

2.1 Shock Compression Phenomena

After several decades of intensive study, the fundamental phenomena governing the shock response of *homogeneous* materials is now well understood, with Meyers [2] and Forbes [3] offering thorough discussions. A foundational assumption of this work is the continuum mathematical description of materials, as represented in the three Rankine-Hugoniot conditions of a perfect shock front in a material: the conservation of mass, momentum, and energy (Equations 2.1, 2.2, 2.3 respectively).

$$\frac{V}{V_0} = \frac{(U_s - U_p)}{U_s} \tag{2.1}$$

$$P = \rho_0 U_s U_p \tag{2.2}$$

$$E - E_0 = \frac{P(V - V_0)}{2} \tag{2.3}$$

In the above equations V is the specific volume of the material, U_s is the shock velocity, U_p is particle velocity, ρ is density, P is pressure, and E is internal energy. These equations relate the thermodynamic parameters of pressure, volume, and energy to the hydrodynamic parameters of shock velocity and particle velocity across a perfect, discontinuous shock front. As a material is shock compressed, it undergoes various dissipative processes depending on its microstructure, intrinsic material properties, and magnitude of the loading. For example, a metallic material will typically undergo first elastic, then plastic deformation if the magnitude of the load exceeds the material's dynamic yield strength, termed the

Hugoniot Elastic Limit (HEL). Some materials (including both metallic and non-metallic) will show temporary or permanent changes in crystal structure under shock-compression. At longer times, complex wave interactions can lead to unique damage and failure mechanisms or simply attenuation of the shock wave.

Based on the Rankine-Hugoniot equations, significant insight into the shock response of homogeneous materials can be gained by recording the temporal histories of relevant parameters. For example, an accurate recording of the velocity of the rear surface (indirectly, the particle velocity) of a shocked metal can provide evidence of several important processes, including the elastic-plastic transition, phase transformations, and dynamic tensile failure (spall). Figure 2.1 shows rear surface velocity of a sample of α-iron shocked to $\sim$23.7 GPa [4]. Several clear transition regions can be observed in the velocity profile, due the differences in wave speed between the elastic, α-plastic, and ϵ-plastic waves speeds. Figure 2.2 demonstrates the characteristic signal of spall failure, which occurs when traveling waves of opposite sense (tensile and compressive waves) meet at an interior point of a material. Models can be derived that relate features of the spall signal (e.g., depth of the pull-back between times 3 and 4 in Figure 2.2b) to a material's resistance to dynamic failure. There are many other important material responses, thermodynamic properties, and failure mechanisms that can be explored via the temporal histories of U_s, U_p, and P. Again, see Meyers [2] and Forbes [3] for additional examples and discussion. It is important to reiterate that many of these approaches are based on assumptions of material homogeneity and uniform, 1-dimensional loading. For many bulk materials, this is reasonable, and such approaches have been shown to work quite well.

Despite these generally well-behaved responses, even traditionally homogeneous systems do still have meso-scale features and behaviors that can influence bulk material responses. As the material becomes more and more heterogeneous, shock loading behavior quickly becomes a complex combination of many different phenomena spanning multiple time and length scales. The intrinsic microstructural, material property, and thermody-

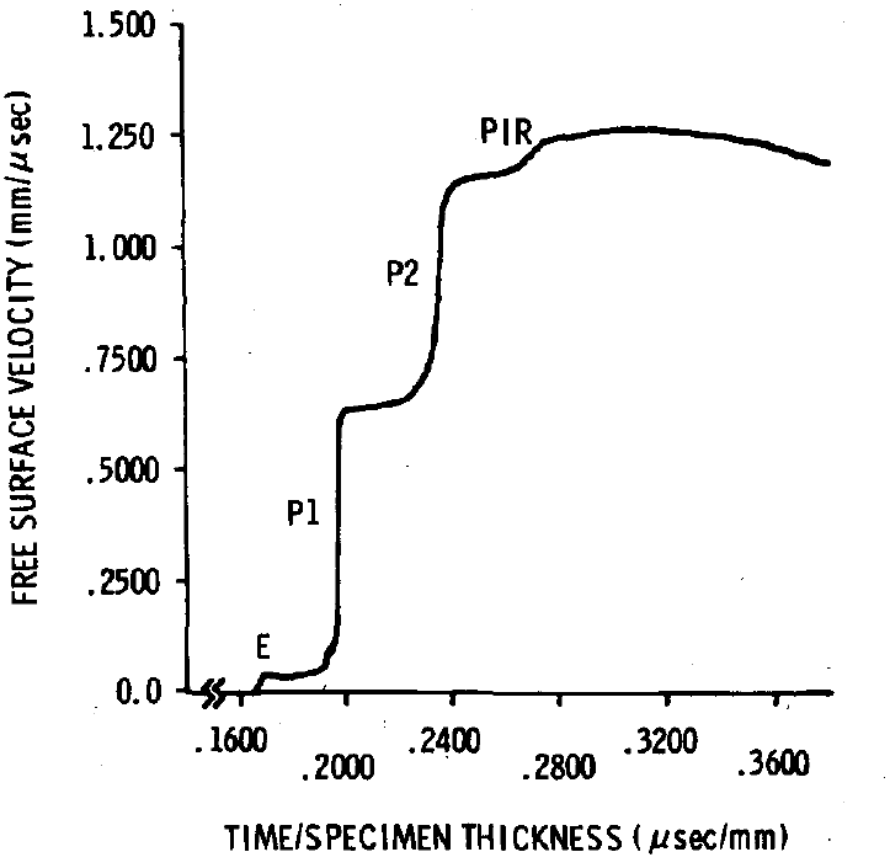

Figure 2.1: The free rear surface of a sample of α-iron shocked to 23.7 GPa from Barker et al. [4]. There are three distinct regions labeled in the velocity profile, each corresponding to a particular material response to the dynamic compression load. Region E corresponds to the fast-traveling elastic precursor wave, followed by the slower α-iron plastic wave at P1. The slower moving ϵ-iron plastic wave arrives later at P2, and finally wave interactions between the $\alpha - \epsilon$ interface and the free surface produce the "artifact" in the PIR region. Figure reused with permission.

namic variation in these systems invalidates the assumption of a discontinuous (or even steep) shock front at the continuum scale, shifting the conservation relationships to the meso-scale and making the standard analysis of velocity profiles suspect. This localization effect can also combine with induced chemical reactions and unique mechanical force transfer and failure modes to interact in an emergent manner, producing a very broad range of shock loading responses in heterogeneous materials. The corresponding literature is broad and constantly developing, and Nesterenko [6] provides a more comprehensive overview of the fundamental challenges to understanding the shock responses of heteroge-

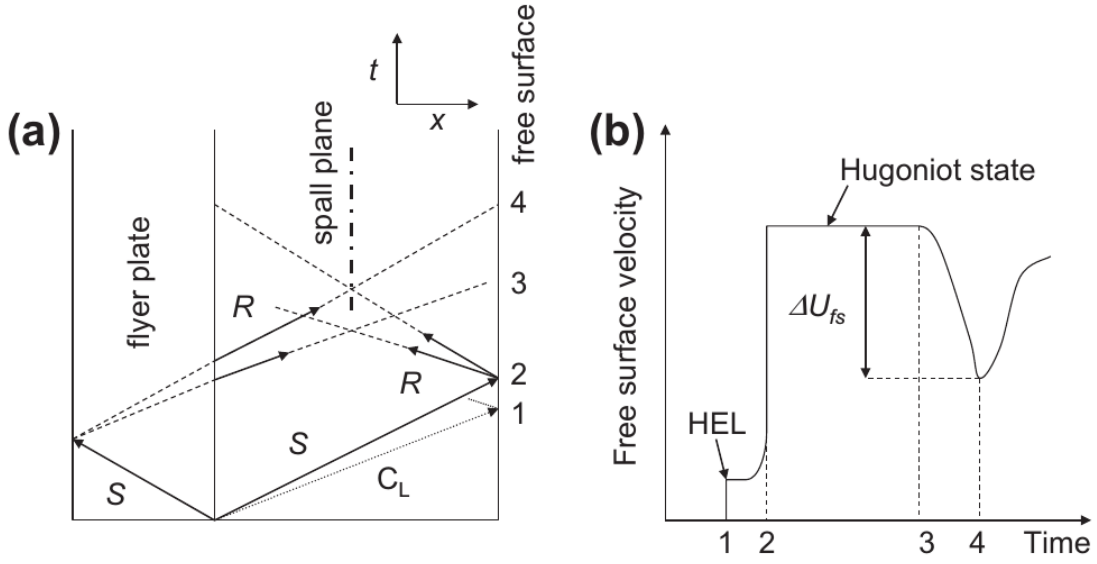

Figure 2.2: (a) Schematic and (b) representative free surface velocity temporal profile for dynamic tensile failure (spall) for a material under a parallel plate impact load from [5]. The failure occurs as two release waves (R) of different sense (compressive and tensile) meet in the sample material along the spall plane, as indicated in (a). Figure reused with permission.

neous materials.

The following sections discuss the role of the meso-scale in various classes of materials in more detail, starting with otherwise-homogeneous polycrystalline solids, and then moving to several types of strongly heterogeneous systems. Finally, as the parameters in equations 2.1 - 2.3 cannot be easily related to meso-scale features in these cases, a fundamental question remains: what experimentally measurable quantities are both obtainable and relevant in understanding the shock response of heterogeneous materials? To that point, Section 2.1.4 explores the salient differences between continuum and meso-scale experimental measurements of shock-compression and the implications of such differences when making inferences about material properties and behaviors.

2.1.1 Meso-scale Phenomena in Polycrystalline Solids

If a "homogeneous" sample of a common aluminum 2024 alloy is shock-compressed, broad consistency in mechanical and thermodynamic behavior is expected. Figure 2.3 from [7] shows the results of over 200 experiments conducted by different researchers, using four different experimental approaches and data analysis techniques. There is remarkable consistency in the data, proving that equations 2.1 - 2.3 are indeed valid under the appropriate conditions, and that the meso-scale differences between each sample are, in this case, negligible.

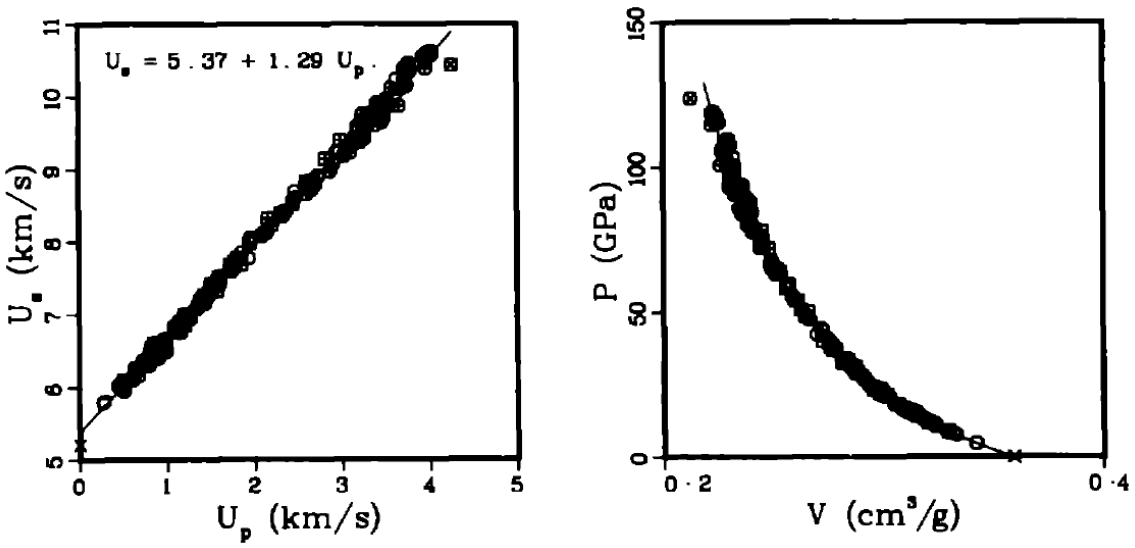

Figure 2.3: Experimental data for the 2024 aluminum alloy as compiled by Marsh [7]. The figure on the left shows the data in the U_s-U_p plane (shock velocity vs particle velocity), and the figure on the right shows the same data converted to the P-V plane (pressure vs specific volume). The data, despite coming from multiple sources and experimental/data analysis methods, is remarkably consistent.

However, subtle behaviors that have been observed at the continuum scale in even such proto-typically homogeneous materials can be attributed to meso-scale heterogeneity [8]. For example, all polycrystalline solids have a distribution of grain sizes and corresponding grain boundaries. Previous work has shown that such meso-scale features play important roles in how a shock front propagates through a material [9, 10]. Figure 2.4 shows an

example of the particle velocity profile of a shocked Al-6064 T4 alloy, and how meso-scale simulations that incorporate grain size distributions and discrete boundaries can reproduce experimentally observed transition features under reloading or unloading of the shocked sample [10].

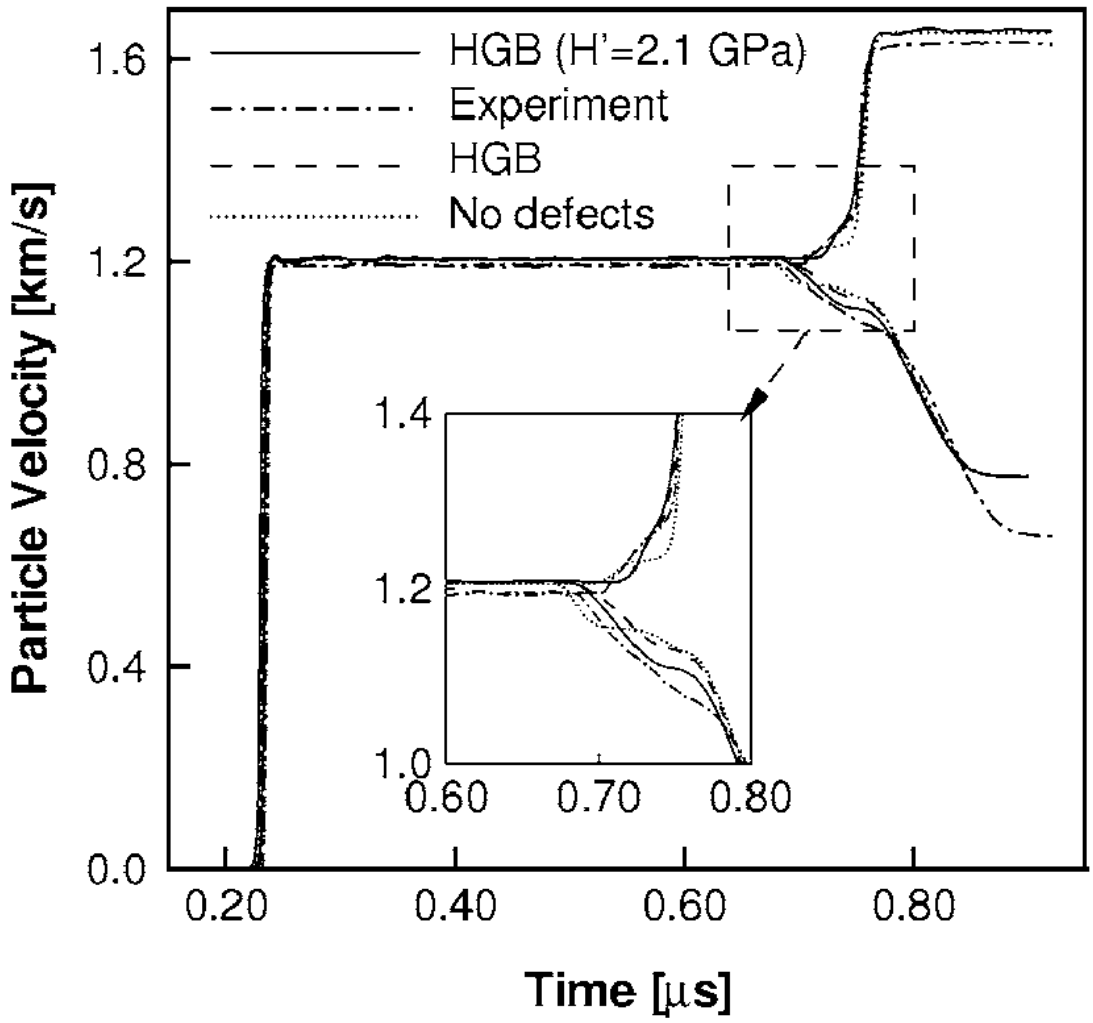

Figure 2.4: Simulated and experimental particle velocity profiles for shock-loaded 6064-T4 aluminum from Dwivedi et al. [10], highlighting the reloading/unloading transition region. Continuum elastic-plastic models predict relatively sharp transitions between these regions, but the meso-scale simulations with discrete, hardened grain boundaries (HGB) are a good match to experimental data. Figure reused with permission.

Another important example of the influence of meso-scale features in otherwise homogeneous materials is the role of material microstructure in dynamic failure. Figure 2.5

shows an image of the spall plane of a shocked AZ31B magnesium alloy [11]. Spallation theory establishes that fractures will nucleate and grow at any point in the material where the local stress state exceeds the material's spall strength. In a homogeneous material, this is most likely to occur uniformly along the spall plane, but in practice the presence of pre-existing voids, inclusions, and defects at the meso-scale act as strongly preferred nucleation sites for crack nucleation and growth, as can be seen in Figure 2.5 b-d. As the scale and complexity of such heterogeneity increases, broad variations in spall strength are observed. For example, Minich et al. [12] have observed significant variation in the spall strength of copper as a function of both crystallographic orientation and grain size, placing the driving mechanisms of such failure behavior firmly at the meso-scale. Whelchel et al. [13] saw similar variations in the spall strength of rolled 5083-H116 aluminum as well as unique fracture modes depending on the orientation of the rolled microstructure with respect to the spall plane.

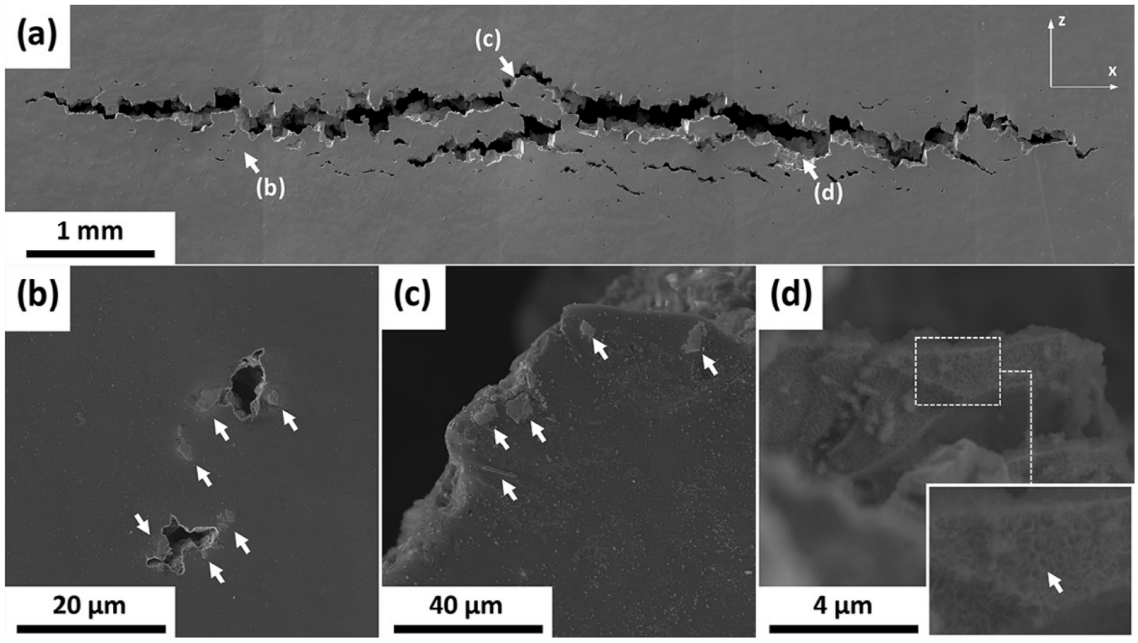

Figure 2.5: Electron microscopy images of the spall fracture surface in shock-loaded AZ31B magnesium alloy samples. The increasing zoom-level from (a) to (d) demonstrate the nucleation and growth of the spall fractures at the interfaces of intermetallic inclusions. Figure reused with permission.

Beyond these examples, a complete discussion of the intricacies of grain boundaries, elemental distributions, particulate inclusions, and other meso-scale features of polycrystalline metals is beyond the scope of this work. As such, a relevant underlying theme can be summarized as follows: even broadly homogeneous materials have important meso-scale features, and their influence on shock-compression behavior can be observed across several different length scales.

2.1.2 Meso-scale Phenomena in Engineered Composites

Engineered composites are a very broad class of heterogeneous materials, and are often also cited as a proto-typical example of both the advantages as well as complexity of exploiting the meso-scale to meet certain performance guidelines for specific engineering or scientific applications. For example, carbon fiber composite structures are used extensively in many different contexts, and the familiar matrix-fiber structure is well known. Similarly, bonded particulate materials ranging from concrete to solid propellants and explosives share many similarities, and generic "simulants" of inert solute particles and matrix binders have been studied extensively to better understand the behavior of such materials under different conditions. More generally, engineered composites combine materials with often disparate mechanical and chemical properties, and typically have well-defined matrix/solute interfaces. Based on the meso-scale complexity of this class of materials, it is no surprise that their behavior under shock loading is complex. Similar to the polycrystalline solids discussed in the previous section, for many engineered composites temporal histories of localized or average particle velocity and pressures can provide indications of specific meso-scale features; however, as the complexity of the heterogeneity increases reasonable inference of specific behaviors or properties can become problematic.

For example, Chen et al. [14] thoroughly examined the stress wave structure of shocked layered composites, linking mesoscale heterogeneities to experimentally observed continuum features of shock wave structure in similar layered composites. Specht et al. [15]

investigated layer material, thickness, and orientation differences in simulations of layered nickel/aluminum composites based on real microstructures (see Figure 2.6), indicating that mesoscale variations associated with the orientation of layers with respect to shock direction, as well as layer uniformity, significantly affects the level of dispersion in the shock front.

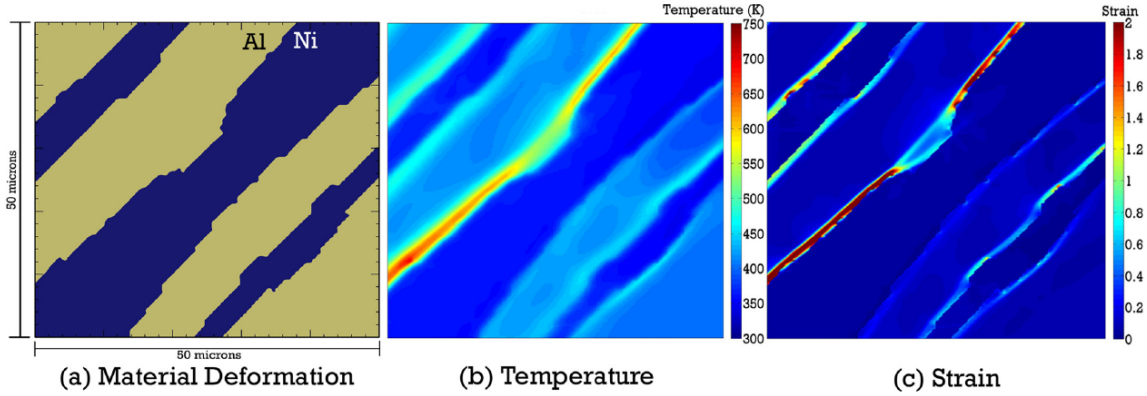

Figure 2.6: Simulated material deformation (a), strain (b), and temperature (c) fields of a shock compressed nickel/aluminum multilayer laminate using real microstructures [15]. Mesoscale variations in layer uniformity combined with an orientation angled at 45 degrees to the direction of shock propagation produce heterogeneous effects that significantly influence the dispersion and dissipation of shock energy in the structure. Figure reused with permission.

Moving toward particulate composites, the shock response of concrete and other strongly-bonded particulates has been extensively studied, and a review of the literature indicates the significant role of component properties, interfaces, and microstructural variation. Riedel et al. [16] demonstrated that a meso-mechanical simulation of shock compressed concrete qualitatively reproduced a wide range of historical experimental data reasonably well, while also providing insight into mesoscale mechanisms and responses. It is important to note that the authors stressed the qualitative nature of this comparison, as the wide variation in sample microstructure, measurement techniques, and concrete mixture composition prevents a more targeted quantitative comparison.

When an engineered composite includes both mechanical and chemical heterogeneity, the important subclass of energetic materials can be defined. Energetic materials have

extensive military, aerospace, and industrial applications, and there is significant interest in understanding their behavior under different conditions. Generally, these systems are composed of hard solute materials surrounded by a much weaker binding solvent matrix, often with small but significant amounts of porosity. A highly studied, specific example would be polymer bonded explosives such as HMX, where the crystalline energetic (RDX) is embedded in a soft polymer binder.

It is well documented that under shock-compression such materials will partially or completely react, with the presence of localized regions of high temperature ("hot spots") the most likely mechanism of initiation as indicated by early work from Bowden [17]. Continued work has indicated that the combination of several different energy dissipation mechanisms contribute to the formation of hot spots [18]. The currently accepted consensus of shock-initiation argues that complex spatial and temporal interactions of initial microstructural variation, highly localized plastic strain, porosity collapse, inter-particle friction, particle failure, and shock dissipation interact to provide sufficient mechanical and thermal energy to initiate energetic chemical reactions [19]. Figure 2.7 shows a mesoscale model of HMX under impact loading, which incorporates many of these mechanisms and behaviors.

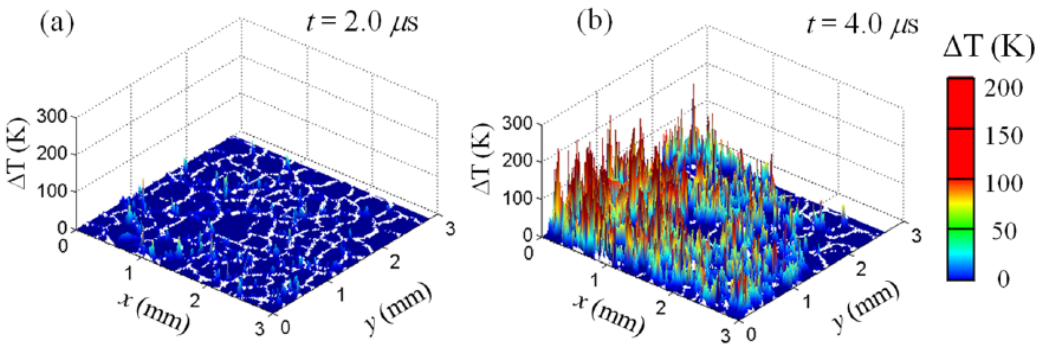

Figure 2.7: Simulated meso-scale temperature fields show thermal hot spot evolution during impact loading of HMX polymer bonded explosive [19]. Meso-scale effects lead to localized deformation of the binder and fracture of individual HMX crystals, producing temperature increases which can create localized reaction initiation events. Figure reused with permission.

Understanding the shock response of energetic materials is an essential safety requirement in many contexts, and this need motivates much of the existing literature. Accurately predicting the temporal and spatial nature of hot spots and corresponding reaction events is absolutely essential in order to fully understand such materials and ensure their safety in specific applications. Extensive effort has been dedicated to this problem, and complex models using a broad range of different computational techniques have produced many meaningful results. However, there still is a distinct lack of high-quality temporally- and spatially-resolved experimental data with which to validate these models [20]. Recent advances in time-resolved pyrometry measurements of temperature evolution in shocked energetic composites have produced compelling arguments for hotspot formation resulting from pore-collapse and product gas heating [21], demonstrating the practical and theoretical utility of increasingly advanced diagnostics. The addition of diagnostics with even a minimum level of spatial sensitivity remains a highly desirable goal in the field.

2.1.3 Mesoscale Phenomena in Particulate Media

Granular materials represent many important systems in manufacturing, military, and geological applications, and often are presented as the extreme case of heterogeneous materials. Common examples include sand or other soils and metal, oxide, or ceramic powder compacts. Beyond the particles themselves, unbonded media such as infiltrated fluids or gases add substantial complexity to these systems. With the many variables of particulate materials, particle size distributions, infiltrates, and packing arrangements, etc., there is a vast combination of different granular systems that make even broad generalizations of consistent behavior somewhat tenuous. As before, a thorough discussion of this expansive complexity is beyond the scope of this work, but several important meso-scale phenomena will be highlighted.

One such important feature of granular materials is constituent particle level interactions. As the bulk material is at most weakly bonded by cohesive forces, mechanical loads

tend to induce complex force transfer mechanisms and particle rearrangements. For example, in both the static and quasistatic compression of granular materials, it is well known that the mechanical load is transferred through the material via discrete networks of contacting particles often called force chains [22]. This behavior is highly relevant to shock-compression, where high magnitude pressure pulses can follow stochastic paths influenced by particle deformation, motion, and fracture. Often, such complex behavior will significantly influence the bulk response of the system in ways that continuum models are incapable of predicting. Dwivedi, et al. [23] demonstrated that exactly such meso-scale particle level features are responsible for projectile penetration instability in granular geologic materials (Figure 2.8). Similar behavior has also been demonstrated experimentally [24].

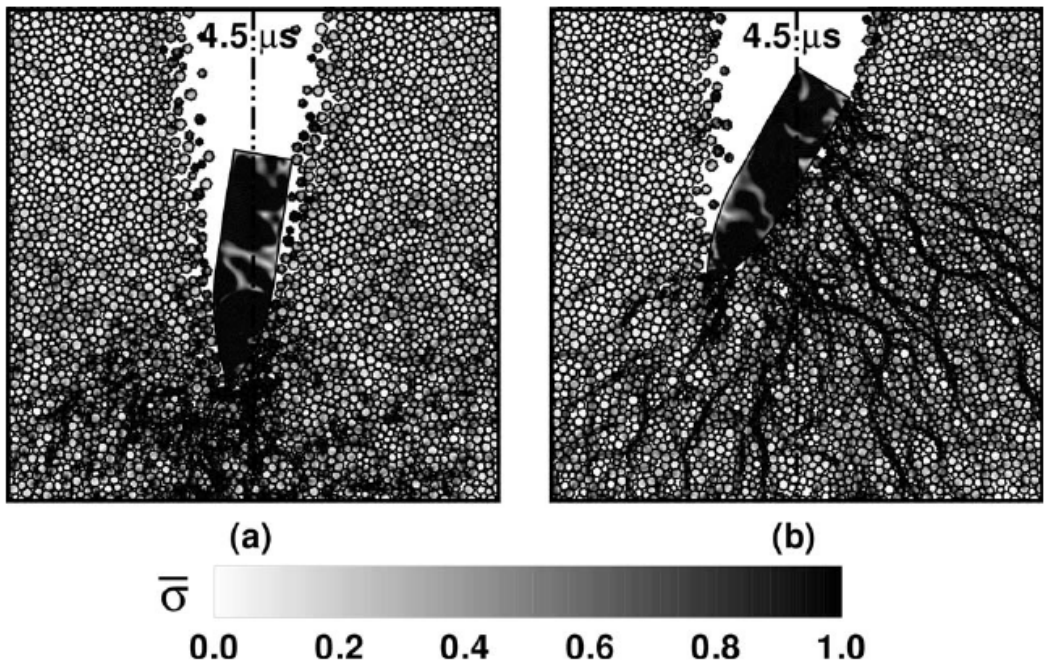

Figure 2.8: Image from a 2D meso-scale simulation of projectile penetration into a granular medium [23]. Projectile trajectory instability is observed even with (a) no friction and (b) addition of friction significantly increases trajectory instability and clearly demonstrates the role of force chains in the dynamic material response. Figure reused with permission.

While sophisticated computational models and well-designed experiments have provided much insight into the roles of such constituent-level interactions in dynamic loading

behavior, experimental diagnostics that can potentially resolve the time and location of evolving force chains, levels and spatial distributions of stresses, stress-states, and particle deformation, and fracture/communition processes will significantly contribute to a more complete understanding of such phenomena.

Another important meso-scale mechanism in granular systems is shock front dissipation and dispersion. In many heterogeneous materials, there are significant differences in the strength and hardness of the individual constituents. Under static loading, this results in partitioning of the mechanical load to the "stronger" constituents. Under shock loading, however, strains of several hundred percent are easily obtained, and disparate mechanical properties of the constituents in the heterogeneous material significantly affect the propagation or dispersion of the shock wave. Daraio, et al. [25] demonstrate that the "softer" constituents will absorb more of the shock energy, decreasing the magnitude of the shock pulse and dispersing the shock front spatially and temporally. Simulations of nickel and aluminum powder compacts with realistic microstructures show such effects (Figure 2.9), with the dispersion attributed to the initial compact density as well as the softer aluminum particles preferentially deforming compared to the harder nickel particles [26]. This dispersive behavior is often desirable, as it can be leveraged to encourage elemental mixing for shock-induced chemical reactions [26, 27], or as an engineered method to absorb and disperse large amounts of energy [25].

The extreme cases of granular material exemplifies the fundamental challenges of understanding dynamic behaviors in such systems, and even heterogeneous systems generally. The meso-scale localization of stress, strain, and energy dissipation and release (e.g., material failure or chemical reactions) is the defining character of their response. These complex interactions do have emergent, measurable effects on the bulk response which traditional diagnostics can measure; but, in many fundamental cases the reverse process (identifying specific meso-scale features directly from bulk measurements) is not deterministic. There are many possible combinations of meso-scale behaviors that can manifest in similar ways

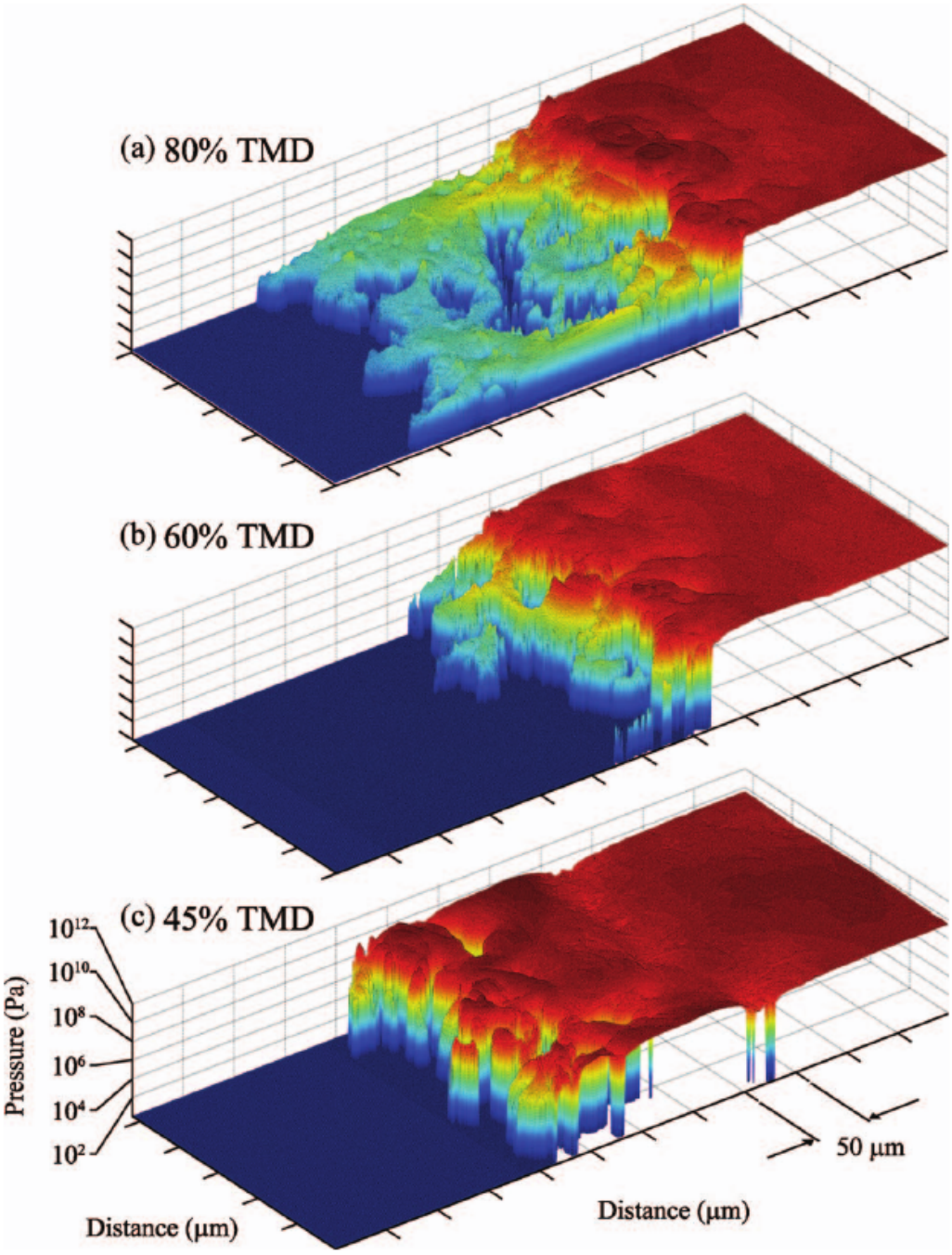

Figure 2.9: Pressures surfaces from 2D meso-scale simulations of Ni-Al powders of various initial densities [26]. Shock fronts at different densities show increasing dispersion and spatial variability due to the heterogeneous response of the powder compact. Figure reused with permission.

on the bulk scale, and frequently no combination of clever experimental design or sample preparation can effectively control for such variability.

2.1.4 Comparing Continuum and Meso-scale Shock Responses

As was just presented, in the fields of high strain rate behavior and shock-compression studies much focus has been placed on identifying meso-scale features and interactions by indirectly observing their effects from continuum measurements, combined with theory and appropriate assumptions. In some cases this approach is quite useful, for example in the association of quasi-elastic unloading and reloading to grain-level effects in polycrystalline metals discussed previously [10]. However, for most heterogeneous materials and shock loading conditions, continuum measurements do not have the appropriate resolution to accurately evaluate meso-scale effects. This is arguably the fundamental challenge in the study of heterogeneous materials, which motivates not only the present work, but also research into advanced characterization methods generally [1]. To make this distinction more tangible, several examples will be discussed that highlight the differences in continuum and meso-scale responses.

First, Vogler et al. have demonstrated this issue with a series of shock-compression simulations in a powder compact of tungsten carbide and aluminum at several different pressures. Figure 2.10 shows distributions of simulated stress in the material. There are several important features revealed in these plots. First, at all impact velocities significant variation in stress evolves spatially and temporally due to the complex mechanisms of shock propagation in granular materials as discussed in the previous section. Second, the average pressure (denoted by the red line) is very smooth for all impact velocities and stresses, but in many cases is an extremely poor representation of the overall heterogeneous stress state in the material. For example, at an impact velocity of 400 m/s the average longitudinal stress is between the bi-modally distributed high and low pressure regions, and thus does not even represent the most likely stress states in the overall material. Similar results are reported for lateral particle velocity and temperature, where average values do not represent the underlying distributions of velocity and temperature in the shocked material. However, the results illustrate an important aspect of meso-scale systems: local-

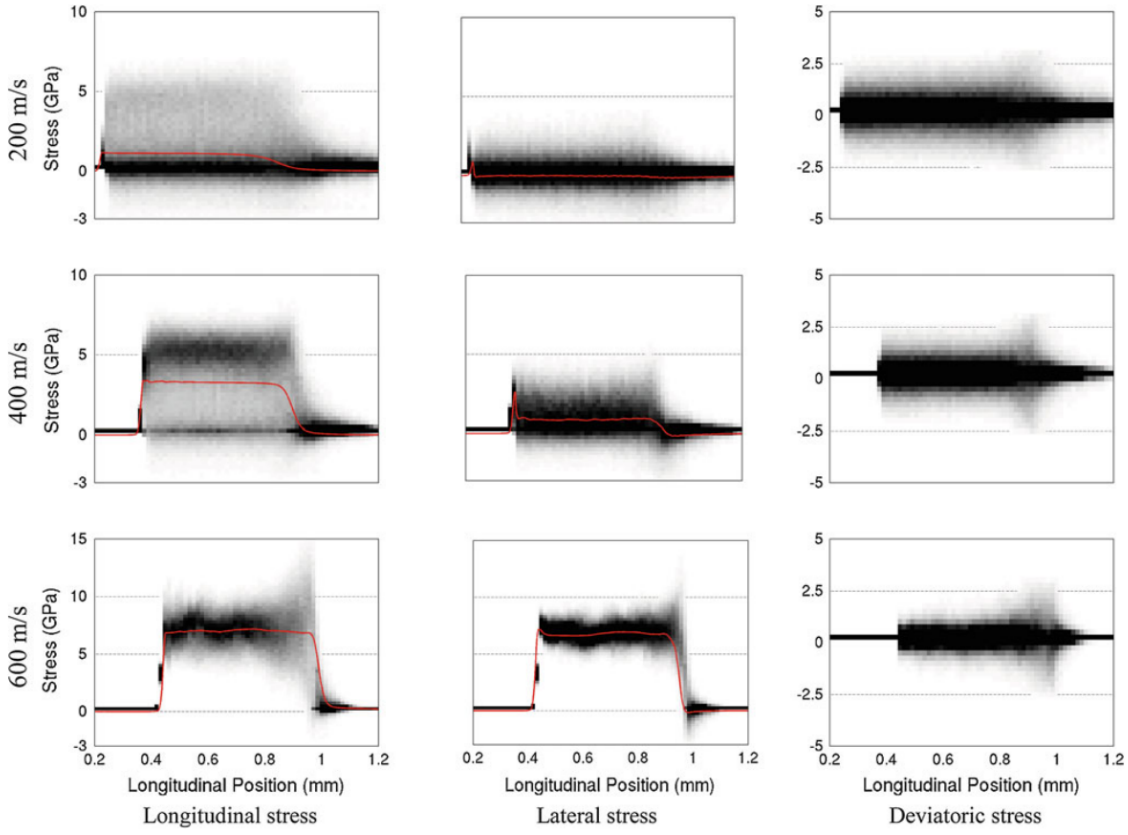

Figure 2.10: Distribution of stresses in the simulated (3D) shock-compression of WC/Al powder compacts at 200, 400, and 600 m/s. Gray lines indicate pressures at individual spatial positions, while red lines indicate the overall average stress. Darker regions indicate a high total number of spatial regions at a given pressure and longitudinal position. Figure reused with permission.

ized material responses can often be described as distributions that vary both spatially and temporally.

Visualizing these distributions of velocity and pressure are unique advantages of meso-scale simulations which demonstrate well the important need for spatially-resolved diagnostics. For a more practical comparison, LaJeunesse et al. [28] use experimental and meso-scale simulation data to explore the distribution of granular sample/window interface velocities using the capabilities of existing experimental diagnostics. Figure 2.11 shows the particle velocity distribution of two different samples composed of ~483 μm ((a) and (c)) and ~133 μm ((b) and (d)) granular particles of silica sand packed to a density of 1.73 $\mathrm{g/cm^3}$ and impacted at ~1440 m/s and ~1000 m/s [28]. Comparison of the average

and individual simulated velocity profiles with experimental data demonstrates several key insights:

1. The distribution of velocity breakout, rise-time, and peak levels show significant variability across the simulated 100 tracer points. This makes accurate determination of certain properties such such as wave transit speed exceedingly difficult.

2. This variability is a function of both particle size (e.g., compare Figure 2.11a and b) and velocity of the impacting flyer.

3. In some cases, the experimental velocity profile can be well-matched to either the average of the simulated tracer points or a single discrete point in the simulations.

These observations illustrate the challenges associated with evaluating meso-scale behavior using continuum diagnostic methods and assumptions. If the spread of measured particle velocities is treated as a statistical distribution, then the experimentally observed velocity profile represents a single random sample of that distribution. In this case, there are two possible interpretations of the such data: as representative of the mean velocity (technically the most likely case), or as a biased instance or even outlier of the overall distribution of velocity histories. In either case, strong inferences about both bulk and meso-scale material responses are impossible as the statistics cannot support such claims with only a single sample. Repeated experiments under similar conditions can provide more inferential power, but in many cases such an approach is cost and/or time prohibitive.

Ultimately, without experimental methods that can accurately measure both continuum and meso-scale information, the mechanistic and quantitative predictions of meso-scale models and theories will remain unvalidated. To that point, Section 2.2 below discusses the state of time-resolved diagnostics in the field of shock-compression, and it also identifies the relevant capability gaps that prevent more rigorous investigations of the dynamic behavior of heterogeneous materials.

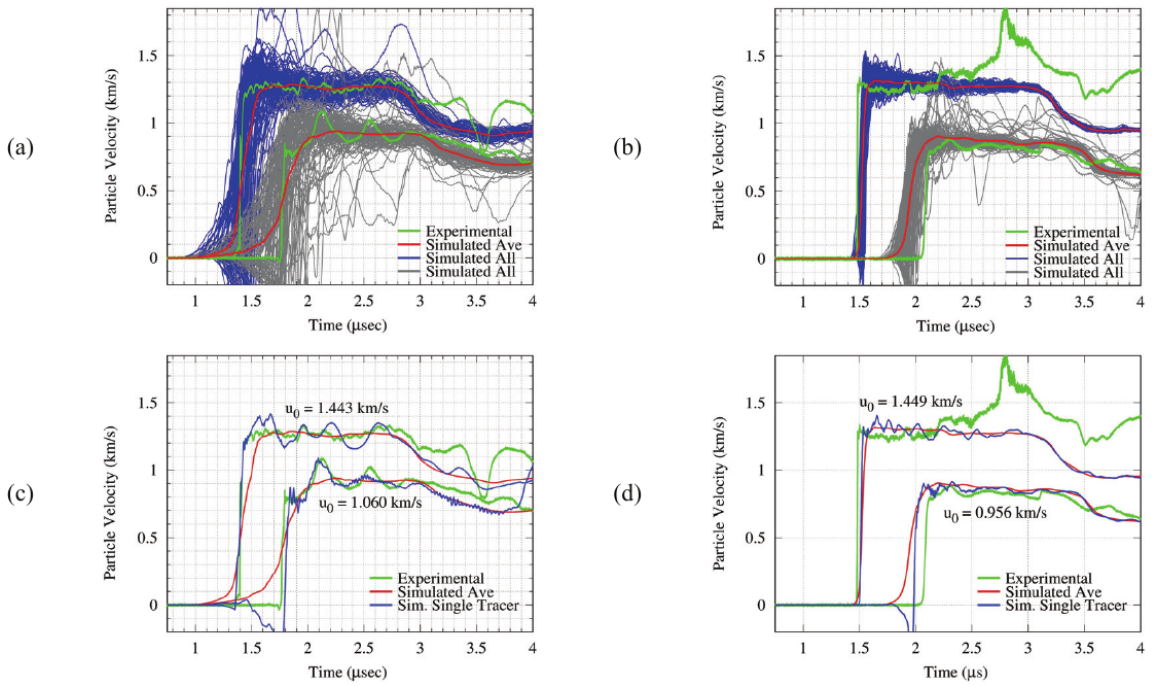

Figure 2.11: Comparison of experimental and computational predictions of sand/window interface velocities for two different samples at two impact velocities. The simulated velocity histories are obtained from 100 distributed tracer points along the simulated interface. (a) and (c) correspond to the ~483 μm sand particles, while (b) and (d) correspond to the ~133 μm particles. The "Single Tracer" shown in (c) and (d) corresponds to one of the 100 simulated tracers selected as the best match to the experimental data. Figure reused with permission.

2.2 Time-resolved Experimental Diagnostics

The existing set of experimental diagnostics used in the study of dynamic material behavior is broad (see Meyers [2], Forbes [3], and Field [29] for thorough discussions); but, in practice a relatively small number of laboratory-scale tools are used by the vast majority of the high-strain-rate and shock physics community. A brief overview of these primary methods are discussed in the following sections, including analysis of each method's application to heterogeneous materials and its ability to provide both temporally and spatially resolved information.

Prior to this discussion, it is important to make a practical distinction in the type of data that the following diagnostics are able to capture. With few exceptions, the existing

standard methods are all variations of point/area measurements *at the surface of a sample, the interface between the sample and a transparent window, or the interface between the sample and the sensor package*. The causes of these limitations are typically inherent to the methods: visible-light based interferometric approaches cannot probe beyond opaque surfaces, and area-based pressure sensors cannot be embedded into a material without creating some form of new interface. Indeed, even the proposed multilayer based sensors are still fundamentally surface/interface diagnostics, though the practical details of the multilayer sensors and their uniqueness will be discussed in later chapters.

It can be argued that time-resolved *in-situ* data is far more desirable than surface/interface data for capturing complex meso-scale phenomena. This is undoubtedly true, but the theoretical attractiveness of this approach belies the general utility and availability of methods capable of producing such data. For example, *in-situ* characterization of materials utilizing high intensity X-ray imaging is an extremely powerful technique, and several facilities including the Linac Coherent Light Source at the SLAC National Accelerator Laboratory, the Advanced Photon Source at Argonne National Laboratory [30], and the Diamond Light Source in the United Kingdom are integrating such capabilities with experimental equipment capable of producing a wide range of dynamic loading conditions. These facilities have significant potential for enhancing understanding of the complex dynamic responses in heterogeneous materials, but highly competitive scheduling and sample limitations can make such experiments impractical for many material systems and research groups. As such, laboratory-scale diagnostics based on surface/interface measurements will continue to play a vital role in the field, and continued research into the development of new diagnostics of this category is still warranted.

2.2.1 Velocity Interferometry

Velocity Interferometry is arguably the most widely used diagnostic in the shock physics and dynamic material behavior communities. Accuracy in velocity records of 1-2% are

relatively easily attained, and the inherent flexibility in the method allows for many different use scenarios. Through the application of the Rankine-Hugoniot equations (see Section 2.1), pressure, volume compression, and even temperature (in combination with a suitable Equation of State) can be calculated from velocity histories [2, 3]. There are several different velocity interferometer systems commonly used in shock physics experiments [3], but in practice, two methods account for the vast majority of usage: Velocity Interferometry for Any Reflector (VISAR) and Photon Doppler Velocimetry (PDV).

First described by Barker and Hollenbach [31] in 1972, VISAR measures surface velocity by splitting the reflected laser light from a moving surface into two separate beams, delaying one of the beams in time through use of a precision optical etalon and then recombining the beams at a fast photo-detector. The resulting "beat frequency" of varying intensity at the detector is measured, and the number of "fringes" (i.e., a complete period of varying intensity) can be directly correlated to the velocity of the measured surface in time intervals down to several hundred picoseconds. One of the most significant disadvantages of the VISAR system is the occasional difficulty in correctly identifying fringes. In such cases, it is often necessary to manually add or remove fringes, move the reference center in the common quadrature analysis method for VISAR, or perform other manipulations of the data. Such methods can substantially change the calculated velocities, adding significant error depending on the validity of the assumptions made during the analysis.

PDV, a newer method introduced by Strand et al. [32] in 2006, does not suffer from such ambiguity. By directly combining a reference beam and the doppler shifted beam from a moving target's surface, a continuously varying sinusoidal signal is produced where the frequency at any given time corresponds directly to velocity. By analyzing this recorded signal with time-frequency digital signal processing methods, velocity traces can be extracted with a high degree of precision. This technique also offers the ability to resolve the velocity of multiple surfaces as several time-frequency analysis methods can separate out individual frequencies from the total response. The major disadvantage to this method

is relatively poor time resolution (practical minimum of approximately 2-5 nanoseconds, depending on signal quality), although newer upshifted PDV systems [33] and rigorous analysis techniques [34] have largely addressed this issue, improving the time resolution to sub-nanosecond intervals. Note that the theory, use, and data analysis process of PDV will be discussed in more detail in Chapter 3 as it was the primary reference diagnostic for this work.

Both PDV and VISAR have been applied to heterogeneous material systems, but their inherent limitations often limit their potential utility. Specifically, both systems measure the velocity of a surface at a signal point, usually of a diameter of a few hundred microns. If the size scale of the heterogeneity is larger than this small spot size, only an isolated localized response is measured. If the size scale of the heterogeneity is smaller, multiple reflected signals can convolute the VISAR signal (and to a lesser extent, PDV signals) to a degree that makes accurate velocity extraction exceedingly difficult.

A modification of VISAR systems, often called ORVIS or line-VISAR [35], allows for spatially resolved (often down to 10s of microns) surface velocity measurements down along a one dimensional line as well as increased time-resolution to tens of picoseconds with a suitably fast streak camera. This system has been applied to heterogeneous material systems, with impressive results [36], and line-VISAR remains one of the most promising techniques for determining shock-compression behavior in heterogeneous materials. At many research facilities and national laboratories globally, line-VISAR is typically considered state-of-the-art. While powerful, most line-VISAR systems are mechanically and optically complex, with an occasionally arduous data analysis process. Similarly, an augmentation of PDV systems that enables the use of multiple probes per digitizer channel ("multiplexing" [37]) allows for mm-scale spatial sensitivity and a relatively simple data analysis process. However, potential cross-contamination of the probe's signals and the requirement for relatively large samples restricts multiplexed PDV to fairly specific applications.

Even with the difficulties and limitations of optical velocimetry based systems, because of their widespread prevalence, they are still the most likely diagnostic method to be seen in the literature even when the focus is on heterogeneous material systems.

2.2.2 Stress Gauges

Instead of the indirect calculation of dynamic stress histories via velocity profiles and the Rankine-Hugoniot equations, pressure can also be measured directly by using a gauge with a suitable stress-sensitive property. In practice, piezo-electric and piezo-resistive materials represent the vast majority of dynamic pressure (stress) gauges, and within those bounds only a few designs represent the vast majority of experimental usage: X-cut quartz, manganin (a copper/manganese/nickel alloy), and PVDF (Polyvinylidene fluoride) gauges. Detailed discussion of gauge design and usage for these three methods can be found in other sources [2, 3, 38, 39, 40, 41]. In brief, for each gauge type, a time-resolved electrical current or voltage signal is measured, and the known changes in resistance or current generation as a function of pressure determine the experimentally measured stress history. As useful as these gauges are in many different types of shock experiments, two inherent limitations severely reduce their usefulness in the study of heterogeneous materials. For any electrically-based diagnostics, physical continuity in the sensing region is required in order for electrical conductivity (and thus signal continuity) to be maintained. Any irregularities in the shock front, which as discussed in Section 2.1 is a characteristic feature of shock in heterogeneous materials, may lead to premature and unpredictable failure of the sensing element and consequently severely inaccurate data.

For example, a piezo-electric quartz gauge is limited to pressures below its Hugoniot Elastic Limit of approximately 5 GPa. Localized pressure increases beyond this point lead to not only non-linear current generation, but also potential material failure at those points, compromising the physical integrity and electrical conductivity of the gauge. Similarly, manganin and PVDF gauges, having a typical thickness of 25 micrometers or less, have

limited structural resilience and will possibly fail or produce unreliable data under even moderate heterogeneous loads. Using meso-scale simulations, Gonzales [42] theorized that PVDF gauges applied directly to a reactive meso-scale mixture of hard titanium and boron powders failed prior to reaching peak pressure, limiting their usefulness in such an implementation. Concerns about gauge survivability can be allayed somewhat by separating the gauge and heterogeneous material by a relatively thick buffer material (which appears to be a common practice in the relevant literature), but this introduces undesirable ambiguity over the relationship between the equilibrated pressure at the gauge-buffer interface and the pressure experienced in the heterogeneous sample material.

A more fundamental problem of pressure gauges is the complete lack of spatial sensitivity. Localized regions of high pressure will produce current/voltage signals that are essentially indistinguishable from spatially uniform loads of lower magnitudes, averaging out any meaningful meso-scale information. Any pressure-based diagnostic that will have significant utility for experiments in complex heterogeneous materials must have some level of spatial sensitivity, and unfortunately none of the existing diagnostics meet this requirement. This is a well known problem (indeed, such a realization is the motivation for this work), and there are some promising designs for meso-scale time-resolved pressure diagnostics. The approach with the most attention may be implementations based on Fiber Bragg Gratings (FBGs), which will be discussed in more detail in Section 2.3.3 as they are somewhat similar to optical multilayer based sensors.

In the last several decades, use of time-resolved pressure gauges in shock physics research has decreased quite substantially, as the fundamental limitations discussed have proven to be not just limiting but often unworkable in many different applications. As the multilayer sensors in this work are essentially pressure sensors, this topic will be revisited in Chapter 7, highlighting important differences and improvements of the multilayers compared to the existing set of pressure-based diagnostics.

2.2.3 Temperature Gauges

Accurately measuring dynamic temperature in even homogeneous materials is an exceedingly difficult task, and there are very few methods that can produce reasonably accurate data. Optical pyrometry (see [43] for a classic review from the National Bureau of Standards) is perhaps the most common method. With suitable resources and expertise, very capable systems based on optical pyrometry that even have spatial sensitivity have been demonstrated [44]. Recent work by Basset et al. [45] demonstrated a novel pyrometer design based on photo-multiplier tubes (PMTs) that combines broad temporal resolution with enhanced accuracy based on a relatively high number of spectral channels. Other potential techniques are embedded temperature gauges [46], time-resolved Raman spectroscopy for suitable materials [47], careful interpretation of Extended X-ray Absorption Fine Structures (EXAFS) data [48], and novel reflectance modulation approaches [49]. Forbes [3] has a more complete discussion of this issue.

As with optical interferometry and pressure sensing based approaches, temperature measurements are limited to surfaces or discrete (typically planar) interfaces. While for particle velocity and pressure sensing, where equilibration time-scales are relatively quick, for many materials and loading conditions the dynamics of temperature distribution and equilibration rates are unknown. This adds relatively more complexity to the use of time-resolved temperature diagnostics and analysis of such data. As such, the average *practical* capability in the field of shock physics for time-resolved temperature sensing is quite limited, although there is significant interest in producing additional temperature diagnostics that can be utilized for time-resolved thermal investigation of many different classes of materials, especially heterogeneous energetic materials. Because of this interest and theoretical importance, the effects of temperature on the proposed multilayer structures will be discussed in more detail in Chapter 4.

2.3 Multilayer Optical Structures

Having established the relevant context in the study of shock responses in heterogeneous materials, and the current state of time-resolved diagnostics in the field, it is now appropriate to discuss the history and development of multilayer optical structures as well as define the concepts and terms that will be used throughout the remainder of this work.

Fundamentally, multilayer optical structures are photonic crystal structures with 1-dimensional periodicity that have characteristic spectral responses (i.e., distinct transmission/reflection profiles) determined by the optical properties of the component materials, the structure of the multilayer, and the type and extent of the periodicity. Broadly, there are two general classes of multilayer structures: Distributed Bragg Reflectors (also called dielectric mirrors) and optical microcavities (also called optical resonators or fabry-perot cavities/resonators). Moving forward, any multilayer structure having features typical of Distributed Bragg Reflectors will be termed a DBR, and any multilayer structure having features typical of a microcavity will be termed an OMC. Each of these general classes is discussed separately below.

2.3.1 Distributed Bragg Reflectors (DBR)

DBRs are optical structures composed of alternating layers of materials with different layer thickness and different material refractive indices. The fundamental mathematical and physical frameworks were first published in the 1950s and 1960s, and Lissberger's [50] review in 1970 provides the foundational references. More rigorous mathematical approaches based in modern optical theory were also developed around this time [51, 52, 53]. Practical fabrication techniques were demonstrated a few years later for both polymer [54] and dielectric multilayers [55]. These referenced works represent merely the more important developments, as DBR-based optical filters, lasers, and mirrors have had significant research and commercial applications for several decades, and the full body of literature is

extensive. The relevant information in the context of the present work is the basic physical features of DBRs and simple analytical models that describe their spectral features.

The schematic shown in Figure 2.12a shows such a representative physical structure for a DBR, along with the form of a typical reflectance spectrum produced from a representative structure, calculated with the transfer-matrix method for periodic structres as implemented in OpenFilters [56]. In this example, the DBR structure is based on alternating layers of two very common dieletric materials in optical thin-film applications: fused silica (SiO_2) and amorphous Al_2O_3, with optical properties for each obtained from [57] and [58], respectively. The layers are of uniform thickness, each 300 nm for a total of 20 individual layers (or 10 bi-layers). The layers are generally deposited on optical-grade substrates that are at least several hundred microns thick.

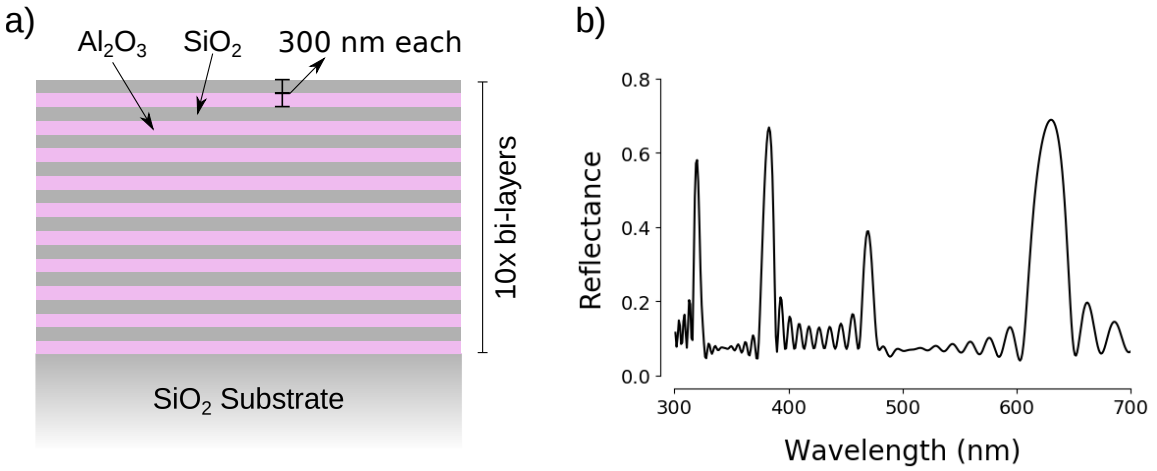

Figure 2.12: (a) The general structure of an example SiO_2/Al_2O_3 DBR device having alternating layers with individual refractive indices n_i and/or thickness d_i. (b) The number of layers can vary greatly depending on the desired spectral features, such as the full width half max (FWHM) and height of the characteristic reflectance peaks. This example structure has 10 bi-layers, or 20 alternating layers of each material.

As broadband light is incident to the multilayer either at the top surface or through the transparent substrate (for simplicity, the light is assumed to be perpendicular to the direction of the periodicity), reflection and refraction occur at the interface of each component layer in the structure. For a given wavelength of light, the optical path length (OPL) for any

given layer is defined as:

$$OPL = n(\lambda)d \tag{2.4}$$

where n is the real component of the refractive index for a non-dispersive material. For a given wavelength of light, the OPL for the combination of layers in the multilayer will lead to either partial/full *constructive* interference, or partial/full *destructive* interference. This phenomenon is what produces the characteristic reflection or transmission profile seen in Figure 2.12b, where specific wavelength ranges produce peaks of high reflectance. The position, width, and height of the peaks (hereafter referred to as reflection peaks) can be rigorously defined via solutions to Maxwell's equations for electromagnetic wave propagation in a periodic medium. However, simpler analytical equations can also be derived that provide a more intuitive, if qualitative, understanding to a broader audience.

The full width half max (FWHM) $\Delta\lambda$, peak position λ_0, and peak height R_{DBR} are defined by Equations 2.5 - 2.7, for a DBR consisting of two dielectric materials with individual layers thicknesses (d_1, d_2), refractive indices (n_1, n_2), and normally incident broadband light. Unless otherwise noted, a zero-valued extinction coefficient k in the complex refractive index $n = n_r + ik$ is assumed, which is accurate for many common dielectrics.

$$\lambda_0 = \frac{2}{m}(d_1 n_1 + d_2 n_2) \tag{2.5}$$

$$\Delta\lambda = \frac{4\lambda_0}{\pi} sin^{-1}\left(\frac{n_2 - n_1}{n_2 + n_1}\right) \tag{2.6}$$

$$R_{DBR} = \left(\frac{n_2^{2N} - n_1^{2N}}{n_2^{2N} + n_1^{2N}}\right)^2 \tag{2.7}$$

In Equation 2.5, m is the order of the reflection peak, and in Equation 2.7 N is the total number of bilayers (i.e., a pair of two adjacent layers, one of each material). The order

(m) of the peak defines its particular position in the reflectance spectrum, with higher order peaks positioned at lower wavelengths. For example, in Figure 2.12 four peaks can be seen, each corresponding to different orders. Based on these equations, it is apparent that a higher refractive index contrast between the two component materials will produce a wider FWHM in the characteristic peak, and that a higher number of bilayers will produce a higher peak reflectivity. The order of the peak (m) also has an effect on the peak width and height, though the relationship is more complex. Lee et al. [59] conducted a more comprehensive analysis of the relationship between all of these variables for custom DBR structures, including comparison of these models to experimental data from fabricated samples. Note that refractive index is also a function of wavelength, which will have an effect on these spectral features, especially for high/low order reflection peaks.

As there is great flexibility in the spectral features of different DBR designs, many of the commercially designed and available filters are optimized for particular performance metrics. To achieve this, typically a large number of layers (sometimes several hundred), many different layer materials (occasionally 3 or more per design), and complex designs (i.e., combined DBRs in a single optical element) are leveraged. While this provides very high quality spectral performance, the mechanical complexity of the DBR becomes prohibitive for sensing applications. As such, a different design process for creating DBRs optimized for dynamic sensing is needed, which will be discussed in more detail in Section 4.1.

2.3.2 Optical Microcavities (OMC)

Optical Microcavities are, in their most general form, 1-dimensional optical resonators composed of a central resonating cavity surrounded by reflective surfaces. A Fabry-Perot cavity [60] is the simplest and oldest form of an OMC, and the many variants developed since then are typically manifestations of this basic design. Valhala [61] provides a thorough overview of modern microcavity designs and applications, which are well beyond the

application of OMCs to this work. In the present context, the simple concept of a Fabry-Perot resonator is sufficient, and further discussion will be focused as such.

The schematic shown in Figure 2.13 illustrates an example structure for an OMC, along with the calculated reflectance spectrum for the design, again using the transfer-matrix method in OpenFilters [56]. The OMC is based on a 500 nm fused silica resonating cavity, with thin layers of silver (125 nm and 35 nm) serving as the reflective mirrors, all deposited on a fused silica substrate. As the mirror layers are different thicknesses, the structure is technically not periodic and as such will be referred to as an asymmetric optical micro-cavity (AOMC). The mechanism of operation is similar to that described for the DBR in Section 2.3.1. The optical path length (cavity thickness times cavity refractive index) of the central cavity (Equation 2.4) will support a resonant cavity mode at a specific and narrow range of wavelengths, and even with high reflectivity mirrors the optical resonance develops extremely quickly as long as at least one of the mirror layers is thin enough to allow sufficient energy from the incident light to transmit partially into the cavity layer. This process produces high transmission and low reflectivity at the resonant wavelength.

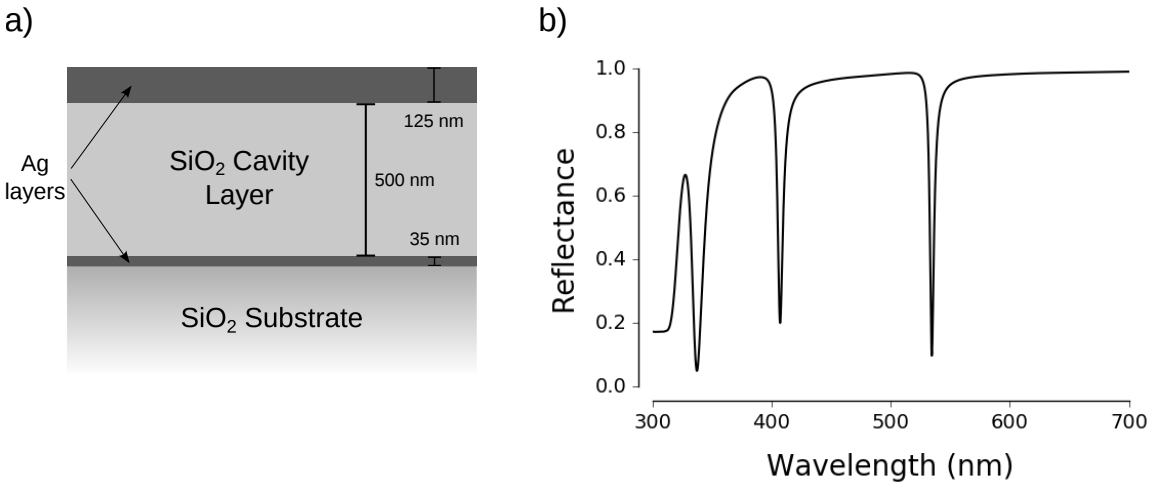

Figure 2.13: (a) The general structure of an AOMC (a) is a central resonating cavity surrounded by high reflectivity mirrors. (b) The typical spectral response of the AOMC depends on the thickness and refractive index of the cavity layer and the quality of the mirror reflection, but generally consists of narrow transmission bands (modes) which are a function of the cavity thickness and refractive index.

Again similar to DBRs, rigorous mathematical analysis based on Maxwell's equations can be formulated for AOMCs, but simpler analytical models based on Fabry-Perot cavities have more utility in the context of this work.

The FWHM ($\Delta\lambda$), peak position λ_0, and the cavity mode depth R_{OMC} are defined as follows for arbitrary cavity and mirror materials:

$$\lambda_0 = \frac{2}{m}(d_{cavity}n_{cavity} + 2d_{mirror}^{skin-depth}) \tag{2.8}$$

$$\Delta\lambda = \frac{\lambda_0^2(1-R)}{2n_{cavity}d_{cavity}\pi\sqrt{R}} \tag{2.9}$$

$$R_{OMC} = \frac{R_{max}}{R_{min}} \approx \frac{4R}{(1+R)^2} \tag{2.10}$$

where d_{cavity} and n_{cavity} are the thickness and refractive index of the cavity material, which is assumed to have a zero valued extinction coefficient k. Note that $d^{skin-depth}$ is the penetration depth of light into the reflective mirrors, and is generally zero for dieletrics and non-zero for metals [62]. In the latter case, the amount of penetration into the mirror layers effectively changes the optical path length of the cavity, which is why this variable must be included in Equation 2.8. Finally, m is again the order of the resonant cavity mode (in Figure 2.13b three modes are visible), and R is the reflectance coefficient for the mirrors. Note that Equation 2.10 is technically a ratio of reflectance values, and thus is a relative rather than absolute measurement. It is apparent from these equations that the quality and material of the reflective mirrors contribute significantly to the spectral response of the OMC, which provides significant flexibility in achieving a desired optical response.

As with DBRs, in practice many commercial optical microcavities utilize specific methods to achieve particular performance metrics. For example, by using dielectric based DBR's as the mirror layers, as well as specific materials and cavity layer thicknesses, very

precise features of the cavity mode can be obtained. This may or may not be useful for sensing applications, as it increases the complexity and thickness of the overall structures. Section 4.1 will again discuss these trade-offs in more detail, with a focus on the application to dynamic sensing.

2.3.3 Optical Multilayer Based Sensors

Based on the mechanisms of operation and equations discussed in Sections 2.3.1 and 2.3.2, it is apparent that any externally induced changes in layer thicknesses and material refractive indices will produce changes in λ_0, $\Delta\lambda$, and R_{DBR} or R_{OMC}. By measuring the changes in these parameters as a function of some externally applied condition, correlations can be made between changes in optical response and the level and type of the external condition. This approach forms the basis for many different types of optical sensors based on multilayer structures.

For example, Kolle et al. [63] demonstrated sensing of mechanical stress and strain for polymer based multilayers by tracking the shift of the characteristic peak as a function of applied in-plane strain. Figure 2.14 shows the results of their experiment, with (a) and (b) demonstrating the shift of the multilayer color and reflectance peak position as strain is applied and (c) showing the peak position as a function of strain compared to predictions of a linear elastic model. This model shows an excellent match to the experimental results, and is based on the combination of Equation 2.5 and the length change relationship for an isotropic, homogeneous medium with a poisson ratio (ν) of 0.5:

$$\left(1 + \frac{\Delta L_{11}}{L}\right)^{-0.5} = 1 - \frac{\Delta L_{22}}{L} \tag{2.11}$$

$$\lambda(\epsilon_{11}) = \frac{\lambda_0}{\sqrt{1-\epsilon_{11}}} = \lambda_0 \left(1 - \frac{\Delta L_{22}}{L}\right) \tag{2.12}$$

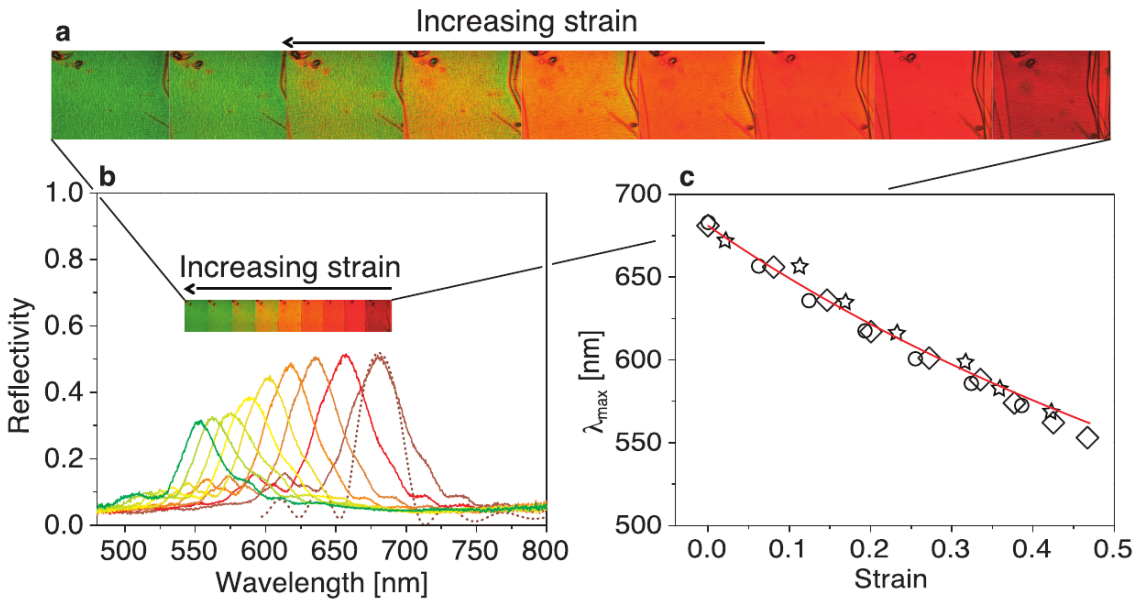

Figure 2.14: Experimental spectra, DBR visible color, and model performance for a polymer-based DBR [63]. (a) shows the visible color of the DBR at increasing levels of strain, (b) shows the shift of the characteristic reflection peak as a function of in-plane strain, and (c) comparison of experimental data to a linear elastic model. The different symbols in (c) correspond to three consecutive strain cycles (circles, diamonds, and stars), demonstrating the repeatability of the behavior. Figure reused with permission.

Where $\Delta L_{11}/L$ is the strain in the x-direction (i.e., parallel to the layers of the DBR) and $\Delta L_{22}/L$ is the strain in the y-direction (perpendicular to the layers of the DBR). The right side of Equation 2.11 is essentially a scaling factor for the layer thicknesses in Equation 2.5, which decreases as the in-plane strain increases from the Poisson effect.

Important to the context of the present work, Kamita et al. [64] have also demonstrated sensing of heterogeneous mechanical strain states. By deforming polymer-based DBRs over pin-holes with increasing levels of air pressure, they observed formation of DBR "bubbles." By probing the spectral response along the curvature of the bubble, they were able to correlate different strain states to each localized spectrum. Figure 2.15 shows the results of this experiment. Crucially, this data empirically establishes the potential for spatially-resolved sensing using multilayers and provides a solid basis to extend the application of these structures to the dynamic loading regime.

Beyond, sensing of stress and strain, multilayer structures have been used to measure

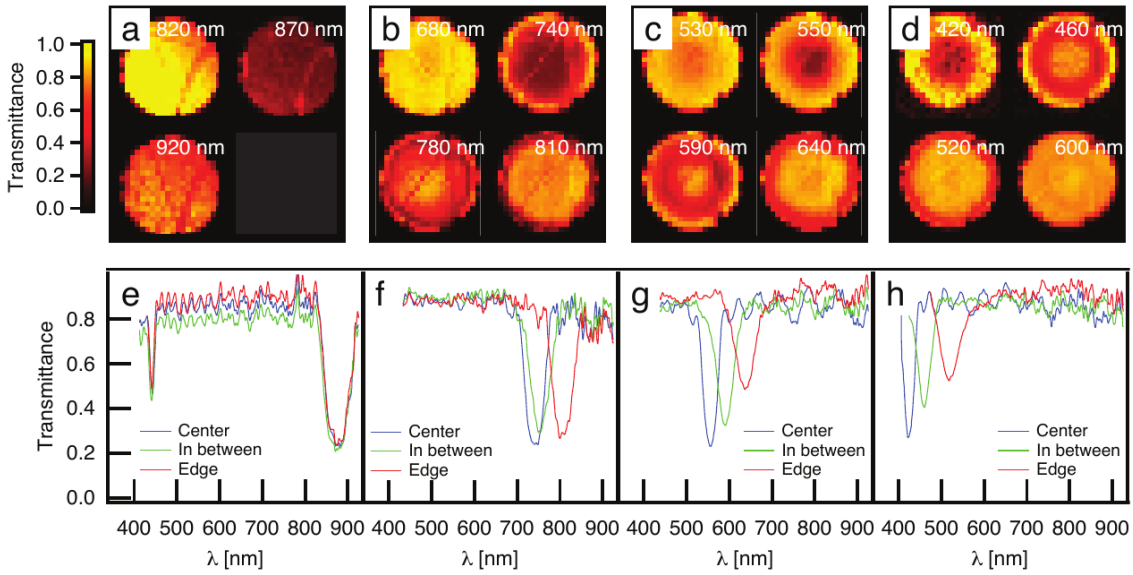

Figure 2.15: Localized spectra and images corresponding to the center, edge, and in-between regions of bubble formed by deforming a polymer-based DBR over a pin-hole with increased atmospheric pressure. (a-d) show images of reflectance intensity and discrete wavelengths at the initial un-deformed state, residual post-deformed state, P = 0.17 bar, and P = 0.27 bar, respectively. (e-h) are spectra corresponding to the states in (a-d), with each curve representing localized spectra from the center, edge, and in-between points of the deformed bubble.

many other variables and responses. Temperature sensing with metal oxide based multilayers has been demonstrated [65, 66], as well as combined thermomechanical sensing [67]. By carefully designing the component materials and structure in the multilayer, precise chemical sensing is even possible [68]. Broadly, a survey of the literature indicates that there are many unique and interesting designs employing variations of multilayer optical structures for sensing purposes, but an exhaustive description of such work is beyond the scope of the present analysis. The important trend to observe is the common factor in this body of research: *designing multilayer based sensors by correlating induced changes in optical responses to externally applied physical or chemical states*.

Despite the potential and demonstrated capabilities of multilayer optical sensors, there is limited research indicating application of such multilayer structures to *dynamic* loading conditions. Kim, et al. [69] demonstrated the time-resolved response of an OMC-tipped

fiber optic to a transient 1.56 Mhz burst pressure wave of approximately 0.3 MPa, and earlier work demonstrated refractive index sensing with a time resolution of 10's of microseconds using a similar design [70]. Similarly, Cranch et al. [71] used fiber optics with tip-mounted sensors of several types (including an OMC) to measure laser-shock induced pressure up to 3.4 GPa with improved time-resolution. Other examples can be found in the literature, with the common theme of 10's of nanoseconds to millisecond time-resolution and magnitudes of mechanical loading typically well under several GPa. Under higher magnitudes and rates of loading, approaching and entering the regime of shock loading, the literature is more scarce. The most relevant existing work is with Fiber Bragg Gratings (FBGs). FBGs can be simplistically described as a standard fiber optic with an embedded DBR perpendicular to the direction of light propagation, producing a characteristic reflection peak/transmission value in the returned/transmitted spectrum through the fiber.

This particular research area has had increasing interest in the recent past, largely due to the well-demonstrated utility of FBG-based sensors for extreme environments in many industrial and commercial applications (see [72, 73] for a survey of the foundational literature). More recently, several examples of time-resolved, high-pressure sensing with FBGs have been published. Deng et al. [74] captured a 1.4 GPa pressure wave in water, deriving the pressure profile from the spectral shift of the FBG spectrum. Rodriguez et al. [75] similarly applied a FBG sensor to a 1.4 GPa pressure wave in polymethylmethacrylate (PMMA), and Cranch et al. [71] conducted similar experiments in PMMA at 3.4 GPa. Similar experimental approaches and pressure ranges were also demonstrated by other groups [76, 77]. Broadly, these initial approaches typically recorded light intensity over time with various methods. Through knowledge of the FBG spectrum, the measured intensity histories could be converted to calculated spectral shifts with varying levels of accuracy. Even more recently, advanced approaches based on time-resolved spectroscopy have captured complete histories of FBG spectra under shock loading. Figure 2.16 shows the response of a polarization-maintaining fiber bragg grating (PM-FBG) sensor under explosively driven

dynamic loads of up to ~0.7 GPa, tracking the spectral position of both the fast and slow (ordinary and extraordinary) spectral peaks as a function of the generated pressure (Rodriguez et al. [78]). A PM-FBG was chosen in an attempt to isolate the effects of temperature and pressure on the spectral shifts, though it was determined that the temperature effect was not rapid enough for such a comparison.

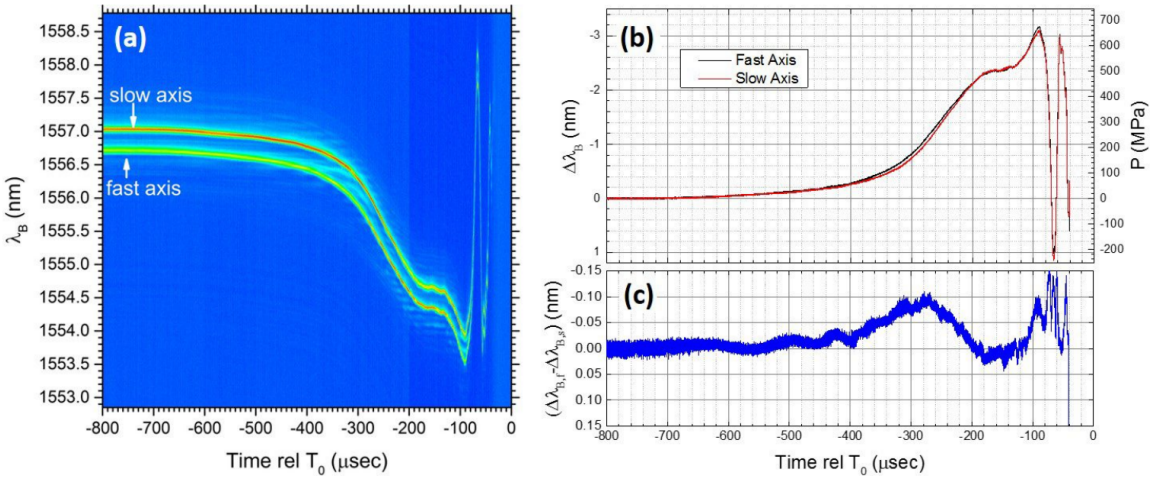

Figure 2.16: Time-resolved spectral response of PM-FBG sensor under explosive dynamic loading [78]. The streak-contour in (a) shows the spectral peaks for both the slow and fast (ordinary and extraordinary) and their spectral position in time with respect to T_0, the point at which the casing for the experimental sample is destroyed. This data is extracted in and shown separately in (b), plotting the spectral shift ($\Delta\lambda_B$) as a function of applied pressure, and (c) shows the difference in spectral shift between the fast and slow optical axis of the PM-FBG.

Other relevant work has shown very promising results in detonation front velocity measurements in explosive systems using chirped FBGs (i.e., FBGs with a slow increase in the periodic spacing and thus a broad reflectance "band"), leveraging the time-resolved change in the width of the reflectance band as the denotation front propagates along the fiber.

Overall, FBG's show very promising results for time-resolved sensing of dynamic loading. However, there are several key differences between dynamic sensing with FBGs and the proposed multilayer pressure sensors investigated in the present work. First, the FBGs as discussed in the existing literature are most often implemented as embedded gauges. Thus, their response is localized to the region surrounding the fiber. Additionally, any dis-

turbance to the surrounding material needs to be accounted for in the analysis of the FBG data, especially if there are heterogeneities of the scale as the fiber (~125 micron). Second, the FBGs typically implemented have lengths in the 1-10 mm range. This improves the spectral quality of the reflectance peak significantly, but also potentially decreases the fundamental temporal resolution of their response, as it takes longer for a pressure pulse to equilibrate along such a length. Short FBGs could show similarly promising results, though the existing literature does not appear to address this directly. Third, the experimental and data collection approaches for FBGs tend to focus on time-resolutions of 10's of nanoseconds and above. While this resolution is sufficient for many applications, it is generally not competitive with many of the existing diagnostics discussed in Section 2.2 and may be insufficient for many complex heterogeneous materials. Again, there are likely ways to increase the temporal resolution of FBG-based dynamic sensors, but existing work does not appear to address this directly. Thus, while FBGs are likely to have much utility in the area of time-resolved sensing, there is much less overlap in both capability and potential applications compared to other multilayer structures than a superficial analysis would indicate.

Overall, the review of the current state of multilayer-based sensing presented in this chapter leads to two primary conclusions. First, there is significant evidence demonstrating the broad utility of multilayer sensors, across mechanical, optical, and chemical sensing applications. Second, there is a small but growing body of work demonstrating that multilayer structures (in various forms) have potential in dynamic sensing, particularly for high strain rate and high magnitude pressure sensing. Nevertheless, there are still several key questions that need to be answered to fully establish the potential of multilayer structures in dynamic sensing:

1. What, if any, are the design criteria that produce multilayer structures with physical and optical characteristics that are best suited for dynamic pressure sensing?

2. What is the theoretical maximum temporal resolution of different multilayer struc-

tures? Is this maximum sufficient to capture important meso-scale phenomena relevant to the dynamic response of heterogeneous materials?

3. Can the mechanical and optical behavior of multilayers under dynamic loading be accurately predicted with physics-based, empirical, or combination models? If so, what insights do these models provide?

4. Can multilayer structures provide spatially-resolved data competitive with or exceeding existing diagnostic methods?

5. What are the practical considerations of implementing multilayer-based sensing into existing methods for dynamic loading experimental work? What are the different approaches for collecting and analyzing data, along with their relative advantages/disadvantages?

The following chapters turn to these questions.

CHAPTER 3
TECHNICAL APPROACH

As the main objective of this work is to rigorously evaluate the potential of multilayer optical structures as time-resolved meso-scale diagnostics, significant effort has been focused on developing experimental and computational methods of investigation that are appropriate for use of multilayers in sensing applications. There are several unique capabilities that need to be developed to conduct such investigations, and Chapter describes the individual components of the experimental and computational systems that were developed in detail.

3.1 Experimental Setup

The experimental evaluation of the multilayer structures to shock-compression is essential as this information is needed to validate the theoretical models discussed subsequently in Section 4.2, and the simulations produced with the methods presented next in Section 3.2. Such a system needs four features in order to produce data of sufficient quality:

1. A shock-compression system capable of producing well-controlled uniaxial-strain shock loading on a scale appropriate to test the multilayer structures (i.e., 10-20 mm^2 shocked area and "steady-state" shocked thicknesses of 10s of microns)

2. A time-resolved spectral collection system capable of recording spectra with nanosecond or sub-nanosecond time resolution while maintaining sub-nanometer spectral resolution

3. A benchmark interferometry diagnostic system that can provide *in-situ*, simultaneous particle velocity data to validate the response of the multilayers

4. A series of collection optics that enables simultaneous illumination and collection pathways for both the spectrograph and the benchmark interferometry diagnostic system

The final version of experimental setup designed and utilized in the present work is shown in schematic form in Figure 3.1, comprising all four requisite capabilities. The features and specifications of the combined system are summarized in Table 3.1, and the details of each component are discussed in the following sections.

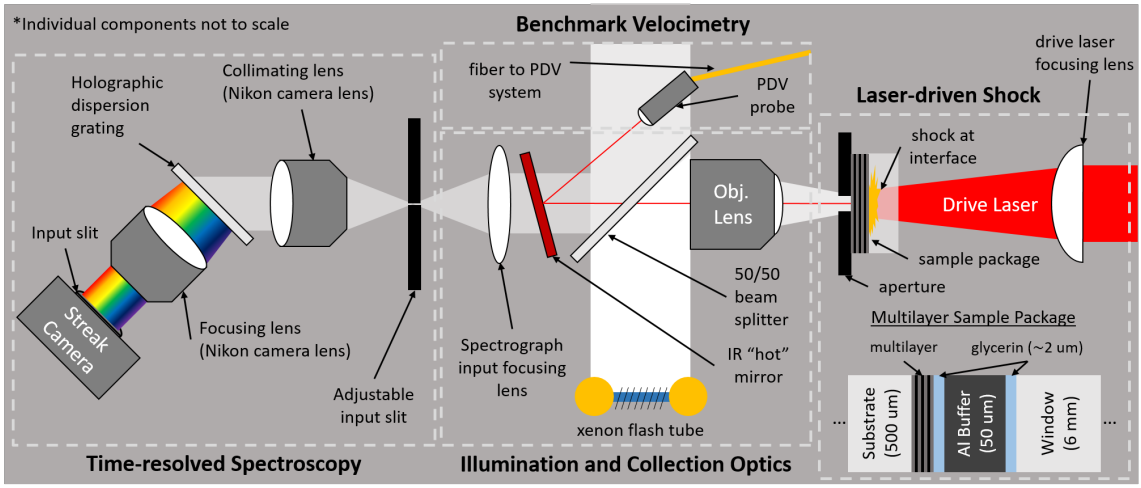

Figure 3.1: Schematic of the developed experimental setup for evaluation of the shock response of multilayer structures, combining laser-driven shock, simultaneous velocimetry (PDV), and time-resolved spectroscopy, all coupled with custom illumination and collection optics.

3.1.1 Laser-Driven Shock Compression

There are many different ways to produce well-controlled uniaxial-strain shock loading for a wide range of material types and sample sizes. A complete discussion of the history and current status of such capabilities can be found in other sources [2, 3]. The method of choice for the present work is laser-driven shock loading. Describing this approach succinctly, when a laser of sufficiently high energy is incident on a opaque material's surface the resulting energy deposition into the material is sufficient to produce a localized plasma,

Table 3.1: Relevant specifications of the combined experimental setup shown in Figure 3.1

System Specifications

Laser-driven Shock Loading	Time-Resolved Spectrograph	Benchmark Diagnostic (PDV)
Pressure Range: 1 - 12 GPa	Temporal Resolution: 225 ps	Temporal Resolution: ~1 ns
Pressure Rise-time: 2-4 ns	Spectral Resolution: ~0.15 nm	Operating Wavelength: 1550 nm
Pressure Profile: Triangular	Spectral Range: ~150 nm	Surface Type: diffuse or specular

which expands rapidly driving a psuedo-1D planar shock wave outwards from the point of incidence. This shock wave can then be allowed to either propagate directly into a sample or launch miniature flyers for impact at high velocities, as illustrated schematically in Figure 3.2.

In the last several decades, this technique has been refined significantly and is typically used to launch miniature flyers at speeds ranging from hundreds of m/s to several km/s [79], or to generate high pressure pulses in a confined or open direct-shock approach [80, 81] with pressure pulse widths ranging from 10's of picoseconds to 100's of nanoseconds. The physics and practical aspects of these shock wave generation methods are quite complex, and Kelly [82] has described a thorough review of this topic.

For the present work, the confined direct-shock approach is utilized due to it's simplified setup compared to miniature flyer launches as well as the high degree of repeatability in the shape and duration of the induced shock pressure load. Figure 3.3 shows a typical rear-surface velocity profile resulting from a confined direct-shock of a 100 μm aluminum foil. This pulse is representative of the pressure pulses that are used to evaluate the shock-compression response of the multilayer structures in the present work.

The drive laser used in this work is a Nd:YAG Continuum Powerlite Precision II, operating at 1064 nm with up to ~2.5 Joules of energy per pulse. The input beam (~10 mm in diameter) is focused onto the sample package using an aspheric best-form condenser

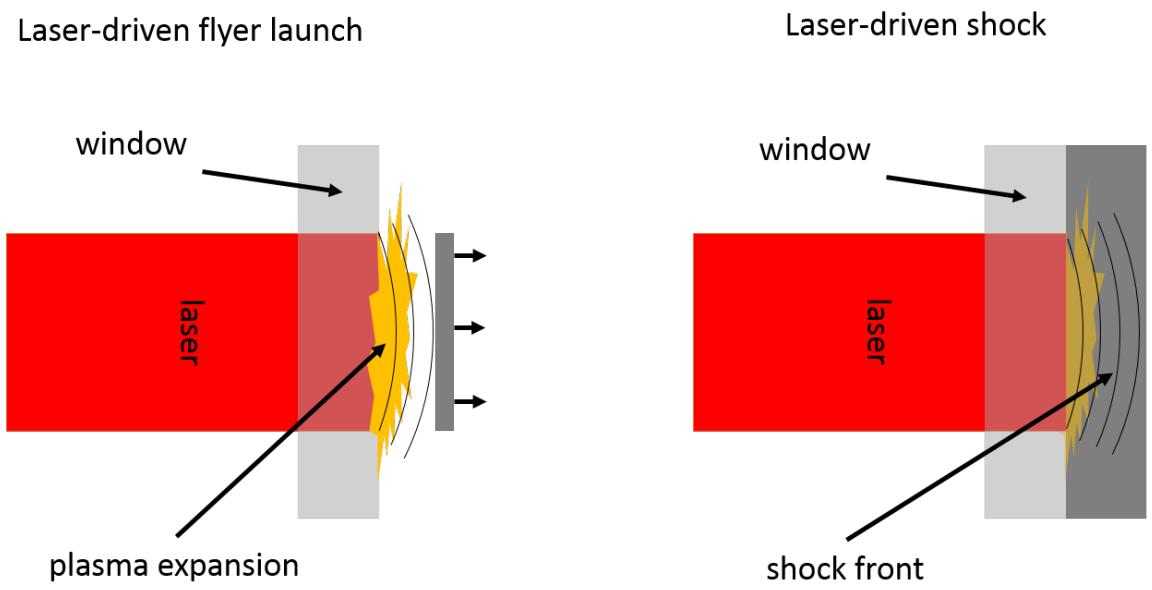

Figure 3.2: Schematics demonstrating the process of laser-launched miniature flyers (left) and confined direct shock (right).

lens (Edmund Optics 89442) to a diameter of 1-4 mm. One particularly relevant aspect of this process is the spatial profile of the input drive laser. Figure 3.4 shows a simplified schematic of the optical setup of the driver laser beam pathway, which includes a beam shaper (π-Shaper 12_12_1064_HP) to convert the super-guassian beam profile into a psuedo-tophat profile. This shaping step is important as it ensures a more uniform pressure load generated by the drive laser, producing an input pressure to the multilayers that can be reasonably approximated as 1-dimensional. Again, Kelly [82] has a more complete description of this particular laser as well as the beam shaping optics.

3.1.2 Time-Resolved Spectroscopy Setup

In traditional spectroscopy, a resolution requirement of < 1 nm is easily met, with numerous commercial options providing such specifications. In the field of shock physics, time-resolved spectroscopy is frequently accomplished with the combination of such commercial spectrographs and a fast optical streak camera [83, 84]. Briefly, a streak camera functions by converting input photons from the spectrograph to electrons via a photocath-

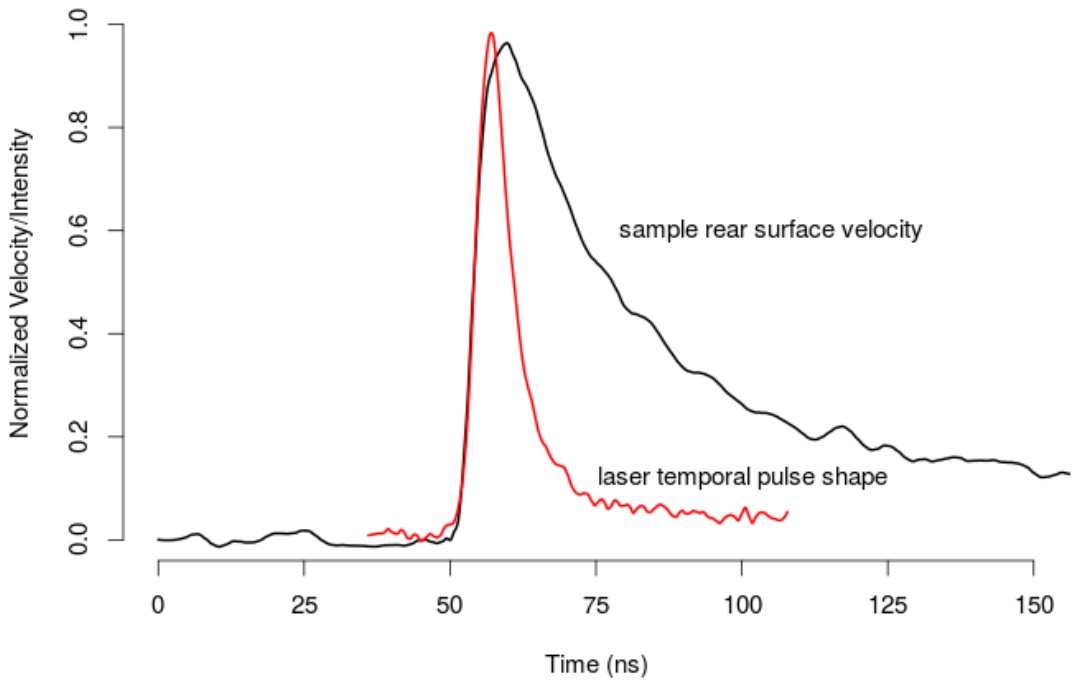

Figure 3.3: Representative profiles of the laser-driven shock velocity profile at a sample's rear free surface as well as the temporal pulse shape of the drive laser. The specific features of the velocity profile such as rise-time and peak pressure are dependent on sample material and thickness.

ode, and then "streaking" the electrons via a time-varying voltage field across a phosphor screen. This produces a 2-dimensional image with wavelength along one axis and time along the other. Figure 3.5 shows a schematic of the internal operation of a Hamamatsu streak camera [85] as well as an image produced from such a spectrograph-streak camera combination capturing chromatic dispersion in a optical fiber. The Hamamatsu document [85] also serves as a useful primer on the fundamentals and operation of streak cameras. Note that the data analysis process for the streak images can be complex as multiple correction steps are required to account for equipment biases. For documentation and examples of this process, see Appendix B.

However, in many cases such spectrograph/streak camera combinations have limited light collection efficiency (i.e., large f/numbers), which limits the signal-to-noise ratio of

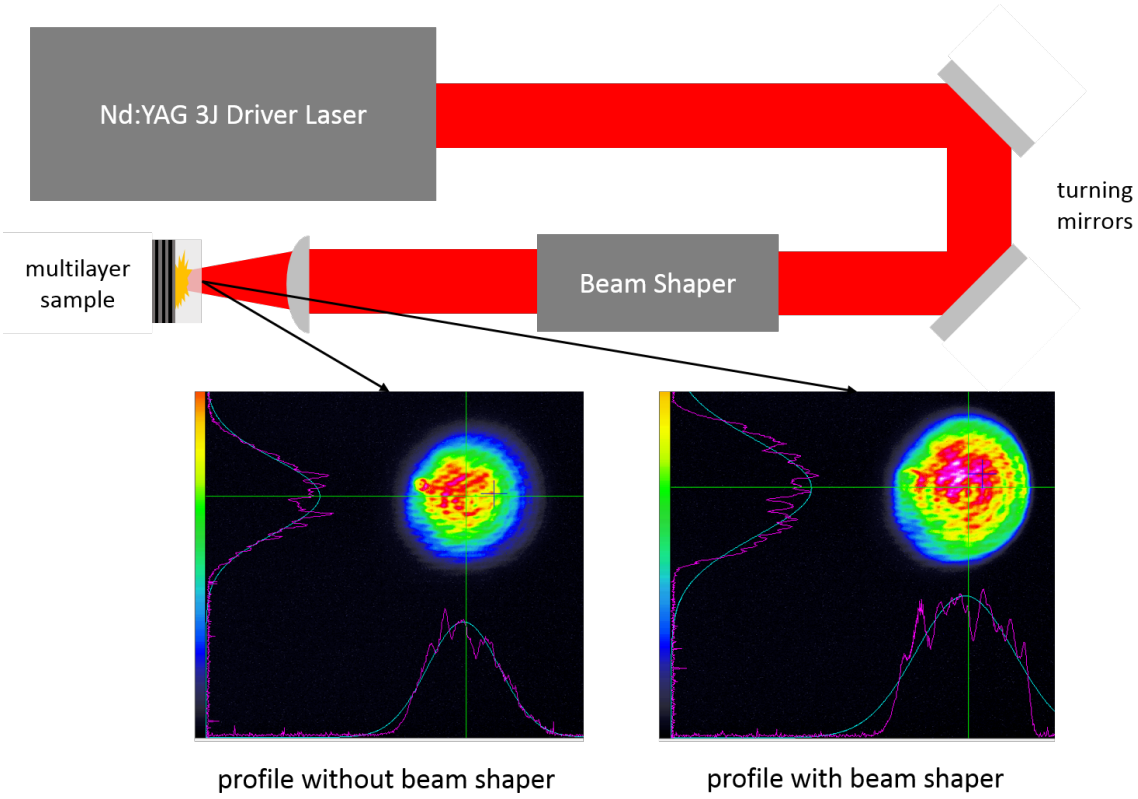

Figure 3.4: Schematic showing the arrangement of the Nd:YAG 3J drive laser with turning mirrors and beam shaping optics. Example beam profiles at the surface of a multilayer sample (~3 mm beam diameter) with and without the beam shaping optics demonstrate the change in the spatial energy distribution in the drive laser beam due to the beam shaper, which takes energy from the tails of the psuedo-gaussian initial spatial profile and deposits it more toward the center of the beam to create a "tophat" profile.

the collected spectra under short-time conditions. This issue is magnified enormously in the present work, as *broadband, visible light* spectra need to be collected on nanosecond time-scales in order to effectively evaluate the response of the multilayers to the nano-second duration shocks from the laser-driven shock setup described in this Section. A high-powered broadband light source can partially address this limitation, but even such sources can have relatively limited power/nm output especially when compared to coherent, narrow wavelength sources. As such, during the development of the complete system shown in Figure 3.1, it was determined that a custom spectrograph designed to optimized light throughput was necessary in order to give the overall system a sufficient signal-to-noise ratio.

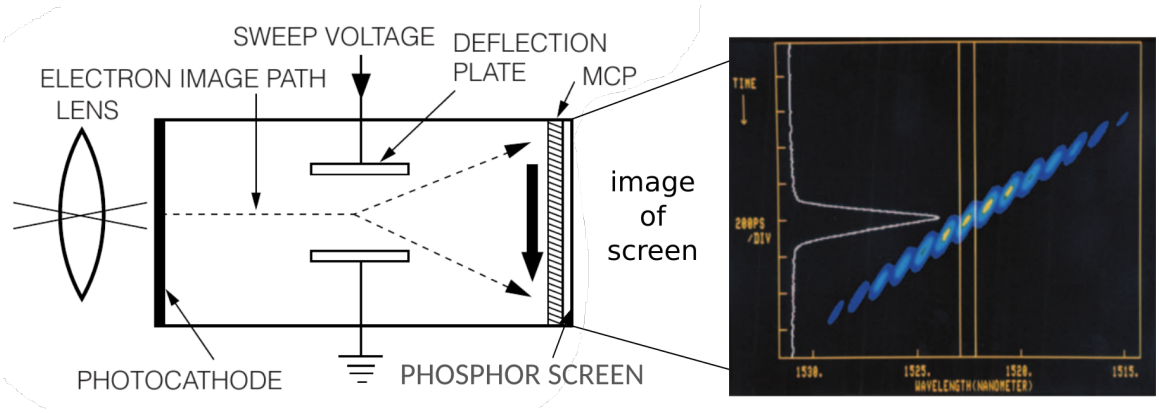

Figure 3.5: Example schematic (left) showing the operation principle of the streak camera. The spectroscopically dispersed input light (focused to a 1-dimensional line) is converted to electrons by the photocathode, and the time-varying sweep voltage "streaks" the electrons along the phosphor screen. A camera images the fluorescent phosphor screen, creating a 2-dimensional image (right), in this case of chromatic dispersion in an optical fiber with time along the sweep direction and wavelength along the input spatial dimension. Both the schematic and example streak image are from [85].

Dlott, et al. [86] have constructed a similar experimental setup based on a streak camera and a custom prism-based spectrograph, with an f/number of ~f/1.6 (NA=0.3). With this approach, many impressive results with excellent signal-to-noise ratios have been obtained even at nanosecond timescales [84, 87, 88]. Based on this example, a similar approach was followed in the construction of the system used in this work. Using a similar design (Dr. Nick Glumac, personal communication, 8/24/2015) based on a dispersive holographic transmission grating (Wasatch Photonics WP-1800/532-50.8) and commercial DSLR camera lenses (Nikon 135 mm f/2 AIS DSLR, Rokinon 85mm f/1.4 AS IF UMC), a spectrograph with an effective f/number of f/1.4 was assembled. Figure 3.6 shows an image of the completed spectrograph coupled to an Optronis SC-20 Streak Camera. The maximum spectral and temporal performance of this combined system was shown in Table 3.1. For more information on the design, construction, and use of this spectrograph, see Appendix A.

Finally, it is important to note that there is an inherent limitation in the spectroscopic probing of the two-dimensional rear surface of the multilayers. In the present setup, the

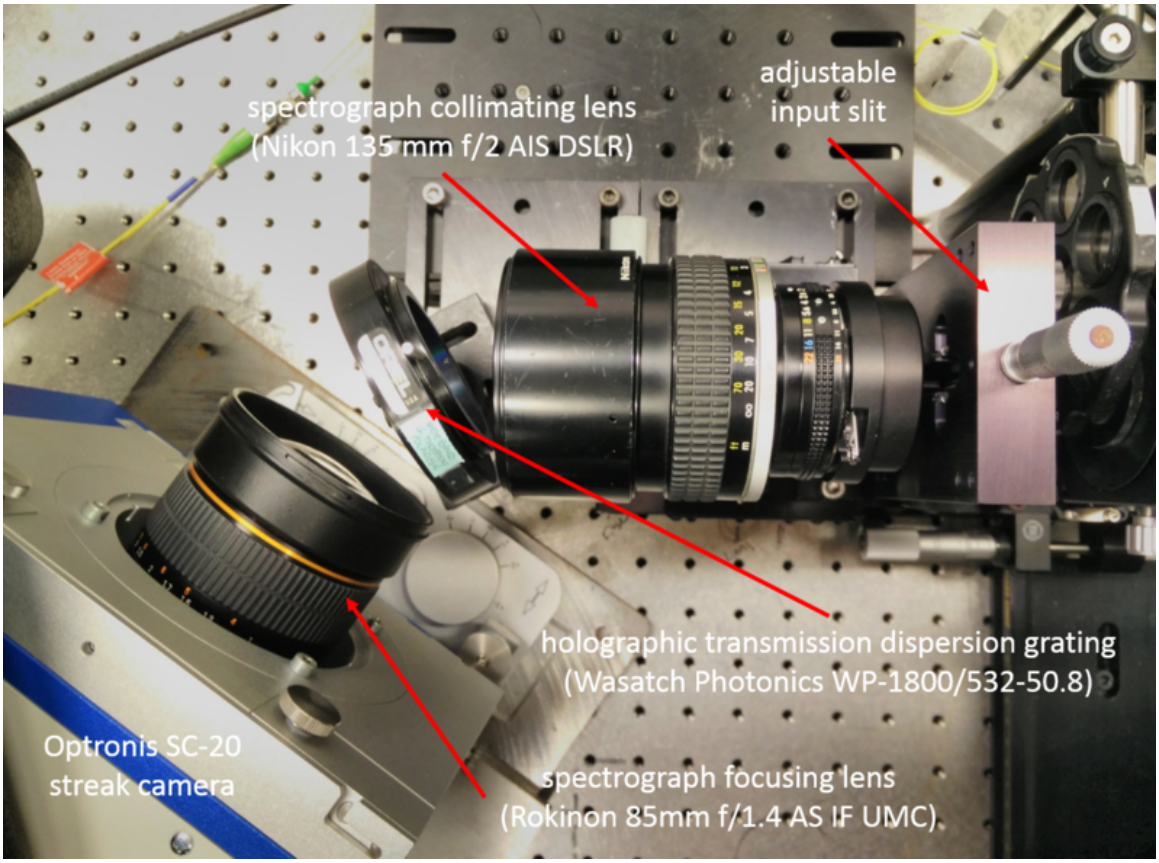

Figure 3.6: Picture of the assembled high-throughput spectrograph when coupled to the Optronis SC-20 streak camera. The collimating lens is adjustable along both the in- and out-of-plane axes for input light alignment, and the holographic dispersion grating is mounted in a rotating 2 inch holder for alignment of the spectrally dispersed output into the focusing lens.

spatial axis on the streak camera is dedicated to collecting the spectral information produced by the grating spectrograph. Thus, the direct spatial image of the multilayer sample surface is lost as the entire area is effectively averaged into the input slit on the spectrograph. This results in a fundamental limit to the information capable of being extracted from the time-resolved spectra. Described differently, the present setup is capable of determining the overall spectral composition (with relative intensities) of light reflected from a two-dimensional surface, but *not* the spatial location corresponding to a given spectral feature. There are other potential experimental setups that would partially mitigate this dimensionality trade-off which are discussed in Chapter 7, but the primary focus of this work

is on the time-resolved spectra of the multilayers as collected by the described system.

3.1.3 Benchmark Velocimetry Diagnostic Setup: PDV

The PDV system utilized in this work is a standard (non-upshifted) 4-channel version built by National Securities Technologies, LLC (NSTec). It operates with a 1550 nm 0-2 Watt fiber laser from IPG Photonics. The fact that this PDV system operates in the mid-IR was an important factor in its selection as it can operate simultaneously with the spectroscopic probing of the multilayers without interfering with the broadband visible light reflectance signal. The PDV probe used to direct and collect the 1550 nm light to and from the sample surface was a collimating probe (OZ Optics LTD), which has a spot size of ~250 micron. The output from the probe is further directed and focused by the illumination and collection optics (see Figure 3.1), so in practice the spot size at the surface of the sample is typically $<$ 100 microns. As the PDV probe is directed at the surface of the sample at normal incidence, no correction for angle reflection is necessary in the data analysis process. An important variable that can significantly affect the performance of velocimetry systems is the preparation of the sample surface. This was a significant concern in the present work as the system would need to accurately measure velocity of two different surface types: diffuse and specular. Based on the sample package shown in Figure 3.1, the PDV probe can either track the relatively diffuse surface of the aluminum driver (i.e., through an IR-transparent multilayer sample, such as a DBR) or the highly IR-reflective silver mirror layers in an AOMC configuration. Fortunately because of the careful alignment of the illumination and collection optics and the robust performance of PDV systems generally with different levels of signal return, the system as shown performs satisfactorily under both surface types.

The data from the PDV system was collected with a Tektronix DPO70804 oscilloscope with an 8 Ghz bandwidth and a sample rate of 25 GS/s. An example waveform from a representative laser-driven shock-compression experiment with a 50 μm aluminum driver and DBR sample is shown in Figure 3.7. The initial break-out, rapid increase and frequency,

and then slow decrease in frequency is indicative of the typical laser-driven shock pressure profile shown in Figure 3.3.

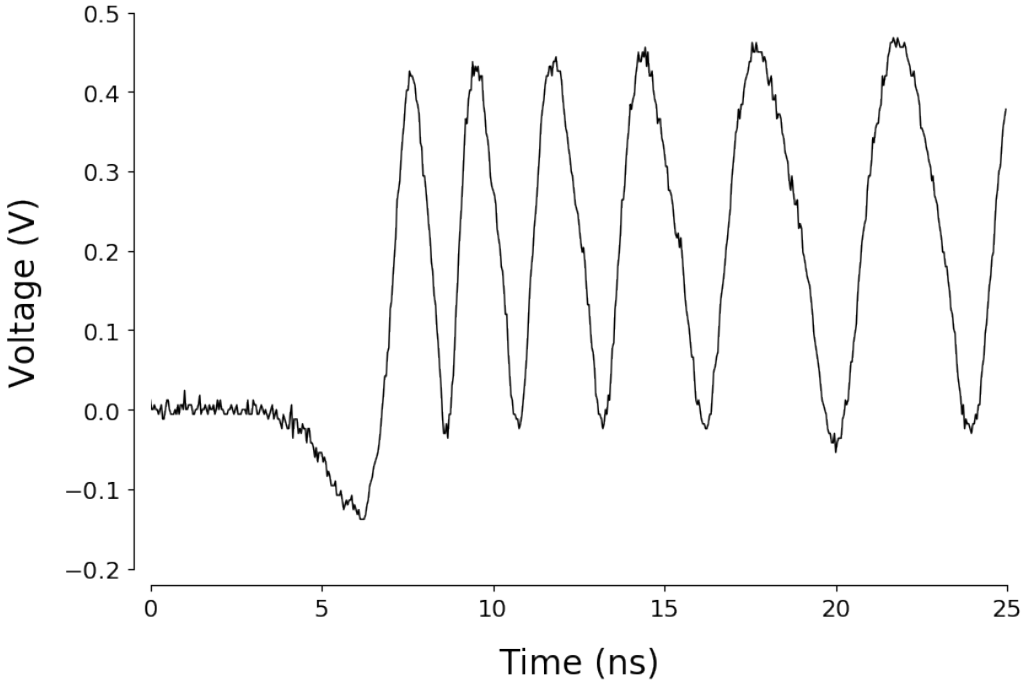

Figure 3.7: Example of raw PDV oscilloscope signal from a laser-driven shock experiment with a DBR multilayer sample. This data is representative of the average quality of PDV data seen in the experiments throughout this work. Only the first 25 ns of the signal is shown as the primary events of interest occur within this window (i.e., shock rise, peak and initial shock relaxation).

The process of extracting the time-resolved velocity from this type of signal is in the domain of time-frequency analysis. This is a broad and established topic in mathematics and signal processing (see Cohen [89] for an introduction) and many different methods have been proposed and used by the shock physics community. However, one particular method is by far the most common: the short-time-fourier transform (STFT). Proposed initially by Strand et al. [32] in the paper first presenting PDV, this method is composed of two analysis steps. First, the raw PDV signal is converted into the time-frequency space using the STFT method, which slides a window function (typically Hamming window) of width w along the signal with stride s, performing a fourier transform at each step. This produces a *spectrogram* image, with frequency along the y-axis and time along the x-axis. The

resolution of each axis is determined by the fourier transform parameters, stride size s, and original sampling rate of the data. The bright spots in the image show the path of the signal "instantaneous" frequency as a function of time. By using an accepted approximation, the corresponding "instantaneous" velocity can be calculated directly from the frequency:

$$v = \frac{\lambda}{2} f \tag{3.1}$$

where v is velocity, λ is the wavelength of the PDV source laser, and f is the instantaneous frequency. The second step of the STFT method extracts the frequency from the calculated spectrogram and converts it to velocity. There are many different algorithms to perform this process automatically (generally, a class of problems known as "ridge" tracking), but the simplest approaches use some variant of peak finding along each column (i.e., timestep) of the spectrogram. Additionally, the "velocity breakout point," defined as the first deviation from the baseline in the raw PDV signal, is often set manually by simple inspection. Figure 3.8 shows the spectrogram obtained from the raw PDV signal shown in Figure 3.7.

Despite the popularity of the STFT method, for certain types of PDV data, it is not the most accurate method to extract velocity. Specifically, velocity histories with relatively low magnitudes ($<$ 500 m/s) and nanosecond-level changes are very challenging to accurately extract, especially with standard (non-upshifted) PDV. This is due to the decreasing number of "beats" in the analysis window as velocity decreases and required time-resolution increases, which negatively impacts the precision of the subsequent fourier transform. However, by employing a variety of time-frequency analysis methods, confidence of the extracted velocity values can be increased. As the type of pressure (and corresponding velocity) histories generated by the laser-driven shock setup employed in this work are firmly in the difficult-to-analyze category, two other methods of PDV data analysis are utilized: continuous wavelet transforms (CWT) and peak/valley/zero-crossing tracking.

Continuous wavelet transforms (CWTs) are related to fourier methods in that they also produce spectrogram-style images when employed for time-frequency analysis. Funda-

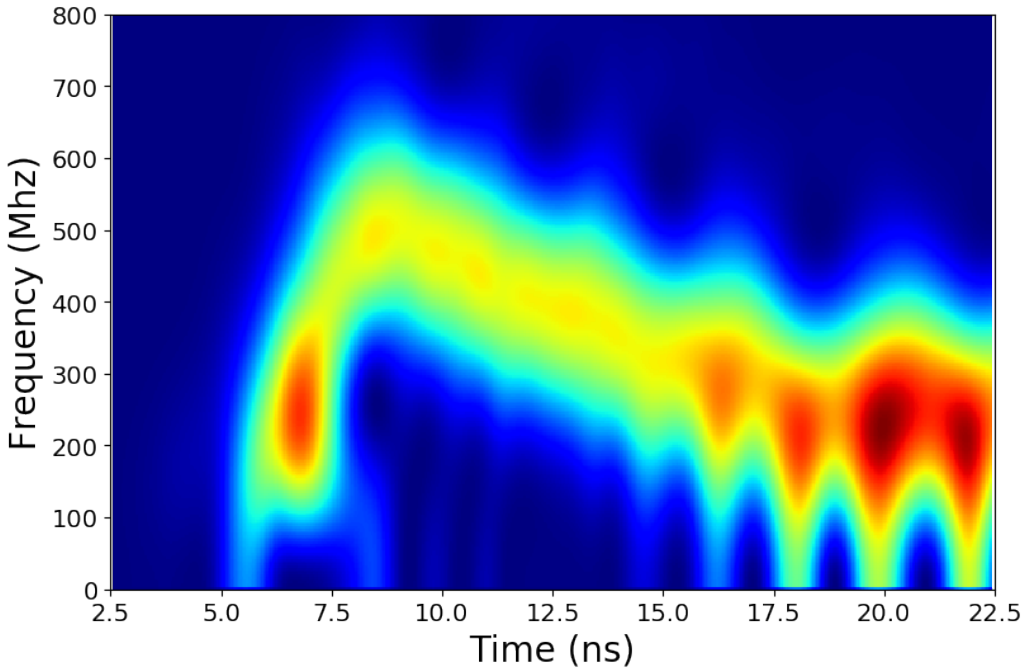

Figure 3.8: Example of a spectrogram calculated from the raw PDV signal shown in Figure 3.7. The high magnitude (red and yellow) regions of the spectrogram indicate that the signal has a strong component at that frequency. Note that the "band" of possible frequencies at any given time is quite wide due to the limited window length (in this example, 5.12 ns) over which the fourier transform estimates the frequency components. Also, the left and right edges of the spectrogram are truncated as the calculated frequency is defined at the center of the window, and in this example signal wrapping/reflection has not been used to extrapolate.

mentally, a continuous wavelet transform calculates the inner-product of a "mother wavelet" function at different "scales" with the raw PDV data, stepping along the signal with stride s just as in the STFT method. A common wavelet used in time-frequency analysis is the Morlet wavelet, which is simply a sinusoid multiplied by a gaussian function. As the wavelet "scales" can be related to frequency, the CWT process produces a "scalogram" image, which can then be treated identically to a STFT spectrogram for various velocity extraction techniques. Due to the discrete-time nature of the mother wavelet, the CWT method can often extract velocity with slightly more precision than the STFT approach when dealing with low-velocity nanosecond-level velocity profiles. However, it should be noted that the CWT is more computationally intensive than the STFT, so this method may not scale

well when dealing with large duration (i.e, microseconds) velocity histories. Figure 3.9 shows the scalogram of the raw PDV signal from Figure 3.7, which compared to the STFT spectrogram is slightly smoother over both time and frequency.

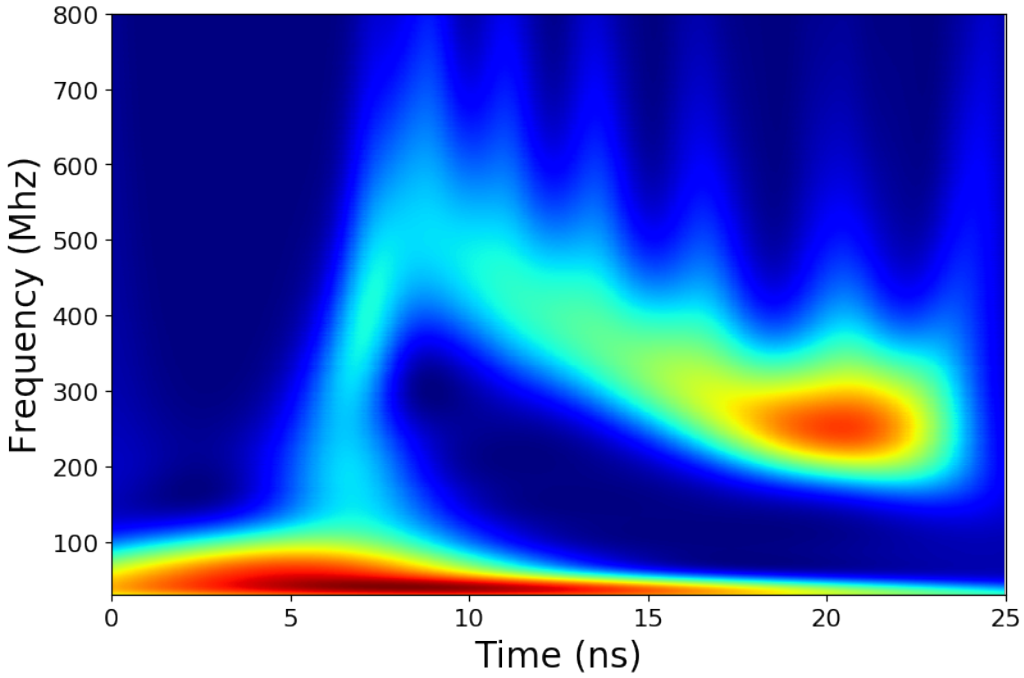

Figure 3.9: Example of a scalogram calculated from the raw PDV signal shown in Figure 3.7. As with the STFT spectrogram, the high magnitude (red) regions of the scalogram indicate that the signal has a strong component at that frequency. The scalogram shows less noise than the spectrogram and results in a smoother overall extracted velocity.

Use of CWT methods in the shock physics community is somewhat limited, though there are several examples in the literature demonstrating the utility of CWTs for PDV data analysis [90, 91]. Kittel et al. [92] describe theoretical discussion of wavelet analysis for microwave interferometry, and the underlying concepts and principles are quite relevant.

Finally, the peak/valley/zero-crossing tracking method is a much more direct method of time-frequency analysis. By tracking each of these points in the raw PDV signal, estimates of average instantaneous frequency can be calculated by taking period fractions and simply

inverting them with the appropriate scaling:

$$f = \frac{1}{aP} \tag{3.2}$$

where a is 0.25, 0.5, 0.75, 1.0, 1.25, etc. By stepping through the identified points, reasonable time-resolved estimates of frequency can be obtained. This method is conceptually simple, but in practice requires significant work to ensure accuracy (e.g., manual inspection of the identified peaks/valleys/zero-crossings to remove spurious points), and a relatively clean, single-frequency signal. Figure 3.10 shows the identified peak/valley/zero-crossing points from the raw PDV signal from Figure 3.7. The data is fit with a 4th order smoothing spline that minimizes first the number of knots in the spline and second the global residuals, and then the identified points are found via numerical differentiation and manual selection as needed. The velocity is then extracted using full periods only, advanced one point for each step.

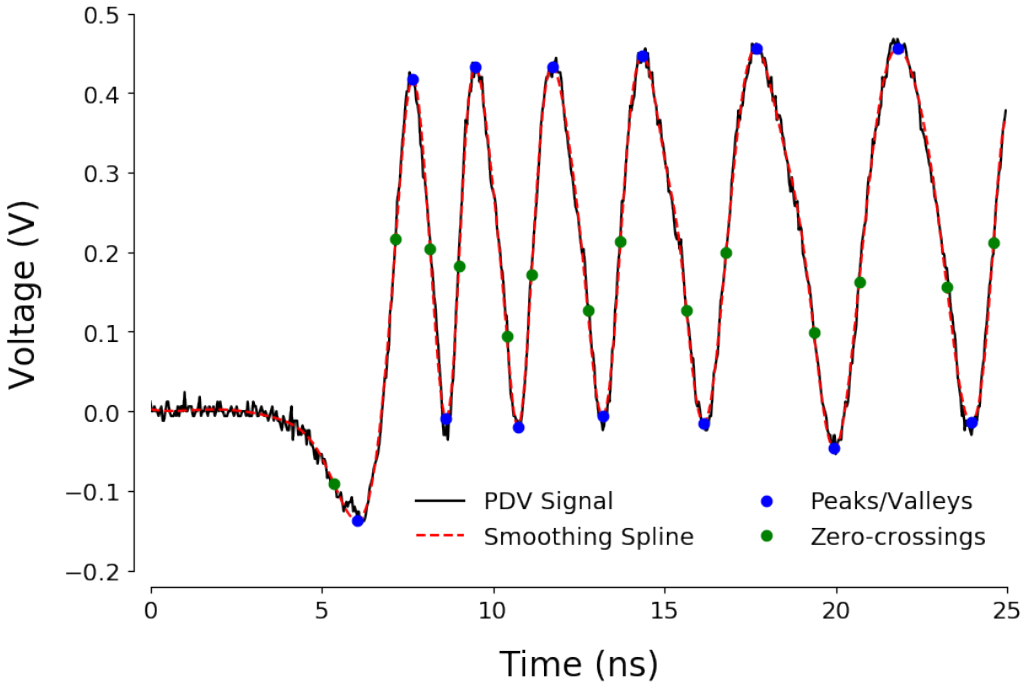

Figure 3.10: Example peak/valley/zero-crossing locations identified from raw PDV signal in Figure 3.7. The points were automatically identified via the differentiation of the 4th-order smoothing spline, and then spurious points are manually removed.

Figure 3.11 shows a comparison of the extracted velocities from each of the three methods. Some manual post-processing of each extracted velocity profile was done to correct for known artifacts in the rise time of the STFT and CWT extracted velocities. The peaks/valleys/zero-crossing method also has some scatter that can be smoothed to produce a profile closer to the STFT and CWT methods. Overall, the CWT method produces the cleanest velocity profile, but all three approaches show good general agreement.

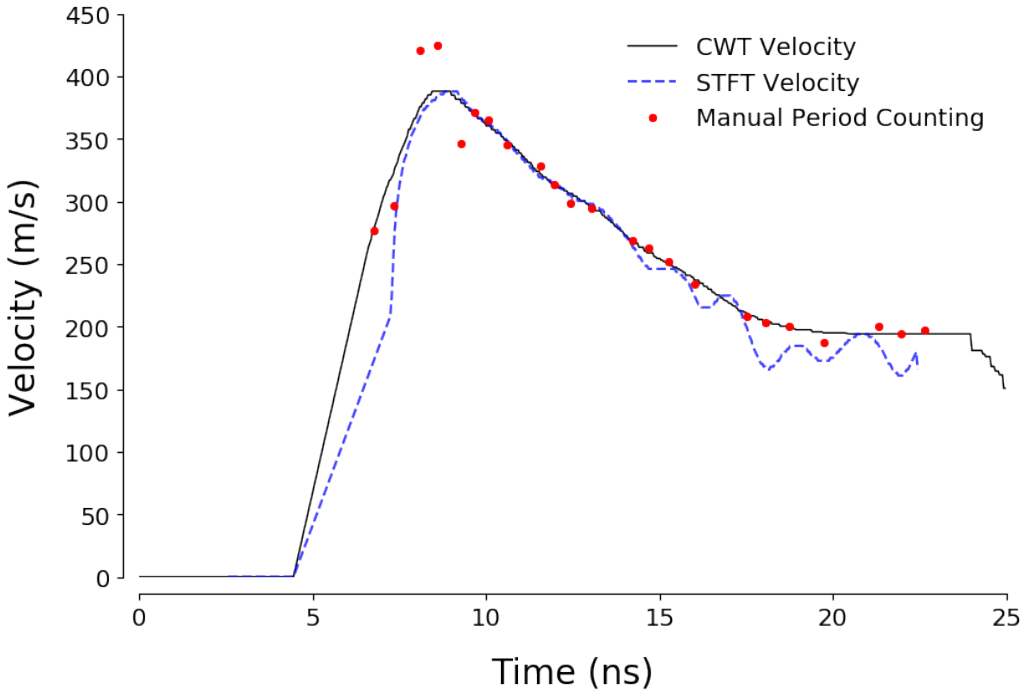

Figure 3.11: Extracted velocities using all three methods (STFT, CWT, and manual peaks/valleys/zero-crossings) for the PDV signal shown in Figure 3.7. All three methods show broad agreement, with the CWT extracted velocity showing the smoothest overall velocity profile.

Ultimately, it is important to note that the mathematical and theoretical background of the STFT, CWT, and other PDV data analysis methods is extensive, and no attempt is made at a rigorous proof of the selected methods' relative advantages, disadvantages, or suitability for the type of PDV data analyzed in the present work. The intent is, rather, to compare each of the three presented analysis methods as needed and use their relative agreement or disagreement as a measure of overall data uncertainty. In this way, reasonable

and quantitative inferences can be made when using the benchmark PDV data to evaluate the shock response of the multilayers, which will be discussed in Chapter 5.

3.1.4 Illumination and Collection Optics

The illumination and collection optics shown in the center of Figure 3.1 play two key roles in overall operation of the entire experimental setup, both of which are performed along the same optical axis. First, the broadband light source passes through the 50/50 beam splitter (Thorlabs BSW10R), which directs 50% of the incident light into the Olympus objective lens (Olympus 4x or 10x Plan Achromatic Objective) and allows 50% to transmit (this light is lost). The objective lens then focuses the light onto the surface of the multilayer sample, which is then reflected back. The objective lens collects and collimates this light and directs it back into the 50/50 beam splitter. At this point the reflected signal represents 25% of the original light input from the broadband light source. The reflected light now passes through the IR hot-mirror (Edmund Optics 47-303) and enters the spectrograph input focusing lens, which focuses the light onto the input slit of the spectrograph. It is important to note that the light source used for this type of time-resolved spectroscopy must have two key characteristics: it must be broadband with sufficient intensity in the spectral range of interest, and it must have continuous output for a minimum of several hundred nanoseconds. This second requirement is particularly important because without continuous output during the duration of the laser-driven shock loading, the full temporal history of the multilayer samples can not be captured. To meet these goals, a 4800 Joule Xenon flash tube (Speedotron MW40QVC) was selected, powered by a Speedotron 206VF/CC Flash Head and Speedotron 4803cx LV Power Supply. This source is one of the brightest possible commercially available options for visible light, and it outputs millisecond long pulses with constant-power regions of 10's of microseconds.

Second, at the same time as the broadband light source, the PDV probe emits 1550 nm laser light directed via the IR hot-mirror into the objective lens, which focuses it onto the

surface of the multilayer sample. The laser light is then reflected back (either specularly or diffusely) and is collected and collimated by the objective lens, and finally redirected back into the PDV probe via the IR hot-mirror. Figure 3.12 shows a photograph of the as-implemented illumination and collection optics in this work, matching the appropriate section of the schematic in Figure 3.1.

The combination of both of these optical paths is what enables simultaneous capturing of both interface velocities and the spectral temporal evolution while the multilayer structures undergo laser-driven shock-compression. It is important to note that because of the use of the 50/50 beam splitter and IR hot-mirror, the shape of the spectra input into the spectrograph is modified and largely truncated to the 400-700 nm wavelength range. The inherent spectrum of the Xenon flash lamp as well as the dispersion transmission grating in the spectrograph will further alter the final spectral power distribution of the overall reflectance signal. A more complete discussion of these effects and their correction can be found in Appendix B.

Finally, it is important to note that while the time-resolved spectra are collected from a moving surface, the doppler effect induced spectral shift is vanishingly small and does not need to be accounted for in the data analysis process. For example, the spectral shift from a surface moving toward the spectrograph at 500 m/s is only 0.00001 nm, several orders of magnitude below the sensitivity of the spectrograph implemented in the present work.

3.2 Opto-Mechanical Computational Framework

The mechanical and optical response of multilayer structures to dynamic loading can be predicted with computational methods. Using the theoretical and empirical models developed and described in Section 4.2 in order to generate simulations that are as comparable as possible to experimental data, a computational framework that can accurately simulate the simultaneous opto-mechanical response of the shock-compressed multilayers is needed.

For mechanical simulations, well-established Finite Element Method (FEM) hydrocodes

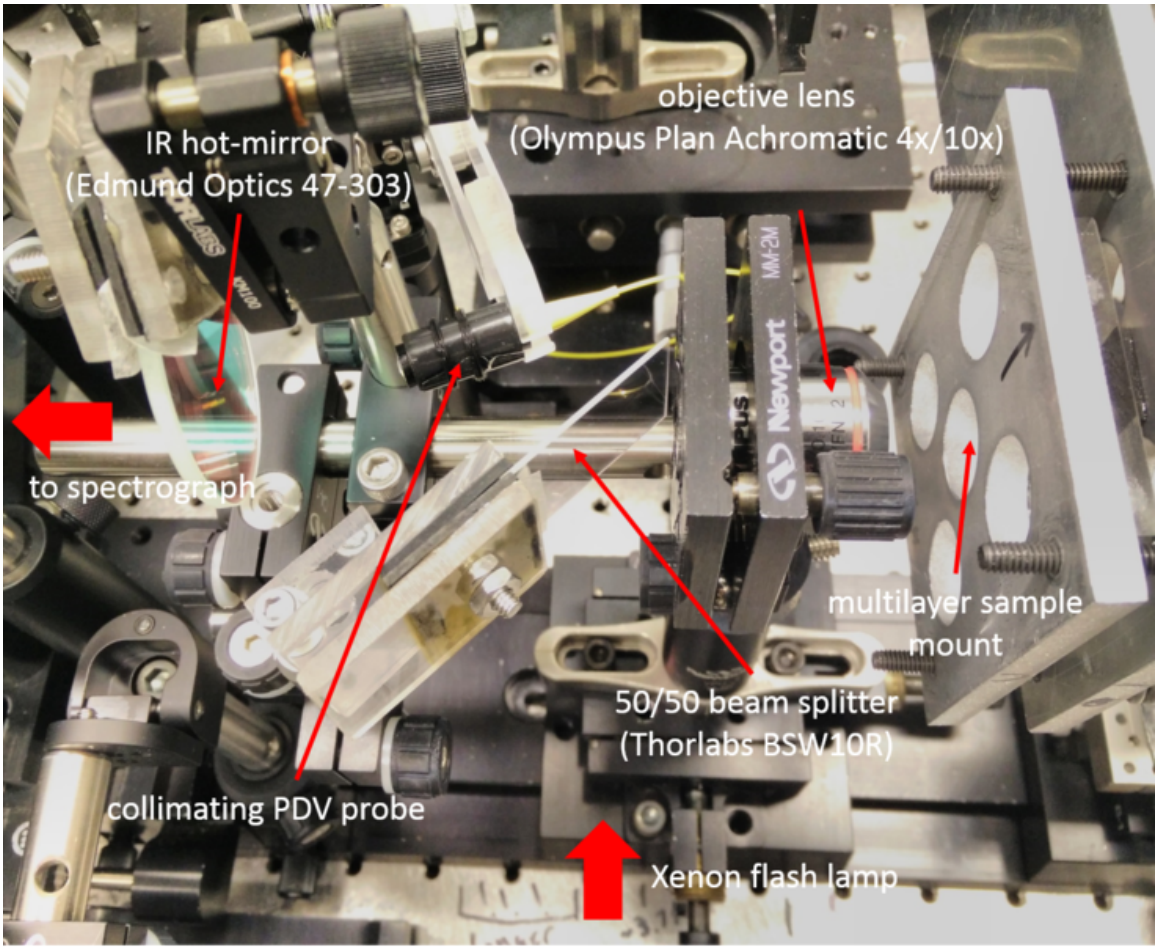

Figure 3.12: Picture of the assembled illumination and collection optics. The IR-hot mirror and PDV probe are each on 3 or 6-axis adjustment stages for easier alignment. The red arrows indicate the flow of light from the Xenon flash lamp broadband source and finally to focusing lens for the spectrograph. These elements are out-of-frame as their position can vary depending on needs of each experiment.

(Abaqus, CTH, ALE3D, LS-DYNA, ALEGRA, etc.) can produce extremely refined predictions of structural changes to individual layers in a multilayer structure. Codes using Finite Domain Time Difference (FDTD, such as MEEP [93]) or FEM (such as COMSOL Multiphysics) to solve Maxwell's equations for electromagnetic wave propagation can predict optical responses in arbitrary structures. For one-dimensional conditions, efficient matrix-transfer methods [56, 94] also have much utility.

Unfortunately, there is currently not (to the author's knowledge) a commercially available code or software that is capable of *simultaneously* performing hydrocode and optical

response calculations due to the orders-of-magnitude difference in the time-step required for the mechanical and optical FEM solution process. Certain academic codes may have such capabilities, but access and documentation is often limited. Consequently, in order to simulate time-resolved mechanical and optical responses, a custom linkage between any available structural and optical simulation software packages is needed. A component of the present work is the development of such a linkage, which is composed of four steps:

1. The mechanical response of the shock loaded multilayer structures is simulated in Simulia Abaqus (version 2016)

2. Time-resolved snapshots of the multilayer structure and mechanical states are saved, and individual deformed geometries and spatial pressure/density fields are exported

3. The time-resolved deformed geometries are imported into COMSOL Multiphysics (version 5.2a), and optical properties are assigned based on the spatial pressure/density fields derived from the mechanical simulations

4. Optical simulations are performed on the deformed geometries, producing an optical response corresponding to the specific time-resolved mechanical and thermodynamic state of the structure

A schematic of this process for an individual temporal snapshot is shown in Figure 3.13.

With this computational framework, the mechanical and optical response of arbitrary multilayer structures under arbitrary loading conditions in both 2D and 3D reference frames can be predicted, although the computational requirements for full 3D simulations may be prohibitive. A major component of the present work is the integration of the developed dynamic optomechanical models discussed in Section 4.2 with this computational framework, enabling predictive modeling of additional multilayer structures and complex loading conditions. This also serves as a valuable investigative tool for determining the types of loading conditions and material systems where the multilayer structures can have the most utility as time-resolved meso-scale diagnostics.

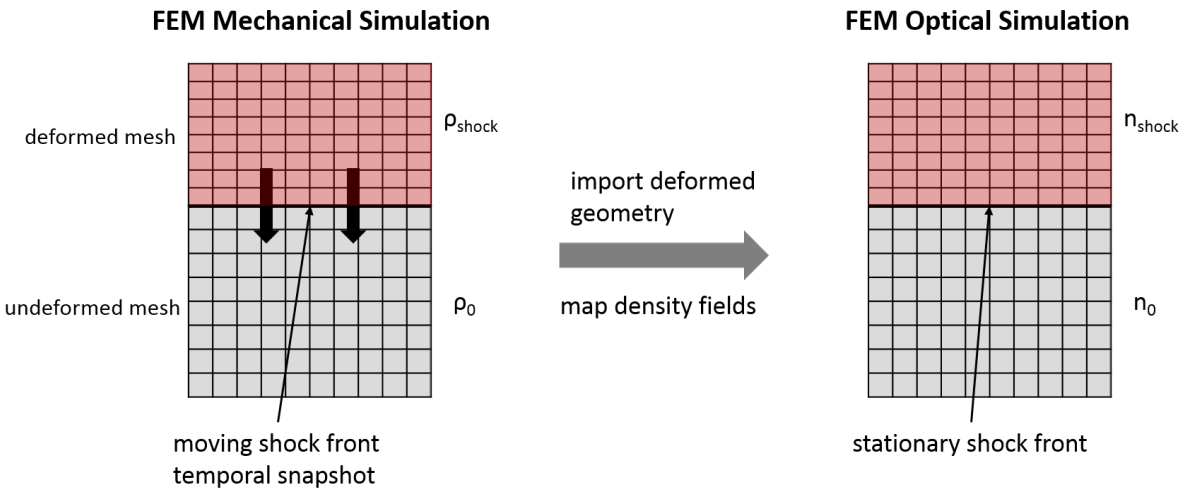

Figure 3.13: Process by which mechanical FEM results can be combined with optical FEM methods to calculate the time-resolved mechanical and optical response of a multilayer structure. Individual snapshots of the mechanical FEM data are exported, and the deformed structure and instantaneous physical and thermodynamic state of the meshed material is used to calculate time-resolved optical properties, using the models developed in Section 4.2.2.

To demonstrate the process of using the framework, an example is shown using an Abaqus simulation of the shock-compression of an AOMC multilayer with a spatially heterogeneous "stepped" pressure load of ~5 GPa where ~50% of the multilayer's surface is shocked. The pressure load has a gradual transition between the high/low pressure states, as a perfectly sharp transition is not physically realistic due to dissipative effects.

The first step of the linkage process is to extract the deformed geometries of all of the AOMC's layers. This is accomplished with node sets and history requests in Abaqus[1]. Figure 3.14 shows the extracted deformed geometries of each layer in the AOMC, using the time-resolved position of the boundary nodes in the FEM mesh for each layer.

Next, the pressure in the cavity layer is extracted using element sets and history requests. As the pressure of each element in the cavity layer is calculated at its integration point(s), spatial coordinates need to be associated with the point(s) in order to create the spatial pressure field. Unfortunately, Abaqus does not allow recording of the integration

[1]Relevant sections of the Simulia Abaqus 2016 documentation: http://50.16.225.63/v2016/books/usi/pt03ch14s04.html, http://50.16.225.63/v2016/books/usi/pt06ch73.html

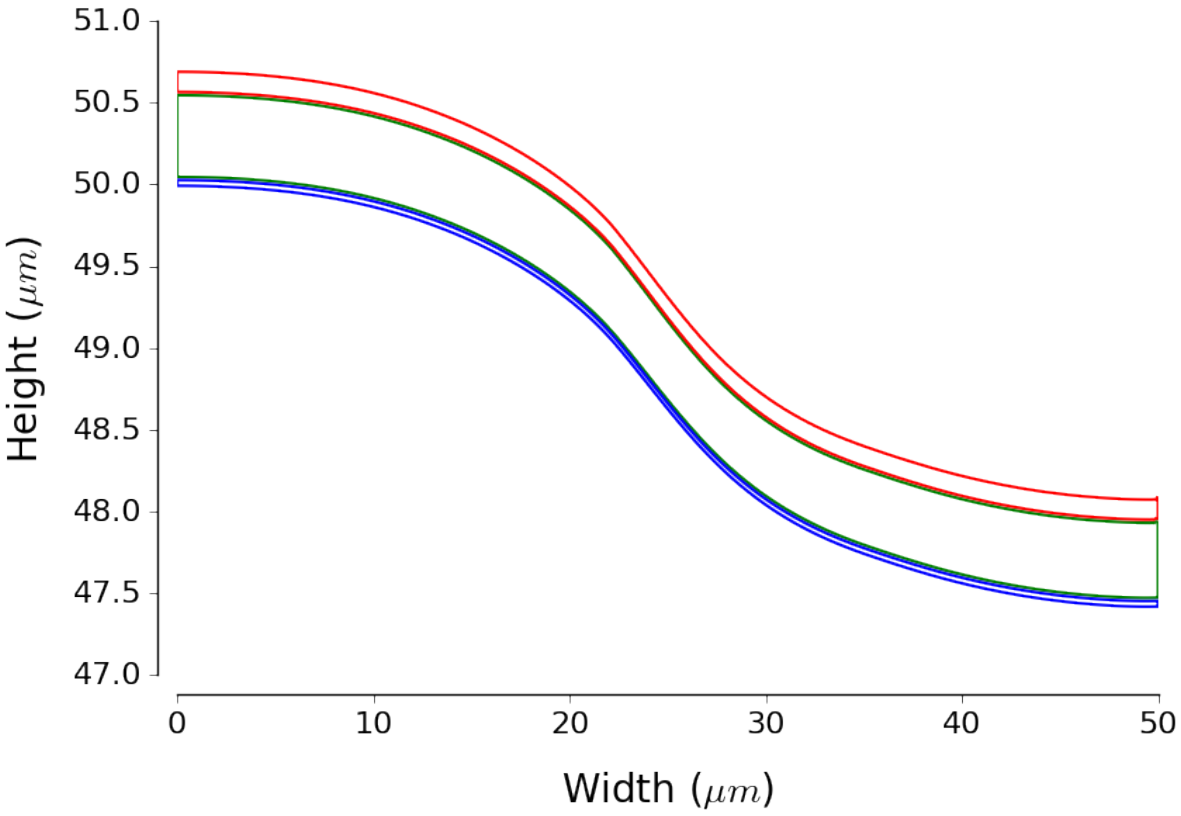

Figure 3.14: Example of deformed geometry of an AOMC multilayer structure deformed by a stepped heterogeneous shock load, with blue outlining the bottom silver layer (measurement side), green outlining the cavity layer, and red the top (thick) silver layer. The right half of the AOMC is compressed by the shock pressure and moved spatially downward due to the compression of the substrate. Note that the axes are scaled independently to better visualize the layer deformation.

point coordinate, so as a substitute the time-resolved element centroid is calculated from its nodal positions. Figure 3.15 shows the pressure field inside the cavity at the same temporal snapshot as shown in Figure 3.14. The pressure transition due to the spatially stepped shock load is clearly visible.

With the necessary information extracted from the Abaqus simulation snapshot, this data can now be imported into COMSOL Multiphysics and used to generate the geometry and material properties for the optical simulation. First, each of the points in the extracted deformed geometries is used as a vertex of a polygon, which COMSOL then converts into a solid geometry object. Second the spatial pressure field data is used to create a

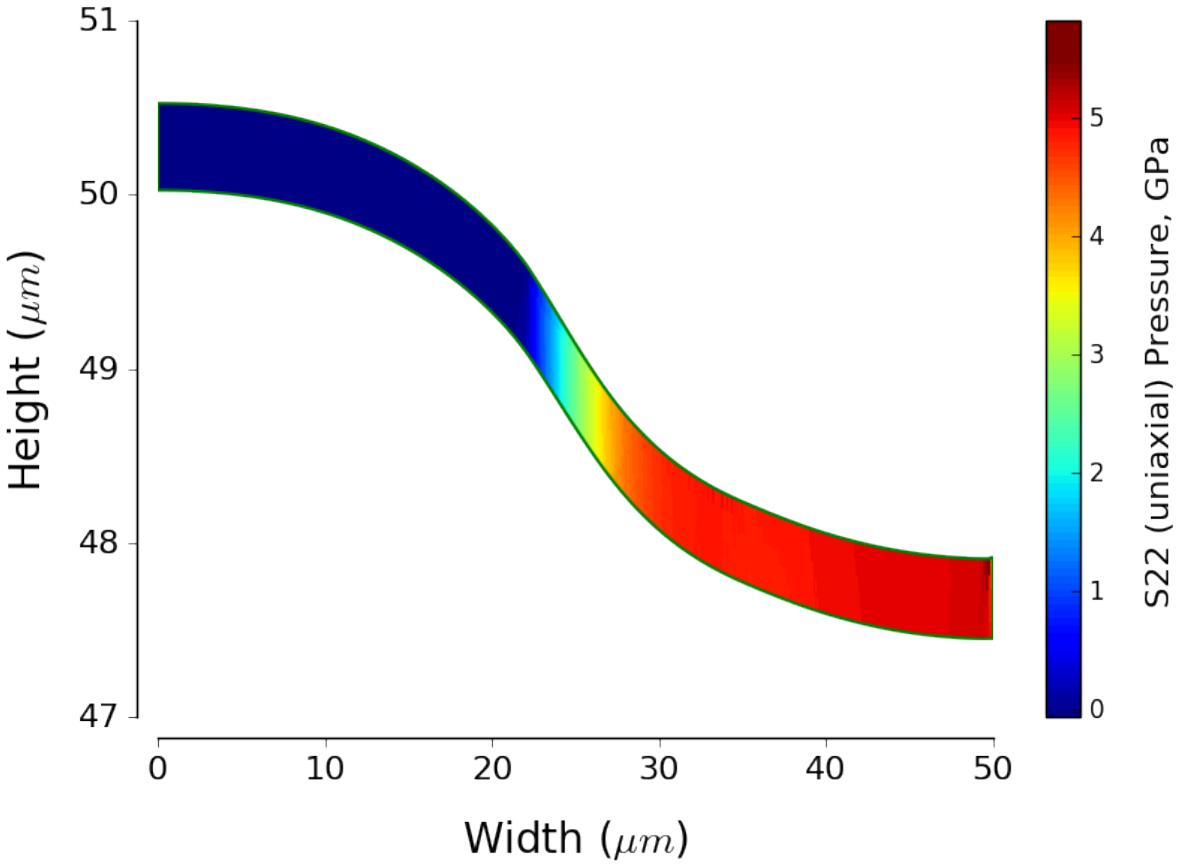

Figure 3.15: Example of pressure contour for the AOMC cavity layer deformed by a stepped heterogeneous shock load. The right side of the layer is at the ~5 GPa "high" pressure of the stepped load, and the transition region to the low pressure side occurs over ~10 microns.

custom spatial interpolation function in COMSOL, which can be assigned to the cavity layer geometry object as a spatially dependent material property [2]. Figure 3.16 shows the result of this process with the COMSOL generated contour map of the AOMC cavity layer refractive index (at 532 nm) and overall AOMC deformed geometry. The refractive index as a function of pressure was calculated via the optomechanical models that will be discussed in Chapter 4.

Once the data extraction, conversion, and import steps are complete, the optical simulation in COMSOL can be performed, producing the spectral response of the multilayer

[2]Relevant tutorial video on this functionality: https://www.comsol.com/video/use-functions-define-material-property

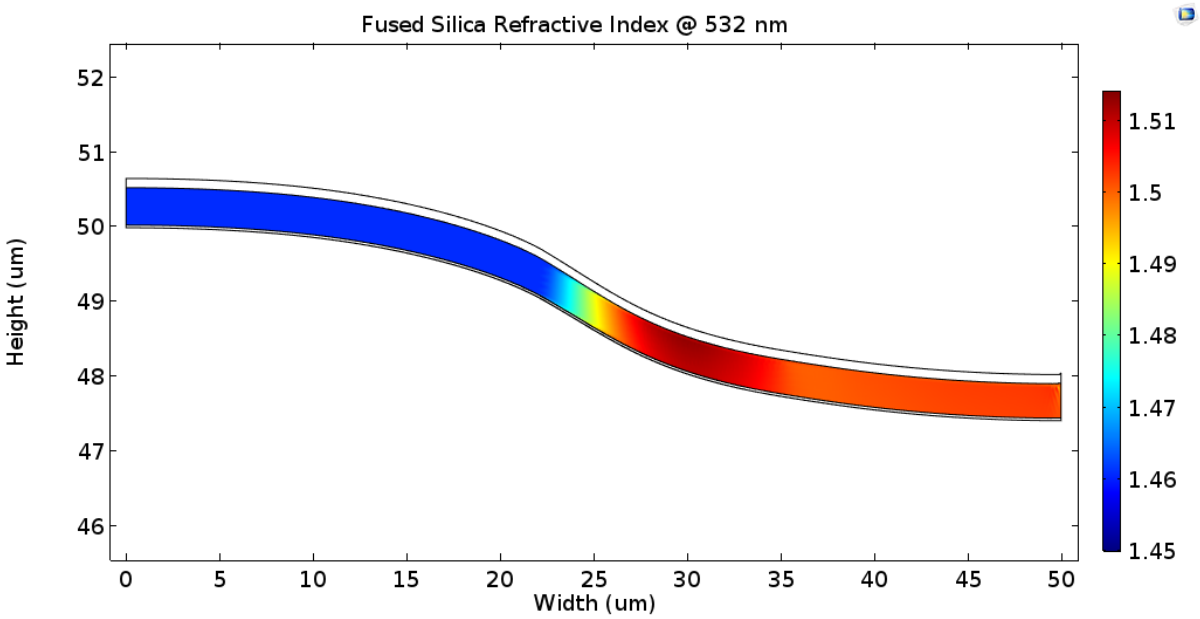

Figure 3.16: Example of COMSOL imported AOMC geometry and cavity layer refractive index contour, based on the time-resolved layer outlines and cavity layer spatial pressure map generated from the Abaqus simulations of a stepped 0/5 GPa heterogeneous shock load. The refractive index spatial distribution closely matches the spatial stress distribution, as the higher pressure causes the localized refractive index to increase.

associated with corresponding snapshot from the Abaqus mechanical simulation. By repeating this process over multiple snapshots, insight into the time history of the optical response is gained. If there are sufficient computational resources, dozens or hundreds of simulations can be combined to create a simulated "streak image" that is more directly comparable to the data produced from the time-resolved spectroscopy setup described in Section 3.1.2. For convenience and automation purposes, the data extraction, conversion, and simulation setup steps for both Abaqus and COMSOL were done with the official Python and MATLAB API's, respectively[3]. The associated scripts used in the present work are also hosted on the author's Github page using Georgia Tech's enterprise license (https://github.gatech.edu/dscripka3).

Beyond the assignment of geometry and material properties, there are many other simulation parameters that can have a significant effect on the accuracy of the simulation results,

[3]Introductions to these API's can be found at the following links: https://www.comsol.com/video/intro-to-scripting-using-livelink-for-matlab, http://50.16.225.63/v2016/books/cmd/pt01.html

such as initial and boundary conditions, mesh properties, material property specification, solver configurations, etc. Unless otherwise noted, all of the simulations in Abaqus and COMSOL presented in Chapters 5 and Chapter 6 utilize the simulation parameters shown in Table 3.2.

Finally, it is important to note that there are two significant assumptions underlying this combined computational approach. First, it is assumed that continuum analytical approaches (i.e., FEM) and bulk material properties accurately model structural changes in multilayer structures composed of individual layers that are only tens to hundreds of nanometers thick. Second, the usage of time-resolved snapshots from the Abaqus simulations assume that the time-resolved mechanical and thermodynamic states of the multilayer are essentially stationary with respect to an electromagnetic wave propagating in the structure. This assumption is likely quite reasonable as the velocity of a moving shock-compression front in a dielectric material is typically in the range of 2 - 15 km/s for low to medium pressures, while the speed of electromagnetic wave propagation is on the order of 200,000 km/s, a difference of over 4 orders of magnitude. These and other assumptions and implications of the model will be discussed again, as appropriate, when comparing the predictions of the framework to the theoretical models and experimental data in Chapters 5 and 6.

Table 3.2: General simulations parameters for Simulia Abaquus and COMSOL Multiphysics in the opto-mechanical simulation framework. Unless otherwise noted, all simulations are two-dimensional.

COMSOL	
Mesh Properties	Free linear triangular mesh, maximum element size of 100 nm
Initial Conditions	Port boundary condition with electric field excitation in the z (out-of-plane) direction for EM wave emission
Boundary Conditions	Perfect Magnetic Conductor (PMC) symmetry boundary conditions for geometry boundaries perpendicular to the EM wave propagation, and Perfectly Matched Layers (PML) as top and bottom domains of simulation to absorb stray power from transmitted/reflected EM wave.
Abaqus	
Material Properties	Tabular Equation of State for volumetric material response, linear elastic shear behavior
Mesh Properties	Linear hexahedral (brick) element, variable element size, but minimum of 1 element along thickness of an individual layer in a multilayer structure
Initial Conditions	Either a pressure load condition (varying spatial distributions and temporal profile), or plate-impact setup with flyer initial velocity
Boundary Conditions	Nodal constraints at edges perpendicular to shock direction only allowing displacement along shock direction, global nodal constrains to enforce plane strain stress state.
Contact Handling	Surface-to-surface contact or Simulia Abaqus General Contact algorithm
Artificial Viscosity	Linear and quadratic artificial viscosity coefficients set at the Abaqus defaults of 0.06 and 1.2, respectively.

CHAPTER 4
DESIGN OF MULTILAYER STRUCTURES AND DEVELOPMENT OF THEORETICAL MODELS

As discussed previously in Section 2.3, multilayer optical structures have many different scientific and commercial applications, and the variation between different multilayer designs is significant as the use of multilayer structures in dynamic sensing is a novel and specific application. Hence, investigation into unique multilayer designs that meet the particular needs of dynamic sensing is necessary. Additionally, theoretical models that are tailored to the novel multilayer designs are also needed to describe and predict the response of the multilayers under shock loading conditions. The following sections discuss these issues in detail.

4.1 Design and Fabrication of Multilayer Structures

The design of a generic multilayer structure is defined by three variables: the material composition of the individual layers, the periodicity (i.e., number and arrangement) of the layers, and the thickness of the individual layers. Other relevant physical features that can affect the optical response of the structures are the quality of the adhesion and the roughness of the interface between the individual layers, as well as the large-area uniformity, roughness, and thicknesses of the starting substrate and as-deposited layers.

In addition to these basic design considerations, the application of multilayer structures to sensing under shock-compression conditions also necessitates consideration of the mechanical response of the structure. Generally, the overall thickness of the multilayer should be minimized to ensure that the mechanical and thermodynamic equilibration of the structure occurs on a time-scale competitive with existing time-resolved diagnostics (i.e., several nanoseconds or less). Similarly, the acoustic impedance difference between the in-

dividual layers should be minimized to ensure both rapid mechanical and thermodynamic equilibration as well as to minimize stress localization at the layer interfaces as this could compromise the mechanical integrity of the multilayer structure under shock loading. The impedance difference between the different layer materials (ΔZ) is defined in Equations 4.1 and 4.2:

$$Z_1 = \rho_{01} C_{01} \quad Z_2 = \rho_{02} C_{02}; \tag{4.1}$$

$$\Delta Z = Z_1 - Z_2 \tag{4.2}$$

where ρ is the material density and C_0 is the material bulk sound speed. Figure 4.1 shows example simulations of the equilibration of the interface pressure between a copper sample and the multilayer. In this configuration, the multilayer substrate essentially acts as a "window" for the shocked sample, with the multilayer itself at the interface between the two (see Forbes [3] for a more detailed discussion of this type of sample configuration). The multilayers in these simulations are based on designs that will be discussed in Section 4.1.1 and have silver mirror layers, fused silica cavity layers, and fused silica substrates. As the thickness of the AOMC cavity layer increases, the equilibration time to the reference peak pressure (the copper/"window" interface with no multilayer) slowly increases due to the impedance mismatch and increasing wave transit time through the thicker multilayer.

In some cases, the impedance mismatch is the dominant factor rather than the overall multilayer thickness. Figure 4.2 shows the same type of simulation as in Figure 4.1, but this time with a Al_2O_3 cavity layer and substrate, which is a much closer impedance match to the silver reflecting layers and the copper driver. As such, the equilibration time is $<<1$ ns and largely independent of the cavity thickness. This behavior can have both positive and negative consequences. Through informed selection of multilayer design based on sample and loading conditions, very rapid equilibration times and thus high time resolution

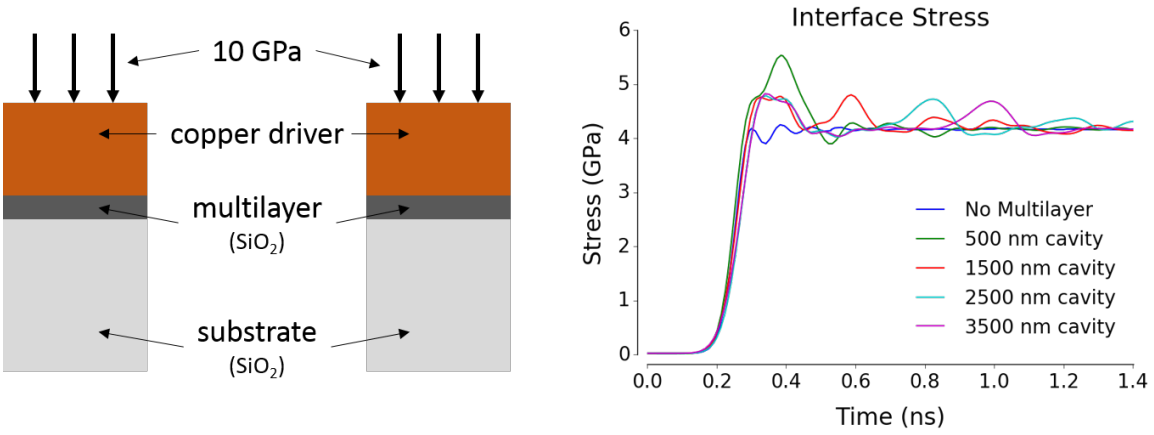

Figure 4.1: Schematic (left) and interface stress (right) for an example simulation showing shock equilibration at the interface between a sample, an SiO_2-based AOMC multilayer, and a fused silica "window" (i.e., the multilayer's substrate). With no multilayer at the interface, a 10 GPa shock wave will equilibrate to the impedance match stress of ~4 GPa with a fused silica window in $<<$ 1 ns, but the addition of the multilayer structure at the interface increases the equilibration time up to ~1 ns, depending on the thickness of the multilayer structure and the impedance match of the layer materials and sample.

is possible; however, if such design flexibility is not realistic then higher equilibration times need to be considered. Nevertheless, even under conditions of relatively high impedance mismatch, equilibration times for many different types of structures should be on the order of a few nanoseconds or less, which is broadly competitive with the existing diagnostics discussed in Section 2.2.

The clear importance of layer material properties leads to another important design criteria: optical materials should be chosen that have well-defined mechanical and optical responses under dynamic loading to better enable accurate models and simulations of the multilayer's response. In some cases, this requirement puts significant restrictions on potential multilayer designs as relatively few materials have both optical and mechanical property behavior under shock loading in the literature. Table 4.1 shows a range of materials identified that meet this standard, along with references to the published material property data.

Once materials are selected, fabrication of the optimized multilayer structure designs can be accomplished with a wide range of deposition techniques. For the present work,

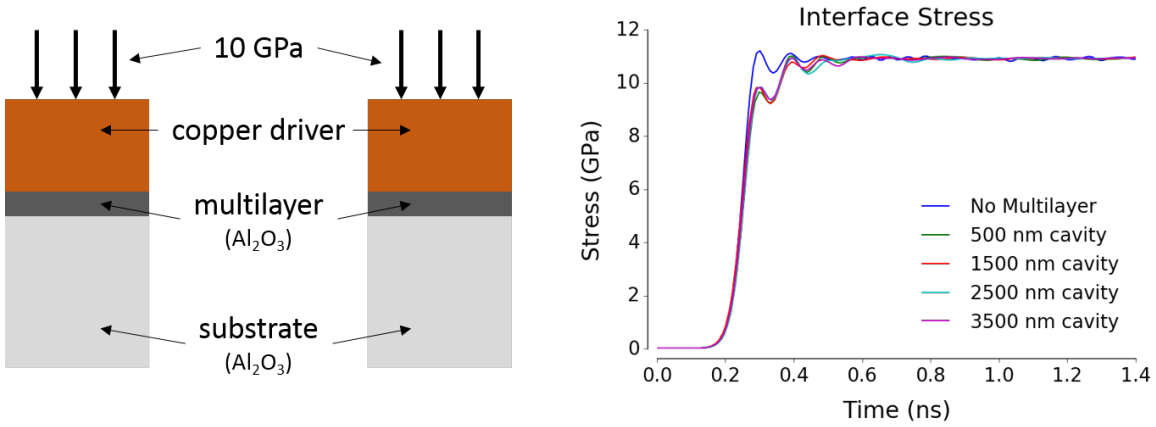

Figure 4.2: Schematic (left) and interface stress (right) for an example simulation showing shock equilibration at the interface between a sample, an Al_2O_3-based AOMC multilayer, and a c-cut sapphire "window" (i.e., the multilayer's substrate). With no multilayer at the interface, a 10 GPa shock wave will equilibrate to the impedance matched stress of ~11 GPa with a Al_2O_3 window in $<<$ 1 ns, and the addition of the AOMC with closely impedance matched materials adds only ~200 picoseconds to the equilibration time, essentially independent of cavity layer thickness.

dielectric materials were deposited utilizing Ion-Assisted Deposition (IAD) (see Martin et al. [118] for a discussion of the advantages of this method), metals were deposited via electron-beam evaporation (a well-established method for thin film deposition of metals in optical applications, see [119]), and polymer materials were deposited via spin coating [120]. These methods are used extensively in both industrial and research contexts. The details of the fabrication processes are the focus of collaborative work by Lee [121] and will not be discussed further in this work. Broadly, the main goal in the fabrication study is the selection and evaluation of methods and procedures that will produce multilayer structures with the previously discussed features and properties that make them well-suited for use as time-resolved meso-scale sensors in shock-compression research.

The following sections will present the AOMC and DBR designs discussed by Lee [121], focusing on representative structure and static spectral properties.

Table 4.1: Candidate materials identified for multilayer structures and associated references to published mechanical and optical property data under shock-loading conditions.

Material	Mechanical Properties	Optical Properties ($n = f(\rho)$)
Fused Silica (SiO_2)	[7, 95, 96, 97]	[98, 99]
Al_2O_3 (various orientations)	[100, 7, 101]	[97, 98, 102, 103, 104]
LiF ([100])	[7, 105]	[106, 107, 108]
PDMS	[7, 109]	[110]
Kel-F	[7, 111]	[110, 112]
PMMA	[7, 113]	[110, 97, 114, 115]
Silver	[7, 116, 117]	NA

4.1.1 AOMC Designs

Several AOMC multilayer structures were considered and fabricated, all based around the same general design: a 400-500 micron substrate, silver reflecting layers, and a 500-1000 nm thick cavity layer. Table 4.2 shows the structure and order of the layers in the AOMC cavities. Note that the optical and mechanical properties are approximate and based on literature values for *bulk* samples of the materials.

The fused silica AOMC was designed to explore a multilayer structure with a moderately stiff cavity (as represented by the bulk modulus listed in Table 4.2) layer and thus an "average" pressure sensitivity. The fused silica AOMC went through several different revisions, primarily due to poor adhesion and stability between the SiO_2 and silver reflecting layers. The addition of the 5 nm Al_2O_3 "adhesion" layers corrected this problem. A 500 nm cavity was the target thickness, but some variation depending on the fabrication run added some variation ($\sim$10 nm variance). Figure 4.3 shows the schematic of the structure, along with a measured as-fabricated spectrum.

The Al_2O_3 AOMC was designed to explore a multilayer structure with a very stiff cavity layer and thus a relatively low pressure sensitivity. This design utilized a c-cut sapphire

Table 4.2: Structure and basic optical and mechanical properties of the AOMC multilayers designed and fabricated in this work. The cavity layer bulk modulus gives an approximate estimate of the AOMC compressibility and thus its "sensitivity" to shock pressure. The cavity layer for each structure is in bold.

AOMC Cavity Material Properties	SiO_2 AOMC	Al_2O_3 AOMC	PMMA AOMC
Cavity Refractive Index (@ 632 nm)	1.457	1.765	1.490
Cavity Bulk modulus (GPa)	37	165	3.3
Layer Order and Thicknesses	Ag (125 nm)	Ag (125 nm)	Ag (35 nm)
	Al_2O_3 (5 nm)	**Al_2O_3 (990 nm)**	**PMMA (500 nm)**
	SiO_2 (500 nm)	Ag (35 nm)	Ag (35 nm)
	Al_2O_3 (5 nm)	C-plane Sapphire (500 μm)	Fused SiO_2 (500 μm)
	Ag (35 nm)		
	Al_2O_3 (5 nm)		
	Fused SiO_2 (500 μm)		

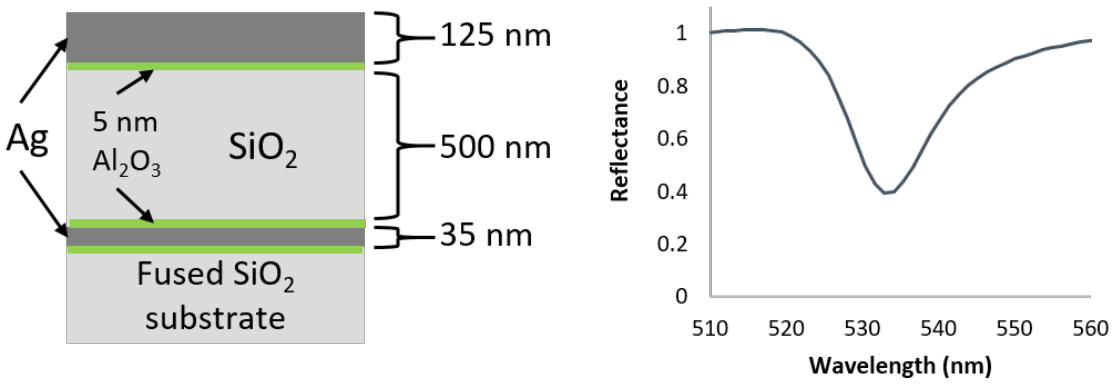

Figure 4.3: Schematic (left) and as-fabricated spectrum (right) for the AOMC multilayer with a fused silica cavity. The Al_2O_3 adhesion layers are between every interface with the silver reflecting layers. The spectrum is focused on a single cavity mode of the AOMC.

substrate and did not require adhesion improving layers at the silver/Al_2O_3 interfaces as adhesion was already sufficient. The as-deposited Al_2O_3 cavity is likely amorphous, based on the fabrication parameters and methods, and the detailed characterization of the cavity's structure was not performed. Figure 4.4 shows the schematic of the structure, along with a measured spectrum of the as-fabricated multilayer. The quality of the spectrum is poor, likely due to insufficient Al_2O_3 deposition quality (again see Lee [121] for additional discussion). More work is needed to optimize the fabrication of this structure.

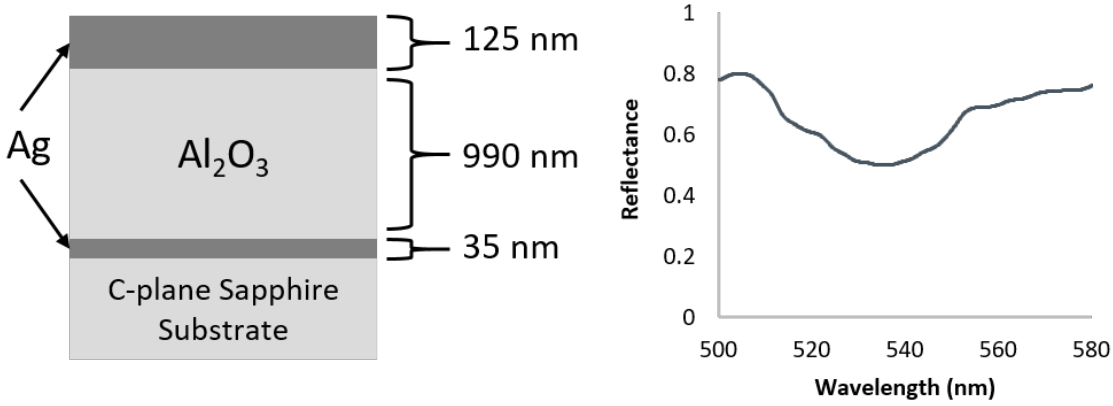

Figure 4.4: Schematic (left) and as-fabricated spectrum (right) for the AOMC multilayer with a Al_2O_3 cavity. The quality of the spectrum is poor, but the features of the cavity mode are still visible.

The PMMA AOMC was designed to explore a multilayer structure with a relatively

soft cavity layer and thus a relatively high pressure sensitivity due to high compressibility of PMMA. The fabrication process for this structure was more complex as the PMMA cavity layer needed to be spin-coated on top of the e-beam deposited silver reflecting layers in multiple steps. Figure 4.5 shows the schematic of the structure along with a measured as-fabricated spectrum of the structure. While the quality of the initial spectrum is quite good, the sample showed very low stability and the spectrum degraded significantly over the course of a few weeks. Additionally, maintaining layer adhesion and uniformity during fabrication was challenging, and more work is needed to optimize the fabrication and stability of this structure.

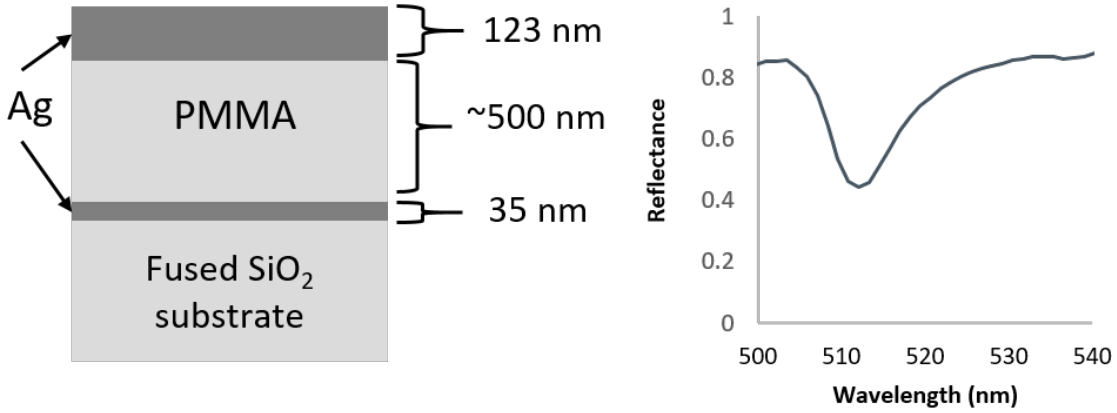

Figure 4.5: Schematic (left) and as-fabricated spectrum (right) for the AOMC multilayer with a PMMA cavity. The target cavity thickness was 500 nm, but in practice significant variation (up to 100 nm) was observed due to the difficulty in maintaining consistent spin-coating thicknesses.

4.1.2 DBR Designs

Several different DBR multilayer designs were explored, including polymer based designs and TiO_2/Al_2O_3 designs. However, no usable samples from these designs were produced due to challenges with fabrication. As such, a new design was created based on controlling the oxygen stoichiometry of SiO_x layers. This enabled simpler fabrication processes, and several different samples with sufficient spectral quality were produced. As was discussed

Table 4.3: Layer properties for the SiO_x based design of the DBR multilayers. Actual fabrication conditions varied, and slightly different layer thicknesses and stoichiometries were obtained for different samples. In general, the thickness and refractive index difference between the layers was 10-15 nm and 0.1, respectively. The estimated bulk modulus is based on a linear interpolation between the bulk moduli of pure SiO_2 and SiO thin films reported by Pivot et al. [122], though it is likely that these values are more qualitative as film properties are strongly dependent on fabrication parameters.

Layer	Thickness	Refractive Index	Oxygen Fraction	Estimated Bulk Modulus
A	~190-250 nm	~1.65	~1.51	~29 GPa
B	~200-270 nm	~1.55	~1.8	~31 GPa

in Section 4.1, the higher overall thickness of the DBR structures may influence the effective temporal response of the DBRs, so samples with varying numbers of layers (11 and 21) were produced to explore this effect. Table 4.3 shows the representative properties of the DBR layers, and Figure 4.6 shows a schematic of the structure and spectrum of the as-fabricated multilayer.

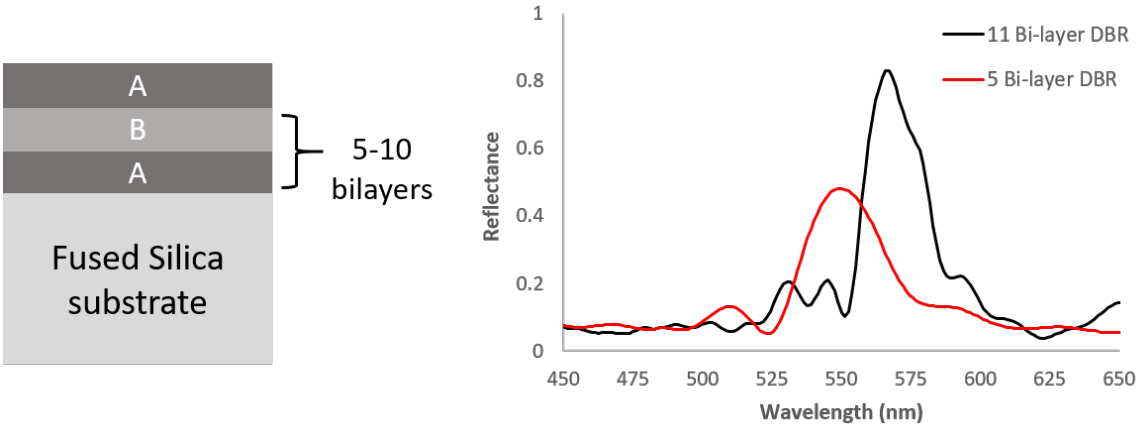

Figure 4.6: Schematic (left) and spectra (right) for the as-fabricated SiO_x DBR multilayers. Each bi-layer (BL) was repeated 5 or 10 times, followed by a final single layer which acts to improve the shape of the reflectance peak compared to an even-numbered layer design. The 10 BL DBR shows a higher and narrower peak compared to the 5 BL as expected based on Equation 2.6.

The total thickness of the 5 and 10 bi-layer DBRs was ~3 and ~5 microns, respectively.

As the bulk moduli of the individual layers are likely quite similar (see Table 4.3), the impedance mismatch between the layers and fused silica substrate is low. This indicates that despite the relatively large thickness of the DBR multilayers, equilibration times should be rapid (on the order of a few nanoseconds or less). Due to a lack of high quality material property data for the SiO_x layers, quantitative simulations of equilibration time are difficult, and this assumption will be compared with the experimental data presented in Chapter 5.

Finally, it is important to note that each of the spectra for the different DBR (as well as AOMC) structures was collected over an area corresponding to < 1 mm^2, and spectral variation does exist at different spatial locations on the multilayer. In some cases, the position of a single reflectance peak/valley mode showed variation of up to ~10 nm over an area of 1000-1500 mm^2. This is most likely due to non-uniform flatness of the starting substrate, non-uniform layer deposition, and other variations in fabrication processes. Tighter control of fabrication parameters can reduce this spatial variation, but some variation may be unavoidable. The implications of such variations will be discussed further in Chapter 7.

4.2 Dynamic Optomechanical Theoretical Model

The overall optical response of the multilayers to shock-compression can be viewed as the interaction between two effects: shock induced changes in the structure of the materials in the multilayer and shock induced changes in the optical properties of the materials in the multilayer. Predicting the time-resolved spectral response of the multilayers is then, in theory, possible by combining models of time-resolved optical and mechanical properties with the multilayer equations defined in Section 2.3. The following sections will present the development of these components and the initial predictions of overall optomechanical dynamic model.

4.2.1 Structural Changes Under Shock Compression

Structural changes under shock-compression include densification, phase changes, and defect generation [2, 3]. Shock-induced structural changes are, in general, well understood for many different bulk materials. The Equation of State (EOS) for a bulk material describes the complete thermodynamic response in the Pressure-Volume-Temperature space, and there exist many high quality EOSs for a wide range of different materials and their forms, including many optical materials.

As discussed in Section 2.3, the structural change that would most affect the optical response of a multilayer is a change in the thickness of the individual layers due to densification under shock-compression. The amount of this dimensional change is defined by the EOS of the material as a function of both the magnitude and rate of the loading. Under 1-D uniaxial strain loading, the change in volume is the same as the change in thickness along the direction of load ($\frac{V}{V_0} = \frac{d}{d_0}$), so the volume change calculated from a material's EOS can be used to calculate the change in the thickness of an individual layer in a multilayer structure under 1-D shock-compression, as shown in Equation 4.3.

$$d_{shock} = \frac{V}{V_0}(d_{initial}) \tag{4.3}$$

The rate of the loading can also have a significant effect on the magnitude of the volume/thickness change. Material compression can occur on isothermal, isentropic, and Hugoniot thermodynamic pathways and infinitely many intermediate thermodynamic pathways. Figure 4.7 shows these three pathways, demonstrating that for a given pressure, the volume compression decreases moving from the isotherm, isentrope, and Hugoniot pathways due to the increasing role of higher temperatures along the same direction. However, the magnitude of these differences typically only become significant at relatively high pressures and temperatures. In the present work the primary focus will be on the structural

response of the multilayers along the shock Hugoniot as the experimental setup described in Chapter 3 is used for generating relatively low pressures along pathways likely between the isentrope and Hugoniot for the materials investigated.

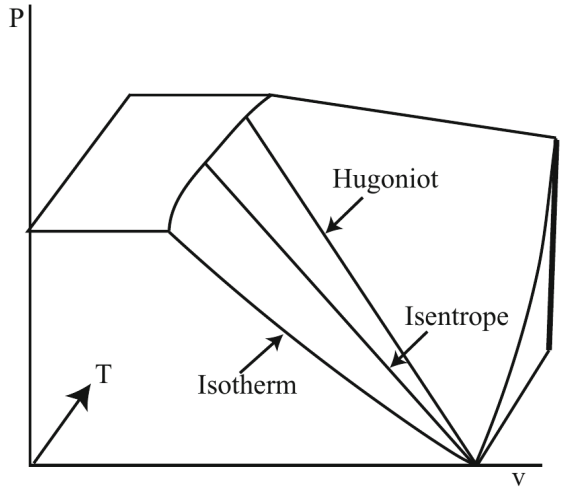

Figure 4.7: Example plot from Forbes [3] of isotherm, isentrope, and Hugoniot curves in the pressure-volume-temperature space. Note that for a given pressure, depending on the loading pathway, the level of volume compression increases from the Hugoniot to the isotherm. In the case of 1-D loading, the rate of the loading (e.g., static compression up to shock-compression) will determine which pathway is followed, and thus the magnitude of the thickness change in the sample.

An example of the EOS for fused silica along the shock-compression Hugoniot is shown in Figure 4.8, plotted in the volume compression (V/V_0) vs pressure space as this is the most relevant to the present context. Several different sources of experimental data are used for this plot [97, 7, 96], and their combination introduces a very important issue: data quality and error propagation. In order to develop an optomechanical model that is capable of quantitative predictions, the sources and amount of error for each component must be carefully tracked and propagated through the entire form of the model. This is especially important when leveraging literature sources as researchers can use many different experimental techniques with varying quality and forms of the reported data. For example, Barker and Hollenbach [97] don't report the raw U_s-U_p values from their experiments and instead provide a 4th order polynomial fit for stress as a function of 1-dimensional strain that "fits

the present data very well to 65 kilobar but also converges to within 1%-2% of Wackerle's data in the 90-95 kbar range." This model is likely accurate in the 0-10 GPa (0-100 kbar) range given the precision in their experiments that Barker and Hollenbach claim. Marsh [7] provides the raw U_s-U_p values, though the precision of these data are not explicitly discussed.

With this knowledge, a combined EOS of fused silica can be generated from the literature sources, making some conservative assumptions about error magnitudes in each reference. The model by Barker and Hollenbach is assumed to have a constant 2% error of the 0-10 GPa range. The Marsh data was handled differently, leveraging a monte-carlo approach. First the raw U_s-U_p data was assumed to have 5% error, and 1,000 monte-carlo datasets in the volume-pressure space were generated based on this error and application of the Rankine-Hugoniot conditions (Equations 2.1 and 2.2). Each of these datasets were fit with a linear equation, and the 95% confidence interval of the predicted mean value from all 1,000 fits across the 11-24 GPa was calculated. Combining these uncertainty ranges from Barker and Hollenbach and Marsh produces the shaded uncertainty band in Figure 4.8.

Note that a clear transition occurs in the ~10 GPa pressure range, which is broadly considered to be the first phase-transformation for fused silica along the shock Hugoniot. On average, the calculated uncertainty band results in an error of 3-5% in the predicted volume compression for a given pressure, which is likely quite conservative. This same approach can be taken for the other materials listed in Table 4.1 as many of the literature sources have similar variability in their data collection and reporting. In general, however, models of volume-pressure with conservative average accuracies of 5-10% are likely obtainable for many different optical materials, and for the present context fused silica will be used as the reference material of choice for development of the overall optomechanical model.

One significant assumption in this structural response analysis (for any material) is the application of bulk mechanical property and EOS data to the <1 μm thin-film layers in

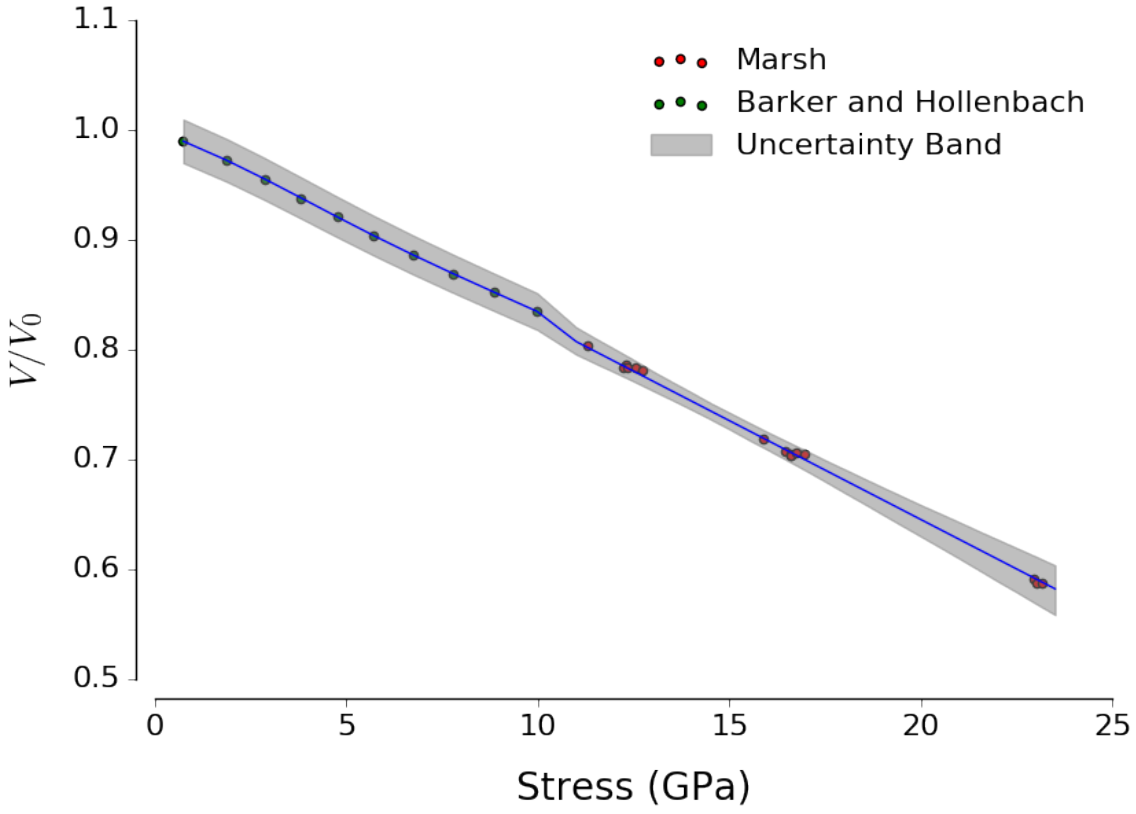

Figure 4.8: Volume-Pressure Hugoniot for fused silica, using data from Barker and Hollenbach [97], Marsh [7], and Wackerle [96].

a multilayer optical structure. For example, it has been observed that the static elastic properties of some materials in thin-film form will be higher than those observed in bulk. For metals, it is theorized that the Hall-Petch grain size effect, as well as dimensionally constrained dislocation motion [123], result in such improved mechanical properties. For amorphous dielectrics like fused silica, the elastic properties can vary substantially above and below bulk values, depending on physical structure, processing conditions, and measurement techniques [124, 125]. Similar size effects on static mechanical properties have been observed in polymer thin films as well [126].

However, many of these effects are primarily observed in films of < 30 nm thickness, which is smaller than the typical layer thickness in the multilayer structures discussed in Section 2.3. Additionally, as was shown in Figure 2.14 and Equation 2.12, Kolle et al. [63] demonstrated that an analytical model based on continuum (bulk) linear elasticity applied

well to a multilayer structure composed of 150 nm and 250 nm thick Polymethylmethacrylate (PMMA) and Polydimethylsiloxane (PDMS) layers under static strain. Under dynamic loading, several researchers [127, 128] have shown that for approximately 500 nm thick PMMA and aluminum films, the experimental data from laser-driven shock-compression matches the reference bulk Hugoniot. Similarly, Bolme [110] conducted femtosecond laser-driven shock-compression of PMMA, PDMS, and polycarbonate samples ranging from 1.6 micron to 8 micron, observing Hugoniot data broadly in agreement with bulk data from Marsh [7]. Ashitkov et al. [129] showed that under femtosecond laser-driven shock, 240 to 1200 nm thick nickel and aluminum films exhibit super-elastic responses that deviate from the bulk Hugoniot at low (~10 GPa) pressures, but related work by Evans et al. [130] indicates that for similar aluminum films the hydrodynamic response returns to the bulk Hugoniot at sufficiently high pressures (~100 GPa). Additionally, this behavior is likely due to the unique conditions of *femtosecond* laser-driven shock and is less relevant in the context of more traditional shock-compression methods.

In summary, in the context of developing predictive models for the typical materials, layer thicknesses, and loading conditions that will be investigated in this work, continuum methods, bulk material properties, and reasonable assumptions of error for layer thickness changes under shock-compression will likely be sufficient. Comparison of the experimental data from Chapter 5 to the optomechanical model will provide important validation (or refutation) of these assumptions.

4.2.2 Optical Changes Under Shock Compression

Optical responses under shock-compression involve changes in the complex index of refraction of a material, $\mathbf{n} = n + ik$, with the nature of the change highly dependent on the bulk thermodynamic state and atomic electronic structure of the material. In contrast to structural changes, similarly complete Equation of State-type models for $\mathbf{n}$ are significantly less common as the underlying physics involving electronic polarizability and electron en-

ergy band transitions can be extremely difficult to model. See Ashcroft and Sturm [131] and Kormer [132] for more complete discussions of the relevant physics.

Attempting to break this complexity into more manageable components, a dynamic optical model can be defined with additive terms, each representing the major thermodynamic variables that influence the complex index **n**.

$$\mathbf{n}(V,T) = A(V) + B(T) \tag{4.4}$$

where A and B are functions that describe the change in **n** as a function of specific volume and temperature, respectively. Even with the lack of rigorous descriptions of A and B, there are simplifying assumptions that can still provide a reasonable match to empirical data.

Beginning with the volumetric response, the well-known Gladstone-Dale [133] approximation (Equation 4.5) produces a reasonable match for many different optical materials under shock-compression. An empirically corrected form of the Gladstone-Dale relationship by Barker [134] can also be used and is shown in Equation 4.6.

$$\frac{n-1}{n_0-1} = \frac{\rho}{\rho_0} = \frac{V_0}{V} \tag{4.5}$$

$$\frac{n-1}{n_0-1} = \frac{\rho}{\rho_0}(1-\epsilon(\rho)); \quad \epsilon = \alpha[\frac{\rho}{\rho_0}-1]^\beta \tag{4.6}$$

Figure 4.9 shows the shift of the real component of refractive index for fused silica as a function of volume compression using Barker and Hollenbach's [97] data, the prediction of the Gladstone-Dale model (Equation 4.5, Setchell's [98] corrected version with parameters of α = 0.02996 and β = 0.6571, and Zha's [99] hydrostatic data converted into uniaxial compression. Note that this conversion requires multiple steps as fused silica displays

non-linear elastic compression in the 0-10 GPa range, and also undergoes a phase transformation at ~8-10 GPa corresponding to the onset of plastic deformation. Thus, Zha's data was converted to uniaxial compression using Equation 4.7 and Zha's poisson ratio data in the ~0-9 GPa range and Equation 4.8 (where Y is the yield strength) and the combined model from Figure 4.8 in the 9+ GPa range.

$$\sigma_x = 3P\frac{1-\nu(P)}{1+\nu(P)} \tag{4.7}$$

$$\sigma_x = P + \frac{2}{3}Y \tag{4.8}$$

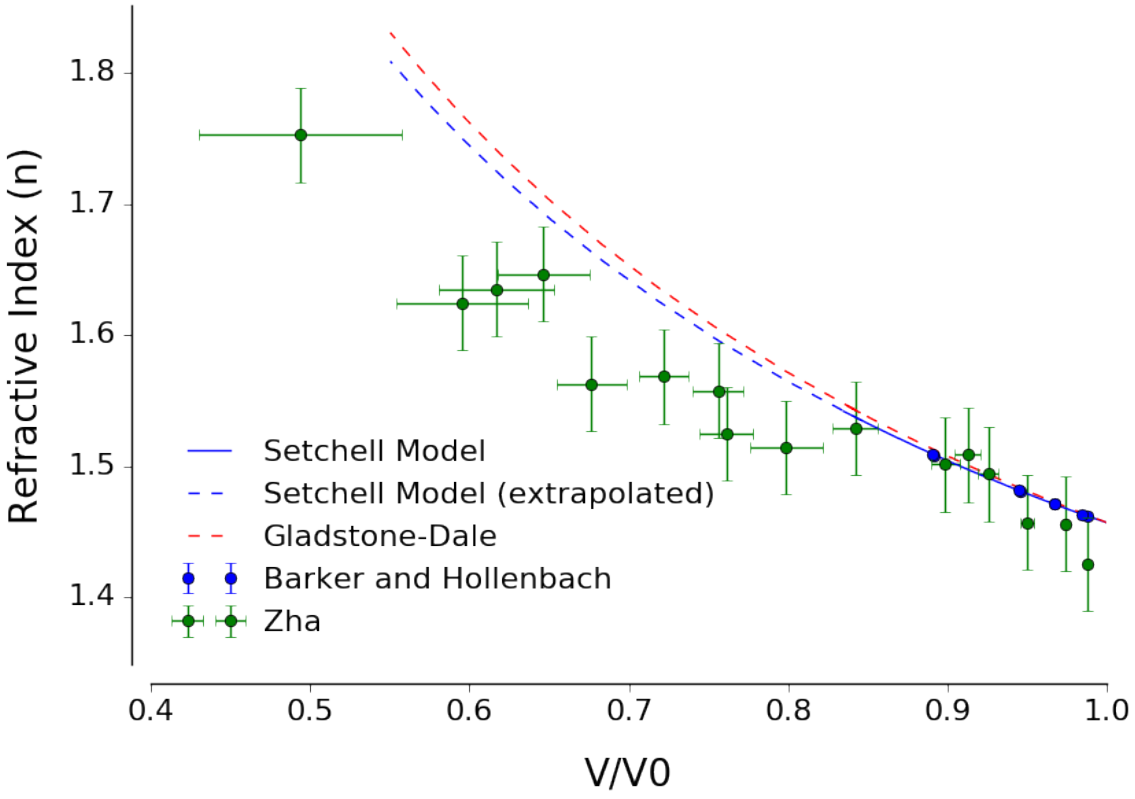

Figure 4.9: Refractive index for fused silica under uniaxial compression, using models and data from Barker and Hollenbach [97], Setchell [98], and Zha [99]. Zha's data was converted to uniaxial pressure from hydrostatic data.

There are several important aspects of these data. First, in the volume-compression

range from 1.0 to 0.9 (~0-6 GPa), both Setchell's model and the simple Gladstone-Dale model are an excellent match to Barker and Hollenbach's low error data and a reasonable match to Zha's higher error data. Beyond V/V_0 of 0.8 ($>$ 10 GPa), both models diverge substantially from Zha's data and less substantially from each other. The clear change in the refractive index trend at this point is indicative of the first of many phase transformations in fused silica at higher pressures and compressions, and to the author's knowledge, there is currently no high-quality literature data of refractive index in these regimes. This illustrates an important practical limitation to the form of the optomechanical models used in this work: they are highly dependent on quality empirical data, and without such sources their predictions will be largely qualitative and *not* suitable as reference or calibration-curves for the multilayer structures, a point which will be discussed further in Chapter 7. However, the models for fused silica are likely reasonably precise in the 0-10 GPa pressure regime that is the focus of the current work and should apply well to the AOMC and DBR structures based on fused silica.

Similar plots can be generated for other materials as well. Figure 4.10 shows such curves for Al_2O_3, PMMA, LiF, and C-cut Sapphire using data and/or models from [110, 135], along with Gladstone-Dale predictions for each material. Note that uncertainty in the data and model predictions for these materials are not shown in the plot, but a similar quantitative analysis could be conducted as was demonstrated for fused silica. It is clear that PMMA is reasonably described by a Gladstone-Dale model (with respect to trends), but LiF and especially C-cut sapphire show diverging trends at higher compressions and pressures. These results further substantiate the importance of empirical data for developing optomechanical models.

Finally, it is important to note that the $dn/d\rho$ behavior of materials is also a function of wavelength, but depending on the material this contribution may or may not be significant. Jenson et al. [135] compared the refractive index as a function of density for several optical materials at both 532 nm and 1550 nm, and while not universal, a simple offset was often

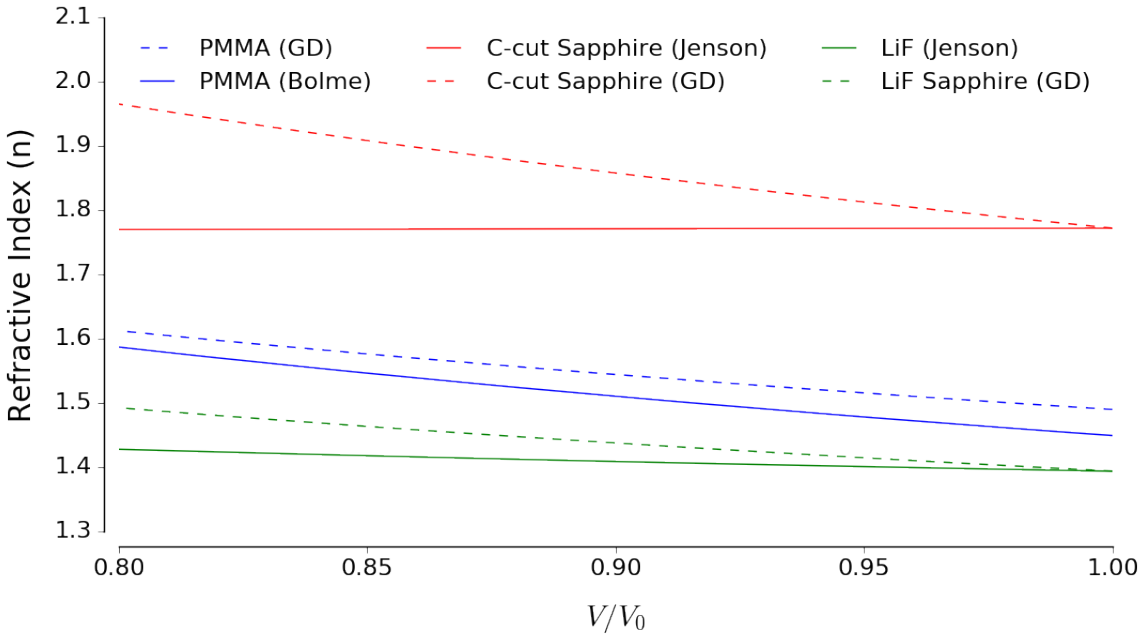

Figure 4.10: Refractive index for PMMA, LiF, and C-cut under uniaxial compression, using empirical models from Jenson et al. [135], Bolme [110], and the Gladstone-Dale (GD) model predictions.

the primary effect of different wavelengths, leaving essentially identical trends. Chapman et al. [114] showed similar effects for PMMA at low pressures. Thus, in the context of the present work where the wavelengths of interest are all within ~150 nm, it is assumed that $dn/d\rho$ is independent of wavelength, and the magnitude of the change in index (Δn) is the same across the relevant spectral range.

Up to this point the discussion of the effects that shock-compression has on optical properties has been limited to selected dielectrics and polymers. As the complex component of refractive index (k) is ~0 for these materials, the analysis is greatly simplified. However, as the AOMC multilayer structures presented in Section 4.1 contain silver reflecting layers, the optical response of silver and potentially other metallic materials to high pressures must also be considered. Under static loading, this can be accomplished with sophisticated ellipsometry methods [136, 137], but obtaining time-resolved measurements of complex indices is significantly more difficult. Dolan et al. [49], Funk et al. [127], Grant et al. [138], and Ali et al. [139] present several techniques used to obtain such data,

but with relatively low quality and quantity.

Generally, the complexity of the optical response of metallic materials is due to their complex electronic structure and the changes in that structure as the material moves along different thermodynamic pathways. For example, Funk et al. [127] attributed trends in the complex index of aluminum under shock-compression to pressure-induced changes in electron interband-transitions at the measured wavelengths and noted that nickel displays the *opposite* trend due to its lack of a similar interband-transition. Dolan et al. [49] have an extensive discussion of attempts to develop a "minimal" model for the dynamic optical response of gold based on experimental data, concluding that "overfitting the problem is a valid concern" due to the six-plus adjustable parameters in their model. Based on these conclusions, it was determined that for the present work no reasonably descriptive quantitative or qualitative model for the dynamic optical response of silver can be developed. Instead, it will be assumed that the contribution of silver to the optomechanical model for the AOMC multilayers will be relatively limited, and the sensitivity analysis discussed in Section 4.2.3 will evaluate the magnitude of the effect from changes in the optical response of silver. The comparison of the models to the experimental data in Chapter 5 will also provide important validation of this assumption.

Moving on to the temperature effect of Equation 4.4, the component is composed of two additive terms, and in differential form:

$$dn = \int_{T_0}^{T} \left(\left(\frac{dn}{dT} \right)_{\rho} - \left(\frac{\rho \partial n}{\partial \rho} \right)_{T} \alpha_V \right) dT \tag{4.9}$$

where α_V is the thermal expansion coefficient. There are several issues immediately obvious with empirical determination of the parameters in this equation. As with any constant volume property, $\left(\frac{dn}{dT}\right)_{\rho}$ can be very difficult to quantify experimentally, $\partial n/\partial \rho$ may not be known accurately (as was just discussed at length), and quantitative measurements of shock-induced temperature increases are quite difficult. Thus, accurate experimental

measurements of the parameters in Equation 4.9 under dynamic loading is potentially intractable for many different materials. However, a useful approach to estimate the overall magnitude of dn/dT for various materials comes from exploiting the differences between thermodynamic loading paths. As shown in Figure 4.7, the isentropic loading path leads to greater volume compression at equivalent pressures compared to the Hugoniot due to the lower overall temperatures reached along the isentrope. If sufficient control over the rate of dynamic loading is possible, data comparing refractive index measurements from isentropic and shock (Hugoniot) loading is obtainable. In other words, **n** is measured at *two different temperatures* but the *same* shock-compressed density allows for independent evaluation of temperature as a variable in the overall change in refractive index. Similar comparisons can be made with isothermal compression data, if available.

This exact approach can be found in the literature for the dynamic optical response of Lithium Fluoride (LiF) under dynamic pressures ranging from a few to several hundred GPa. The consensus ([115, 106, 107]) indicates that the refractive index change in LiF is primarily a function of density changes, and not a significant function of temperature even at high dynamic pressures and temperatures. Similar results for PMMA were observed for quasi-isentropic pressures up to 17 GPa [115] and under shock pressures ranging up to 22 GPa [140, 127, 141] where observed changes in the refractive index of PMMA followed the Gladstone-Dale model (Equation 4.5) to within experimental error. According to Bloomquist et al. [142], shock-induced temperature rises of over 500 °C would be expected for PMMA under a shock pressure of just 5 GPa, indicating that like LiF, the temperature effect on the refractive index is negligible for PMMA under shock-compression. Unfortunately, similar data for fused silica is not present in the literature due to lack of quality data for refractive index changes under shock pressures greater than ~10 GPa, prior to which shock-induced temperature increases are negligible (< 20 K). More investigation of shock-induced temperature effects on the optical properties of fused silica is needed, especially at pressures beyond the first phase transformation at ~10 GPa; however, for the present

work it is assumed that dn/dT for fused silica is also negligible. In summary, despite the inherent complexity of shock-induced changes in optical properties, with empirical models and prudent assumptions, reasonable estimations of refractive index under shock loading are obtainable.

4.2.3 Initial Predictions of Optomechanical Theoretical Model

The combination of the data, assumptions, and models of the previous sections leads to an overall optomechanical model based primarily on the layer thickness and refractive index changes as a function of the dynamic load. Combining equations 4.4 and 4.3 with the analytical equations in Section 2.3, the net optical response of a multilayer structure to a dynamic load can, in theory, be predicted. For example, the height, width, and spectral shift of the primary reflectance valley for generic AOMC multilayer structure can be described as:

$$I(P) = \frac{4R(P)}{[1 + R(P)]^2} \tag{4.10}$$

$$\Delta\lambda(P) = \frac{\lambda_0^2[1 - R(P)]}{2 * n_{cavity}(P) d_{cavity}(P) \pi \sqrt{R(P)}} \tag{4.11}$$

$$\lambda_0(P) = \frac{2}{m}[d_{cavity}(P) n_{cavity}(P) + 2d_{mirror}^{skin-depth}(P)] \tag{4.12}$$

where $n_{cavity}(P)$, $d_{cavity}(P)$, and $R(P)$ vary depending on the layer materials and models chosen. However, these analytical equations are primarily illustrative approximations and do make certain assumptions. Specifically, refractive index is a function of wavelength, and thus Equations 4.11 and 4.12 would require numerical solutions to solve directly.

Alternatively, the computational methods for optomechanical simulations presented in Section 3.2 make far fewer assumptions and can be easily combined with the material models developed to produce simulated data points which can then be fit with polynomial functions (or just compared directly to experimental data) to create the combined optomechanical model. With this approach, the simulated data can even be tailored to the specific conditions of the experimental data, enabling a more relevant direct comparison. It should be noted that this approach, while practical, is somewhat removed from a ground-up phenomenological model. However, forming such a model may not be possible given the challenges already discussed, and may not generalize well even if one is identified.

To demonstrate the approach, the behavior of the silver and fused cavity based AOMC fabricated in this work (Figure 4.3) was simulated, focusing on the 0-10 GPa uniaxial strain shock pressure range. In the simulations, $R_{Ag}(\lambda, P)$ is assumed to be $\approx R_{Ag}(\lambda)$ (provided by Rakic [143]), and $n_{cavity}(P, \lambda)$, $d_{cavity}(P, \lambda)$ for fused silica are defined by Barker and Hollenbach's models [97], inverting the stress-strain relationship using a 4th-order polynomial fit where stress is in GPa and is defined as the uniaxial stress (i.e., σ_{11}). For fused silica $n_0(\lambda)$ is provided by Malitson [57]. The thickness of the silver mirrors is assumed to follow the linear Mie-Gruneisen EOS defined by Marsh [7] at the equilibrated pressure of the fused silica cavity layer. As the loading is one dimensionsal, the volume compression is equal to the unaxial compression, leading to Equations 4.14 and 4.17.

$$\left(\frac{V}{V_0}\right)_{SiO_2} = 1 - 1.0796x10^{-2}\sigma - 2.2182x10^{-3}\sigma^2 + 2.6848x10^{-4}\sigma^3 - 1.0311x10^{-5}\sigma^4 \tag{4.13}$$

$$d_{SiO_2} = d_0 \left(\frac{V}{V_0}\right)_{SiO_2} \tag{4.14}$$

$$n = \frac{n_0 - 1}{(V/V_0)_{SiO_2}} \left(1 - \alpha \left[\frac{1}{(V/V_0)_{SiO_2}} - 1\right]^{\beta}\right) + 1$$

$$\alpha = 0.02996,\ \beta = 0.6571 \quad (4.15)$$

$$\left(\frac{V}{V_0}\right)_{Ag} = \frac{1 + 0.5\left(\sqrt{1 + \frac{4SP}{\rho_0 C_0^2}} - 1\right)(1 - 1/S)}{1 + 0.5\left(\sqrt{1 + \frac{4SP}{\rho_0 C_0^2}} - 1\right)}$$

$$C_0 = 3270\ m/s,\ S = 1.55,\ \rho_0 = 1049\ kg/m^3 \quad (4.16)$$

$$d_{Ag} = d_0 \left(\frac{V}{V_0}\right)_{Ag} \quad (4.17)$$

The COMSOL simulated spectra for the SiO_2 AOMC are shown in Figure 4.11, over a pressure range of 0-10 GPa.

Figure 4.12 shows the peak features for the simulated SiO_2 AOMC spectra as a function of pressure, where peak position is defined as blueshift relative to the P = 0 (i.e., initial) condition, peak width is the width at 1/2 the peak height (i.e., FWHM) and peak depth is the calculated reflectance value at the peak position. Note that peak width and depth are normalized to the P = 0 initial condition.

To explore the effect that silver has on the optical response, the effects on the AOMC spectra from shock-induced optical changes in silver are also shown with an arbitrarily substantial change of $\pm$ 0-40% (linearly increasing/decreasing over the 0-10 GPa range) in n and k for silver assumed. Note that this most likely overestimates the magnitude of any shock-induced changes in n_{Ag}. The peak position (blueshift) shows a smooth trend

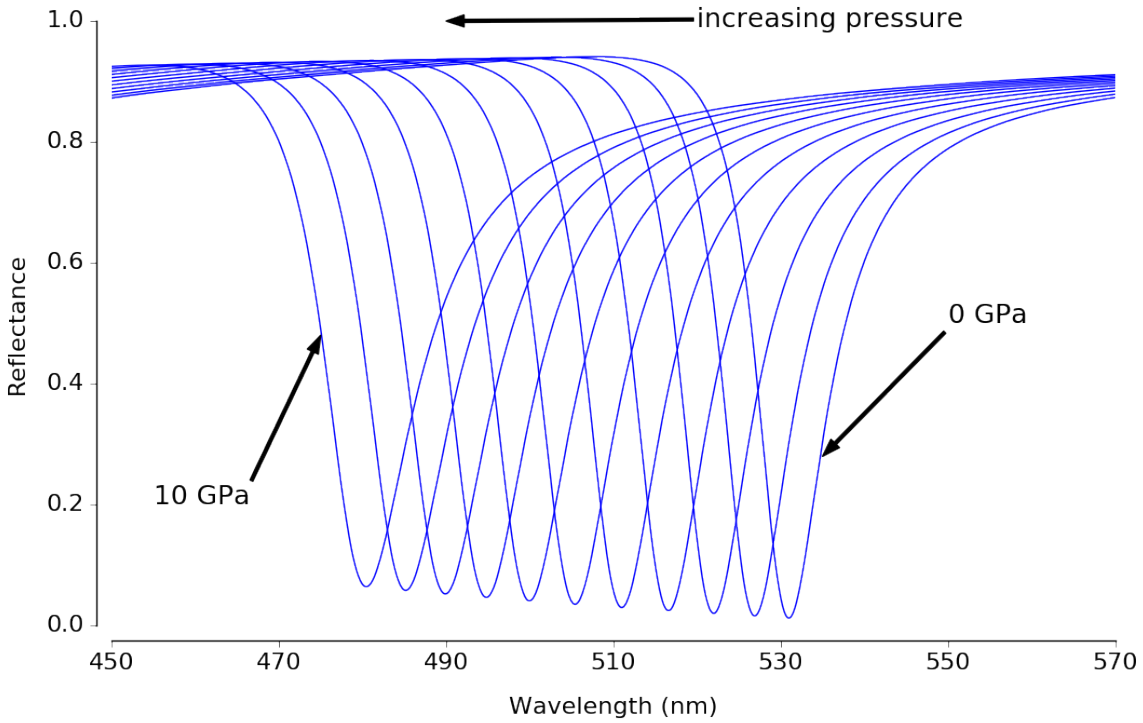

Figure 4.11: Simulated spectra of the SiO_2 based AOMC multilayers using the models described by Equations 4.13 - 4.17 and COMSOL Multiphysics under a uniaxial pressure of 0 - 10 GPa.

up to ~50 nm at 10 GPa with some small non-linearity due to the elastic compression response of fused silica. Changes in n_{Ag} have no discernible effect on the blueshift, while changes in k_{Ag} increase or decrease the magnitude of the blueshift, with decreasing k_{Ag} having the strongest effect. Peak depth only varies slightly (~0%-5%) with both increasing/decreasing n_{Ag} and k_{Ag} having similar trend effects on the peak depth. Peak width also varies up to ~30% at 10 GPa, with n_{Ag} generally having a small effect on peak width, and increasing/decreasing k_{Ag} having very substantial widening/narrowing effects.

For the PMMA and Al_2O_3 based AOMC multilayers the same type of model is defined using Equations 4.13 - 4.17 for the silver volume compression response and equation of state data from the literature for PMMA and Al_2O_3. The volume compression-pressure relationship for PMMA was modeled as a 3rd-order polynomial fit to the combined data from several sources ([97, 7, 113]), and the volume compression-pressure relationship for Al_2O_3 as a 2nd-order polynomial fit to the linear Us-Up model defined by Setchell et al.

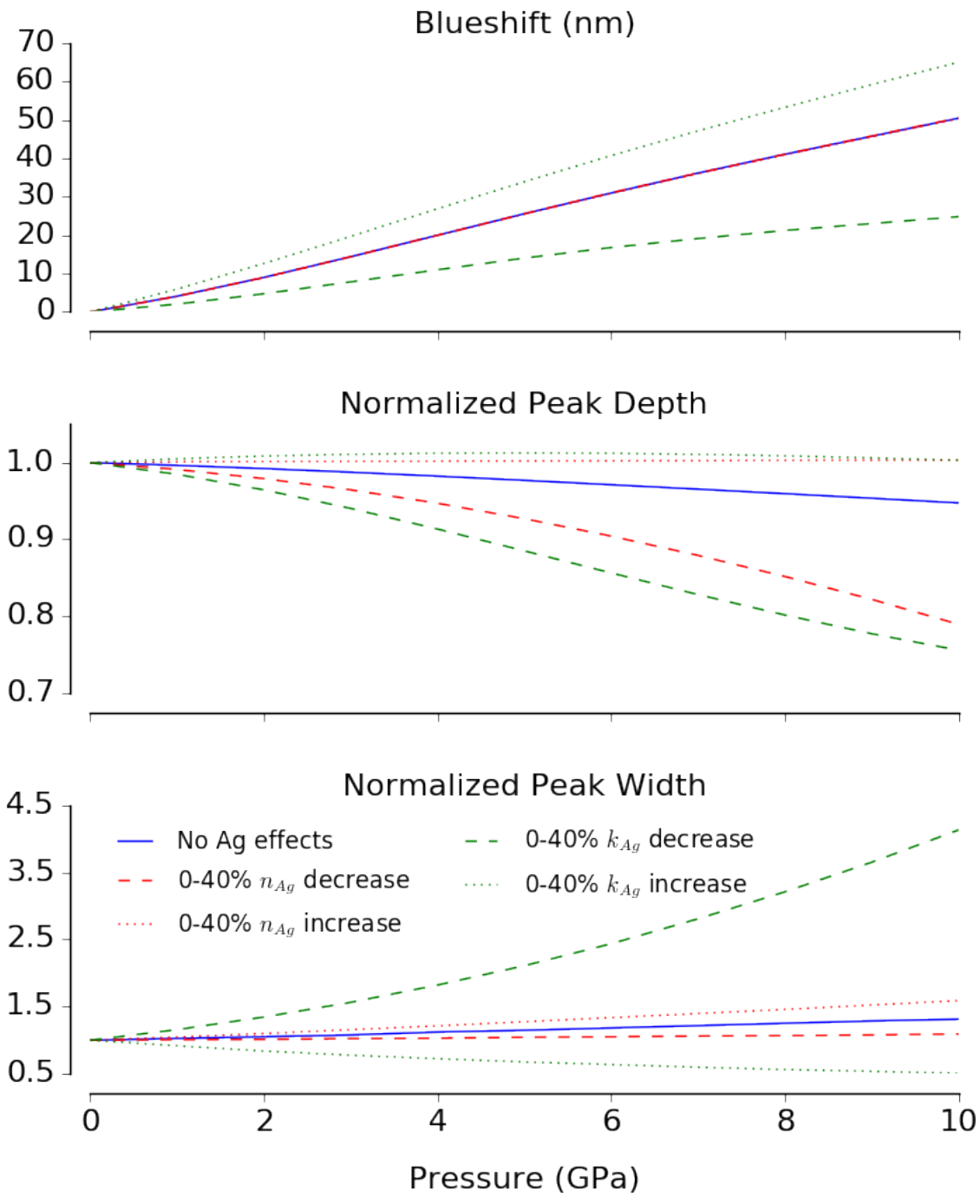

Figure 4.12: Extracted peak depth, width, and position from the simulated spectra of the SiO_2 based AOMC multilayers using the models described by Equations 4.13 - 4.17 and COMSOL Multiphysics under a uniaxial pressure of 0 - 10 GPa. The dotted and dashed lines show the change in the AOMC peak features as the n and k values for the refractive index of silver are linearly varied 0 to $\pm$ 40% over the same pressure range.

[98] ($U_s(km/s) = 11.19 + 1.0U_p$). Refractive index behavior as a function of pressure is modeled with Barker and Hollenbach's Al_2O_3 form of Equation 4.15 with $\alpha = 0.8280$ and $\beta = 0.9606$, and simply the standard Gladstone-Dale model for PMMA which has been shown to fit the experimental data for PMMA well. Figure 4.13 shows the predictions of these models for spectral blueshift along with the fused silica based AOMC model for comparison purposes.

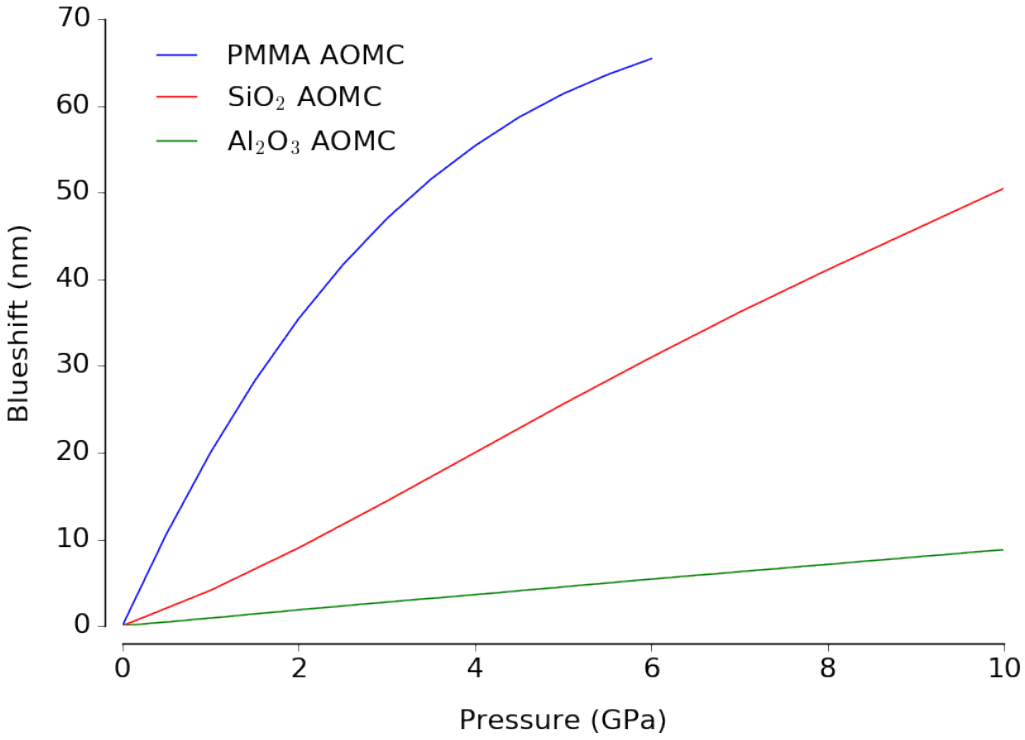

Figure 4.13: Predictions of the spectral blueshift as a function of pressure for the three different AOMC multilayer structures (fused silica, Al_2O_3, and PMMA cavity layers). Each curve is based on the corresponding optomechanical model using the framework shown by Equations 4.13 - 4.17, informed by empirical data from the literature.

The high predicted sensitivity of the PMMA based AOMC is clear from the large blueshifts at relatively low pressures due to the high compressibility of PMMA, and the opposite behavior from the very low compressibility of the Al_2O_3. As the experimental data for these structures presented subsequently in Chapter 5 is limited the predicted peak width and height from the optomechanical models is not shown and the focus will be on the magnitude of the measured blueshift.

Extending this type of optomechanical model and its predictions to the SiO_x DBRs follows a similar process, but requires additional assumptions due to a lack of quality empirical data for refractive index of SiO_x at varying stoichiometries and pressures. Consequently, the refractive index of the SiO_x layers is estimated as the linear interpolation between the refractive index for SiO and SiO_2 at a given value of x, and the pressure-dependent response is assumed to be the same as that for SiO_2 (Equation 4.15). Figure 4.14 shows the refractive index for SiO and SiO_2 as a function of wavelength from [144] and [57], respectively, and the interpolated value at an x value of 1.8 and 1.51 as listed in Table 4.3 for the fabricated DBR structures. It is assumed that the non-zero but small value of k for SiO_x is negligible and is not included in the optical models for this SiO_x DBR structures.

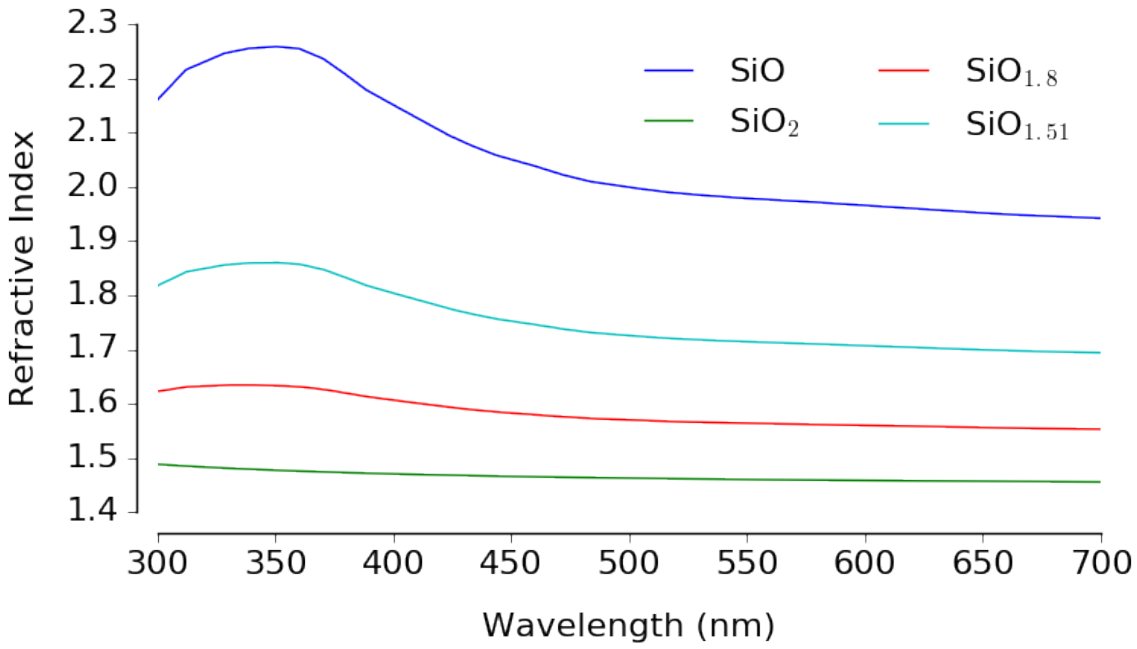

Figure 4.14: Refractive index for SiO ([144]) and SiO_2 ([57]) as well as linearly interpolated values for SiO_x at x values of 1.8 and 1.51.

The COMSOL simulated spectra for the 10 bilayer SiO_x DBRs over a pressure range of 0-10 GPa are shown in Figure 4.15. The DBR design was based on that specified by Lee et al. [59], and had 252 nm "A" layers with $SiO_{1.51}$ stoichiometry, and 267 nm "B" layers

with $SiO_{1.8}$ stoichiometry, using the appropriate refractive index interpolation as shown in Figure 4.14. These parameters produced a starting spectrum that reasonably matched the position, width, and height of the experimental spectra, validating the refractive index model assumptions.

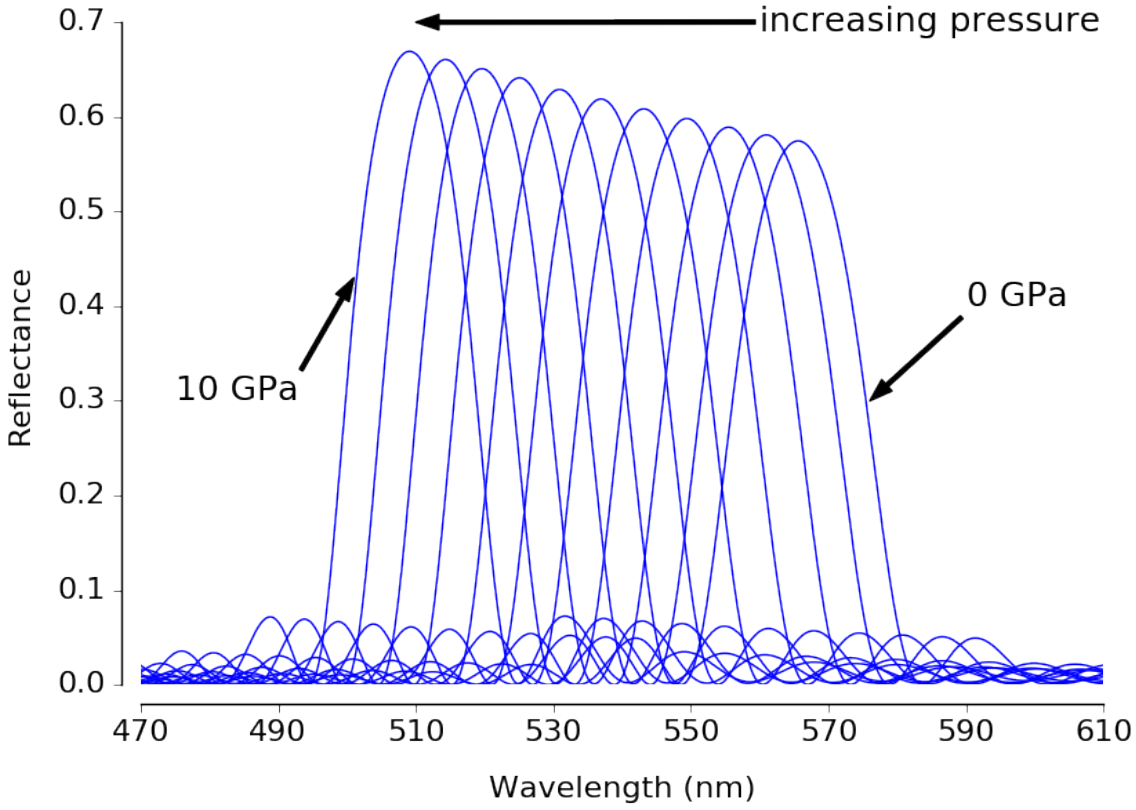

Figure 4.15: Simulated spectra of the SiO_x based DBR multilayers using the models described by Equations 4.13 - 4.15, Figure 4.14, and COMSOL Multiphysics under a uniaxial pressure of 0 - 10 GPa.

Figure 4.16 shows the peak features for the simulated SiO_x DBR spectra as a function of pressure, where peak position is defined as blueshift relative to the P = 0 (i.e., initial) condition, and peak width and height are normalized to the P = 0 initial condition. The peak position (blueshift) shows a similar, though slightly larger, change as a function of pressure compared to the SiO_2 AOMC. Peak height actually increases with pressure up to ~17% at 10 GPa, and peak width decreases to a smaller degree (~8%) at 10 GPa.

At this point, the complete spectral response of the AOMC and DBR multilayer struc-

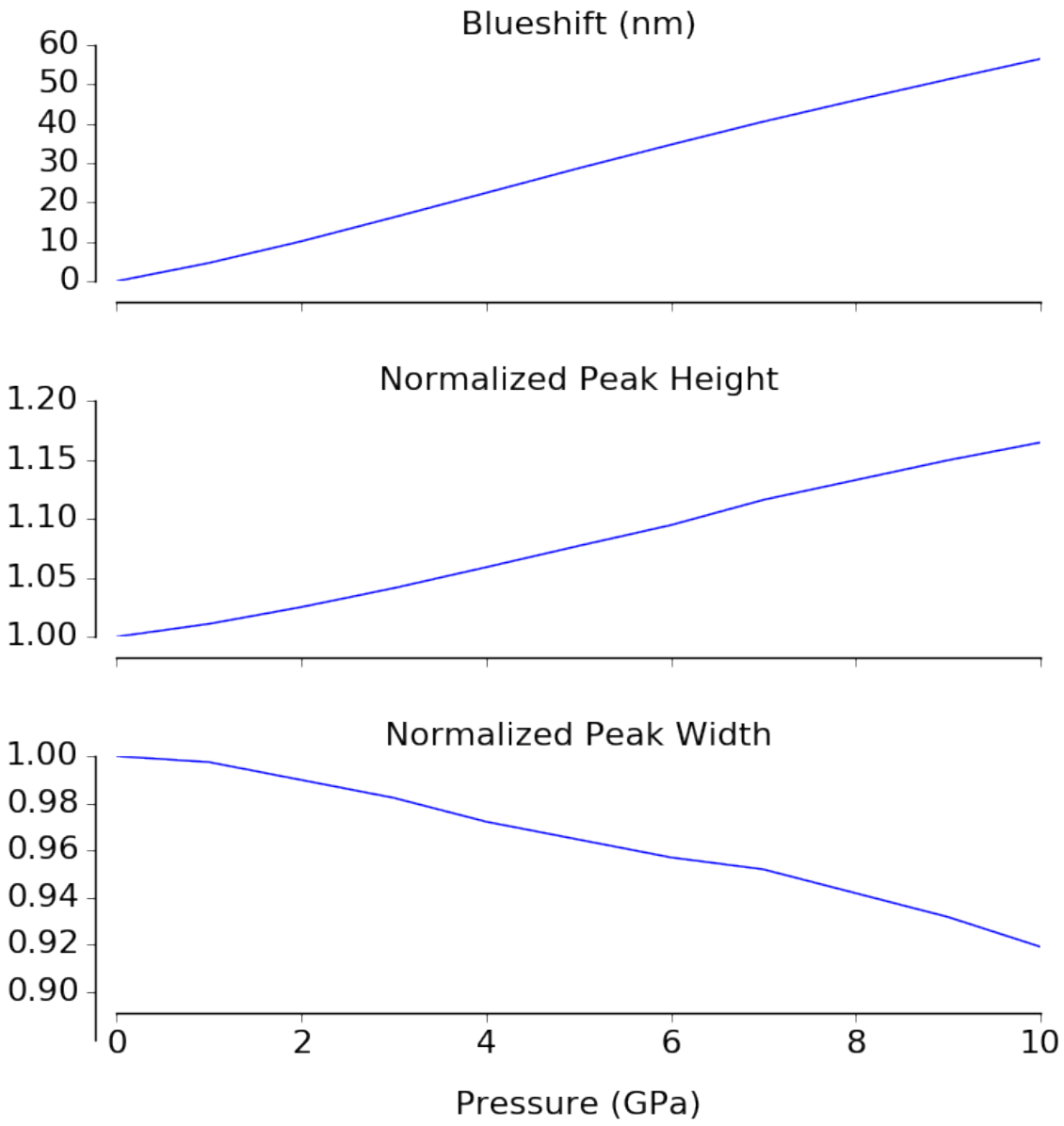

Figure 4.16: Extracted peak height, width, and position from the simulated spectra of the SiO_x based DBR multilayers using the models described by Equations 4.13 - 4.15, Figure 4.14, and COMSOL Multiphysics under a uniaxial pressure of 0 - 10 GPa.

tures to shock-compression loads has been qualitatively described, and quantitatively predicted. The combined optomechanical models are based on reasonably well-understood theories and empirical data, so there is good reason to assume that it will, at minimum, describe the trends observed in the spectral responses. In the following chapter, the predictions of these models will be compared to experimental data for the AOMC and SiO_X

DBR multilayers, testing the validity of this claim.

CHAPTER 5
MULTILAYER RESPONSES TO 1-D SHOCK-COMPRESSION

This chapter presents the results of the uniaxial shock-compression experiments on the fabricated multilayer samples presented in Section 4.1 using the experimental setup described in Section 3.1. As the experimental parameters varied within and between different multilayer samples and types, Table 5.1 provides a summary of the pertinent details for each individual experiment. The spectroscopically probed area and drive laser spot size are important for two reasons: a larger probed area may be affected more by the uniformity of the multilayer sample, and a smaller driver laser spot size will be slightly less "flat top" due to the performance of the beam shaping optics and focusing lens described in Section 3.1.1. The implications of these variables will be discussed, as needed, for each individual experiment. Note that the results of only a selected subset of experiments are presented in detail in Sections 5.2 and 5.3 as many of the results are very similar and provide little extra information. However, all of the usable experimental data are included in the comparison to the optomechanical model predictions in Sections 5.2.4 and 5.3.3.

5.1 Experimental Data Analysis

Prior to examining the experimental results, a brief discussion on data analysis and error estimation is warranted. In Section 4.2.3, the primary peak features measured in the predictions of the optomechanical model were peak depth/height, width, and position. These values are discrete and easily extracted with the smooth simulation data, but the inherent and unavoidable noise in the experimental data requires a more robust method to extract the peak features. To accomplish this, several different approaches are possible.

One useful approach is the method of moments from Brown et al. [84], where peak depth is the zeroth moment ($M^{(0)}$), position is the first moment ($M^{(1)}$), and width is the sec-

Table 5.1: Summary of relevant experimental parameters for the shock-compression and time-resolved spectroscopy experiments of the AOMC and DBR multilayer structures.

#	Type	Driver	Spectroscopically Probed Area	Laser Spot Size	Peak Pressure
FS0	SiO_2 AOMC	100 μm Al	3 mm	3 mm	0.8 GPa
FS1	SiO_2 AOMC	100 μm Al	3 mm	3 mm	1.5 GPa
FS2	SiO_2 AOMC	100 μm Al	3 mm	3 mm	3.2 GPa
FS3	SiO_2 AOMC	100 μm Al	2 mm	2 mm	5.6 GPa
FS4	SiO_2 AOMC	100 μm Al	2 mm	2 mm	5.6 GPa
FS5	SiO_2 AOMC	100 μm Al	2 mm	2 mm	5.9 GPa
FS6	SiO_2 AOMC	100 μm Al	2 mm	2 mm	6.1 GPa
FS7	SiO_2 AOMC	50 μm Al	1.5 mm	1.5 mm	8.6 GPa
FS8	SiO_2 AOMC	50 μm Al	1.5 mm	1.5 mm	9.9 GPa
FS9	SiO_2 AOMC	50 μm Al	1.5 mm	~1.3 mm	10.5 GPa
SP1	Al_2O_3 AOMC	50 μm Al	~1.5 mm	~1.5 mm	~8.5 GPa
PMMA1	PMMA AOMC	~25 μm Al	4.0 mm	4.0 mm	~2.0 GPa
SIO10-0	10 BL SIO_x DBR	50 μm Al	2 mm	2 mm	2.7 gpa
SIO10-1	10 BL SIO_x DBR	50 μm Al	2 mm	2 mm	4.5 gpa
SIO10-2	10 BL SIO_x DBR	50 μm Al	2 mm	2 mm	7.0 gpa
SIO5-0	5 BL SiO_x DBR	50 μm Al	2 mm	2 mm	4 GPa
SIO5-1	5 BL SiO_x DBR	50 μm Al	2 mm	2 mm	5.1 GPa
SIO5-2	5 BL SiO_x DBR	50 μm Al	2 mm	2 mm	6.5 GPa

ond moment ($M^{(2)}$). These statistics-based measures of the spectral features are very useful as they are relatively insensitive to noise and not dependent on particular peak shapes. They are also easily computed, which is an important criteria as each experiment with the setup described in Section 3.1.2 produces 1,024 individual spectra to analyze. Equations 5.1 - 5.3 show the definition of the moments for spectral measurements.

$$M^{(0)} = \int_0^\infty I(\lambda) d\lambda \tag{5.1}$$

$$M^{(1)} = \frac{1}{M^{(0)}} \int_0^\infty \lambda I(\lambda, t) d\lambda \tag{5.2}$$

$$M^{(2)} = \left[\frac{1}{M^{(0)}} \int_0^\infty (\lambda - M^{(1)})^2 I(\lambda) d\lambda \right]^{1/2} \tag{5.3}$$

However, one disadvantage of the moment approach is their sensitivity to the integration bounds. In practice, the bounds need to be limited to the spectral region immediately near the spectral peak, and the overall streak image needs to be well-corrected for intensity uniformity and spectral relative intensity. It was observed that for some experimental data, the correction process was only partially successful, leaving the calculated moments highly sensitive to the somewhat arbitrary integration bounds. Consequently, a different, multi-step approach was chosen for the spectral feature extraction:

1. The standard streak image correction process as described in Appendix B is performed

2. The location of the peak is first roughly located via the minimum/maximum value of

the spectra

3. A smoothing spline is then fit to the local region of the peak, using a static offset of 15-20 nm on either side of the rough peak location

4. The fitted peak location and height are extracted from the spline fit, and the peak width is defined as the width of the spline at 1/2 the fitted height

5. This process is repeated for every column of the streak image, as needed

Figure 5.1 shows this process on a single column of a streak image from a shock-compressed AOMC multilayer sample. The fit limits and smoothing parameters are set globally for each streak image at values that optimize the performance of the algorithm across the entire image (i.e., pre-shock and shocked spectra). In some cases, this may make the smoothing spline under/over fit the spectra to a small degree but not enough to significantly alter the extracted peak features in the vast majority of cases.

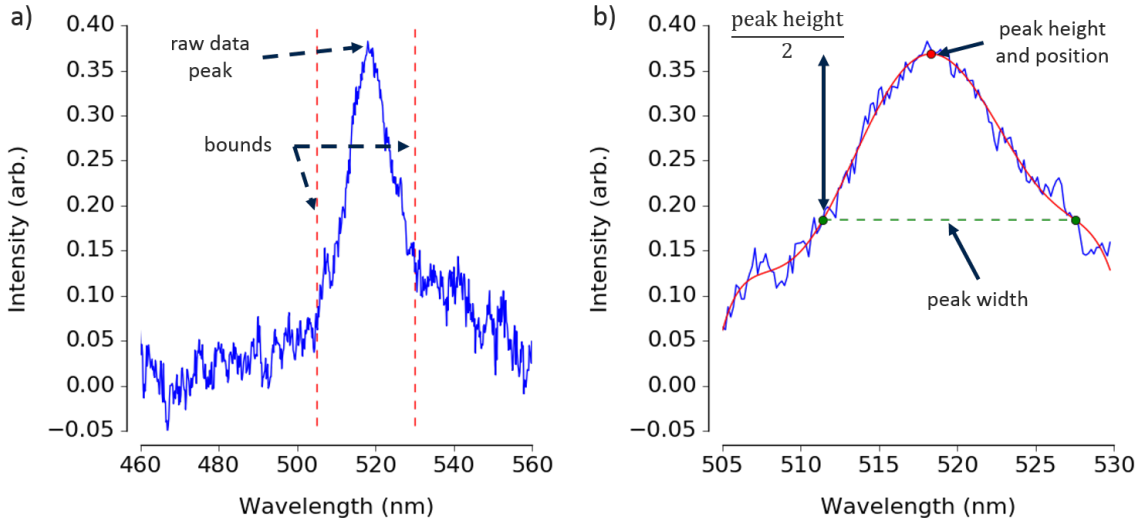

Figure 5.1: Peak feature extraction process from a single (inverted) column of an experimental streak image from a shock-compressed AOMC multilayer sample. (a) raw data and the selected offsets from the rough peak position, and (b) zoomed plot of the selected local region with the smoothing spline (red line) and calculated peak height, position, and width.

This process, while slightly more complex, required less hand-tuning than the method of moments and thus is a more objective measure of the spectral features of the multilayer.

It also produces measurements of peak features that are much closer to the direct approach used for the simulation data, enabling a more one-to-one comparison of the experimental data to the predictions of the optomechanical model.

Producing reasonable estimates of uncertainty in the extracted peak features offers it's own challenges. There are two sources of uncertainty in any experimental data: random and systematic. As many sources of systematic error as possible were identified and corrected using the streak camera correction process described in Appendix B, and spectral calibration measurements were collected prior to every set of experiments. Nonetheless, the streak camera correction process is not free of assumptions, and the spectral peaks from the calibration lamp are relatively sparse in the visible wavelength, so some systematic error will be present. In comparison to the random error, however, it is likely negligible and is not included in the overall uncertainty estimation process for the streak data. Another source of systematic error comes from the PDV analysis process, as discussed in Section 3.1.3, though quantitative and objective values of this error are difficult. Random error in the streak data is almost entirely due to the inherent noise in the streak camera image, as defined by the signal-to-noise ratio. The random error in the PDV data is assumed to be very low due to the precision of the DPO70804 oscilloscope and the relative insensitivity of PDV analysis methods to random noise.

With these assumptions, uncertainties for the following specific experimental variables were defined. Each variable was calculated in the region of the laser-driven pressure pulse corresponding to the maximum "steady-state" pressure, which was typically the 2-5 ns immediately following the pressure rise as shown in Figure 3.3.

- **Peak Height/Depth**: The peak height/depth error is the root-mean-square (RMS) sum of the standard deviation of the height/depth of the smoothing spline in the "steady-state" pressure region and the standard deviation of the height/depth of 20 pre-shock spectra from the same streak image.

- **Peak Width**: The peak width error is the root-mean-square (RMS) sum of the stan-

dard deviation of the width of the smoothing spline in the "steady-state" pressure region and the standard deviation of the width of 20 pre-shock spectra from the same streak image.

- **Peak Position**: The peak position (blueshift) error is the root-mean-square (RMS) sum of the standard deviation of the position of the smoothing spline in the "steady-state" pressure region and the standard deviation of the position of 20 pre-shock spectra from the same streak image.

- **"Steady-State" Pressure**: The "steady-state" pressure error is more difficult to define due to the difficulties and somewhat subjective nature of analyzing nanosecond-scale data from a standard PDV system as discussed in Section 3.1.3. Consequently, a semi-qualitative approach is taken. First, the "steady-state" velocity is selected manually from the appropriate region of the extracted velocity profile. For fused silica, pressure is calculated using the P-U_P fit to experimental data by Barker and Hollenbach [97] and the window correction data (fit with a 3rd order polynomial) also by Barker and Hollenbach. For Al_2O_3, pressure is calculated using a linear fit to the Us-Up relationship from Setchell et al. [98] and the window correction data at 1550 nm from Jensen et al. [135]. In both cases, the pressure error is then defined based on one of three categories, corresponding to the subjective quality of the PDV data and the agreement between various methods of velocity extraction: "low" error of 5%, "medium" error of 10%, and "high" error of 15%.

For the peak feature variables (depth/height, position, and width), the addition of the standard deviation of those values for the spline-fitted pre-shock spectra is to attempt to capture the variation of the smoothing spline fit on features that should, in the absence of random noise, be static over the pre-shock region. Figure 5.2 shows an example streak image and PDV velocity profile with the pre-shock and "steady-state" pressure regions highlighted. Note that these regions must be hand-selected for each experiment due to

relatively significant overall timing variances between experiments.

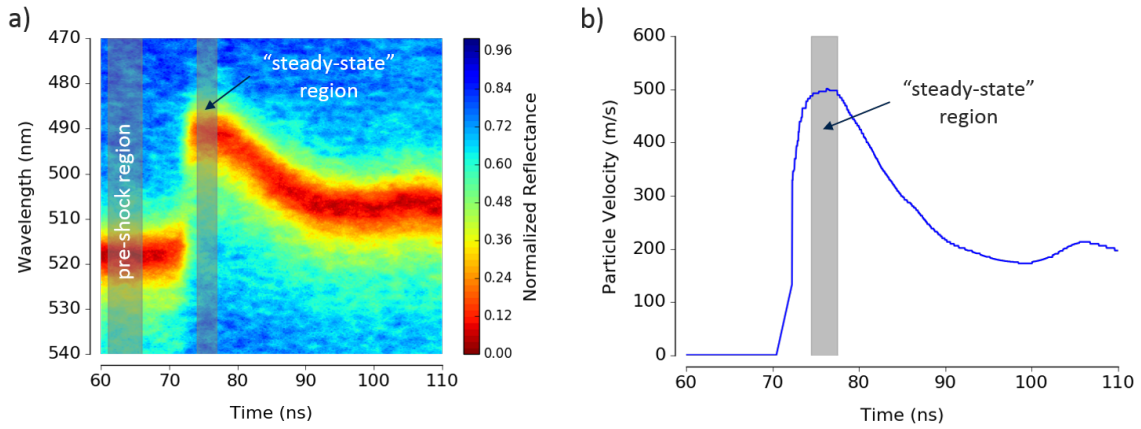

Figure 5.2: (a) Example streak image and (b) PDV particle velocity profile for a shock-compressed AOMC multilayer showing the pre-shock and "steady-state" peak pressure regions. These regions are hand-selected for each experiment, and the streak image and PDV "steady-state" velocity may not be at precisely the same times depending on the quality of the data and match between the streak image and velocity profile.

Overall, every attempt has been made to make the data analysis and uncertainty estimation process as objective and repeatable as possible. Nonetheless, in order to remain conservative in any quantitative use of the experimental data, all reported error values for the spectral features are *at the 2-sigma level*. Ideally, this buffer will cover the existence of uncorrected systematic error, unknown sources of potential bias, and the few components of the analysis process that require "hand-tuning."

5.2 Optical Microcavities

5.2.1 SiO_2 based AOMCs

Experiment # FS1: ~1.5 GPa

The extracted time-resolved peak position, depth, width, and corrected streak image for experiment #FS1 is shown in Figure 5.3. There is a clear shift in the AOMC peak to shorter wavelengths as the pressure wave crosses the multilayer with the entire rise, "steady-state," and release behavior of the laser driven shock-compression captured. The peak depth and

width show momentary changes in the vicinity of the rise but quickly return to values likely within the noise of the pre-shock values.

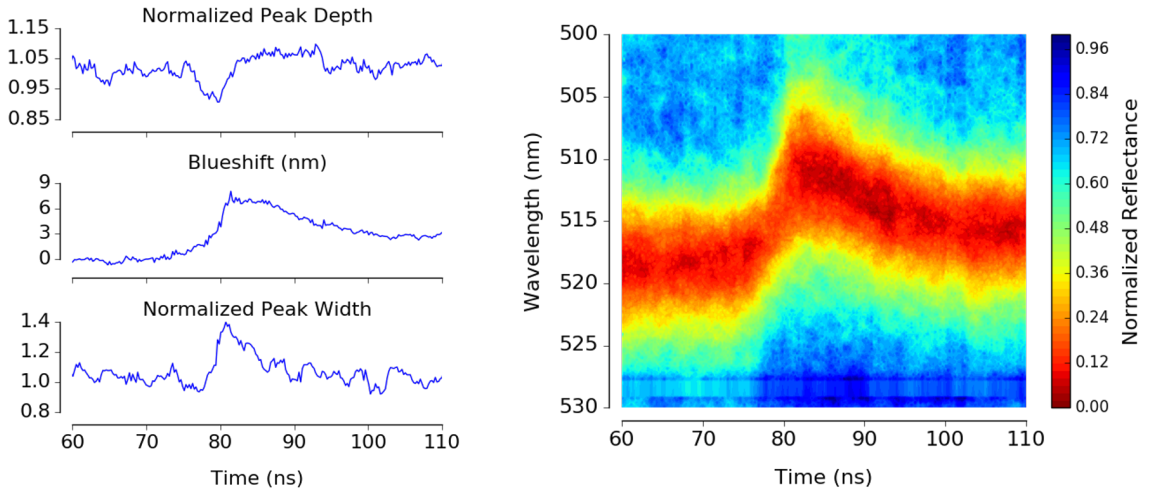

Figure 5.3: Extracted time-resolved peak features (blueshift, normalized width and depth) and streak image for experiment #FS1 at a "steady-state" pressure of ~1.5 GPa.

Experiment # FS2: ~3.2 GPa

The extracted time-resolved peak position, depth, width, and corrected streak image for experiment #FS2 is shown in Figure 5.4. The peak shift with the applied laser-driven shock-compression remains very clear and shows similar features to the lower pressure experiment. The peak depth and width show similar momentary changes in the vicinity of the rise but at a much larger magnitude and take longer to return to the pre-shock values.

Experiment # FS3: ~5.5 GPa

The extracted time-resolved peak position, depth, width, and corrected streak image for experiment #FS3 is shown in Figure 5.5. The peak shift with the shock load remains exceptionally clear, although the region associated with the rise is barely visible, with the blueshift plot showing a discontinuity. The peak width also shows no discernible trend unlike the previous lower-pressure experiments (FS1 and FS2).

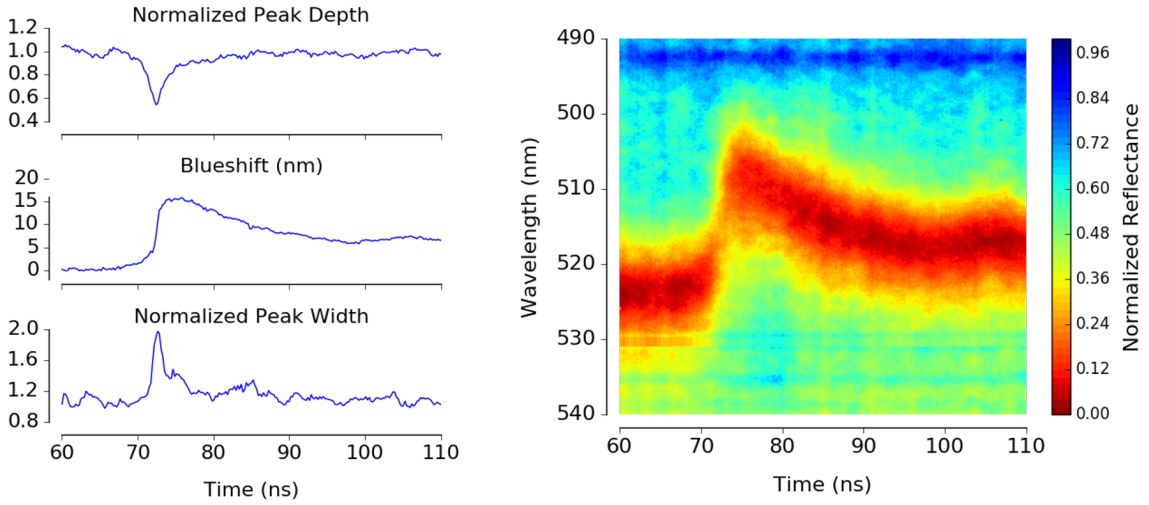

Figure 5.4: Extracted time-resolved peak features (blueshift, normalized width and depth) and streak image for experiment #FS2 at a "steady-state" pressure of ~3.2 GPa.

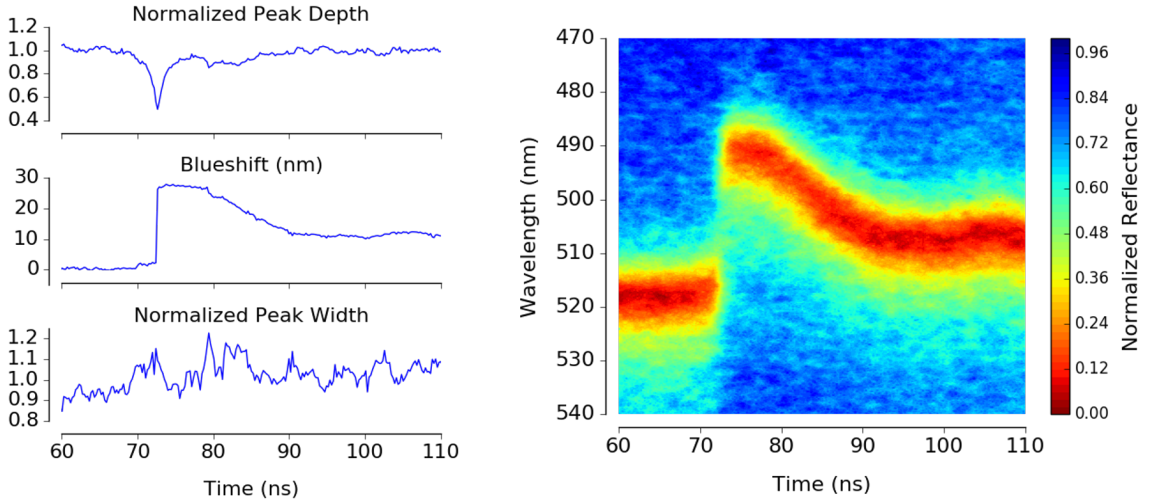

Figure 5.5: Extracted time-resolved peak features (blueshift, normalized width and depth) and streak image for experiment #FS3 at a "steady-state" pressure of ~5.5 GPa.

Experiment # FS7: ~8.5 GPa

The extracted time-resolved peak position, depth, width, and corrected streak image for experiment #FS7 is shown in Figure 5.6. The peak shift remains clear, but the discontinuous nature of the spectral shift in the region associated with the pressure rise remains. Normalized peak depth and width also show substantial changes with recovery times taking longer than the duration of the "steady-state" pressure load. As listed in Table 5.1, this ex-

periment was conducted with a ~1.5 mm spot size (spectroscopically probed and shocked), which may have subtle effects on the uniformity of the drive-laser and corresponding decreases in the overall spatial uniformity of the pressure pulse. This may partially explain the significant increase in the peak width due to the shock load observed.

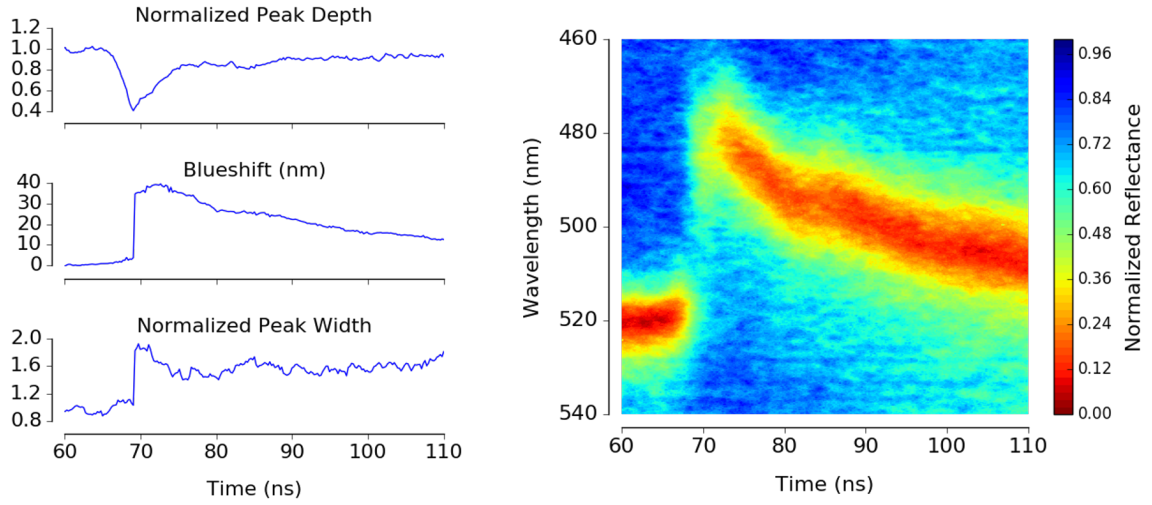

Figure 5.6: Extracted time-resolved peak features (blueshift, normalized width and depth) and streak image for experiment #FS3 at a "steady-state" pressure of ~8.5 GPa.

Experiment # FS9: ~10.5 GPa

The extracted time-resolved peak position, depth, width, and corrected streak image for experiment #FS9 is shown in Figure 5.7. The features and temporal trends in the peak features are very similar to experiment #FS7. In particular, the peak width shows extensive broadening potentially due to the smaller shocked area (~1.3 mm) and the slightly larger 1.5 mm spectroscopically probed area.

Combined Results and Comparison to Benchmark Velocimetry Diagnostic

The plots in Figure 5.8 show the combined results of the selected fused silica AOMC experiments (#'s FS1, FS2, FS3, FS7, FS9), illustrating the temporal profiles for each experiment's peak features (blueshift, depth, and width, respectively).

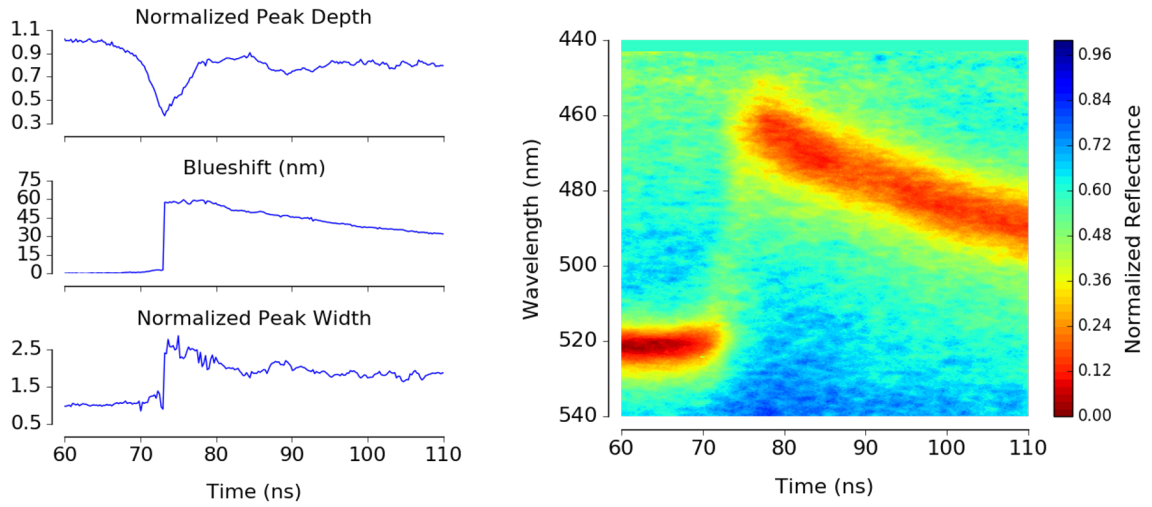

Figure 5.7: Extracted time-resolved peak features (blueshift, normalized width and depth) and streak image for experiment #FS9 at a "steady-state" pressure of ~10.5 GPa.

The data have several aspects worth highlighting. First, the blueshift in each experiment shows a consistent trend across the range of pressures tested with clear "steady-state" regions at the peak of the laser-driven shock pressure pulse. Contrasting that, the peak depth and width show more complex behaviors. Notably, the times corresponding to the "steady-state" region of the blueshift profiles do *not* show similarly "steady-state" behavior in the peak width and depth profiles. There are several partial explanations for this behavior. First, the discontinuity observed in the streak image at the onset of the blueshift and the generally large decrease in peak depth are challenging for the peak feature extraction algorithm presented in Section 5.1 to handle accurately. Second, insufficient background correction/removal on the streak data will bias the peak depth (and peak width, to a smaller degree) magnitude and temporal profile. However, it is unlikely that the lack of a "steady-state" region in the peak width and depth temporal profiles are solely due to these analysis limitations. This does not mean that there are not general trends in the peak width/depth as a function of pressure; it is clear that depth decreases and width increases with increasing pressure, just not with the clarity shown in the blueshift profiles. It is also clear that peak depth and width show marked changes at and slightly before the arrival of the pressure pulse (with the one exception of experiment FS3 at 5.6 GPa), indicating that there are in-

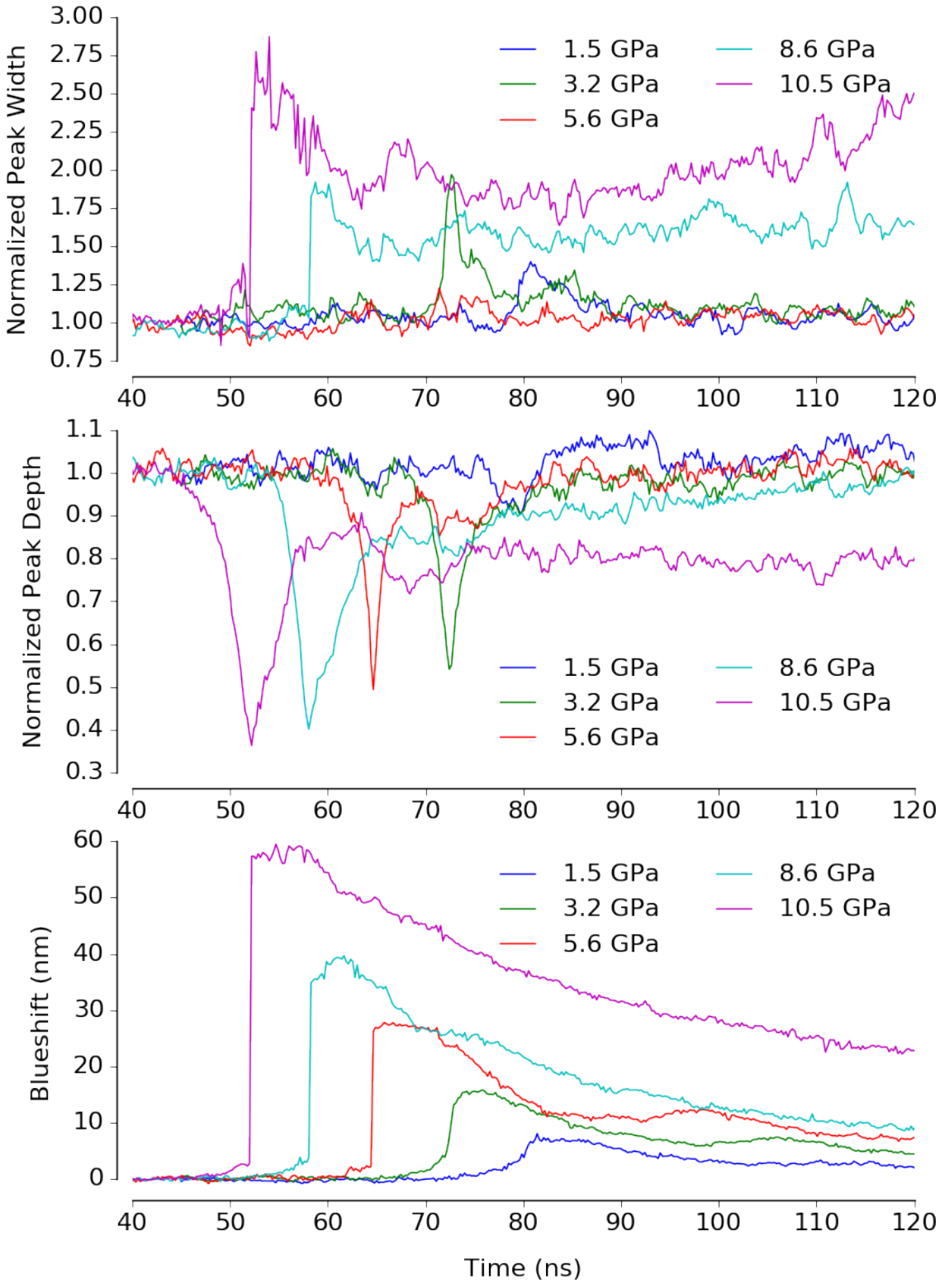

Figure 5.8: Combined plots of time-resolved peak features (blueshift, peak depth, and peak width) for fused silica based AOMC experiments FS1, FS2, FS3, FS7, FS9. Note that each profile has been arbitrarily offset in time to improve visibility and interpretability of each experiment's profile.

deed pressure-induced effects on these peak features that operate on similar time-scales to the blueshift.

Based on the quality of the blueshift profiles, a comparison to the *in-situ* particle velocity is particularly useful as there should be good correlation based on the observed trends. Figure 5.9 shows the blueshift from experiment #FS2 overlaid with the extracted particle velocity (upper plot) and compared to the raw PDV trace (lower plot). Figure 5.10 shows the blueshift from experiment #FS3 overlaid with the extracted particle velocity (upper plot) and compared to the raw PDV trace (lower plot). Figure 5.11 shows the blueshift from experiment #FS7 overlaid with the extracted particle velocity (upper plot) and compared to the raw PDV trace (lower plot).

These comparisons also have several interesting features. First, all three comparisons show excellent, nanosecond-level correlation along the blueshift/velocity rise and approximate "steady-state" regions of blueshift/velocity. This is an important result as the rise/"steady-state" region is the most direct comparison to the Rankine-Hugoniot conditions of a perfect shock and indicate that the spectral responses of the multilayer structures as manifested in the blueshift are behaving as time-resolved stress/pressure sensors, as theorized. Looking at the longer time pressure-release behavior of each experiment, the correlation varies somewhat. Experiment #FS3 shows a superb match throughout the release, #FS7 a quite good match, and #FS2 a reasonable match. Inspecting the raw PDV traces is informative to understanding this variation in the quality of the correlation. For example, #FS3 has the best quality PDV data while #FS2 and #FS7 have notable regions of low signal-to-noise ratio and anomalies in the beat pattern. In particular, the anomaly at ~80 ns in the PDV trace for #FS2 has a significant effect on the extracted velocity profile, leading to some skepticism of the second velocity peak. Additionally, such an immediate second peak is generally not expected from the laser-driven shock-compression system in this work. Similarly, the drop in the signal-to-noise ratio between 75-79 ns for experiment #FS7 may explain the sharper shoulder seen in the velocity profile compared to the corresponding blueshift release be-

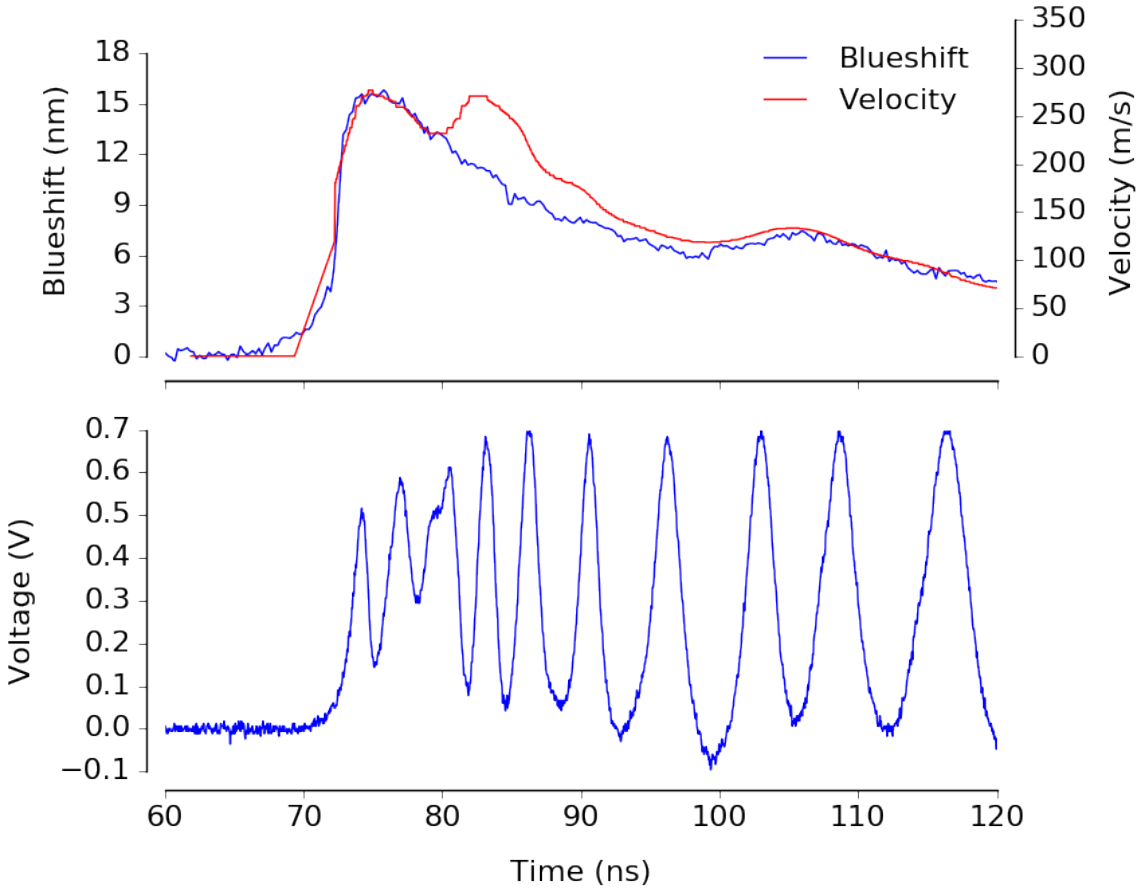

Figure 5.9: Comparison of the extracted blueshift and PDV particle velocity (upper plot) for experiment #FS2 (~3.2 GPa) along with the raw PDV data (lower plot). Note that the PDV extracted velocity was manually aligned with the blueshift profile using the rise and peak "steady-state" regions to allow a more direct comparison of each profile's temporal features.

havior. Additionally, comparison of velocity and pressure along the pressure-release path is somewhat fraught as it technically follows a different thermodynamic pathway compared to the pressure-rise, though the mostly elastic behavior of fused silica in this pressure range makes it difficult to quantify the degree of deviation.

Overall, however, the very close (often sub-nanosecond) correlation of the particle velocity profiles and the spectral blueshift of the fused silica AOMC structures is strong, unambiguous evidence that the fundamental theory of the proposed sensing mechanism of the multilayers is sound. For the other experiments in the FS category that are not shown, the match between the blueshift and particle velocity ranges from good to excellent, in

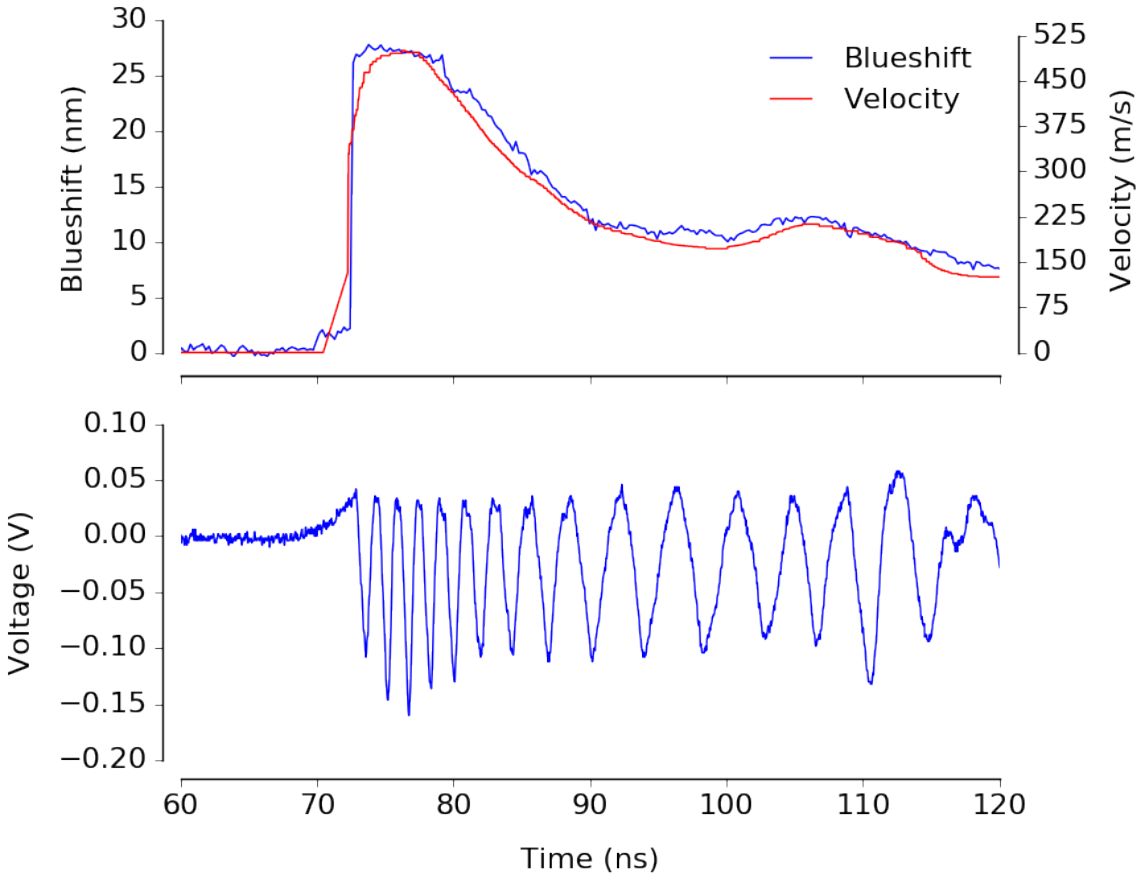

Figure 5.10: Comparison of the extracted blueshift and PDV particle velocity (upper plot) for experiment #FS3 (~5.6 GPa), along with the raw PDV data (lower plot). Note that the PDV extracted velocity was manually aligned with the blueshift profile using the rise and peak "steady-state" regions to allow a more direct comparison of each profile's temporal features.

general. The few exceptions having very poor quality raw PDV traces that confound the comparison.

5.2.2 Al_2O_3 based OMC

Experiment # SP1: ~8.5 GPa

The extracted time-resolved peak position, depth, and the corrected streak image for experiment #SP1 is shown in Figure 5.12. It is clear that the quality of the streak image is low for this experiment. This was due to several factors including poor sample quality and insufficient background correction. Relatedly, this prevented extraction of the peak

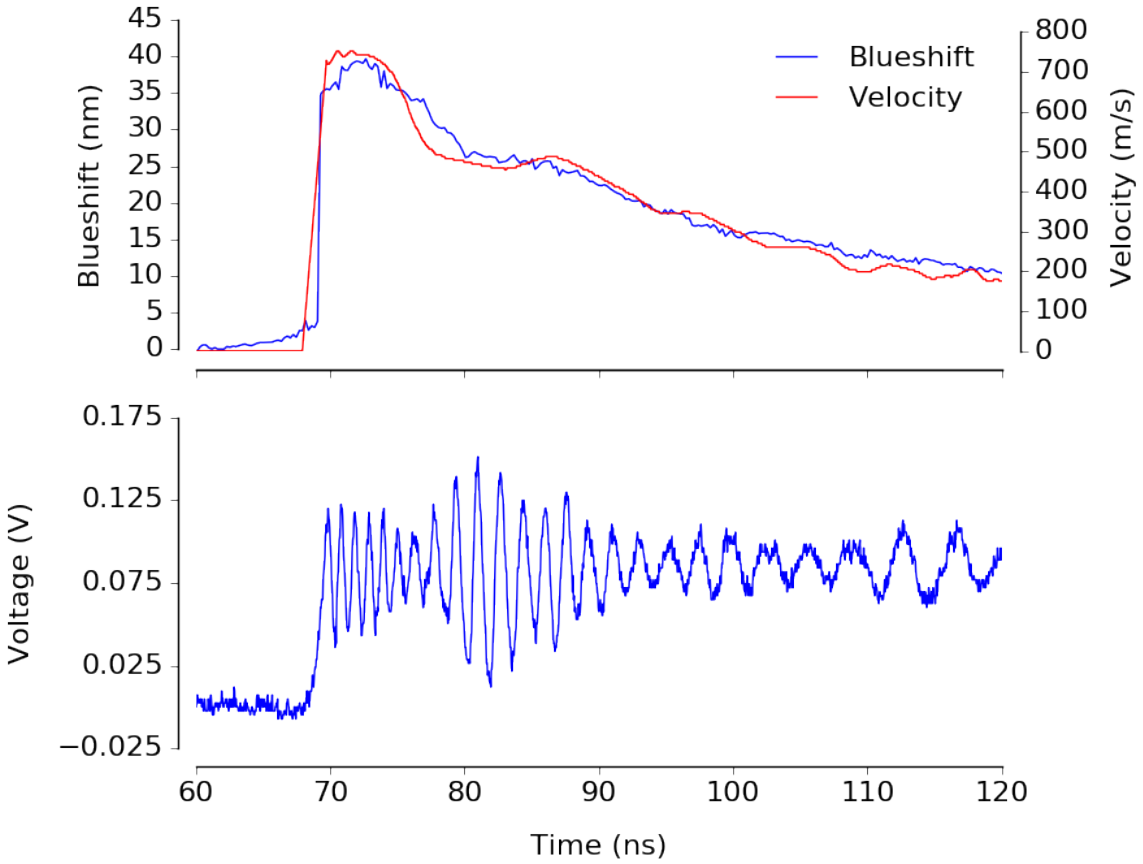

Figure 5.11: Comparison of the extracted blueshift and PDV particle velocity (upper plot) for experiment #FS7 (~8.6 GPa), along with the raw PDV data (lower plot). Note that the PDV extracted velocity was manually aligned with the blueshift profile using the rise and peak "steady-state" regions to allow a more direct comparison of each profile's temporal features.

width as a time-resolved variable and caused the apparent blueshift rise-time anomaly. Despite the data quality, however, there is still clearly a well-defined blueshift profile that has roughly the expected temporal profile of laser-driven shock-compression. Notably, the blueshift is of a much smaller magnitude compared to the fused silica AOMC multilayer at similar pressures, which was expected based on the much stiffer Al_2O_3 cavity and the theories/models presented in Chapter 4.

Figure 5.13 shows the blueshift from experiment #SP1 overlaid with the extracted particle velocity (upper plot) and compared to the raw PDV trace (lower plot). The quality of the PDV data is adequate, and the correlation between the time-resolved blueshift and

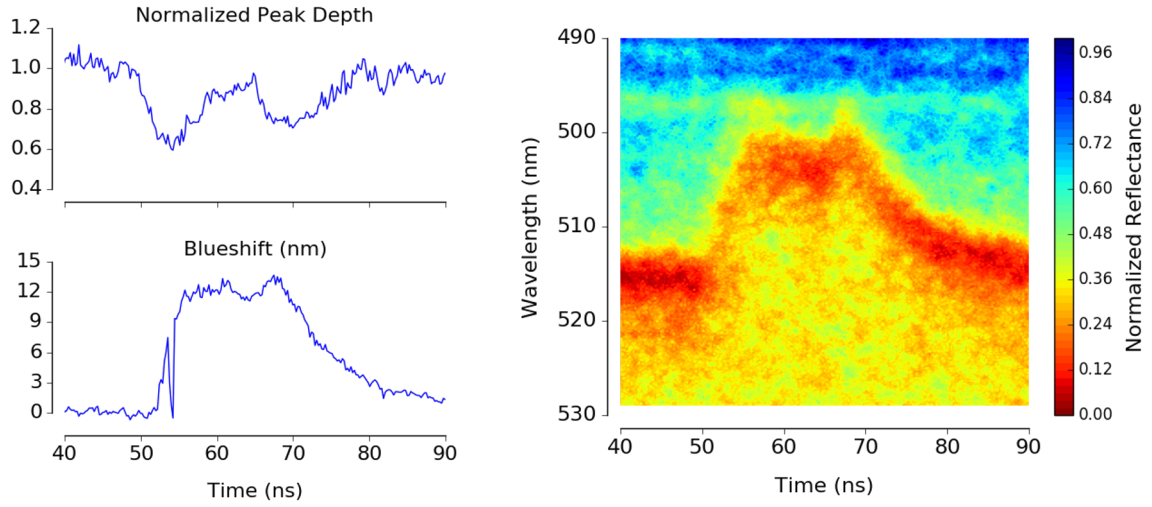

Figure 5.12: Extracted time-resolved peak features (blueshift, normalized width and depth) and streak image for experiment #SP1 at a "steady-state" pressure of ~8.5 GPa.

particle velocity is reasonable, though not as well-matched as the fused silica AOMC multilayers. However, this may simply be due to limited experiments and poor streak camera data quality for the Al_2O_3 AOMCs. The important point to emphasize is that there is still a well-defined blueshift as a function of pressure for this AOMC design with a magnitude in-line with the intuitive behavior of a stiffer AOMC cavity material.

5.2.3 PMMA based AOMC

Experiment # PMMA1: ~1.5 GPa

The extracted time-resolved peak position, depth, and the corrected streak image for experiment #PMMA1 is shown in Figure 5.14. It is clear that the quality of the streak image is very low for this experiment. This was due to several factors including very poor sample quality, insufficient background correction, and an earlier implementation of the time-resolved spectroscopy experimental setup that was much less efficient in light collection. These limitations led to the inability to extract the peak width and the largely uninformative peak depth temporal profile. Nevertheless, again there are still several key features that are evident in the data. For example, the blueshift is still visible in the streak image and by

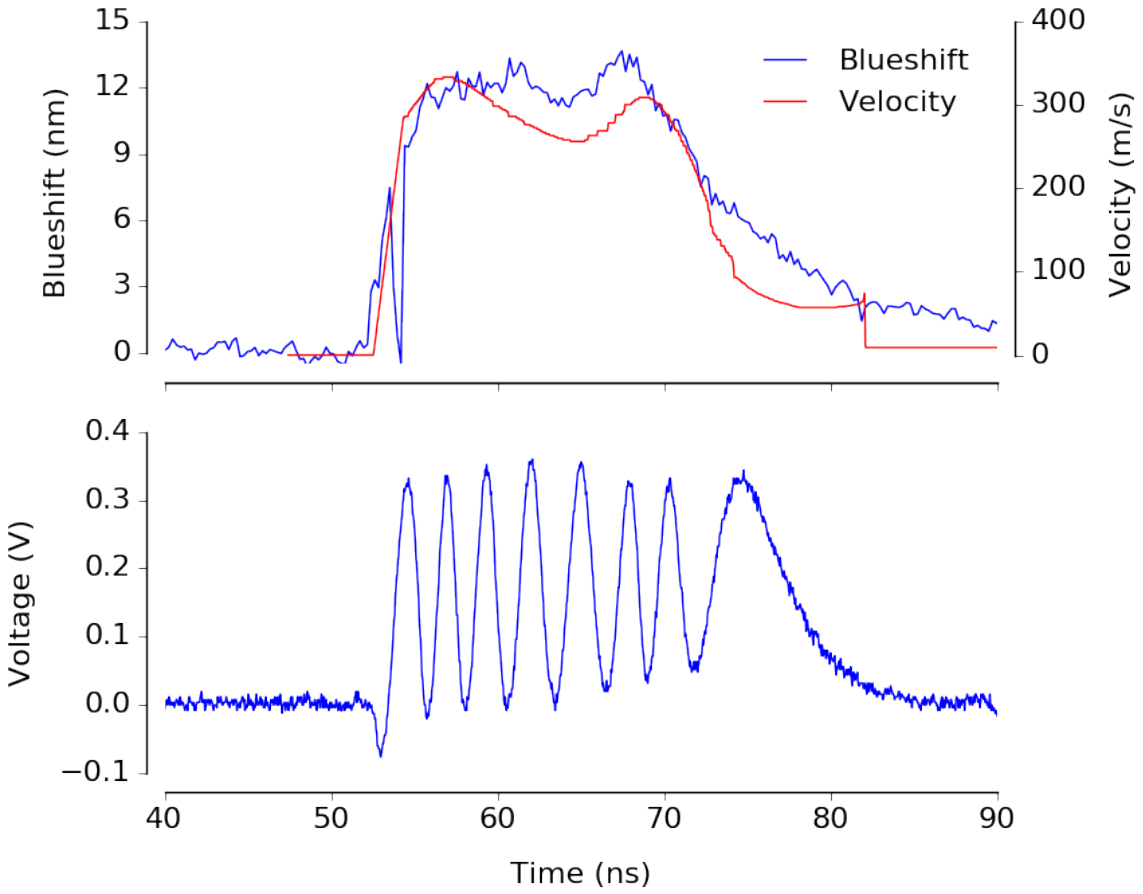

Figure 5.13: Comparison of the extracted blueshift and PDV particle velocity (upper plot) for experiment #SP1 (~8.5 GPa) along with the raw PDV data (lower plot). Note that the PDV extracted velocity was manually aligned with the blueshift profile using the rise and peak "steady-state" regions to allow a more direct comparison of each profile's temporal features.

smoothing the extracted blueshift (gray in the same plot is the raw extracted blueshift) the same expected laser-driven shock pressure profile is evident. However, the blueshift profile is elongated in time by a factor of 2-4 times compared to the fused silica AOMC multilayers. Unfortunately, simultaneous particle velocity data was not collected during this experiment to independently verify this behavior. While initially surprising, very similar temporal elongation effects have been observed in shock-compressed PMMA by Banishev et al. [145]. Even more relevant, Kang et al. [88] saw very similar temporal elongation scales in the time-resolved spectral response of CdTe quantum dots embedded in a polymer matrix when compared to similar quantum dots in a glass matrix. In both cases, it is

theorized that the viscous response of the polymer to the shock-compression creates the temporal elongation effect. Consequently, it is presumed that similar mechanisms are at play in the PMMA AOMC multilayer. Finally, the magnitude of the blueshift (~30 nm at ~1.5 GPa) is quite large, which again is in line with the qualitative predictions of the underlying theorized sensing mechanism of the multilayers.

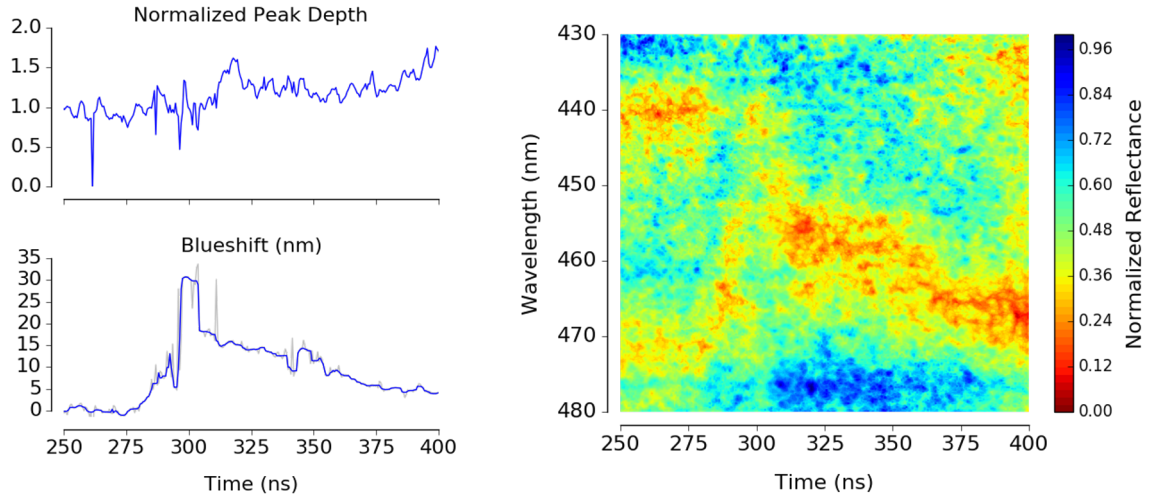

Figure 5.14: Extracted time-resolved peak features (blueshift, normalized width and depth) and streak image for experiment #PMMA1 at a "steady-state" pressure of ~1.5 GPa. The blueshift temporal profile was lightly smoothed with a median filter to remove the sharp, spurious peaks visible in the unsmoothed data (plotted in light gray).

5.2.4 Comparison to Optomechanical Model Predictions

With the experimental data available for the different AOMC structures, the time-resolved peak features can be compared to the predictions from the optomechanical models presented in Section 4.2.3. Figure 5.16 shows the extracted blueshift, peak height, and peak width compared to the model prediction curves first shown in Figure 4.12. All of the experimental points correspond to the spectral features extracted at the "steady-state" pressure condition with 2-sigma error bars for the peak feature values.

The result of this comparison is somewhat mixed. Perhaps most importantly, the experimental "steady-state" blueshift is an excellent match to the model predictions with a

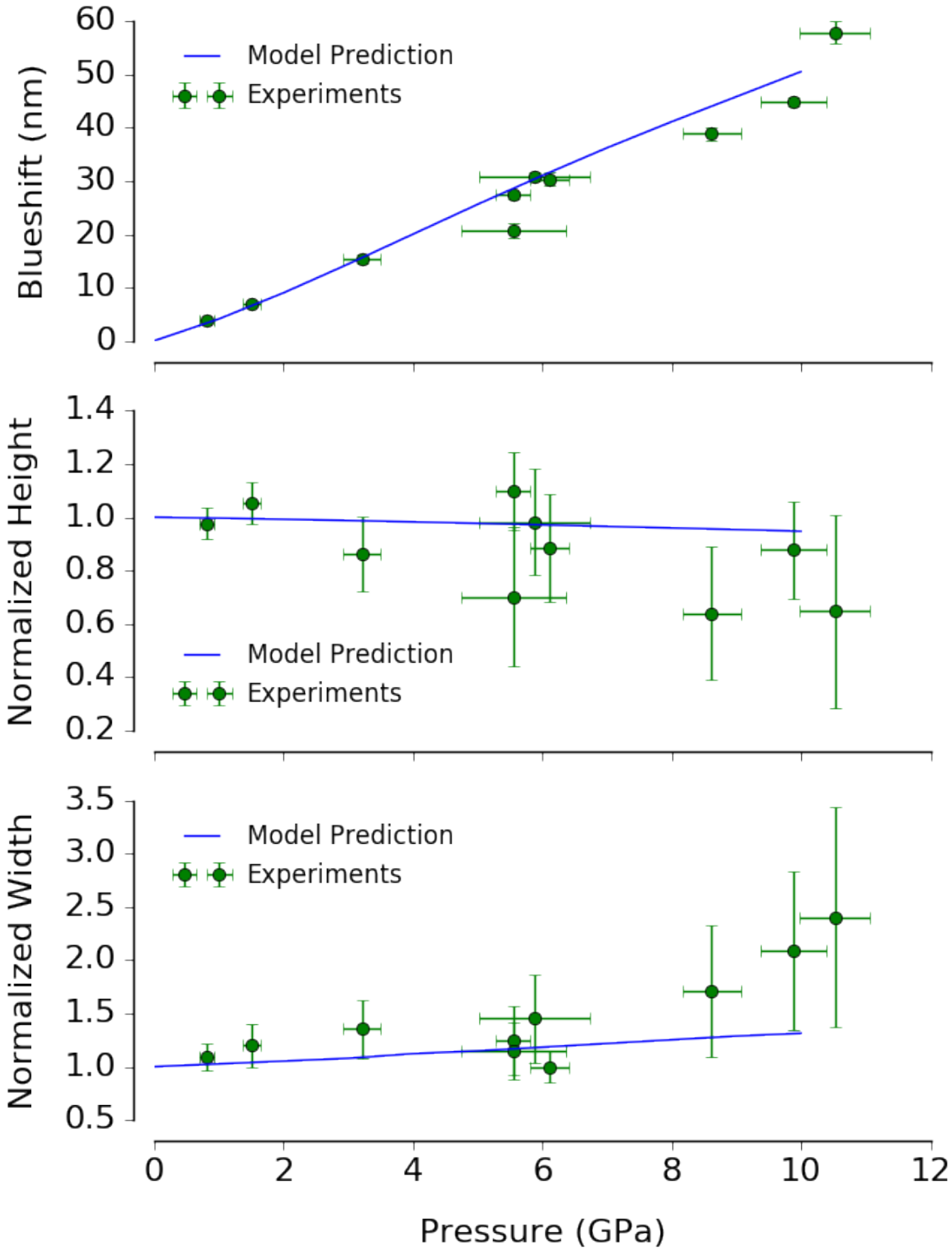

Figure 5.15: Comparison of the collected experimental data to the predictions of the optomechanical model presented in Section 4.2.3. The data points have 2-sigma error bars in the y axis, and the qualitative $\pm$ 5%, 10%, 15% error on the x axis.

few moderate exceptions at higher pressures where the known elastic-plastic transition in fused silica may begin to have an effect. This is a very encouraging result as the spectral blueshift was theorized to be the primary sensing mechanism for the multilayers. However, expanding the observations made regarding Figure 5.8, the peak height and width do not show clear, quantitative matches to the model predictions. These comparisons are made especially difficult in that background correction, spectral feature extraction, and lack of a clear "steady-state" region in the width/depth temporal profiles all contribute to the substantial error bars in the corresponding experimental data. Fortunately, this means that more accurate determinations of the peak width/depth are likely possible but unfortunately not with the present experimental data.

Figure 5.16 shows the combined model-predicted and experimental blueshift data for the fused silica, Al_2O_3, and PMMA based AOMC multilayers. As there are only single experiments for the Al_2O_3 and PMMA structures, validation of the overall trend is not possible and instead is just a general comparison of the model's prediction at a given pressure.

The PMMA AOMC experiment is well-matched to the model, but the magnitude of the error bars and the clearly low signal-to-noise of the streak camera data in Figure 5.14 make a quantitative claim suspect. The Al_2O_3 AOMC experiment is slightly above the predictions of the corresponding model predictions but still very reasonable given the model's assumptions. One potential explanation is the material structure of the deposited Al_2O_3 cavity layer. The model assumes hard, crystalline C-cut sapphire, but in reality the cavity layer is likely slightly softer amorphous or partially amorphous Al_2O_3. This would cause the model to underestimate the magnitude of the blueshift at a given pressure, which is the offset observed in the single Al_2O_3 AOMC experiment. Broadly, the different "regimes" in the blueshift vs. pressure space as a function of AOMC cavity material are clearly visible in both the experimental data and model predictions, which is an important validation of the underlying theory of multilayer based pressure sensors.

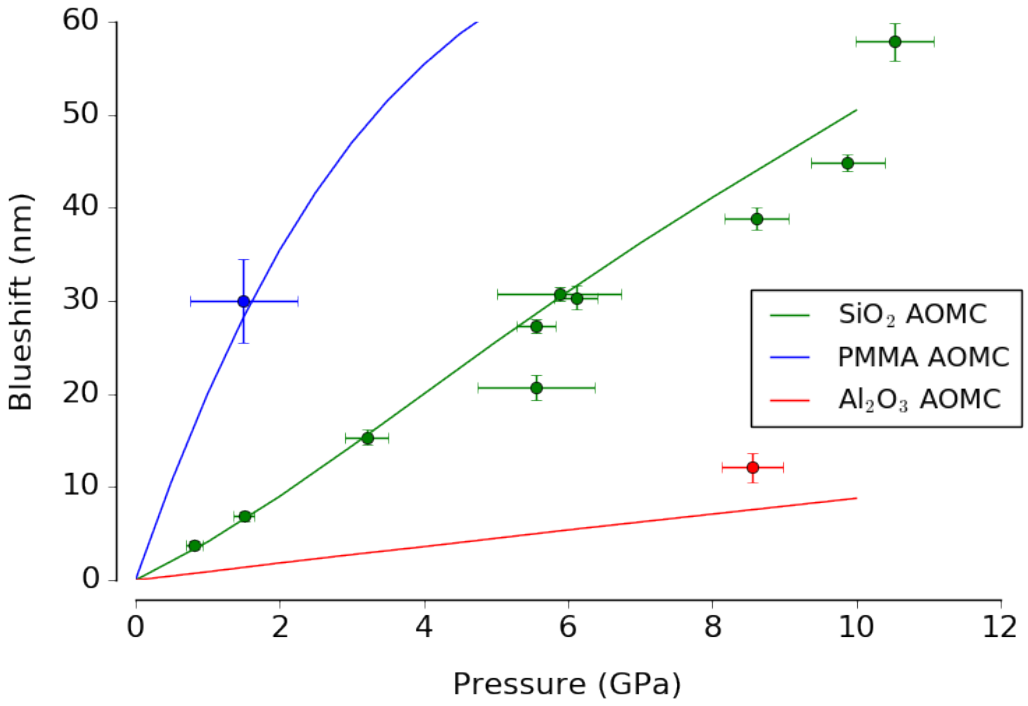

Figure 5.16: Comparison of the collected experimental blueshift data for all three of the AOMC multilayers to the predictions of each corresponding optomechanical model presented in Section 4.2.3.

5.3 Distributed Bragg Reflectors

5.3.1 10 Bilayer SiO_x DBR

Experiment # SIO10-0: ~2.7 GPa

The extracted time-resolved peak position, height, width, and corrected streak image for experiment #SIO10-0 is shown in Figure 5.17. There is a clear shift in the DBR reflectance peak to shorter wavelengths as the pressure wave crosses the multilayer with the entire rise, "steady-state," and release behavior of the laser-driven shock-compression captured. Broadly, this result is very similar to that observed for the AOMC multilayers. In some ways, the results from the SiO_x DBR are even more clear as the spectral shift remains clearly resolved during the pressure rise and does not display the discontinuous nature that was frequently observed in the AOMC multilayers.

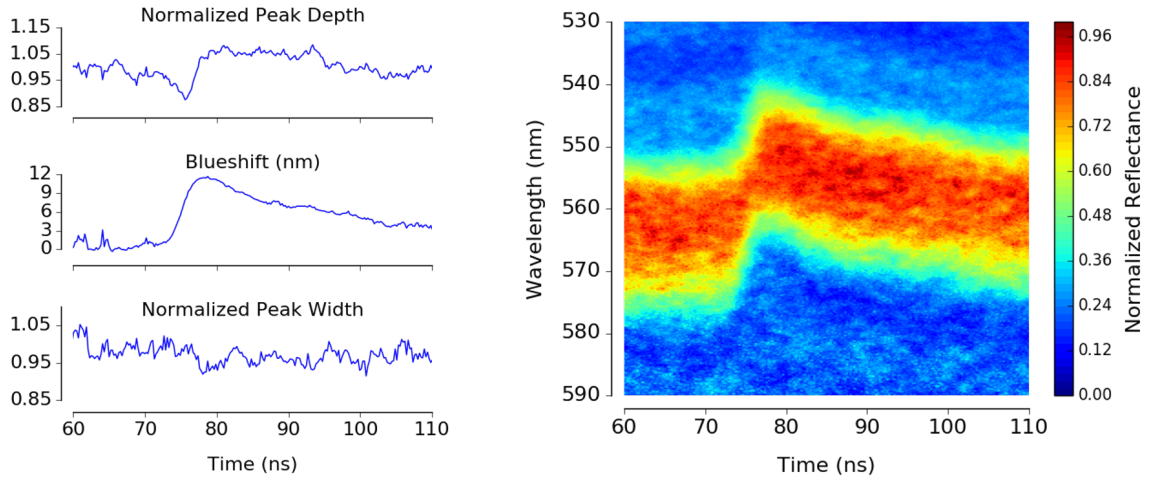

Figure 5.17: Extracted time-resolved peak features (blueshift, normalized width and height) and streak image for experiment # SIO10-0 at a "steady-state" pressure of ~2.7 GPa.

Experiment # SIO10-1: ~4.5 GPa

The extracted time-resolved peak position, height, width, and corrected streak image for experiment #SIO10-1 is shown in Figure 5.18. These data are quite similar to those from the previous experiment with an increased time-resolved blueshift due to the increased peak pressure.

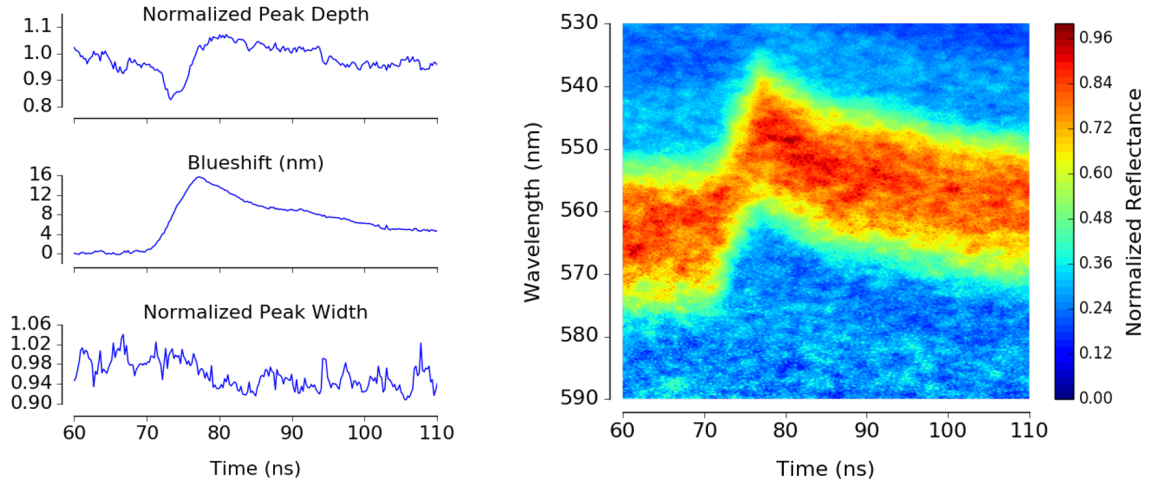

Figure 5.18: Extracted time-resolved peak features (blueshift, normalized width and height) and streak image for experiment # SIO10-1 at a "steady-state" pressure of ~4.5 GPa.

Experiment # SIO10-2: ~7.0 GPa

The extracted time-resolved peak position, height, width, and corrected streak image for experiment #SIO10-2 is shown in Figure 5.19. Again, a very similar trend is observed with more visible effects on the peak height and width during the rise. The peak remains resolved during this temporal region, but some characteristics of the streak image begin to show a discontinuous response similar to the AOMCs.

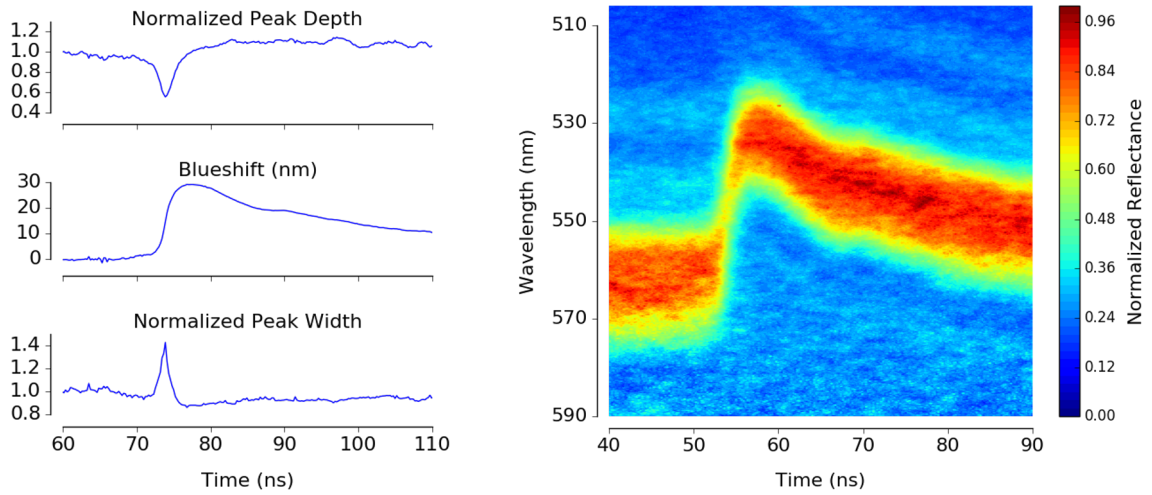

Figure 5.19: Extracted time-resolved peak features (blueshift, normalized width and height) and streak image for experiment # SIO10-2 at a "steady-state" pressure of ~7.0 GPa.

Combined Results and Comparison to Benchmark Velocimetry Diagnostic

Figure 5.20 shows the combined results of the 10 bilayer SiO_x DBR experiments (#'s SIO10-0, SIO10-1, SIO10-2), showing the temporal profiles for each sample's peak features (blueshift, depth, and width, respectively).

As with the AOMC structures, there are many aspects of these temporal profiles that are informative. The blueshift profiles continue to show the well-defined shape typical of the laser-driven shock pressure, which confirms that the same mechanisms theorized for the AOMCs are indeed operating for the DBRs as well. There are a few anomalous spikes in the blueshift (particularly apparent for the experiment at 2.7 GPa) in the pre-shock region.

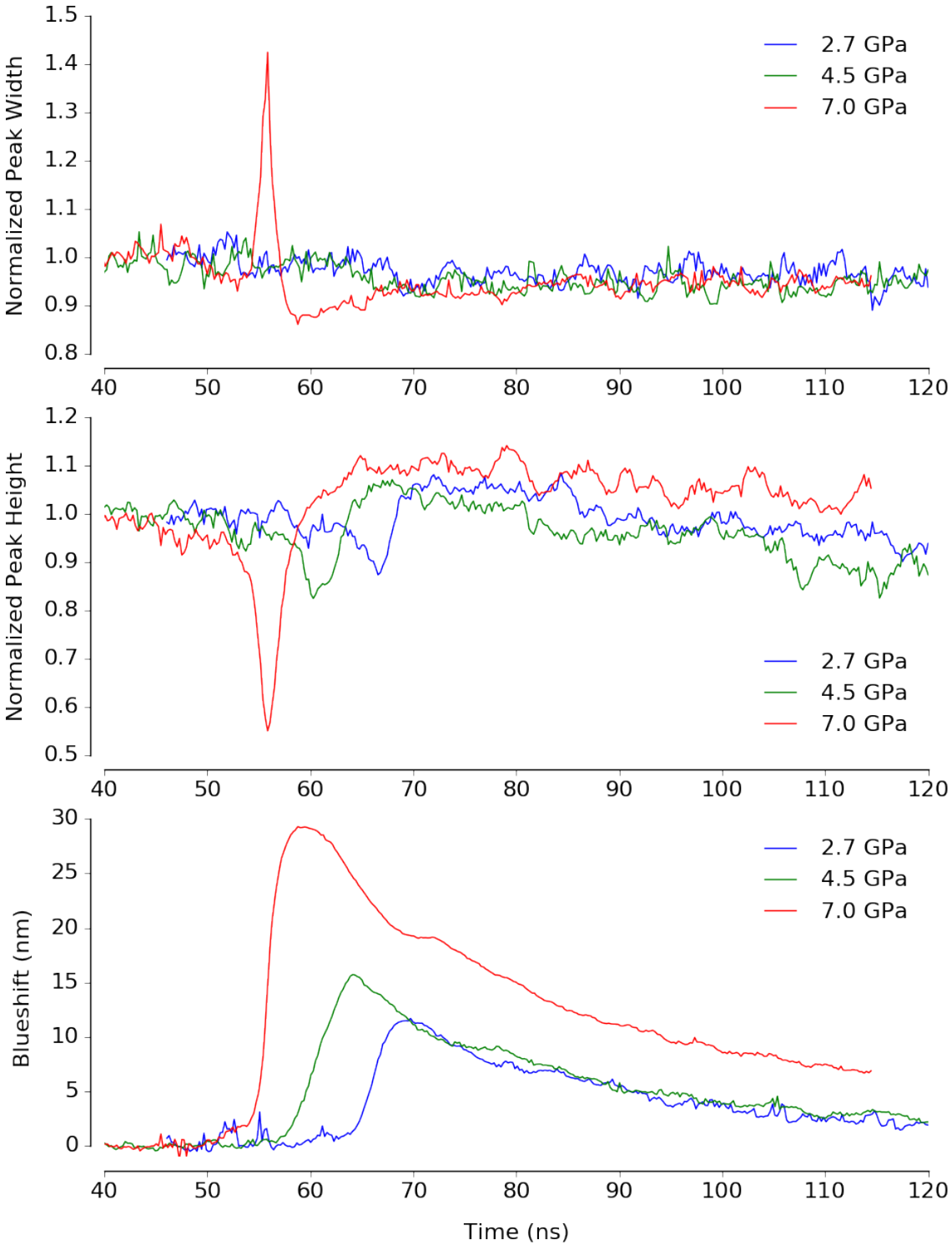

Figure 5.20: Combined plots of time-resolved peak features (blueshift, peak height, and peak width) for the 10 bilayer SiO_x experiment #'s SIO10-0, SIO10-1, SIO10-2. Note that each profile has been arbitrarily offset in time to improve visibility and interpretability of each experiment's profile.

This is likely due to an interaction between the peak feature extraction algorithm described in Section 5.1 and the much broader width of the reflectance peak of the DBR compared to the AOMC peak. In essence, random variations in the data will occasionally cause a brief, but relatively large, change in the shape of the time-resolved peak that manifests as an apparent blueshift. This is one potential disadvantage of the DBR multilayers, at least with this method of peak feature extraction. Other approaches (such as the method of moments) may be less susceptible to these small perturbations. The peak height and width, again, are less well-defined but in this case generally do have a more "steady-state" region that corresponds temporally with the associated "steady-state" blueshift. Identification of trends as a function of pressure are difficult due to the limited number of data points, but peak width seems to decrease at higher pressures and peak height increases at higher pressures.

Comparison to the *in-situ* particle velocity for the 10 bilayer SiO_x experiments are shown in Figures 5.21 - 5.23. Note that unlike the AOMC multilayers, due to the transparency of the SiO_x DBRs to the 1550 nm laser from the PDV system, the velocity measured is technically that of the aluminum driver/multilayer interface.

In general, the time-resolved blueshifts show a reasonable match to the *in-situ* particle velocity. Experiment # SIO10-0 has a near perfect match throughout the rise, "steady-state", and release regions, while experiments # SIO10-1 and # SIO10-2 show less favorable agreement. In particular, the velocity rise-time for # SIO10-1 is several nanoseconds faster than the blueshift, and for # SIO10-2 the double-peak behavior seen in the velocity profile is not seen in the blueshift, though this feature itself may be spurious as it is not seen in any of the other laser-driven shock-compression experiments. Broadly, the SiO_x DBRs have similar or slightly worse temporal matching to the *in-situ* particle velocity compared to the AOMC multilayers.

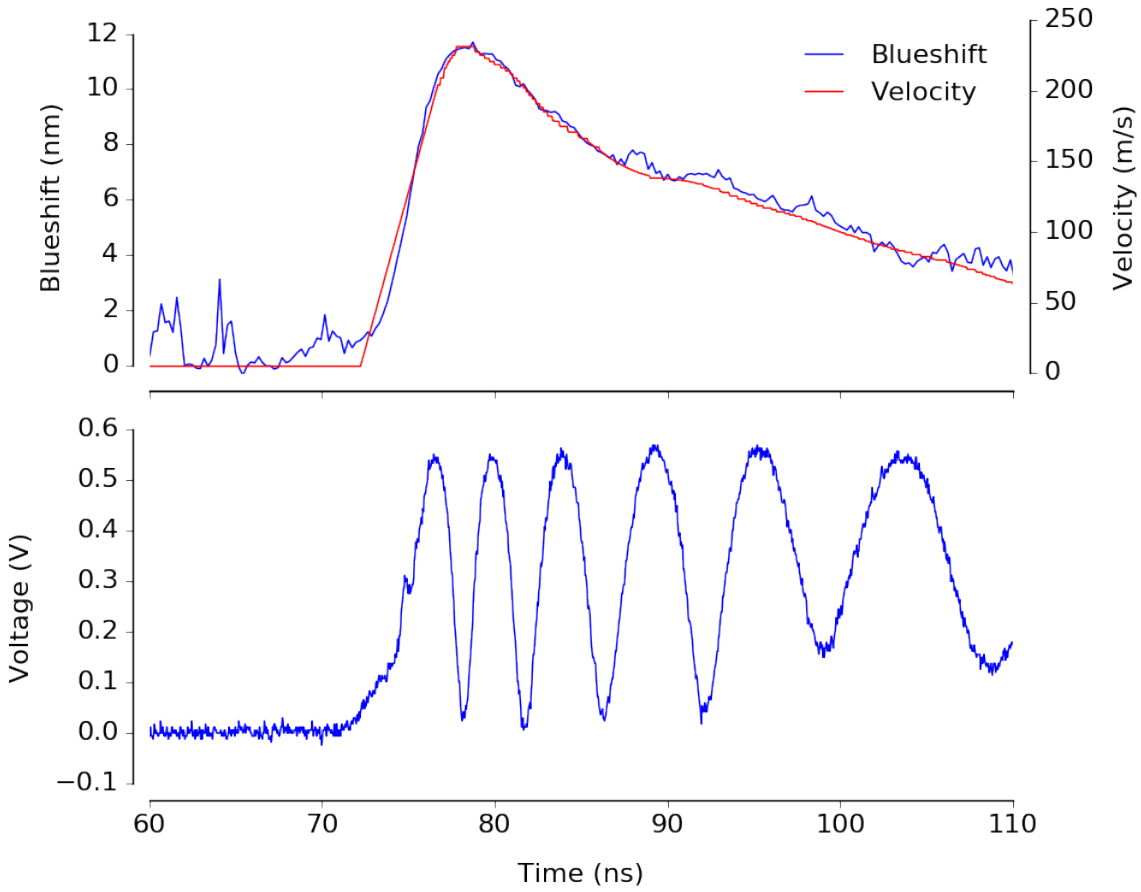

Figure 5.21: Comparison of the extracted blueshift and PDV particle velocity (upper plot) for experiment #SIO10-0 (~2.7 GPa) along with the raw PDV data (lower plot). Note that the PDV extracted velocity was manually aligned with the blueshift profile using the rise and peak "steady-state" regions to allow a more direct comparison of each profile's temporal features.

5.3.2 5 Bilayer SiO_x DBR

Experiment # SIO5-0: ~4.0 GPa

The extracted time-resolved peak position, height, width, and corrected streak image for experiment #SIO5-0 is shown in Figure 5.24. While the signal-to-noise ratio in the streak image is poor, the shock-compression induced spectral shift is still clear, as shown by the extracted blueshift temporal profile.

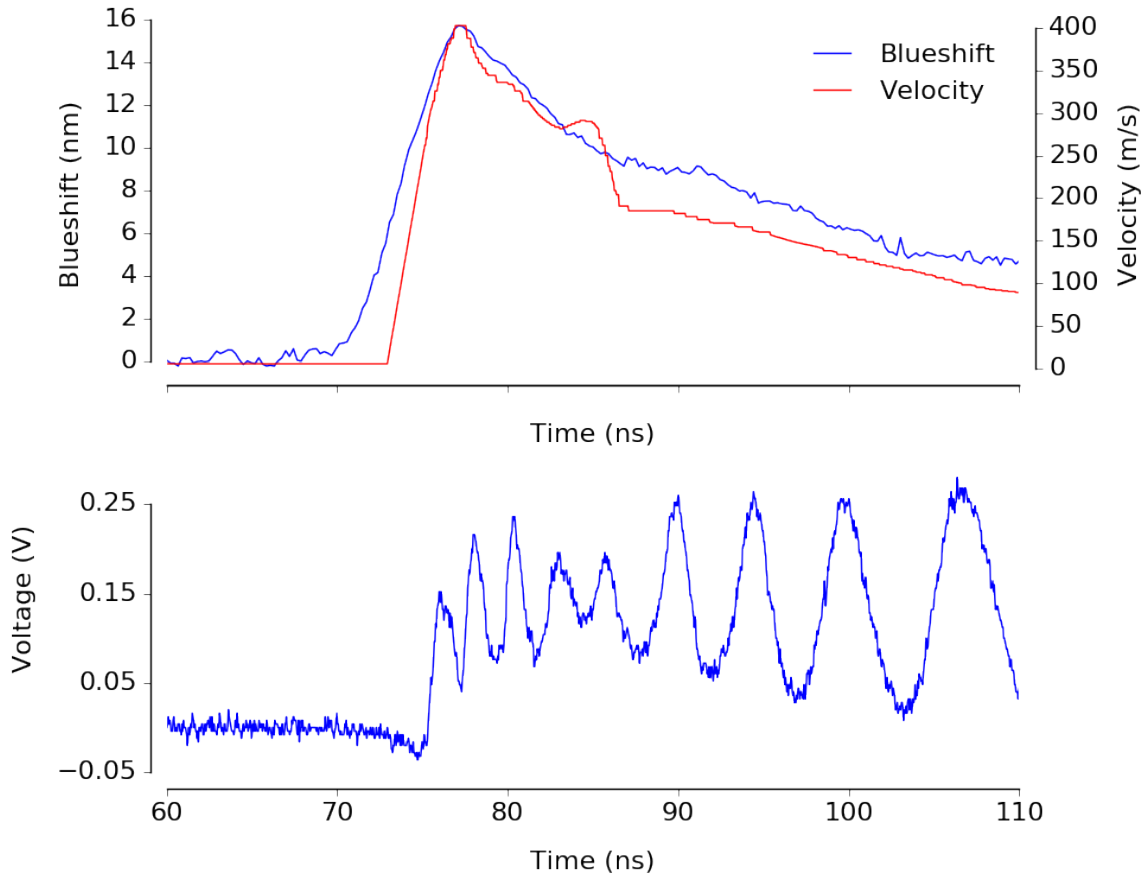

Figure 5.22: Comparison of the extracted blueshift and PDV particle velocity (upper plot) for experiment #SIO10-1 (~4.5 GPa) along with the raw PDV data (lower plot). Note that the PDV extracted velocity was manually aligned with the blueshift profile using the rise and peak "steady-state" regions to allow a more direct comparison of each profile's temporal features.

Experiment # SIO5-1: ~5.1 GPa

The extracted time-resolved peak position, height, width, and corrected streak image for experiment #SIO5-1 is shown in Figure 5.25. Signal-to-noise ratio in the streak image remains poor, and the magnitude of the blueshift is only slightly larger.

Experiment # SIO5-2: ~6.5 GPa

The extracted time-resolved peak position, height, width, and corrected streak image for experiment #SIO5-2 is shown in Figure 5.26. At 6.5 GPa this experiment shows the largest

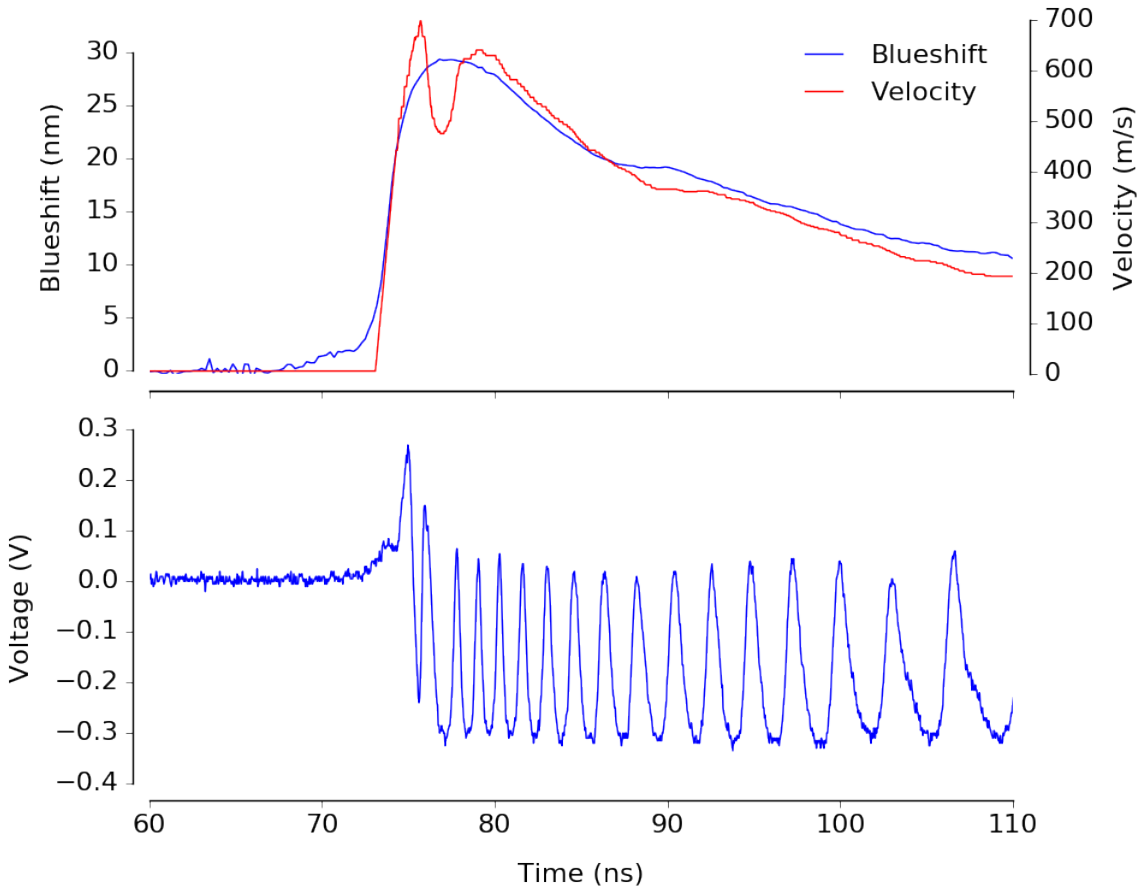

Figure 5.23: Comparison of the extracted blueshift and PDV particle velocity (upper plot) for experiment #SIO10-2 (~7.0 GPa) along with the raw PDV data (lower plot). Note that the PDV extracted velocity was manually aligned with the blueshift profile using the rise and peak "steady-state" regions to allow a more direct comparison of each profile's temporal features.

magnitude blueshift, though still relatively low compared to the 10 BL DBRs and fused silica AOMC multilayers.

Combined Results and Comparison to Benchmark Velocimetry Diagnostic

Figure 5.27 shows the combined results of the 5 bilayer SiO_x DBR experiments (#'s SIO5-0, SIO5-1, SIO5-2), showing the temporal profiles for each sample's peak features (blueshift, depth, and width, respectively).

These data largely show qualitatively similar trends as Figures 5.8 and 5.20 did for the fused silica AOMCs and 10 bilayer SiO_x DBRs, respectively. The time-resolved blueshift

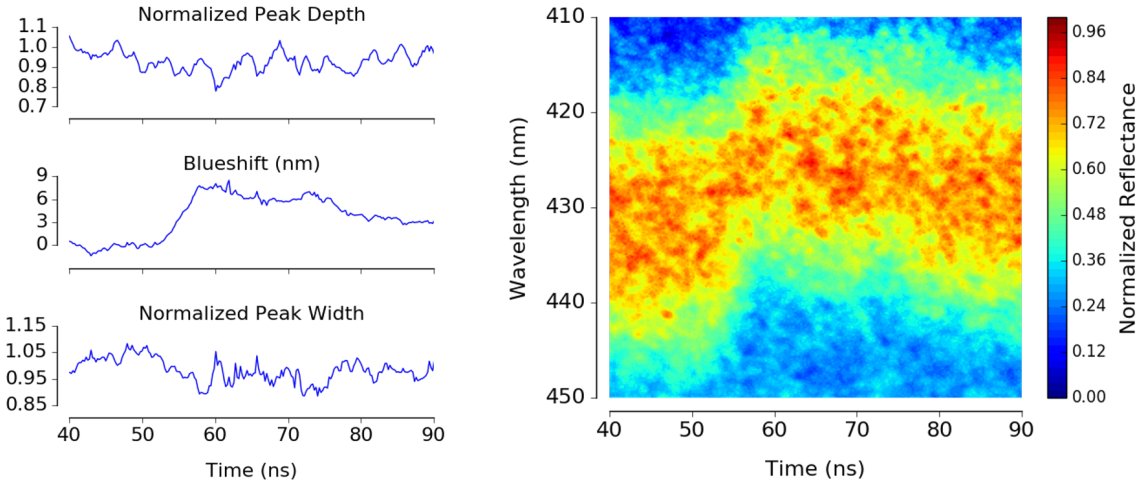

Figure 5.24: Extracted time-resolved peak features (blueshift, normalized width and depth) and streak image for experiment # SIO5-0 at a "steady-state" pressure of ~4.0 GPa.

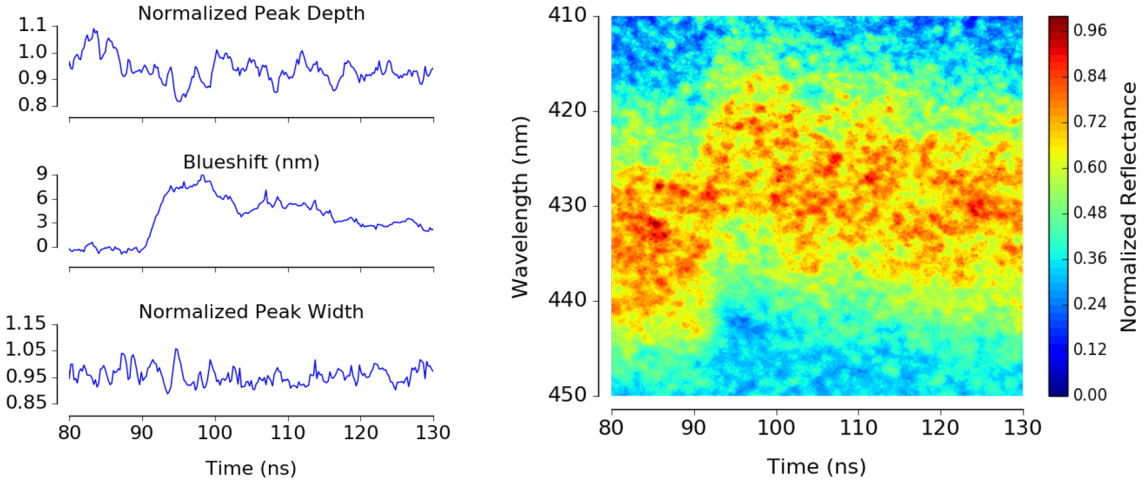

Figure 5.25: Extracted time-resolved peak features (blueshift, normalized width and depth) and streak image for experiment # SIO5-1 at a "steady-state" pressure of ~5.1 GPa.

remains clear and well-formed, while the peak width and height are fairly noisy with less-clear trends as a function of pressure. One unique aspect of the 5 BL DBRs is the relatively low blueshift magnitude as a function of pressure and the very low signal-to-noise ratio from all experiments. The latter issue is due to several factors, most of which are related to experimental or sample fabrication variables. First, the initial reflectance peak for these 5 bilayer DBRs is centered around ~433 nm as they comprised an earlier set of fabricated samples when the layer deposition procedure was less optimized. This low wavelength

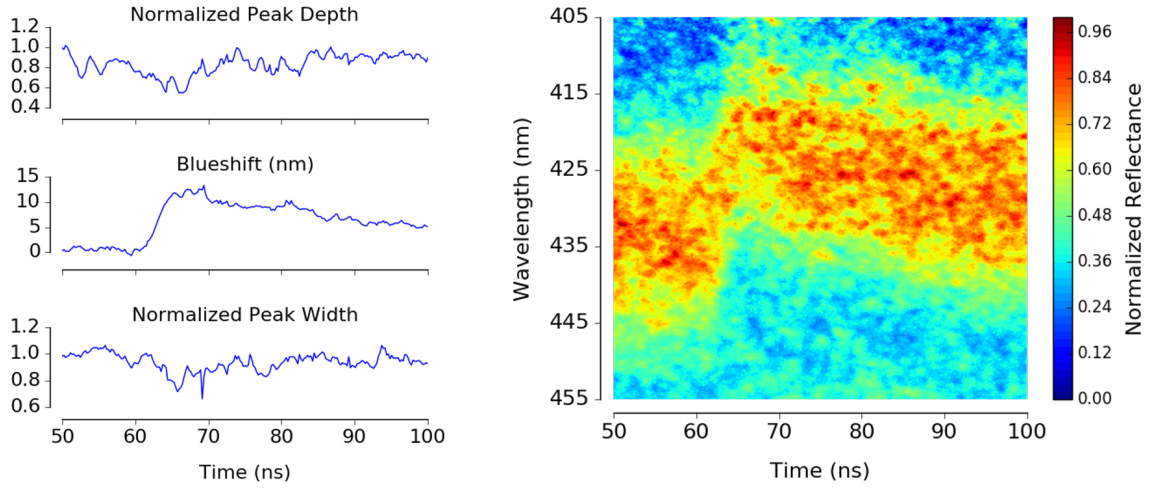

Figure 5.26: Extracted time-resolved peak features (blueshift, normalized width and depth) and streak image for experiment # SIO5-2 at a "steady-state" pressure of ~6.5 GPa.

is very near the detectability limit of the time-resolved spectroscopy setup described in Section 3.1.2. This is the primary contributor to the low signal-to-noise ratio of the data. Second, as was defined in Equation 2.7, a smaller number of bilayers naturally leads to a lower reflectance peak height which further decreases the signal-to-noise ratio of the streak image. Comparison to the *in-situ* particle velocity for the 5 bilayer SiO_x experiments are shown in Figures 5.28 - 5.30.

These 5 bilayer DBR samples show likely the worst match between the blueshift and particle velocity, though low data quality in either the blueshift or velocity hamper a quantitative comparison. However, one particular aspect of the comparison is worth exploring further: both the PDV and blueshift temporal profiles show well-aligned rise-times. As was discussed in Section 4.1.2, one of the key questions regarding the DBR multilayers was the effect of the thicker (3-5 micron) structure on the temporal response of the blueshift due to increased equilibration times. As the AOMC multilayers (with ~600-1000 nm thicknesses) show very rapid, even instantaneous rise-times, a more useful comparison would be between the 5 bilayer and 10 bilayer DBRs as this properly isolates the thickness of the multilayer and its effect on the blueshift rise time. Figure 5.31 shows this comparison, normalizing each blueshift profile between 0 and 1 for better profile-to-profile contrast.

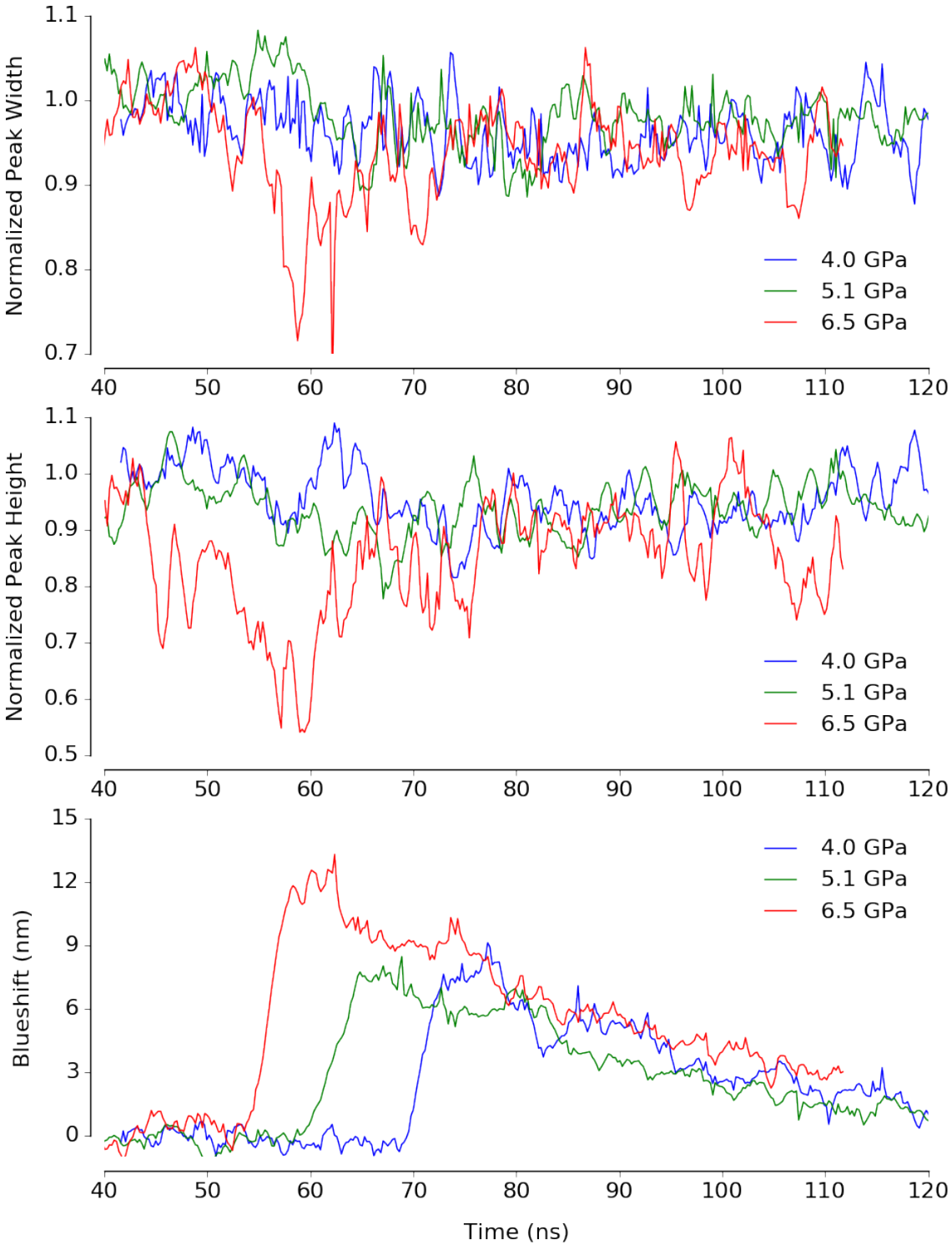

Figure 5.27: Combined plots of time-resolved peak features (blueshift, peak height, and peak width) for the 5 bilayer SiO_x experiment #'s SIO10-0, SIO10-1, SIO10-2. Note that each profile has been arbitrarily offset in time to improve visibility and interpretability of each experiment's profile.

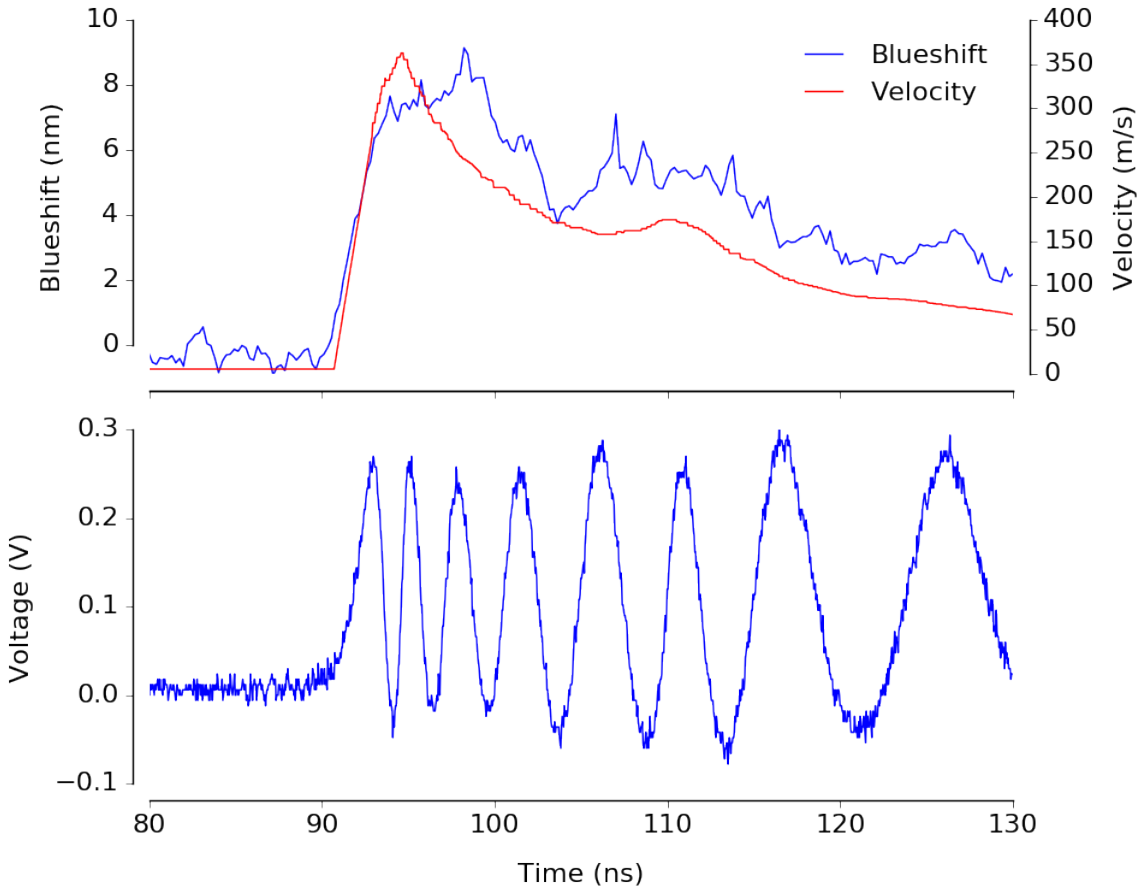

Figure 5.28: Comparison of the extracted blueshift and PDV particle velocity (upper plot) for experiment #SIO5-0 (~4 GPa), along with the raw PDV data (lower plot). Note that the PDV extracted velocity was manually aligned with the blueshift profile using the rise and peak "steady-state" regions to allow a more direct comparison of each profile's temporal features.

Of the six experiments, four are closely clustered with a rise time of 3-4 ns, and two are longer with a rise time of 5-6 ns. However, there is no obvious difference between the 5 bilayer and 10 bilayer DBR samples as each DBR type is represented in both the 3-4 ns and 5-6 ns rises. This is an encouraging result, and confirms the theory that the low impedance mismatch between the individual SiO_x layers maintains high temporal resolution of the spectral response even at relatively large thicknesses. Thus, there may be more flexibility in the number of layers design criteria than previously assumed. Additional experiments with a less well-matched impedance driver material (aluminum is very close to both fused silica and the SiO_x layers) would provide more confirmation of the temporal resolution as

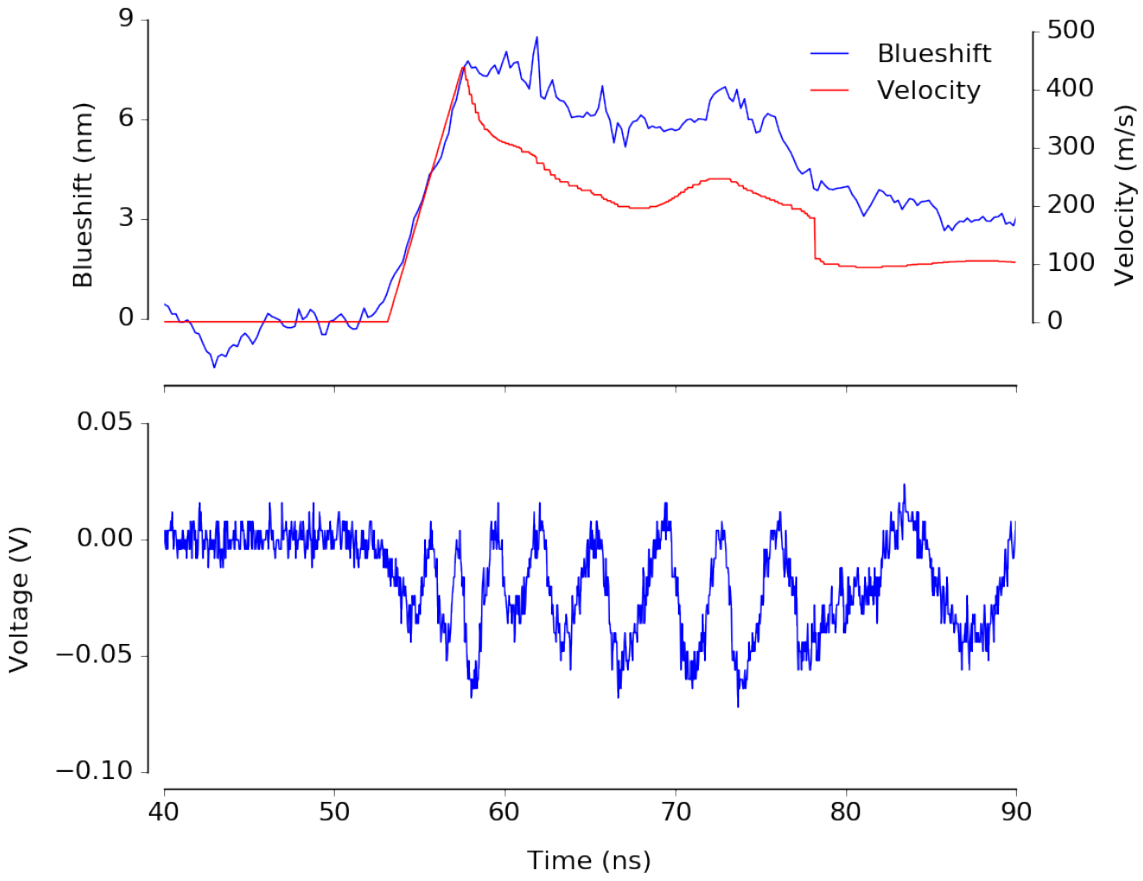

Figure 5.29: Comparison of the extracted blueshift and PDV particle velocity (upper plot) for experiment #SIO5-1 (~5.1 GPa) along with the raw PDV data (lower plot). Note that the PDV extracted velocity was manually aligned with the blueshift profile using the rise and peak "steady-state" regions to allow a more direct comparison of each profile's temporal features.

a function of number of layers for the DBR structures.

5.3.3 Comparison to Optomechanical Model Predictions

With the experimental data for the 10 bilayer SiO_x DBR multilayers, the time-resolved peak features can be compared to the predictions from the optomechanical models presented in Section 4.2.3. Figure 5.16 shows the extracted blueshift, peak height, and peak width compared to the model prediction curves first shown in Figure 4.12. All of the experimental points correspond to the spectral features extracted at the "steady-state" pressure condition with 2-sigma error bars for the peak feature values. Note that the results from the 5 bilayer

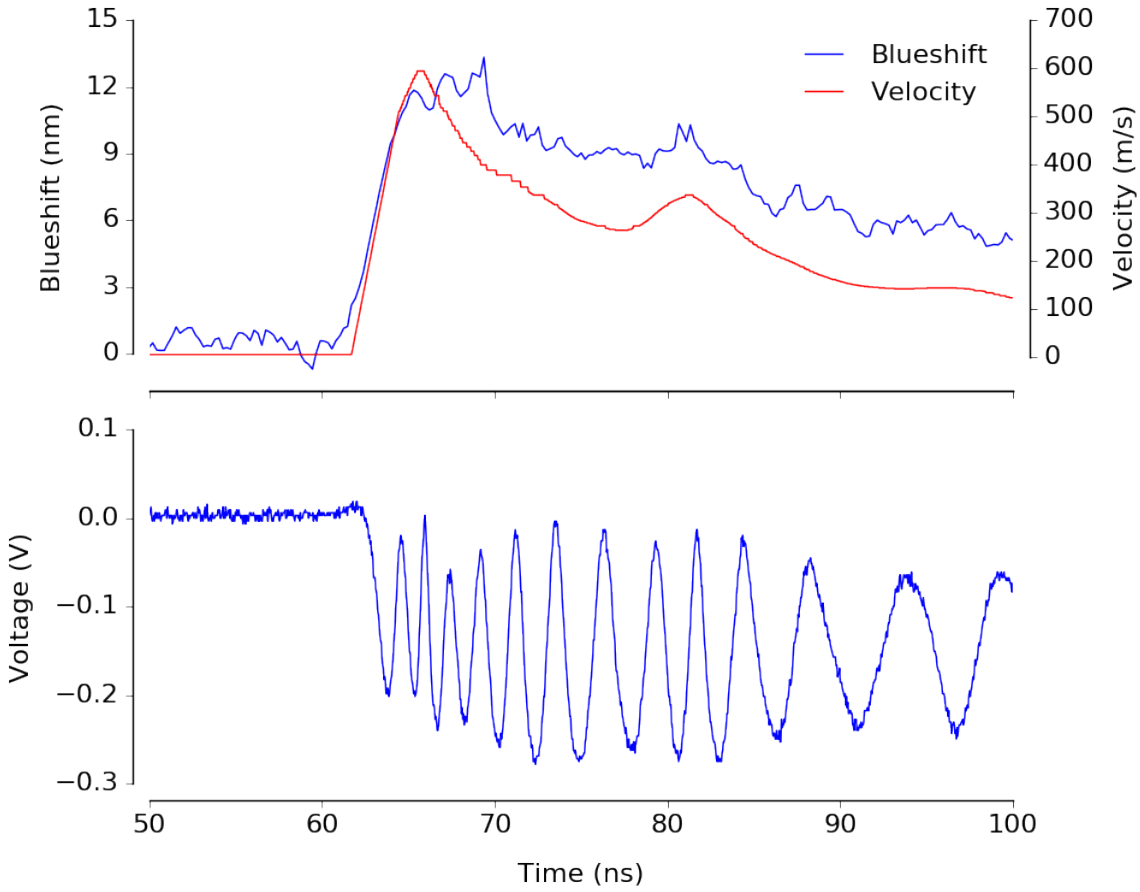

Figure 5.30: Comparison of the extracted blueshift and PDV particle velocity (upper plot) for experiment #SIO5-2 (~6.5 GPa) along with the raw PDV data (lower plot). Note that the PDV extracted velocity was manually aligned with the blueshift profile using the rise and peak "steady-state" regions to allow a more direct comparison of each profile's temporal features.

SiO_x DBR samples are not shown, as the optomechanical model for the DBRs was not optimized for these structures.

Similar to the fused silica AOMC structures, the maximum blueshift as a function of pressure is generally well-behaved; although, in this case, the optomechanical model predictions over-estimate the magnitude of the shift at a given pressure. The peak height and width continue to have large errors due to non-"steady-state" behavior in the respective temporal profiles compared to the blueshift profiles, but the data do not indicate a substantially different qualitative behavior compared to the model predictions. In fact, inspection of Figure 5.20 clearly shows that peak height generally increases compared to the pre-shock

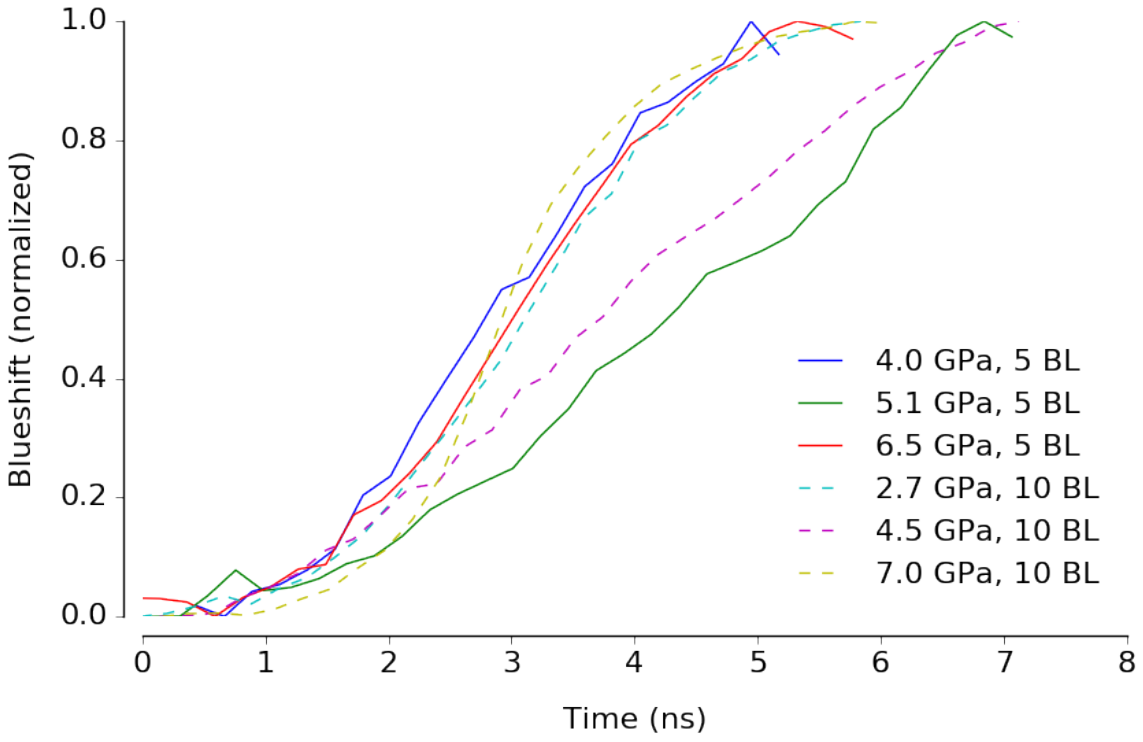

Figure 5.31: Comparison of the isolated and normalized rise time region in the time-resolved blueshift profiles for the 5 and 10 bilayer SiO_x DBRs. Note that each profile is normalized and offset in time to make a visual comparison more effective. There is no clear difference in blueshift rise-time between the 5 and 10 bilayer DBRs, accounting for experiment-to-experiment variance.

state at a given pressure, and that the magnitude of the increase correlates with increasing pressure, behavior predicted by the optomechanical model. As with the fused silica AOMC multilayers, improvement in background correction and experimental controls would enable more quantitative comparison of the peak width and height.

As the blueshift is the primary peak feature of interest, it is worthwhile to explore further why the optomechanical model over-predicts the magnitude of the blueshift as a function of pressure. As was discussed in Section 4.2.3, the initial model for the DBR multilayers was based on material properties and refractive index models for fused silica. The assumption was that this was, at minimum, a reasonable basis for the DBR model. However, the experimental data clearly show that the model must be modified either in the mechanical response or the optical response of the SiO_x layers. As there is no empirical

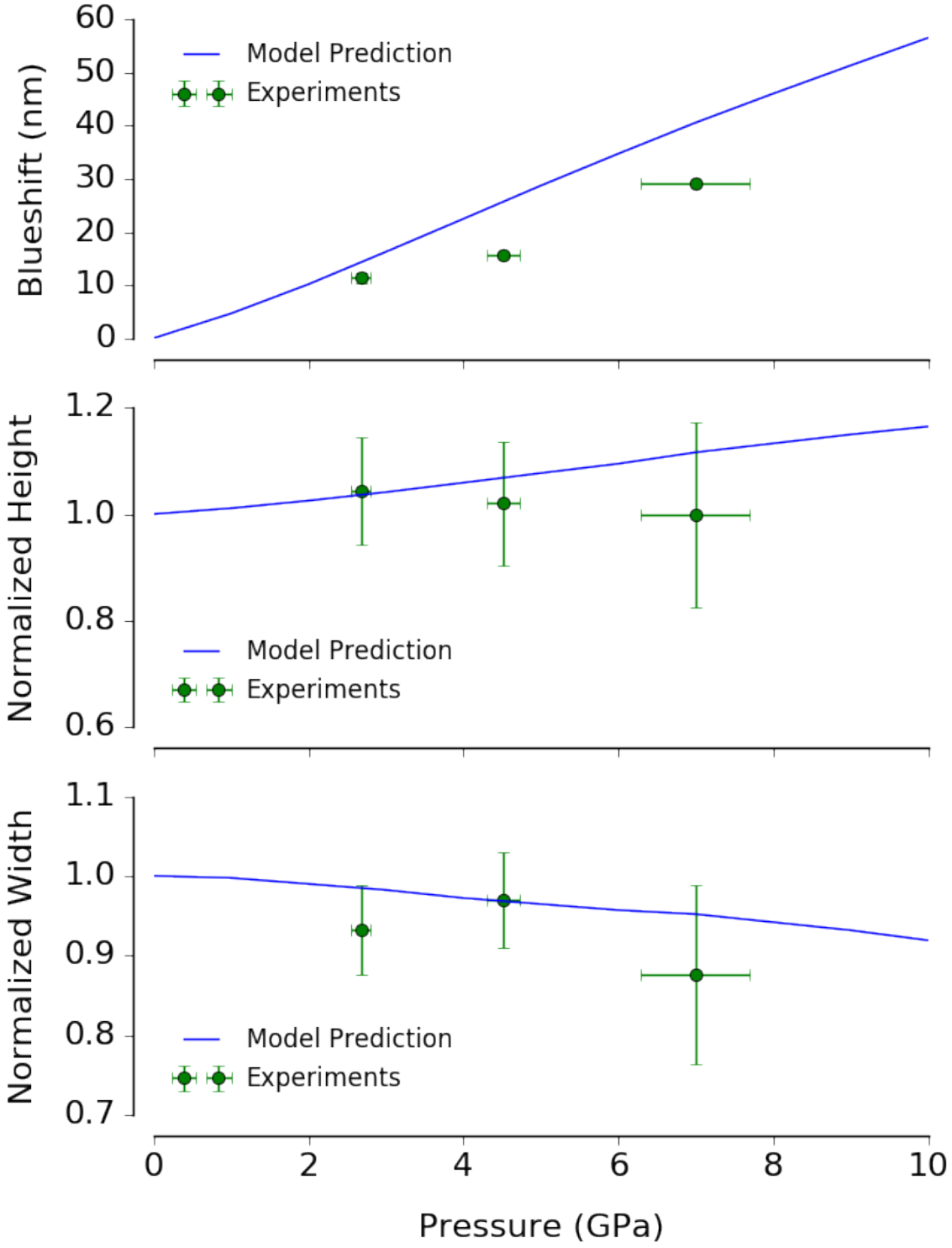

Figure 5.32: Comparison of the collected experimental data extracted at the "steady-state" pressure for the 10 bilayer SiO_x DBR to the predictions of the corresponding optomechanical model presented in Section 4.2.3. The data points have 2-sigma error bars in the y axis, and the qualitative $\pm$ 5%, 10%, 15% error on the x axis (pressure).

data for either of these responses for thin-film SiO_x, only somewhat arbitrary changes to the model are possible at this point. Based on the trends observed for the refractive index of fused silica (SiO_2) as a function of pressure in Figure 4.9, it seems somewhat unlikely that reducing the oxygen content will drastically change these trends. Further, since the refractive index effects are generally secondary to the layer compression effect on the magnitude of the pressure-induced blueshift, changes in the refractive index model are unjustified in the absence of quality experimental data. This leaves a different mechanical response of the SiO_x compared to that of fused silica as a possible cause of the optomechanical model's blueshift prediction. Pivot et al. [122] measured the effect of oxygen ion implementation in SiO thin films and saw an increase in elastic modulus at an effective composition of $SiO_{1.8}$, though still less stiff than reguluar SiO_2. However, the exact structures and mechanical properties of SiO_x thin films are likely to be very complex and highly dependent on fabrication parameters. It is beyond the scope of this work to even speculate into the mechanisms that could affect the mechanical response of the SiO_x layers, but the data in Figure 5.32 seems to indicate less overall compression compared to SiO_2. If this is the case, as a first order test, the mechanical response portion of the optomechanical model can be simply scaled to simulate a "harder" layer with less volume compression under shock loading. Figure 5.33 shows the blueshift predictions of the original model and of a modified model that assumes a 20% reduction in the layer compression along with the experimental data.

The modified model shows a much better match to the data, though with the limited number experiments a rigorous fit is not claimed. However, the fact that a simple scaling operation on the mechanical response of the SiO_x layers produces a more accurate blueshift versus pressure trend is indicative of the both the flexibility and predictive power of this form of an optomechanical model.

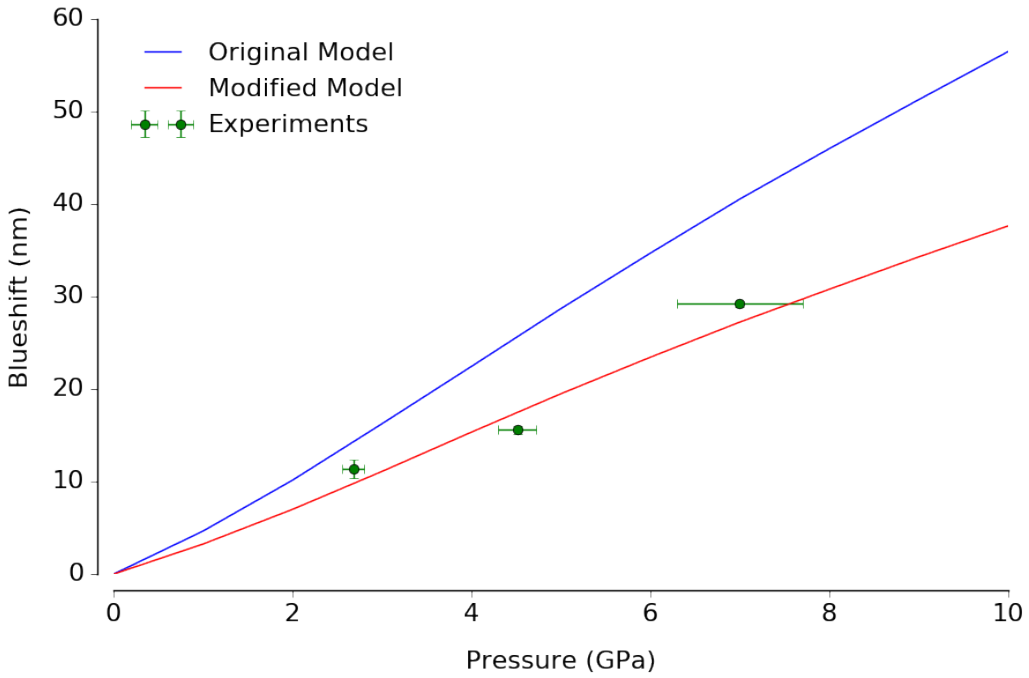

Figure 5.33: Comparison of the collected experimental data extracted at the "steady-state" pressure for the 10 bilayer SiO_x DBR to the predictions of the original (blue) and modified (green) optomechanical model. The modified model uniformly reduces the volume compression of the SiO_x layers as a function of pressure by 20%.

5.4 Summary of 1-D Shock-Compression Responses

This chapter has presented detailed information on the laser-driven shock-compression response of five different multilayer optical structures: fused silica, Al_2O_3, and PMMA based AOMCs, and 5 and 10 bilayer SiO_x DBRs. The purpose of these experiments was to evaluate the spectral response of the multilayer structures, and validate both the theorized mechanisms and quantitative optomechanical model predictions presented in Chapter 4. Broadly, these goals were accomplished with the following specific conclusions:

- All of the multilayer samples tested show unambiguous time-resolved blueshifts under shock-compression very similar to the expected pressure profile of the laser-driven shock loading configuration.

- With a few exceptions, all of the multilayer samples had blueshift profiles with reasonable or excellent temporal correlation to the *in-situ* particle velocity as captured with the benchmark velocimetry diagnostic, PDV. This temporal correspondance remained high throughout the rise, "steady-state" region, and release of the laser-driven pressure load.

- All of the multilayer structures showed very fast pressure rise/equilibration times, generally with nanosecond-level or better matches to the measured rise time from the benchmark velocity diagnostic. However, the the fused silica AOMC structures often showed a discontinuous jump in the blueshift temporal profile due to a loss of spectral signal during the rise. Contrasting this, the SiO_x DBR multilayers resolve the entire blueshift rise with the total rise-time largely independent of the number of layers (i.e., thickness) of the DBR.

- The experimental data for "steady-state" blueshift as a function of pressure for the fused silica AOMC multilayers are an excellent match to the predictions of the developed optomechanical models. For the 10 bilayer SiO_x DBR, the model over-predicts the blueshift, but a linear scaling of the SiO_x layer volume compression (i.e., assuming a stiffer response) under shock aligns the model to experimental data.

- For both the AOMC and DBR structures, the secondary time-resolved peak features (peak depth/height) and width are at best qualitative matches to the optomechanical model predictions. This is due to several factors, including both inherent aspects of the secondary peak feature's time-resolved responses and biases introduced by experimental implementation and data analysis processes. Accounting for these factors could enable quantitative comparison of the secondary peak features to model predictions in the future.

With the fundamental mechanism and principles of multilayer-based sensing defined, modeled, and experimentally proven, the following chapter will focus on the ultimate goal

of this new class of time-resolved sensor: measuring heterogeneous, multi-pressure shock states.

CHAPTER 6
MULTILAYER RESPONSES TO HETEROGENEOUS SHOCK-COMPRESSION LOADS

The spatially-resolved response of the multilayer structures can be demonstrated in many different ways, and there is significant potential opportunity for many different applications. In the scope of the present work, the primary narrative will focus on an incremental increase in loading complexity to facilitate a systematic analysis of the multilayer's spectral responses. The following sections will present initial theoretical and computational predictions, several experimental demonstrations, and finally more expansive simulations of complex loading scenarios.

6.1 Theoretical Predictions

6.1.1 Stepped Binary Load

To properly evaluate the ability of the multilayers to resolve multiple pressures, it is advisable to start with very simple, controllable loading configurations with the minimum number of pressure states: two. One example of this type of load is that of a binary step, a non-zero pressure transitioning discontinuously to a zero pressure state over one or more spatial dimensions. This configuration was presented previously in Section 3.2. Based on the theories and optomechanical models of the multilayers, the expected spectral response is the presence of two spectral peaks, each associated with the non-zero and zero pressure states of the step-load.

Figure 6.1 shows schematics of this configuration with a fused silica AOMC multilayer along with a qualitative predicted spectral response simulated with COMSOL Multiphysics.

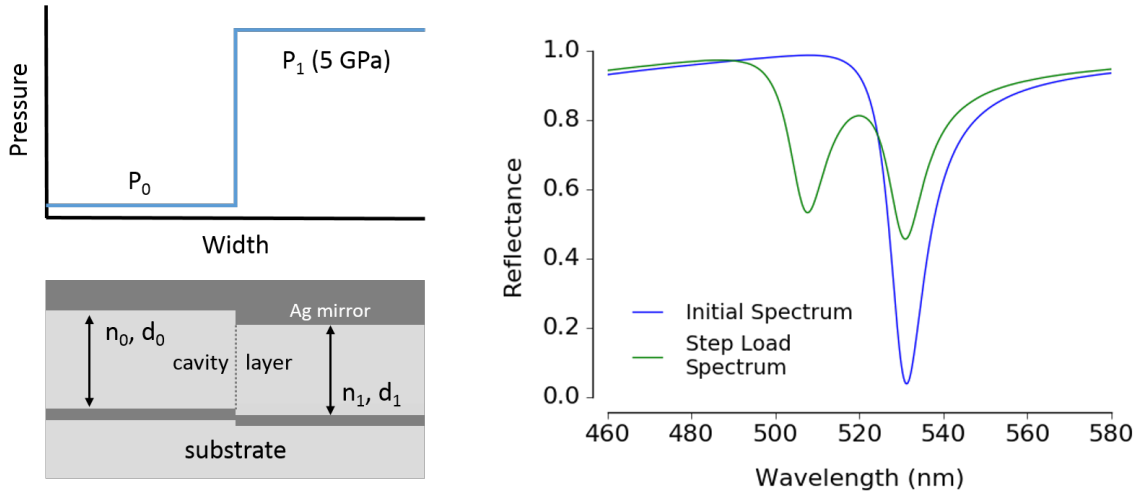

Figure 6.1: Schematics (left) of binary step-load and resulting AOMC structure and the corresponding simulated spectra (right) from COMSOL Multiphysics. The initial unloaded spectra is also plotted for comparison.

As expected, the spectrum associated with the binary stepped pressure load shows two distinct peaks. The first peak is at the same position as the initial spectrum and corresponds to the zero-pressure portion of the spatial step-load. The second peak is shifted to short wavelengths by ~25 nm and corresponds to the non-zero pressure portion of the spatial step-load.

Practically, however, there are more complex issues that may affect the multilayer's spectral response under this simplified load. First, a true discontinuous pressure jump is not obtainable due to dissipative effects, and there will be some transition region with a non-zero width. Second, as can be seen in Figure 3.14, the vertical displacement of the multilayer on the non-zero pressure area of the load can be significant due to compression of the fused silica substrate. The effect of this asymmetric displacement on the spectral response is unknown but is important to model explicitly versus the simplified deformed multilayer shown in Figure 6.1. Fortunately, as presented in Section 3.2, the optomechanical computational framework is well-equipped to handle both of these issues and produce more realistic simulated spectra of the dynamic step-load loading configuration. Figure 6.2 shows a more detailed schematic of a simulation with the spatial step-load, explicitly

modeling a pressure transition region and the resulting snapshot of the deformed geometry produced from Abaqus. The pressure load temporal history was defined as a sigmoid step with a rise time of ~3 ns.

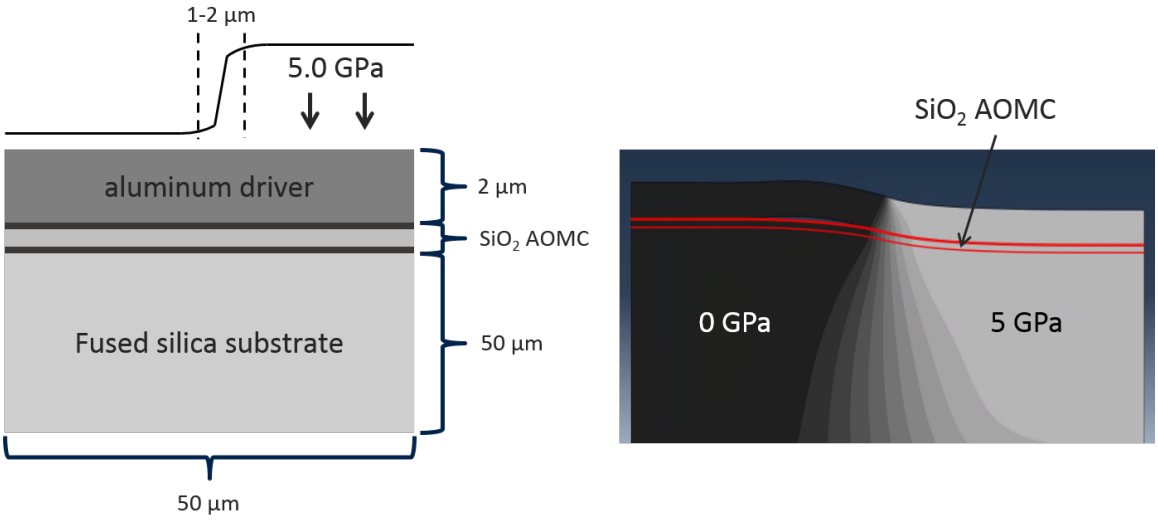

Figure 6.2: Schematics (left) of simulation setup for stepped pressure load and resulting sample package pressure map with geometry deformation (right), with the AOMC structure outlined in red. The dynamic simulation was performed in Abaqus using the parameters and boundary conditions listed in Table 3.2.

Passing the information from this simulation to COMSOL Multiphysics, the spectrum for this step-load simulation can be predicted while accounting for the deformed multi-layer geometry as well as the pressure-dependent refractive index. Figure 6.3 shows this simulated spectra compared to both the initial spectrum and the simulated spectra from the "ideal" configuration in Figure 6.1. The simulated spectrum is very close to that predicted by the ideal simulation with slight differences in the peak heights and small (< 1.5 nm) differences in peak positions. Based on the results of these simulations, there is good reason to expect that measuring the spatially resolved spectral response of the multilayers remains an effective sensing method even under more complex, realistic loading configurations.

Finally, to provide an intuitive example of the type of data that would be collected by the time-resolved spectroscopy experimental setup under a similar step-load configuration, a full, synthetic streak image of the step-load configuration was simulated using the full

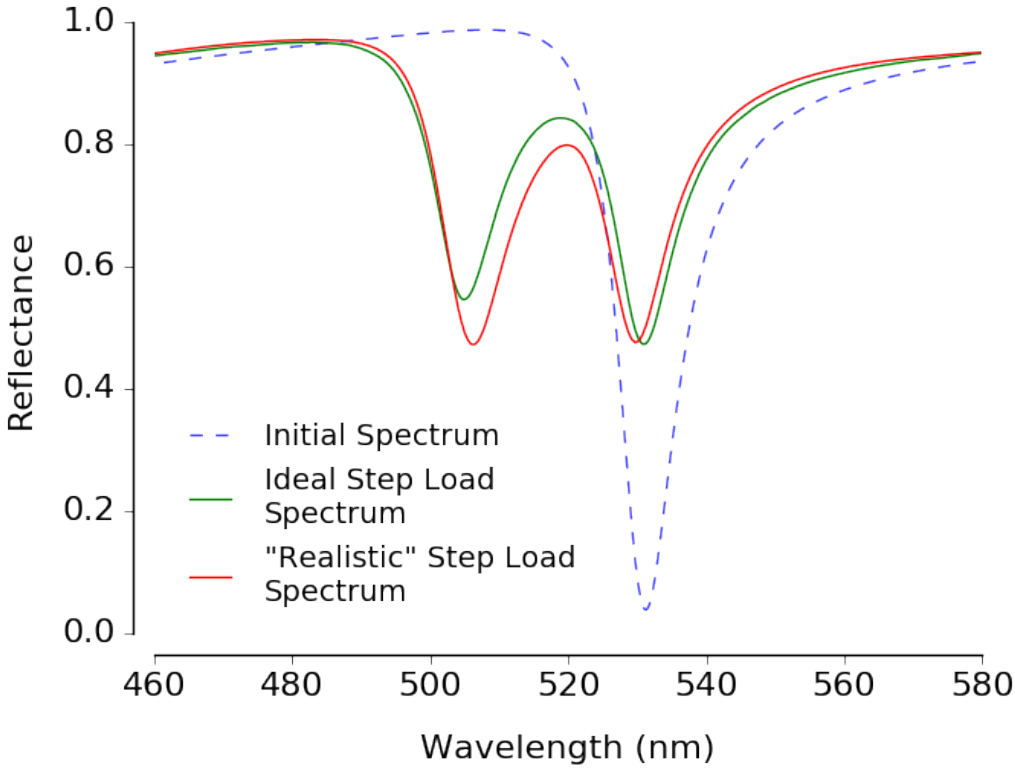

Figure 6.3: Simulated spectra of a fused silica AOMC multilayer under a 0/5 GPa stepped pressure load, using the full optomechanical computational framework presented in 3.2. The initial spectrum and the "ideal" step-load spectrum are also plotted for comparison.

optomechanical computational framework. A prototypical laser-driven pressure temporal profile (in fact, the same profile shown in Figure 3.3) was provided as an input to the Abaqus simulation described in Figure 6.2, and the time-resolved spectra was calculated for each point along this pressure history. Figure 6.4 shows the resulting simulated streak image.

As the non-zero portion of the step-load arrives, the starting spectral peak clearly splits into the two peaks shown in Figure 6.3, and then slowly releases in pressure following the expected laser-driven pressure profile until it begins to recombine with the un-shifted, non-zero pressure peak. This is an excellent demonstration of the intuitive interpretation and information density of the time-resolved spectra.

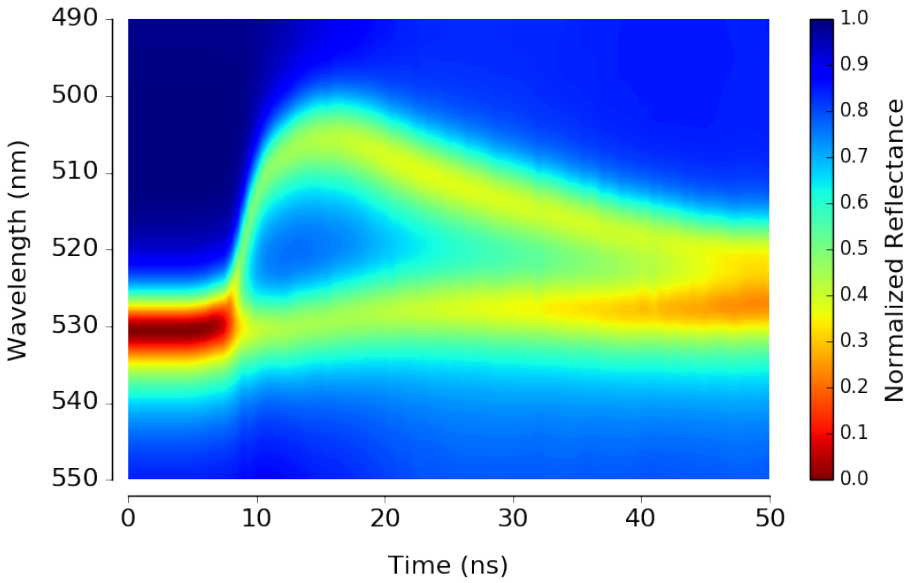

Figure 6.4: Simulated synthetic streak image of laser-driven stepped pressure load using the full optomechanical computational framework.

6.1.2 Maximum Spatial Sensitivity

Based on the simulated spectral response of a binary step-load, an important related consideration is the inherent spatial sensitivity of the structures. That is, given a perfect, discontinuous binary pressure state, the smallest spectroscopically probed area that still produces spectra that resolve the multiple pressure states. Put another away, the smallest sub-area ($dxdy$) of a multilayer that can produce spectra that are still meaningful in the context of time-resolved pressure sensing. This limit represents (somewhat indirectly) the maximum theoretical spatial sensitivity of the multilayer, below which the ability to resolved multiple pressure states is not possible and places fundamental limits on the material systems or loading configurations where the multilayers will have utility.

To explore this question, a series of simulations using the same configuration as in Figure 6.1 was performed with the spectroscopically probed area centered on the step-load discontinuity incrementally decreasing in width. While this is a two-dimensional simulation only, symmetry allows the width of the probed area to accurately represent the area in a full, three-dimensional configuration. Figure 6.5 shows the simulated spectra associated

with each probe width.

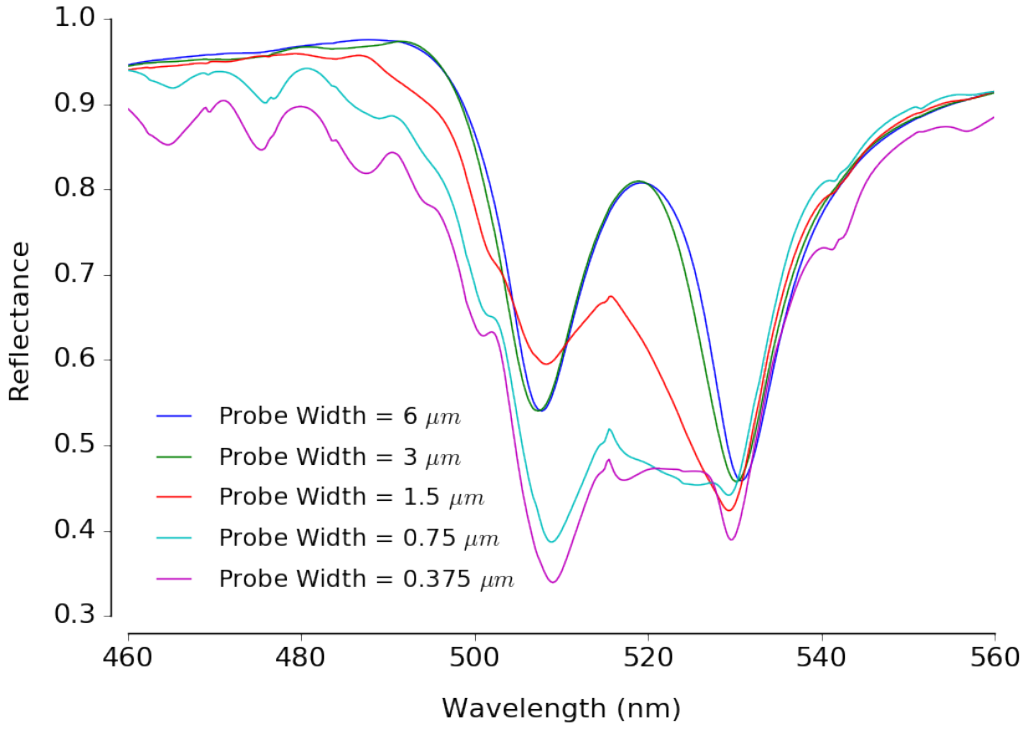

Figure 6.5: Simulations of the spectral response of a fused silica AOMC under a stepped pressure load, centered on the transition from zero to non-zero pressure. Below a 1.5 micron probe width, the quality of the spectra decrease significantly.

The simulations show that probe widths of 6 and 3 μm are essentially identical, 1.5 μm begins to show anomalous spectral features, and below 1 μm micron the spectral quality is low. At these probe widths, which are on the same order as the thickness of the cavity layer, investigating the quantum mechanics-based mechanisms for this optical behavior are quite complex and beyond the scope of the present work. The salient conclusion is that the trend in spectral quality implies that the multilayer sensors (at least the fused silica AOMC's) have up to a theoretical micron-level spatial sensitivity. Of course, practical restrictions on experimental implementation likely make the realistic spatial sensitivity somewhat lower. Nevertheless, this is an impressive result and further establishes the unique potential of the multilayers in temporally and spatially-resolved pressure sensing.

6.1.3 Separability of Global Spectral Responses

While all of the methods and assumptions presented in Section 5.1 for analysis of the time-resolved spectra are still relevant, there are additional considerations under heterogeneous loading that increase the complexity of the data analysis process. For example, consider a multilayer structure on the surface of a sample undergoing shock-compression where the sensor area is 10 mm^2. If, like the experiments presented in Chapter 5, the spatial distribution of pressure is uniform (i.e., 1-D loading), the spectral response of the entire multilayer sample will be indistinguishable regardless of the area of the sample spectroscopically probed. That is, the time-resolved spectra of the full 10 mm^2 sensor area will be identical to the time-resolved spectra of a *smaller sub-region of this area*, assuming there is sufficient light intensity to maintain equivalent signal-to-noise ratio in both cases. This is an intuitive deduction as the structures are inherently 1-dimensional in design and their spectral response can not depend on the variation in the direction parallel to the multilayer's surface. Logically expanding this fact and stating it mathematically:

$$I(\lambda)_{global} = \frac{1}{mn}\int_0^n \int_0^m I(x,y,\lambda)dxdy = \frac{1}{mn}\left[\lim_{n,m\to\infty}\sum_{j=1}^{n}\sum_{i=1}^{m} I(x_i,y_j,\lambda)\Delta x\Delta y\right] \tag{6.1}$$

that is, the global spectral response ($I(\lambda)$) of the entire spectroscopically probed area is the sum of the individual spectral responses of smaller sub-areas ($dxdy$) centered at (x_i, y_i). Assuming that this relationship holds under conditions of heterogeneous loading, the global spectral response would be the sum of the individual localized spectral responses associated with the localized pressure variations. This has numerous implications on the data analysis process and a particularly powerful conclusion: the global spectral response can be decomposed into individual spectra that correspond to localized responses, a classic inverse problem.

As a simple case, the "ideal" step-load simulation can be leveraged to test this as-

sumption. Figure 6.6 shows the simulation setup chosen along with the five 4 μm wide sub-regions used to calculate the local spectral responses. The global response is along the entire 20 μm width of the simulation domain. It is clear that the two spectra (global

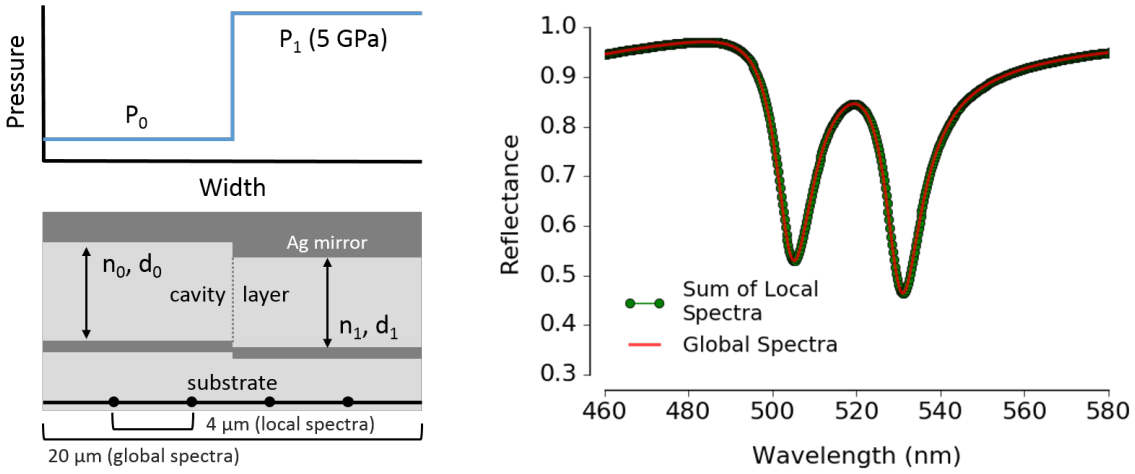

Figure 6.6: Simulations of the global and summed local spectral responses of a fused silica AOMC under a stepped pressure load. The local spectral responses are 4 μm wide, evenly-spaced sub-regions of the global 20 μm probed region. The two spectra (right) are identical for all practical purposes.

and summed-local) are identical, confirming that Equation 6.1 is valid even under hetergeneous, multi-pressure states. However, these simulations are an idealized case, and there are several practical limitations that must be considered. First, while Equation 6.1 is written as an integral, in reality there are physical limits on the size of the sub-area ($\Delta x \Delta y$) below which the individual spectra are not easily interpretable. This is precisely the finding of the previous section and represents the maximum spatial sensitivity of the structure, ~3 μm^2 in the case of the fused silica AOMC. Second, the presence of multiple spectral peaks, or heavily overlapping peaks, can complicate the one-to-one mapping of spectral features to pressures. Peak deconvolution on the global spectral signal may be possible, but with many possible solutions to this problem, some knowledge of the sample and loading conditions is needed to identify the most likely number and location of the contributing peaks. The method of moments presented in Section 5.1 may have more utility in this context as it makes no assumption of standard spectral peak shapes and provides an aggregated measure

of peak shape.

Another useful consequence of Equation 6.1 relates to the magnitude of the relative contributions of the locally probed areas to the global spectrum under heterogeneous loading conditions. For example, the stepped pressure load simulations presented to this point are 50/50 divisions between the zero and non-zero pressure regions. Changing the ratio of the zero/non-zero pressure areas should have a predictable effect on the resulting global spectrum. Generally, for n sub-areas with area A_n (which need not be the same size) of a global area A:

$$I(\lambda)_{global} = \frac{1}{A}\sum_{1}^{n} A_n I(A_n, \lambda)_{local} \tag{6.2}$$

For the simplified case of an "ideal" binary shock step-load (n=2), the ratio of the peak heights/depths can be used to back-calculate the area fractions A_1 and A_2 (shocked, and un-shocked areas, respectively). For example, Figure 6.7 shows several spectra from simulations of varying area fractions in the binary step-load case along with the relationship between the peak depth ratio ($R_{shocked}/R_{un-shocked}$) and the area ratio ($A_{shocked}/A_{total}$).

The peak depth ratio versus area ratio trend is well-behaved, and asymptotic as area fractions approach 0 and 1 as would be expected. As the value of n in Equation 6.2 increases with the complexity of the loading, an accurate solution to Equation 6.2 using peak height/depth ratios becomes increasingly difficult. However, relative comparisons of area fractions are still possible and can be quite valuable in many contexts.

6.2 Experimental Results: Stepped Binary Load

The preceding sections have computationally explored many different aspects of a controlled heterogeneous step-load and the corresponding spectral response of the fused silica AOMC multilayer. Based on the good agreement of the experimental data to the model predictions in Figure 5.16 and the rigorous implementation of the optomechanical simulation

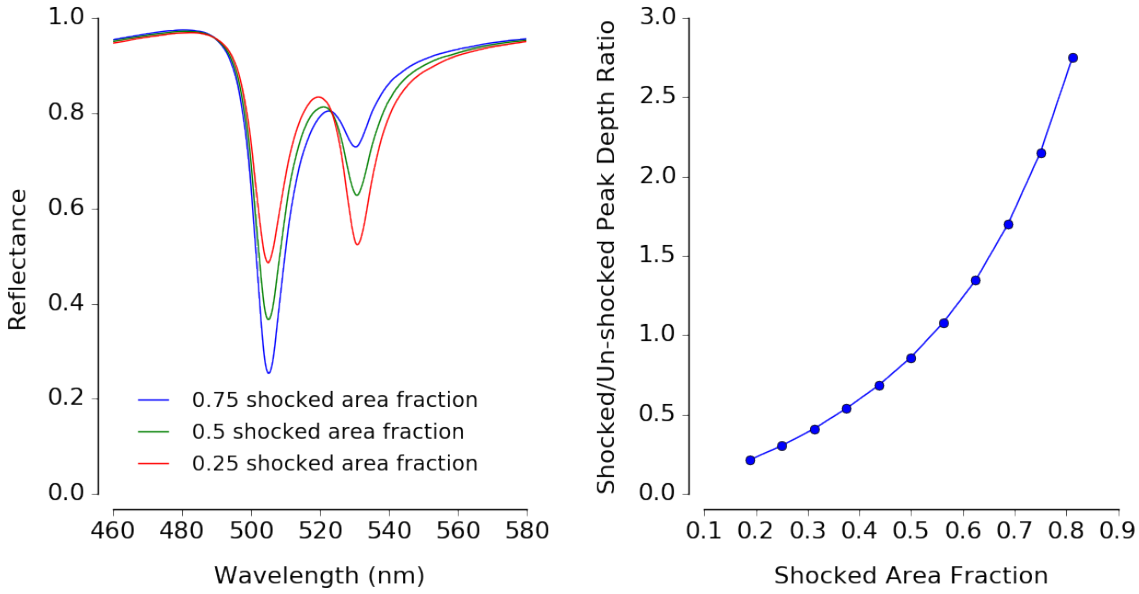

Figure 6.7: Simulations of the global spectral responses (left) of a fused silica AOMC under a stepped pressure load of varying fractions (0.25, 0.5, 0.75 shocked area fraction). The switching of the peaks between the zero pressure and non-zero pressure spectral peaks is clear as the area fraction passes 0.5, and the ratio of the peak depths (non-zero/zero) follows a well-behaved trend versus area fraction (right).

framework, it is likely that these conclusions are reasonable. To validate this assumption, experimental testing of the same step-load configuration would be ideal. Fortunately, the laser-driven shock-compression setup presented in Section 3.1.1 is flexible enough to produce this type of loading, and Figure 6.8 shows the appropriate modification. Note that while this configuration prevents the simultaneous measurement of *in-situ* particle velocity, the pressure step magnitude can still be estimated by using the optomechanical model predictions for the fused silica AOMC multilayers.

With this simple augmentation, a fairly direct experimental implementation of the simulated step-load scenario is available. Two such experiments were conducted in this configuration, the details of which are listed in Table 6.1. The detailed results of each experiment are presented separately below.

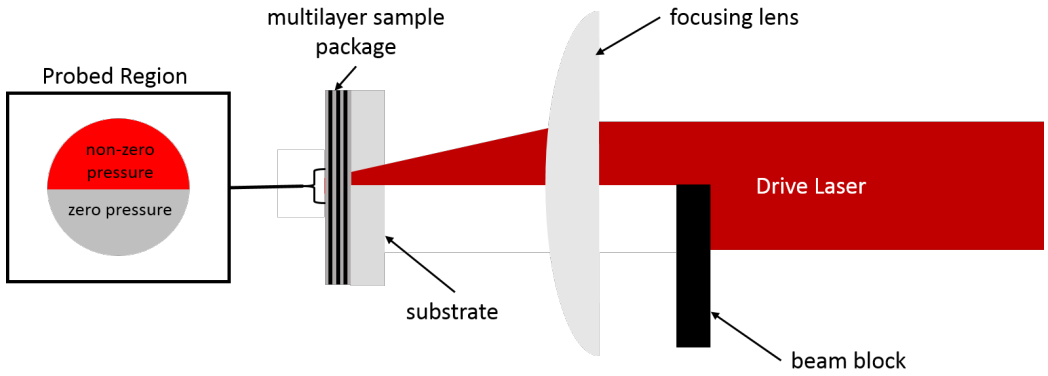

Figure 6.8: Modification of the laser-driven shock-compression experimental setup to produce a heterogeneous stepped pressure load. By inserting a beam block into the path of the drive laser that intercepts 50% of the beam, the focusing lens then creates two semi-circular areas with zero and non-zero laser energies and corresponding zero and non-zero induced pressures propagating through the multilayer sample package.

Table 6.1: Summary of the two heterogeneous stepped pressure load experiments using the fused silica AOMC multilayers and the modified laser-driven shock-compression configuration shown in Figure 6.8.

#	Type	Driver	Spectroscopically Probed Area	Laser Spot Size	Pressure Step Magnitude
HFS0	SiO_2 AOMC	~25 μm Al	~3.75 mm	~3.75 mm	~0/4 GPa
HFS1	SiO_2 AOMC	~100 μm Al	~3.0 mm	~3.0 mm	0/2.75 GPa

Experiment # HFS0: ~0/3.75 GPa Step Load

The corrected streak image for experiment # HFS0 is shown in Figure 6.9. At ~15 ns, there is a clear partitioning in the initial spectral peak due to the arrival of the stepped pressure pulse, and the temporal evolution of the non-zero pressure peak closely follows the expected profile of the laser-driven shock-compression. Note that this experiment used a different batch of AOMC samples with spectral peaks centered on ~565 nm. The extracted blueshift (right plot) uses a smoothing spline to track the separate peaks along each column and shows the split and eventual recombination of the two peaks as the pressure releases down. This result is very encouraging and provides important experimental proof for the

underlying motivation and claim of the present work: that the multilayer structures are capable of spatially resolved pressure sensing while maintaining nano-second level temporal resolution.

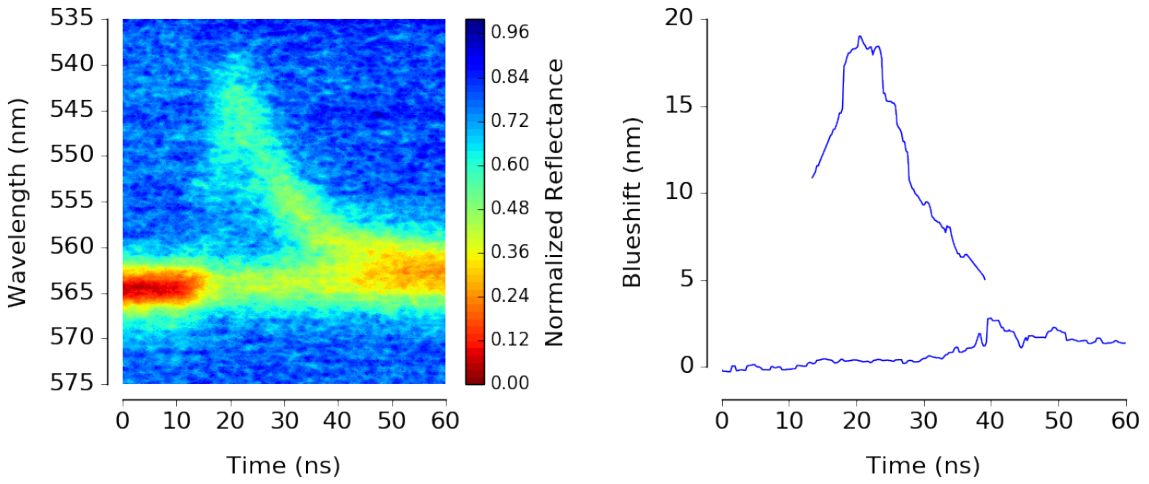

Figure 6.9: Corrected streak image and extracted blueshift temporal profiles for the ~0/3.75 GPa stepped pressure load experiments using the fused silica AOMC multilayers. The blueshift profiles were extracted using a smoothing spline along each column of the streak image (i.e., the time-resolved spectra) and appropriate thresholding.

Figure 6.10 shows the individual spectra associated at times 10 ns, 20 ns, and 35 ns from the streak image in Figure 6.9, representing the initial state, peak pressure state (i.e., point of maximum separation between the two pressure states), and near complete release state of the stepped pressure load. While the signal-to-noise ratio could be improved, the spectral evolution is clear and each peak is clearly resolvable. The small (~1 nm) base-line shift of the un-shocked spectral peak visible in the extracted blueshift (Figure 6.9) is also clearly observable in the 20 and 35 ns spectra. This is likely due to low magnitude surface waves propagating away from the spatial pressure step.

Finally, it is also very encouraging to see the excellent correspondence of the experimental streak image to the synthetic streak image for the stepped pressure load simulation in Figure 6.4. The peak separation, release, and recombination are clearly visible in both the experiments and simulation, and even subtle features such as the baseline shift of the un-shocked spectral peak are reproduced by the simulation. This provides further valida-

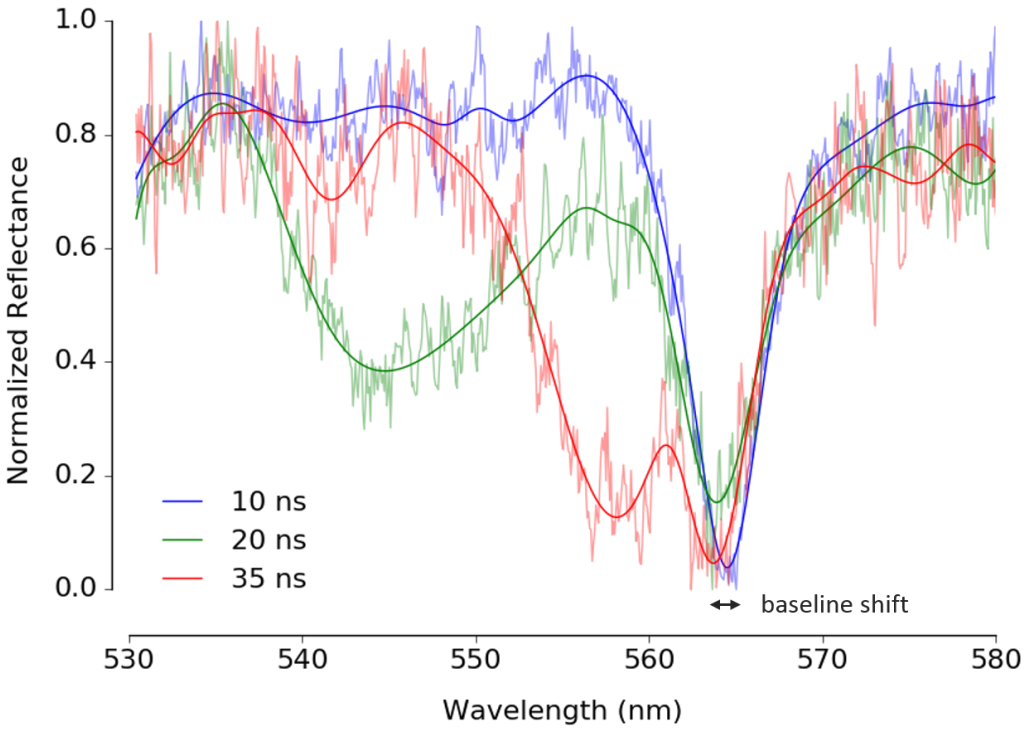

Figure 6.10: Individual time-resolved spectra extracted at t = 10, 20, and 35 ns from the streak image shown in Figure 6.9 for experiment # HFS0. Each spectrum is fit with a smoothing spline with the raw data also plotted to illustrate fit quality and signal-to-noise ratio.

tion of the optomechanical computational framework and clearly demonstrates its utility.

Experiment # HFS1: ~0/2.75 GPa Step Load

This experiment was similar to experiment # HFS0 with three key differences as seen in Table 6.1: a smaller shocked and spectroscopically probed area, a much thicker aluminum buffer (100 micron vs 25 micron for # HFS0), and a smaller pressure step of 0/2.75 GPa. These differences provide a useful analysis of the multilayer's performance as the thicker aluminum buffer will tend to decrease the sharpness of the spatial step due to dissipation, and the smaller pressure step and collection area reduce the total usable optical signal. Figure 6.11 shows the corrected streak image for experiment # HFS1 along with the extracted blueshift of the two separate peaks.

There are several subtle differences in these data compared to those for experiment #

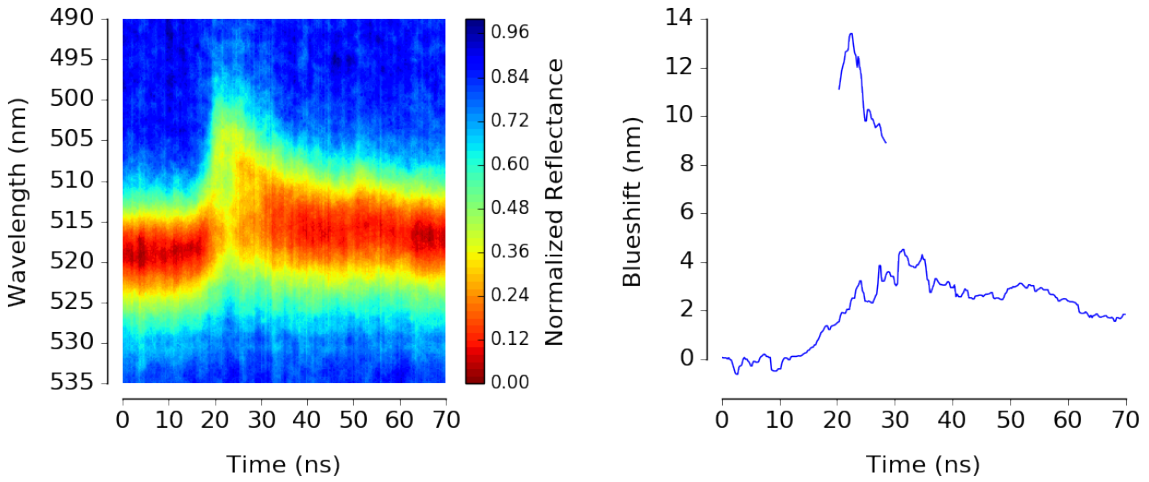

Figure 6.11: Corrected streak image and extracted blueshift temporal profiles for the ~0/2.75 GPa stepped pressure load experiments using the fused silica AOMC multilayers. The blueshift profiles were extracted using a smoothing spline along each column of the streak image (i.e., the time-resolved spectra) and appropriate thresholding.

HFS1. First, the separation of the two peaks, while still visible, is much less clear in the streak image (left) due to the smaller pressure step. Consequently, the extracted blueshift (right) has a much smaller temporal profile for the second peak ("non-zero" pressure) as it quickly recombines with the "zero" pressure peak. Both of these spectral responses would be expected given the differences in loading conditions and confirms that the underlying mechanisms that govern the response to heterogeneous loads remain the same. Second, while experiment # HFS0 showed a small shift of ~0.5 nm in the baseline "non-zero" pressure peak (likely due to surface waves and dissipative effects), experiment # HSF1 shows a much larger baseline shift of ~3 nm. This also is expected as the much thicker 100 μm aluminum driver will result in extensive "smearing" of the spatial pressure step as it propagates through the driver, resulting in a small (but decidedly non-zero pressure) even on the unshocked side of the spatial distribution.

Figure 6.12 shows the individual spectra associated at times 10 ns, 23 ns, and 30 ns from the streak image in Figure 6.11, representing the initial state, peak pressure state (i.e., point of maximum separation between the two pressure states), and near complete release state of the stepped pressure load. The signal-to-noise ratio is significantly improved compared

to experiment # HFS0 as much care was taken to achieve optimal alignment of the time-resolved spectroscopy setup. The small base-line shift in the primary peak is clearly visible as well as the secondary peak from the stepped pressure load manifesting as a shoulder at lower wavelengths.

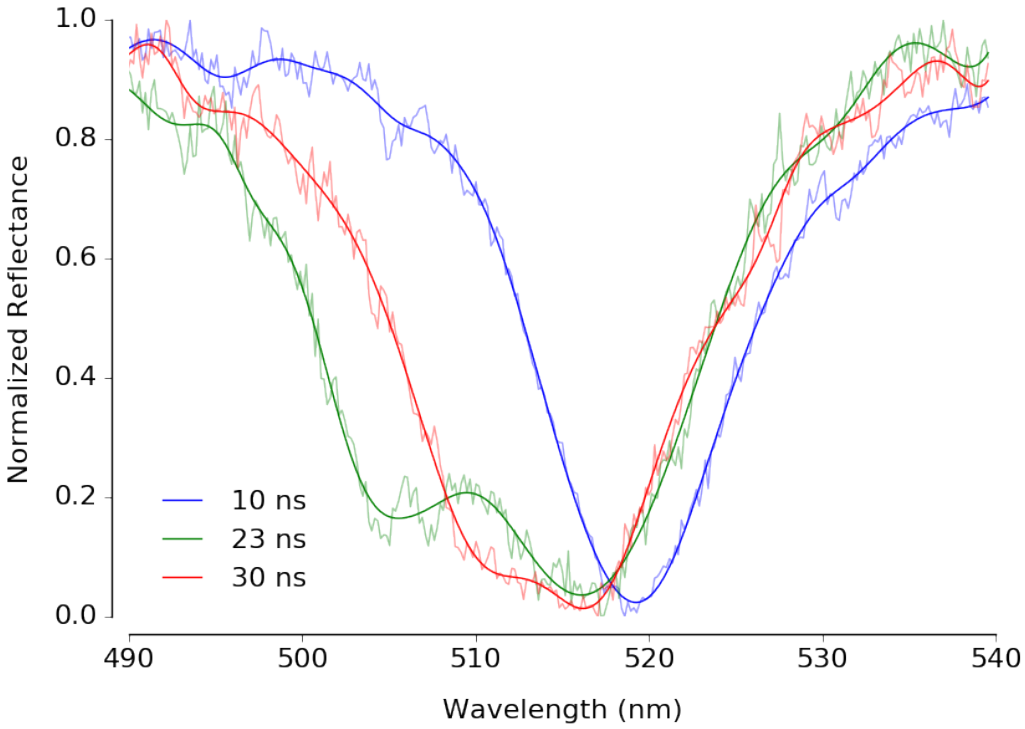

Figure 6.12: Individual time-resolved spectra extracted at t = 10, 23, and 30 ns from the streak image shown in Figure 6.11 for experiment # HFS1. Each spectrum is fit with a smoothing spline with the raw data also plotted to illustrate fit quality and signal-to-noise ratio.

Overall, this experiment is an excellent demonstration that many of the more complex features of heterogeneous loads are indeed captured by the time-resolved spectral responses of the multilayers.

6.3 Simulations of More Complex Heterogeneous Loading

The previous sections presented experimental data and optomechanical model predictions that clearly demonstrate the potential of the multilayers structures in spatially-resolved meso-scale sensing. Because the optomechanical computational framework is very general

in its operation, there is the unique opportunity to explore carefully controlled loading scenarios that would be difficult to implement experimentally and are beyond the scope of the present work. Drawing inspiration from the bonded engineered particulate systems introduced in Section 2.1.2, several such simulations were performed. As the potential microstructures of such materials can be extremely varied, the simulations focus on single and multi-particle monolayers in a soft polymer matrix (estane). In this way, the unique features and dynamic responses of these systems can be highlighted, demonstrating the potential utility of the multilayers as meso-scale sensors.

Single-particle Simulation

Figure 6.13 shows the simulation setup for a single-particle composite simulation under a uniform 6 GPa pressure pulse with a 3 ns rise time (left), and a temporal snapshot (right) showing the deformed geometry and pressure contours at a time when the pressure pulse has saturated the composite material and fused silica AOMC multilayer. Material properties for the aluminum and estane are obtained from Meyers [2] and Marsh [7], respectively, while all other material properties followed the same sources and models as those presented in Section 4.2.3.

The complexity of this simulation required slightly different simulation methods compared to the general configuration described previously in Table 3.2. Specifically, the estane binder material is significantly softer than the other materials in the simulation, and the deformation and flow of the binder near the vicinity of the aluminum particle proved too excessive for a Langrangian FEM solution. Consequently, the simulation was modified to be a coupled Lagrangian-Eulerian implementation, with the estane matrix as an Eulerian material and all other components Lagrangian. The Abaqus General Contact algorithm maintains realistic contact conditions between the Eulerian and Lagrangian materials, enabling the estane matrix to show realistic extensive deformation while maintaining the accuracy of the aluminum particle and fused silica AOMC deformation and time-resolved

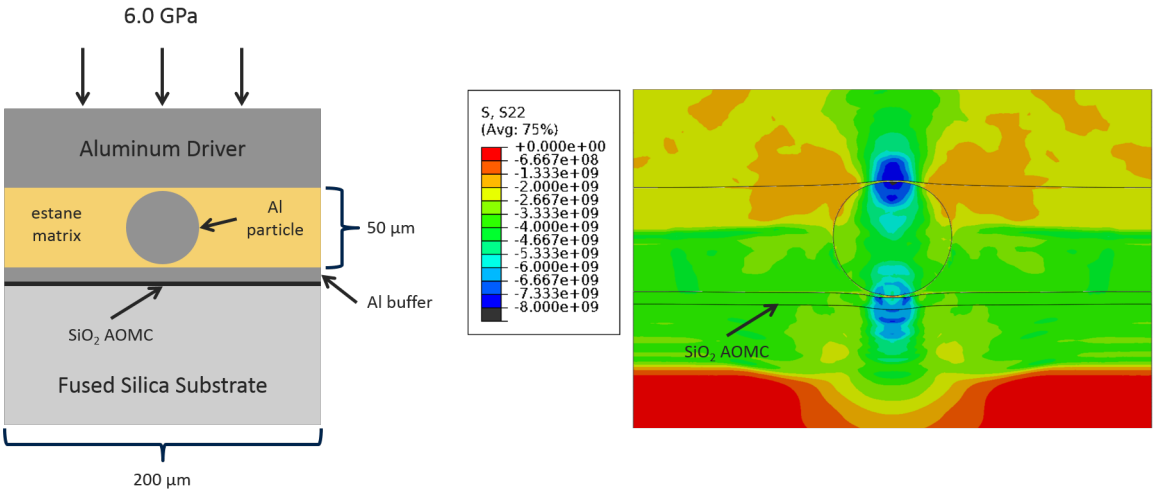

Figure 6.13: Setup for the single-particle composite simulation and a temporal snapshot of the pressure, showing the point where the pressure wave has fully saturated the composite material and the fused silica AOMC multilayer.

pressure states afforded by the Lagrangian reference frame.

There are two interesting features immediately apparent in the temporal snapshot shown in Figure 6.13: the perturbed shock front and elevated pressure due to the presence of the aluminum particle in the estane matrix. These material responses are typical of this class of materials, and accurate measurements of these behaviors could provide much insight into the shock response of such composite systems. Figure 6.14 shows a surface plot of the pressure in the AOMC cavity as a function of time (left) and two lineouts at specific locations along the width (right) demonstrating the difference between the response immediately below the aluminum particle and the unperturbed estane matrix.

It is clear from Figure 6.14 that the shock front travels more quickly through the aluminum particle and arrives at the AOMC multilayer ~8 ns sooner compared to the estane matrix and subsequently reaches 1.5 to 2 times higher peak pressure. To explore whether the multilayers are capable of capturing these important meso-scale features, the full optomechanical computational framework was utilized to produce a synthetic streak image for the simulation to represent what could be recorded using the multilayer structures and time-resolved spectroscopy. Figure 6.15 shows the synthetic streak image along with select

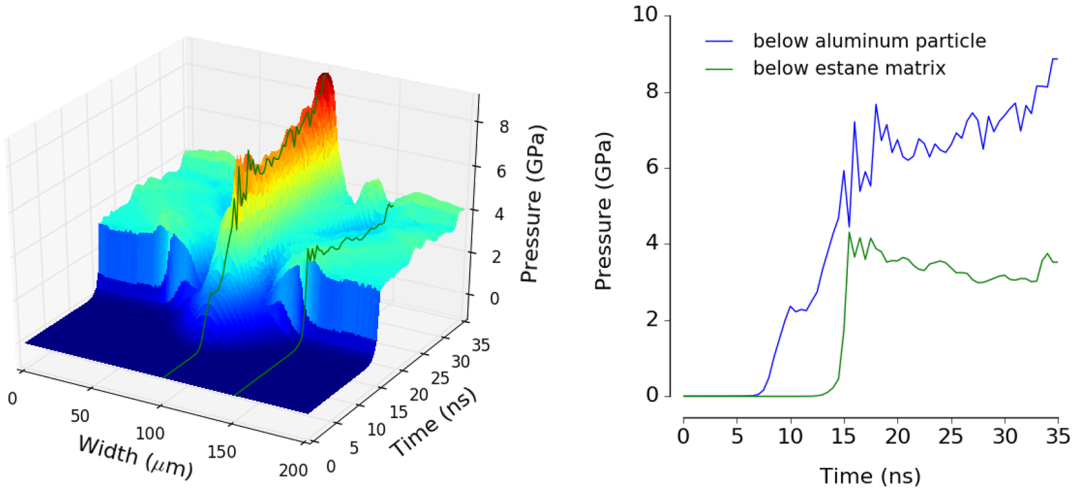

Figure 6.14: Time-resolved pressure surface (right) showing the pressure in the AOMC cavity layer in the single-particle composite simulation. Lineouts of time-resolved pressure at widths x = 100 μm (below particle) and 150 μm (below estane) are also shown in the pressure surface plot and plotted directly (right) in the pressure versus time space.

temporal line-outs to highlight certain spectral features.

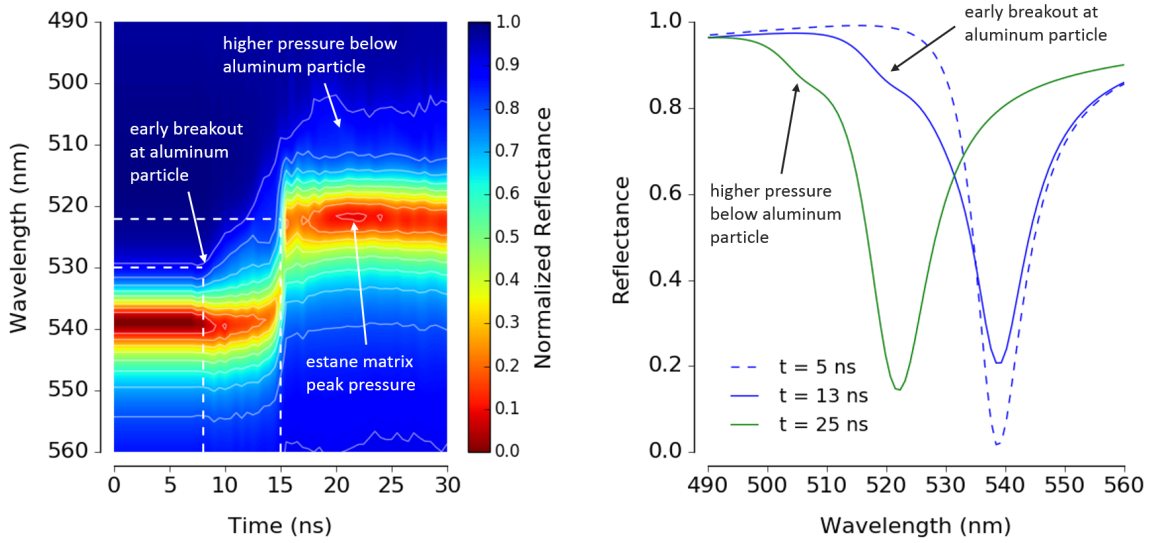

Figure 6.15: Synthetic streak image (right) calculated with the optomechanical computational framework for the single-particle composite simulation presented in Figure 6.13 along with spectral line-outs at t = 5, 13, and 25 ns. The early shock wave arrival and higher peak pressure of the shock wave through the aluminum particle manifests in the data as the lower-wavelength shoulder alongside with the equilibrated matrix (estane) pressure spectral peak.

There are many interesting features in the synthetic streak data, illustrating the infor-

mation density of the time-resolved spectroscopy approach. First, the early breakout of the shock wave through the aluminum particle is visible in the emergence at ~7 ns of the spectral shoulder at ~530 nm. This shoulder continues grow until the arrival of the primary shock wave through the estane matrix at ~15 ns. At this point, the matrix peak pressure is clearly defined at ~522 nm, while the spectral shoulder continues to grow and eventually equilibrates ~5 ns after the matrix. Comparing the observation of these features and their temporal evolution to the simulated pressure traces in Figure 6.14, there is remarkable correspondence. This is a strong indication that many of the meso-scale features in the simulation are indeed captured by the time-resolved spectra of the multilayer, which can then be used to make meaningful inferences about the material's response to shock-compression.

Multi-particle Simulation

Expanding on the single-particle simulation, a similar configuration was run with three particles instead of one. Figure 6.16 shows the simulation setup and a snapshot of the simulated pressure contour.

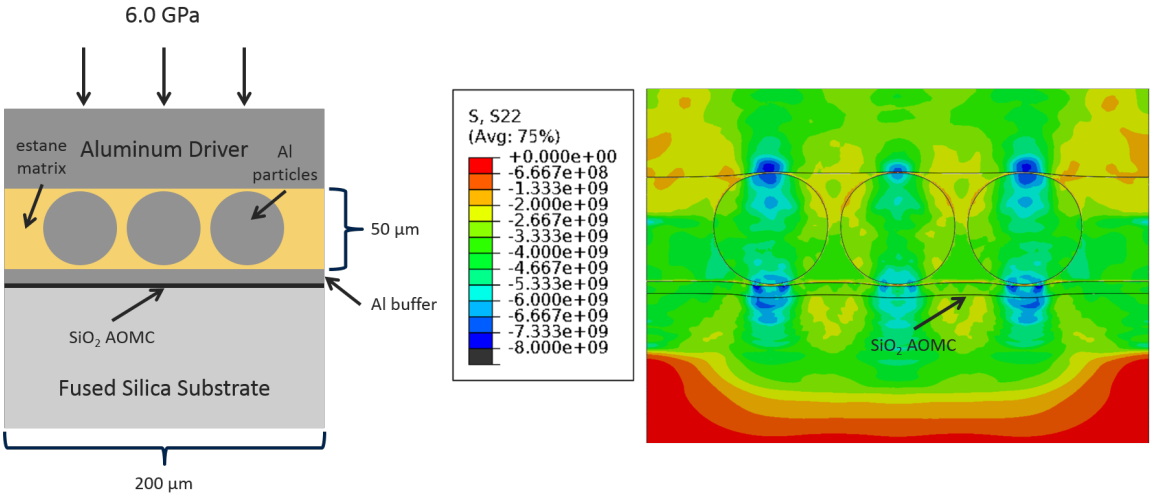

Figure 6.16: Simulation setup for the three-particle composite simulation and a temporal snapshot of the pressure, showing the point where the pressure wave has fully saturated the composite material and the fused silica AOMC multilayer.

Similar features are evident compared to the single-particle composite simulation with some differences given the larger contribution of the aluminum particles to the overall response. Figure 6.17 shows the time-resolved pressure in the AOMC cavity layer for the three-particle simulation (left) and three lineouts at specific locations along the width (right) demonstrating the material's response below and between the aluminum particles and in the relatively unperturbed estane matrix.

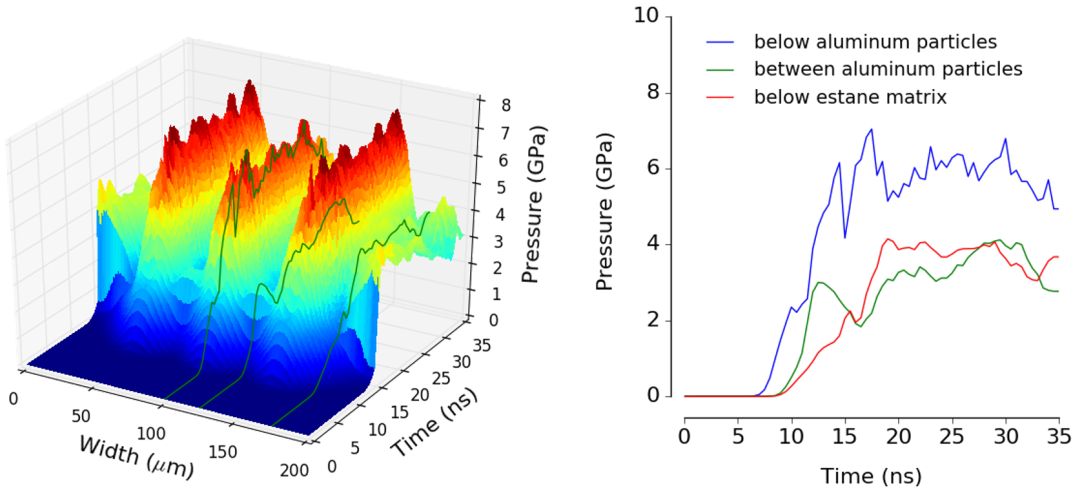

Figure 6.17: Time-resolved pressure surface (right) showing the pressure in the AOMC cavity layer in the three-particle composite simulation. Lineouts of time-resolved pressure at widths x = 100 μm, 125 μm, and 175 μm are also shown in the pressure surface plot, and plotted directly (right) in the pressure versus time space.

Figure 6.17 demonstrates that the shock front still travels more quickly through the aluminum particles compared to the estane matrix, but due to the increased number of particles the overall response of the composite is more affected. This leads to general broadening of the shock-front to ~5-8 ns even in the estane matrix, a significant increase compared to the ~1 ns rise seen in Figure 6.14. Also, there is a clear "dip" in the time-resolved pressure (green line in Figure 6.17 right) associated with the inter-particle region due to the complex wave-interactions between the matrix and particles. At later times the equilibrated pressure beneath the particles reaches 1.5 to 2 times higher peak pressure compared to the estane matrix. The synthetic streak image for the three-particle composite simulation obtained via the optomechanical computational framework is shown in Figure

6.18 along with temporal lineouts to highlight certain spectral features.

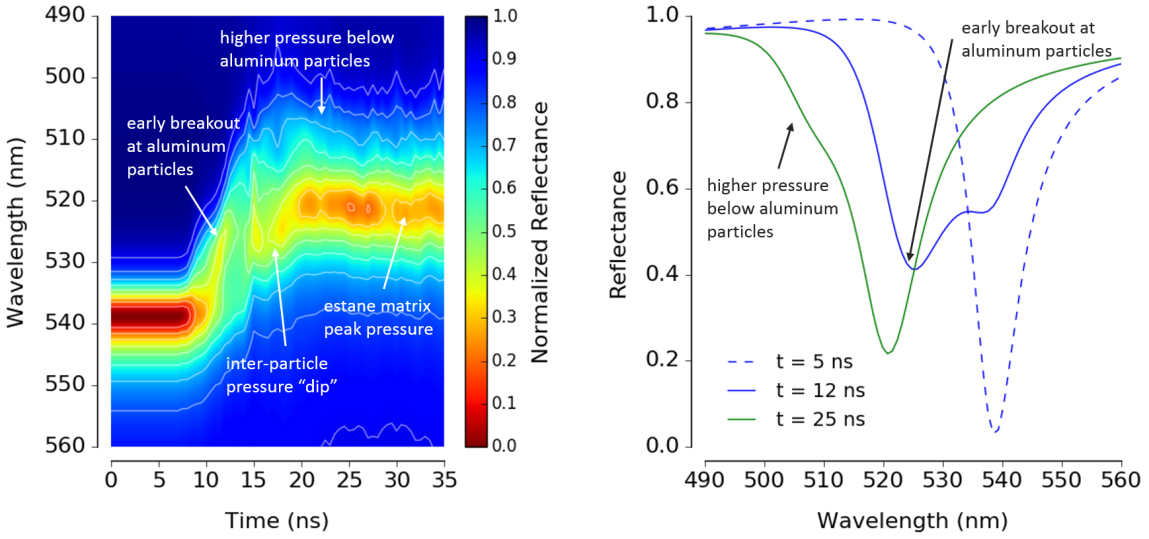

Figure 6.18: Synthetic streak image (right) calculated with the optomechanical computational framework for the three-particle composite simulation presented in Figure 6.13 along with spectral line-outs at t = 5, 12, and 25 ns. The early shock wave arrival and higher peak pressure of the shock wave through the aluminum particles manifests in the data as the detailed structure on the lower wavelength side of the equilibrated matrix (estane) pressure spectral peak.

The synthetic streak image is noticeably different than that seen in Figure 6.15. The early breakout through the aluminum particles is now very visible, and the resulting rise to the equilibrated pressure for both the aluminum particles and estane matrix is now longer and more complex. The lower wavelength shoulder is now much more pronounced throughout the entire temporal history as the three particles contribute much more to the overall spectral response as discussed in Section 6.1.3. Notably, the pressure "dip" in the inter-particle region is also visible in streak image along with the lower wavelength shoulder. This indicates that both of these responses in the material are occuring at *the same time*, an interpretation explicitly supported by the pressure lineouts in Figure 6.17. The time-resolved spectral lineouts (Figure 6.18 right) are also very similar to those for the previous single-particle composite simulation, with the primary difference being the size of the spectral shoulder corresponding to the aluminum particles at t = 25 ns.

6.4 Summary of Heterogeneous Shock-Compression Response

This chapter has presented a theoretical, computational, and limited experimental investigation of the time-resolved response of the multilayer structures to heterogeneous shock-compression. While important features of these responses were covered, this topic is nearly limitless in breadth when the many different heterogeneous materials and possible loading conditions are considered. This is to be expected, and a more complete discussion was not the focus of both this chapter and this work generally. Rather, several targeted conclusions were drawn that will inform future investigations of the multilayers' responses and their application to meso-scale sensing. These conclusions are summarized as follows:

- Models, rigorous optomechanical simulations, and experiments all demonstrate that the AOMC multilayer structures are capable of clearly resolving the multi-pressure state of a stepped shock load with nano-second level time resolution. The time-resolved spectra provide both an intuitive and data-rich history of the heterogeneous load, capturing obvious and subtle features of the response.

- The AOMC multilayers have a theoretical micron-level spatial sensitivity, and the separability of the global spectra into local responses enables the assignment of particular spectral features (i.e., pressures) to quantitative area fractions. Thus, the *relative spatial sizes* of different pressures can be inferred in addition to their magnitudes.

- Optomechancial simulations of simple aluminum-estane composite microstructures demonstrate that the multilayers are capable of capturing the unique features of the shock-compression response in this class of materials, such as temporal evolution of localized stresses and shock-front dispersion.

Finally, while this chapter has focused on the fused silica AOMC, most of the mechanisms and behaviors identified are driven by the general structure of the multilayers and would also apply to other AOMC designs as well as the DBR structures. Certain aspects of

the experimental implementation and the data analysis process may require more attention depending on the multilayer design, but the inherent flexibility of the multilayers allows for specific designs to be tailored to the application or material system of interest.

CHAPTER 7
PRACTICAL CONSIDERATIONS OF MULTILAYER STRUCTURE BASED SENSING

The preceding chapters have presented the theory and initial results of multilayer-based time-resolved meso-scale sensors, demonstrating their unique and significant potential utility in shock-compression studies. Extending this foundational work toward a well characterized, robust multilayer-based sensing system is the next logical step, although such efforts are beyond the present scope. Nevertheless, there are several relevant issues that have been identified that deserve a additional discussion: large-scale sensor fabrication and characterization, experimental implementation and data collection approaches, and data analysis methods. Each of these areas is discussed separately in the following sections in the context of using the multilayer-sensors in a scaled-up, application focused context.

7.1 Multilayer Sensor Production and Characterization

As discussed in Section 4.1 and in more detail by Lee [121], the design and optimization of the different multilayer structures is an important and complex process in and of itself. However, one of the ancillary benefits of the generally simple multilayer structures motivated by shock-optimized responses is the relatively easy device fabrication. The AOMC structures, for example, only require three to six deposition steps using well-known and readily available materials. Similarly, the SiO_x DBR multilayers can be deposited in single deposition run using IAD. While the fabrication of the samples in this work at Georgia Tech was done using the research facilities, the route of commercial fabrication is also a viable option.

To explore this commercial production option, Spectrum Thin Films [1], a fabrication

[1] http://spectrumthinfilms.com/stf

company based in Hauppauge, NY, was asked for a quote and comments on the fused silica based AOMC multilayer design. By providing the layer order, thickness, material composition, and desired tolerances on layer thicknesses and uniformity, Spectrum Thin Films was able to use their in-house simulation toolset to predict the as-fabricated spectrum of the AOMC. The predicted spectra (Figure 7.1) was essentially identical to that predicted and observed in the samples produced at Georgia Tech at a very cost-effective price as low as *$2.00 per* cm^2, depending on substrate selection and procurement. Another advantage of commercial fabrication options is guaranteed spectral and physical quality metrics, typically scaling the cost as more/less precision in the multilayer structures is desired.

Regardless of the fabrication methods selected, sufficient characterization of the predicted shock-compression responses of the multilayers is another key requirement of large-scale sensing applications as knowledge of the spectral feature/pressure relationship per fabrication batch will define the "calibration curve", in a sense, of that batch of sensors. As discussed extensively in Chapter 5, some structures (such as the fused silica AOMCs) have spectral responses that are well-described by optomechanical models. In such cases, characterization of an entire fabrication batch (representing up to many hundreds of potential sensors) could be accomplished with a combination of theoretical and empirical approaches. However, with other structures (such as the SiO_x DBRs) theoretical characterization may be insufficient, and more empirically based testing of production batches may be required, especially when component materials in the multilayers have unknown or poor tolerances on material properties.

In addition to multilayer material characterization, the physical aspects of the fabrication batch also affect the spectral responses. As the equations in Section 2.3 indicate, the spectral responses of the multilayers are also a function of λ_0, the initial peak position, and uniformity across the surface of a single substrate (or multiple) substrates will affect the initial peak position. For example, Figure 7.2 shows the predicted blueshift as a function of pressure using the optomechanical model defined in Section 4.2.3 for a fused silica based

Incident Angle (deg): 0.00
Reference wavelength (nm) 510.00

Layer	Material	Refractive Index	Extinction Coefficient	Optical Thickness (QWOT)	Physical Thickness (nm)
Substrate	Ag	0.05100	2.96000		
1	Al203	1.67260	0.00000	0.06559216	5.00
2	SiO2	1.46180	0.00000	5.73255795	500.00
3	Al203	1.67260	0.00000	0.06559216	5.00
4	Ag	0.05100	2.96000	0.01400000	35.00
5	Al203	1.67260	0.00000	0.06559216	5.00
6	SiO2	1.46180	0.00000	5.73255795	500.00
Medium	Air	1.00000	0.00000		
				11.67589236	1050.00

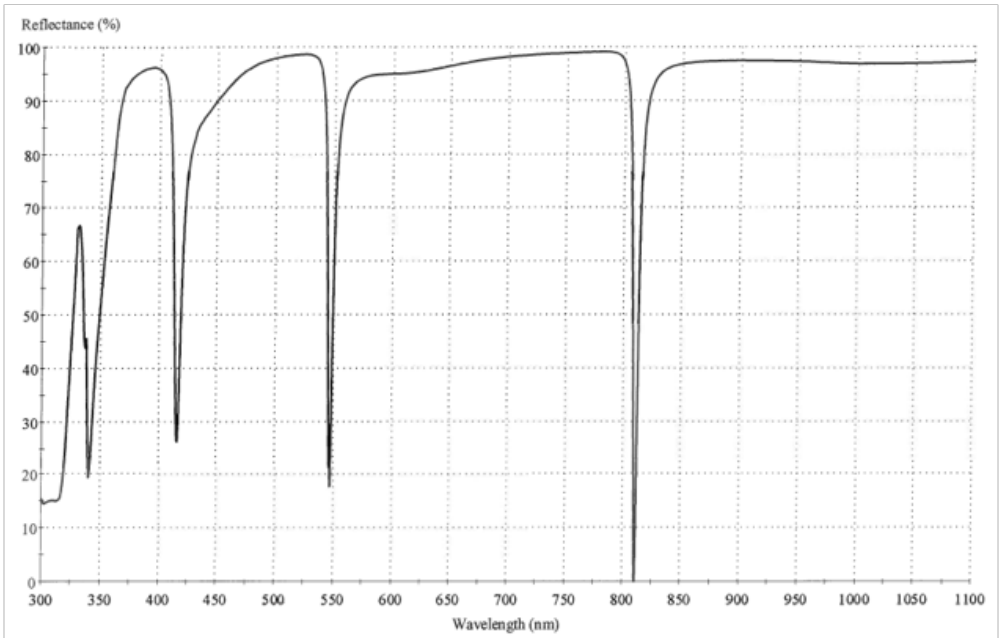

Figure 7.1: Predicted spectrum for a copy of the fused silica AOMC designs created during this work as produced by Spectrum Thin Films (http://spectrumthinfilms.com/stf/), a thin-film fabrication company based in Hauppauge, NY, USA. This quote was provided by Spectrum Thin Films at the request of the author.

AOMC with static peak positions of ~532 nm and ~580 nm. Generally, the magnitude of the blueshift increases as the initial peak position moves to higher wavelength positions with the ~580 nm AOMC showing a 12% larger shift compared to the ~532 nm AOMC.

In other words, the uniformity variances across a substrate lead to variances in the predicted and observed spectral responses as a function of pressure, though the *magnitude* of these variances may or may not be significant depending on the demands of the sensing application.

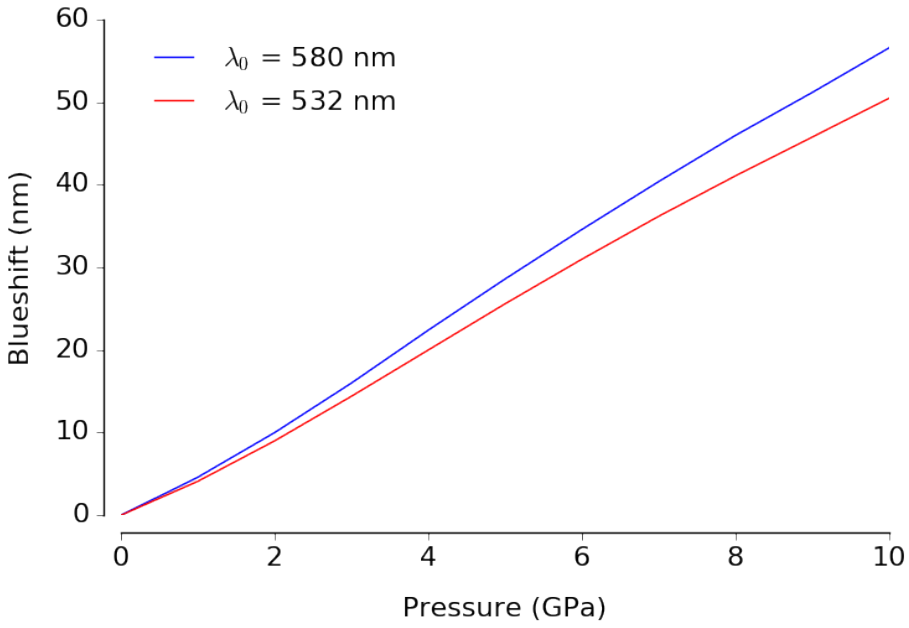

Figure 7.2: Predicted blueshift as a function of pressure for fused silica AOMC multilayers with initial peak positions (λ_0) ~580 nm and 532nm. The AOMC with the higher starting peak position has ~12% larger shifts as a function of pressure.

A final consideration of multilayer sample fabrication and characterization is potential aging/stability effects as a function of environment over both short and long time-scales. In general, the samples optimized and fabricated at Georgia Tech during this work were stable over 6-18 months. Some notable exceptions are the PMMA AOMCs and some early DBR designs where sample quality degraded substantially over only several weeks. In addition, the fabricated samples have generally been stored with minimal ambient light, temperature, and humidity variation. In certain applications, the age of the sample and storage/application environment may have effects on multilayer stability that influence the spectral responses of the sensors. While there may be some simple solutions to mitigate stability concerns, such as post-fabrication polymer/oxide overcoats and/or tuned deposition parameters, further study is needed to understand the magnitude of these effects.

7.2 Data Collection Approaches

Section 5.1 described the experimental approach and data collection system constructed and optimized for this work, but one of the advantages of the multilayer structure sensors is the flexibility in implementation and data collection approaches. Generally, there are two main categories of data collection methods with the multilayers: time-resolved spectroscopy and time-resolved intensity/reflectometry.

Time-resolved spectroscopy, the method of choice for this work, is the most "natural" data collection approach as it enables direct capture of the evolving spectral properties of the multilayers during the shock loading. This approach does require a streak camera and high-throughput spectrograph system, but it arguably captures the most information per experiment. However, there is one fundamental limitation of the time-resolved spectroscopy approach: the loss of spatial information. As previously stated, the spectrograph results in an unavoidable dimensional reduction by collecting and spectrally separating the *total* reflected signal from the entire probed area of the multilayer, i.e., the sum of each spatial spectral response. As was shown in Chapter 6, careful data analysis and informative simulations can increase the amount of usable data that may be extracted from the combined spectral history, but there are also practical limits on these approaches as well.

An alternative approach based on time-resolved reflectometry essentially chooses a different dimensional reduction: capturing time- and spatially-resolved localized intensity maps of the multilayer sensor, discarding the spectral information. This method exploits the same blueshift of the primary peak/valley from the multilayers as the sensing mechanism, but relies on narrow/single wavelength illumination to produce a pressure-induced reflectance change. Figure 7.3 demonstrates this mechanism with a fused silica based AOMC sample with single wavelength illumination of 532 nm. Essentially, as the AOMC valley blueshifts under pressure, the 532 nm source "sweeps" along the right side of the AOMC spectra, producing a smoothly varying reflectance change as a function of pressure. A

similar relationship can be created with a broadband light source filtered through a narrow bandpass filter centered on 532 nm, similar to a monochromator.

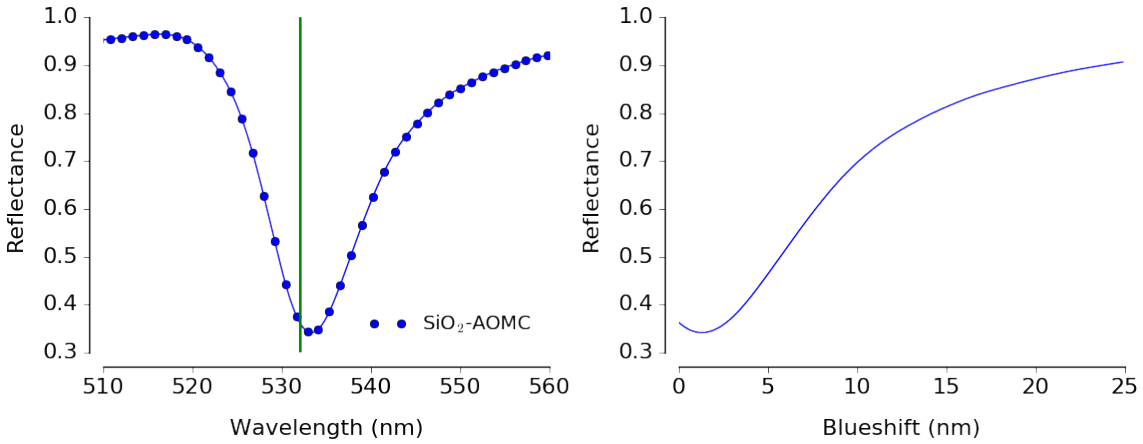

Figure 7.3: Spectrum from a fabricated fused silica AOMC sample (right) with line illumination at 532 nm and corresponding reflectance versus blueshift signal (right). As the original spectrum shifts to shorter wavelengths, the 532 nm illumination line "sweeps" along the right side of the spectrum, producing a reflectance as a function of blueshift curve.

The potential strength of this approach is fully realized with a camera-based measurement of the spatially-localized reflectance variation. For example, a high-speed framing camera can capture nanosecond-level, high-resolution images of relatively large areas of the multilayer sensor. Combined with the reflectance-pressure curve from Figure 7.3, time-and-spatially resolved pressure maps are, in theory, obtainable.

However, this reflectometry-based approach also has several limitations depending on the demands of the particular sensing application. First, the reflectance-pressure "responsivity" curve is highly dependent on the initial spectra of the multilayer, and certain spectral shapes are more conducive to this application than others. Narrow spectral peaks with steep edges would provide high contrast in that relatively small changes in pressure would lead to large changes in reflectance at a given wavelength, but would provide limited total pressure range as reflectivity is strictly limited to between 0 and 1. Alternatively, wide and flat spectral peaks would provide much more pressure range but at the expense of relatively small changes in reflectivity that may be difficult to capture experimentally. In practice,

custom multilayer structures that have the desired reflectance-pressure response at a given wavelength would need to be designed and optimized, while still remaining within the design constraints discussed in Section 4.1 for shock-compression applications. Finally, perhaps the most significant challenge with the time-resolved reflectometry approach is the independence of the measurement. While the blueshift that is directly measured with the time-resolved spectroscopy method is quite independent (i.e., there are essentially no other explanations for the observed blueshift other than shock-compression effects), there are several different mechanisms by which perceived reflectance could change: shifts in sample alignment angles during the loading, the sample surface moving in/out of focus during the loading, time-varying intensity from the illumination source, etc. Many of these issues can be mitigated by augmenting the experimental configuration with simultaneous measurements of source intensity, sample position/angle, etc., but at the cost of significantly increased complexity. Overall, the time-resolved reflectometry approach has much potential but would need a similar level of attention and validation as was required for the time-resolved spectroscopy method presented in Chapter 3.

While the direct spectroscopy and reflectometry methods are perhaps the most straightforward methods for data collection with the multilayers, the inherent flexibility of the multilayers provides many other potential approaches based on variations and combinations of these two base methods. For example, as the primary disadvantage of the time-resolved spectroscopy approach is the loss of spatial information, the addition of more spectrograph-streak camera systems and the appropriate collection and directing optics can retrieve some of the lost spatial data. Halves or quadrants of the probed area could each be directed to these separate collection systems (assuming there is sufficient signal intensity), and the spectral features measured can then be attributed to those spatial regions. While this method is complex and potentially cost-prohibitive, it arguably provides the most dense form of data collection possible with the multilayers. Similarly, the time-resolved reflectometry approach can be altered to utilize arrays of photomultiplier tubes

(PMTs) or photodiodes instead of a high-speed framing camera, which would provide significantly more temporal resolution at the cost of spatial resolution. Further augmentation with bi or tri-wavelength illumination (e.g., multiple laser sources) could also increase the pressure sensitivity of the reflectometry approach by retrieving additional amounts of spectral information.

7.3 Data Analysis Process

For any experimental diagnostic, the different methods of data analysis and their respective ease-of-use and accuracy play a very important role in not only the viability of the diagnostic but also the number of different applications where it can demonstrate utility. This remains the case for the multilayer structures as regardless of the data collection method chosen, the information density of the recorded data is high. In general, there are several particular aspects of data analysis processes that, in practice, have a significant impact on the overall accuracy of the final data.

For the time-resolved spectrometry approach, the most influential steps of data analysis are streak camera static distortion correction, spectral calibration, and background/reference intensity correction. When these steps are performed well, with high quality calibration/correction data, the resulting quality of the time-resolved spectra can be quite high. However, in some contexts it will not be feasible for one (or all) of these steps to be performed with precision. This will have significant, but predictable, effects on the type and accuracy of the extracted data. Static distortion correction primarily effects the accuracy of peak position and temporal scaling with relatively small impacts on spectral width and depth/height. Spectral calibration, as the name implies, strongly determines the accuracy of blueshift and peak width features but does not effect peak height/depth. Background/reference intensity correction has significant effects on peak height/depth, moderately impacts peak width, and has almost no impact on blueshift. It is apparent that there are trade-offs with respect to data quality that may be tolerable for certain applications. However, as was

discussed in Chapter 6, when applying the multilayers to complex heterogeneous loads, it is vitally important to have confidence in the time-resolved spectra, especially when attempting to correlate subtle spectral features to specific material behaviors and responses. Whether or not such fidelity is obtainable in practice is dependent on the requirements of the application.

For the time-resolved reflectometry approach, the background/reference intensity correction is the most important step of the analysis process, especially if the probed area has non-uniform illumination. The accuracy of this correction is highly dependent on the repeatability of the collection and/or the detail of any simultaneous reference measurements. In practice, a "perfect" correction is likely not possible, especially when accounting for the added random noise from the high-speed camera itself. In addition, the relatively small number of available frames (typically 8-16 for nanosecond-level framing cameras) can make construction of temporal histories challenging, particularly if the reflectance-spectral curve of the multilayer structure is highly non-linear or non-monotonic.

Finally, for both data collection approaches the signal-to-noise ratio of the data plays a significant role in quality of the extracted data. For applications with demanding requirements on data fidelity, there is a limit to signal enhancement from correction steps and sophisticated spectral/image analysis methods and algorithms. In the specific context of nano-second level shock-compression of heterogeneous materials, it is likely that the dominant limiting factor is, in fact, the signal-to-noise ratio. This is why for these applications it is so important to develop an experimental system that is optimized for light throughput and an illumination source (either broadband or single wavelength) that has sufficient intensity over the temporal regimes of interest.

7.4 Comparison to Existing Time-resolved Diagnostics

While the advantages and disadvantages of existing time-resolved sensing methods were previously discussed in Section 2.2, the much more comprehensive understanding of the

capabilities and performance of the multilayer structures gained over the course of this work enables a more detailed, practical comparison to the most common diagnostics.

Existing Stress Gauges

As the multilayers are also fundamentally stress gauges, perhaps the most direct practical comparison is to existing time-resolved stress gauges, such as PVDF and manganin gauges. The most obvious difference is the level of spatial sensitivity. Since PVDF and manganin have no inherent spatial sensitivity, the multilayer sensors will have more utility in applications where the expected load is heterogeneous. In addition, due to the piezoelectric/piezoresistive operation of PVDF and manganin, localized regions of high pressure can cause unknown biasing effects that compromise the accuracy of the entire sensor. That is, a single high pressure spot within the larger area of the PVDF/manganin sensor affects the accuracy of the entire sensor, even those areas that are indeed under a uniform load. In contrast, due to the passive reflectance based sensing mechanism of the multilayers, localized areas of high pressure will not bias other areas of the sensor, and further provides the opportunity to capture all of the localized responses. This also makes the multilayers less sensitive to damage and premature mechanical failure of the sensor, as unlike PVDF/manganin electrical conductivity does not need to be maintained.

However, this does not mean that the multilayers are not without disadvantages in certain contexts. While the multilayers are resilient to localized failure, loading over a long period of time (microseconds to milliseconds) may cause the periodic structure of the multilayer to become less defined, compromising the spectral signal of the sensor. As these time-scales were not the focus of the present work, it is unknown what changes (if any) would be observed in the time-resolved spectra under such conditions. As such, PVDF/-manganin gauges may have a slight advantage in the specific case where time-extensive pressure histories are required. Also, as the multilayers depend on the reflectance of visible light, embedded sensing in opaque materials is not possible without the use of a trans-

parent window. While embedding PVDF/manganin gauges has its own implementation challenges, the optical transparency of the sample is not a concern. Finally, a very similar requirement of PVDF, manganin, and the multilayer sensors is the need for a calibration curve, either empirical, theoretical, or combination theoretical/empirical. Typically, manufacturers of PVDF/manganin gauges provide such a calibration curve with a given set of sensors, usually with a specified tolerance in a particular pressure regime. While the same could be done with the multilayers, it is likely a more involved process as the underlying sensing mechanism is more complex. However, the potential usable pressure range of the multilayers is broad, especially when considering designs tailored to high pressures such as LiF based AOMCs. Compared to the relatively low range of ~0-20 GPa for PVDF and manganin gauges, there is incentive to perform the necessary characterization of the as-fabricated multilayers.

VISAR and PDV Velocimetry

A direct comparison of the multilayers to velocimetry methods is difficult, as each diagnostic is measuring a fundamentally different parameter (i.e., pressure/stress vs velocity). Additionally, the data analysis process for velocimetry is not dependent on calibration curves or models and is more theoretically driven. Nevertheless, there is overlap in the potential applications between the multilayers and velocimetry, and some useful practical comparisons can be made.

First, similar to the stress gauges, standard velocimetry diagnostics (i.e., point probes with spot sizes of 50-500 μm) are not well-suited to heterogeneous loads due to the effect that multiple moving surfaces (within the probe's area) have on the resulting interferometry signal. For example, PDV will record the multiple velocities as the sum of the time-resolved frequencies, leading to a complex multi-frequency signal. While the STFT and wavelet analysis methods presented in Section 3.1.3 can in some cases separate the individual frequencies, this is not guaranteed and is particularly challenging when nano-

second level velocity histories are needed. Standard quadrature-based VISAR analysis, on the other hand, is extremely sensitive to multiple moving surfaces and isolating a particular velocity history is often not possible without significantly compromising the accuracy of resulting data. Thus, the multilayers again present a compelling alternative for applications with heterogeneous loads compared to standard velocimetry approaches. One point of similarity between the multilayers and velocimetry methods is the requirement of optical access to the probed surfaces. While PDV has some flexibility in that some materials are transparent at low-to-mid IR wavelengths (for example, silicon has ~50% transparency at 1550 nm), in general the restrictions on window materials and sample configurations will be similar between the multilayers and velocimetry.

Perhaps the strongest feature of velocimetry methods is the wide range of velocity magnitudes that can be captured. A PDV system with a sufficiently fast oscilloscope or a VISAR system with variety of delay etalons can record velocities from 10's of m/s up to several km/s. Multilayers structures are also capable of this wide range of dynamic loading magnitudes, but likely only with several different designs focusing on different pressure regimes. As each design will need its own calibration curve and data collection approach, the practical use of the multilayers in applications with substantial pressure ranges will be more challenging. Ultimately, a substantial advantage of the multilayers is the ability to provide spatially-resolved information under heterogeneous loading conditions without the data ambiguity problems of velocimetry approaches.

Line-VISAR and Multi-plexed PDV

Line-VISAR/ORVIS and multi-plexed PDV systems are significant modifications of the corresponding original diagnostics and are most similiar to the multilayers in their spatially-resolved sensing capacity. Line-VISAR was introduced in Section 2.2, and its advantages and disadvantages relative to the multilayers are relatively simple: line-VISAR offers similar or better levels of spatial resolution and measurement range but only along a one-

dimensional line and with a quite complex experimental setup and data analysis procedure. In this sense, the multilayers could be considered complimentary to Line-VISAR with each potentially more suited to particular applications.

Multi-plexed PDV systems offer another competitive comparison to the potential utility of the multilayer structures. Without going into extensive detail, by integrating multiple frequency shifts similar to up-shifted PDV systems along with temporal delay paths, Daykin et al. [37] combined as many as 8 individual PDV probes capable of being recorded on a single fast digitizer. With a standard 4-channel oscilloscope, this offers 32 individual point probes with the same extensive velocity range and nano-second level precision of standard PDV. Often, this system modification can be accomplished with readily available commercial communication equipment, which is typically in the mid-IR. However, the primary disadvantage to multi-plexed PDV is geometric constraints on probe configuration and sample geometry. Essentially, each probe needs to collect its own reflection from the sample surface without contaminating other channels, which places constraints on how small of an area the multiple probes can be focused on. In practice, many of the more advanced implementations of multi-plexed PDV are focused on relatively large (100's of cm^2 and up) samples where sufficient space is available, and measurements of small (10's of cm^2) sample areas are not practical. This is again a unique advantage of the multilayer structures, where spatial resolution is possible on scales of mm^2 and is generally limited by the data collection approach or signal-to-noise, not the inherent limitations of the diagnostic itself. As such, there is likely less potential overlap in the applications of multi-plexed PDV and the multilayer structures, leading to a similar complimentary relationship.

CHAPTER 8
CONCLUSIONS AND FUTURE WORK

In this work the theory, development, and testing of novel multilayer optical structures as time-resolved pressure sensors with meso-scale spatial sensitivity has been presented. Through the use of time-resolved spectroscopy, a combination of theoretical and empirical models, and coupled optomechanical computational simulations three primary research outcomes have been identified as major conclusions and are summarized below.

8.1 Research Outcomes

Multilayer Responses to 1-D Shock-compression

Three AOMC designs with silver reflecting layers and fused silica, Al_2O_3 (most likely amorphous), and PMMA cavity layers were subjected to laser-driven shock-compression in the range of ~0-10 GPa. The time-resolved spectral responses of the multilayers were recorded along with *in-situ* particle velocities. All of the AOMC multilayers showed clear spectral shifts (blueshifts) with temporal profiles matching the expected temporal profile of the laser-driven shock pressure as well as quantitative temporal correspondence to the *in-situ* particle velocities within <1 to several nanoseconds. With increasing pressure, the spectral blueshift began to show a nearly discontinuous shift to the "steady-state" blueshift, a phenomenon that is not yet fully understood but nonetheless demonstrates the high temporal response of the multilayers. Trends were also observed in the time-resolved spectral peak width and depth, though data and analysis limitations make these observations qualitative for the purpose of this work.

Two different SiO_x DBR designs with 5 and 10 bilayers were also subjected to laser-driven shock-compression, recording the same time-resolved spectral responses and *in-situ*

particle velocities. Both DBR structures showed clearly resolved spectral shifts (blueshifts) with temporal profiles also showing similarly quantitative correspondence to the *in-situ* particle velocities (~1-3 ns). The height and width of the DBR spectral peak also showed a time-resolved and pressure-dependent response, but trends again are qualitative for the data presented in this work. Unlike the AOMC multilayers, the spectral blueshift of the DBRs remains clear throughout the pressure rise to the "steady-state" condition, although some decrease in the spectral peak height was observed at higher pressures during the rise. Despite the relatively high thickness of the DBR multilayers (several microns), the length of the blueshift rise was esentially identical between the 5 bilayer (~3 μm) and 10 bilayer (~5 μm) DBR samples indicating that the temporal resolution of the DBR structures is still at the nanosecond level due to the high-level of impedance matching between the individual SiO_x layers.

Accuracy of Optomechanical Model Predictions

An optomechanical model informed by theory and empirical data was defined for the AOMC and DBR multilayer structures, incorporating the pressure-dependent layer thicknesses and material refractive indices. Using COMSOL multiphysics, the complete spectral response of the multilayers was predicted over a range of 0-10 GPa. The 1-D laser-driven shock-compression experimental data was compared to the model predictions, with varying results. The fused silica AOMCs showed an excellent match to the model predictions, while the PMMA and Al_2O_3 AOMCs showed reasonable matches but with only a single experimental data point for comparison. Generally, however, the cavity-material dependent response of the AOMC structures was clearly observable in both the models and the experimental data, with the magnitude of the blueshift as a function of pressure decreasing from the very high compressibility PMMA cavity to the low compressibility Al_2O_3 cavity. Model predictions for spectral peak width and depth can not be effectively compared to the experimental data for reasons described previously, but the qualitative trends of decreasing

peak depth and increasing peak width in the data are also predicted by the model.

For the SiO_x DBRs the optomechanical models over-predicted the blueshift compared to the experimental data. However, these predictions were based on empirical data for fused silica (SiO_2) as relevant data for the different SiO_x stoichiometries is not available. To determine whether the model could be modified to better match the experimental data, the volume compression response of the SiO_x was reduced by 20% (i.e., stiffer layers were assumed) which brought the magnitude of the predicted blueshift in line with the data. Given that a significantly different refractive index response as a function of pressure between SiO_x and SiO_2 is unlikely, this simple scaling behavior indicates that the underlying form of the optomechanical model still applies to the SiO_x DBRs and simply requires more accurate empirical material property data. As with the AOMC multilayers, model predictions of spectral peak width and height for the DBRs can not be compared quantitatively to the experimental data, but qualitative trends of increasing peak height and decreasing peak width observed in the experimental data are also predicted by the model.

Multilayer Responses to Heterogeneous Shock-compression

To explore the ability of the multilayers to capture multi-pressure states at nanosecond time-scales, investigations of controlled "binary" step loads of zero and non-zero stress states were conducted using the fused silica AOMCs. The experimental data clearly indicated the evolution of multiple spectral peaks each corresponding to the zero and non-zero stress states and following the expected temporal profile of the laser-driven shock-compression shock load. More in-depth theoretical predictions of the spectral response to a spatial step-load confirmed this observed behavior, and also enabled predictions of micron-level maximum spatial sensitivity and fundamental relationships between spectral features and spatial load area fractions. Additionally, coupled optomechanical simulations using both Abaqus and COMSOL produced simulated time-resolved spectra very similar to that observed experimentally validating the results of the overall simulation framework.

Expanding this last success, simulations of shock-compression in controlled heterogeneous composite materials were performed, focusing on single and three-particle monolayer microstructures in an estane matrix. Important aspects of the time-resolved pressure state of the composite structure, such as stress partitioning and shock front dispersion, were captured in the features of time-resolved simulated spectra, providing strong evidence that the multilayers are capable of meso-scale spatial sensitivity at the nanosecond time scales needed for shock-compression studies in this class of materials.

8.2 Future Work

To further explore the potential of the multilayer structures in time-resolved meso-scale sensing applications there are several specific areas that need more in-depth investigation: application-tailored multilayer design and fabrication, optomechanical model improvement and continued validation, and application of the multilayer structures to a wide range of "real-world", heterogeneous dynamic loading conditions. The potential direction of each of these topics is summarized briefly below.

Novel Multilayer Designs

Beyond the specific multilayer designs discussed in this work, there are many other potential configurations that fit within the design constraints discussed in Section 4.1, providing much flexibility to tailor unique multilayer structures to specific applications. For example, the multilayers designed and tested in this work were focused on the low to medium pressure regimes up to tens of GPa. At significantly higher pressures an accurate understanding of pressure-dependent material properties is essential in order to predict and interpret the time-resolved spectral response of the multilayer. For example, of the materials listed in Table 4.1, [100] LiF is very well defined up to several hundred GPa and a [100] LiF based AOMC structure may be especially suited for such high-pressure applications. Similarly, DBR structures based on Al_2O_3, LiF, MgO, and other optical materials with both high re-

fractive index contrast and sufficient high-pressure optical property characterization may prove compelling for applications where all-dielectric structures are preferred. Each new multilayer design would also require investigations into the most effective fabrication options. While the ion assisted deposition and electron beam evaporation methods proved effective for the designs in this work, more complex structures and/or different component materials may require different fabrication methods and equipment. Ultimately, the flexibility and tunability of multilayer-based sensing provides a unique advantage for time-resolved applications and deeper exploration of the multilayer design space is likely to be productive.

Optomechanical Model Improvement

The development of the optomechanical models in Section 4.2 while reasonably thorough does leave areas for improvement. For example, the current models are heavily reliant on empirical data for pressure-dependent optical properties and EOS (equation of state) information. While for materials with high quality literature data this proved effective, multilayer designs with less well-studied materials are more challenging to model. Detailed characterization of the structure in the deposited layers would enable more accurate interpretation and modification of existing data/models, as well as the potential for first-principle calculations of pressure-dependent material responses. While such explorations may prove challenging, given the importance of the blueshift/pressure "calibration curve" for a given multilayer design, the effort would likely prove worthwhile and enable broader use of the multilayers in different environments and applications.

Also, to this point temperature effects on the time-resolved spectral response of the multilayers have not been considered. As was argued in Section 4.2, for many applications and multilayer designs the temperature effect is likely to be negligible. However, a targeted study of the issue is needed to validate this assumption and identify important exceptions.

Real-world Testing and Evaluation

Finally, perhaps the most important research direction for the multilayers is continued testing and evaluation using real-world heterogeneous material samples and loading conditions. While this work has demonstrated the potential for the multilayers to effectively capture important features of complex multi-pressure loading, the enormous breadth in the structure and properties of heterogeneous materials necessitates a broader investigation. An appropriate starting material system would be bonded particulate composites as the optomechanical computational framework may help with the interpretation of the experimental data as demonstrated in Section 6.3. This class of materials is also similar to many different types of energetic composite materials, a highly-studied and very important area of research where the multilayers may have significant utility. Ultimately, it is important to acknowledge that the use of the multilayers as time-resolved meso-scale sensors is challenging, and appropriate thought needs to be given in how to best leverage their capabilities. The scientific community is well aware of the difficulty in understanding heterogeneous materials, and it should be expected that any diagnostic capable of providing detailed insight into their behaviors under extreme conditions will require similar levels of commitment.

Appendices

APPENDIX A

HIGH-THROUGHPUT SPECTROGRAPH CONSTRUCTION AND USAGE

The custom high-throughput spectrograph presented in Chapter 3 is well-suited to the present work, but its targeted capabilities do lead to a few idiosyncrasies compared to standard spectrographs. Primarily, the additional complexity comes down to the initial and per-experiment alignment process, which leads to several requirements for the experimental configuration presented in Figure 3.6. First, both of the DSLR camera lens will need proper mounts that have, at minimum, three translational degrees of freedom as while the low f/number lens are fairly tolerant to off-axis light, for the best performance precision alignment of each lens is crucial. Second, the holographic dispersion grating has directionality in its dispersing elements and requires a rotating optical mount (perpendicular to the optical input axis) to ensure that the spectrally dispersed signal is in the same plane as the spectrograph input slit. Additionally, as the highest diffraction angle of the dispersion grating is at ~45 degrees to the input axis, a rotation axis parallel to the optical input axis is needed as well. In Figure 3.6 all of these adjustments was obtained with relatively simple and inexpensive optical mounts and posts, but the configuration could be improved to enable easier initial setup and alignment. Third, an input slit is strongly recommended to ensure that the sufficient spectral resolution is obtainable, which also requires at minimum three translational degrees of freedom. Finally, as this spectrograph is lens based, consideration does need to be given to the wavelength dependent effects and performance. The DSLR lens used in this setup have very low chromatic dispersion in the *visible wavelength range*, as they are primarily intended for photography purposes. If spectroscopy in the near-UV to low-IR is desired, this type of lens will show increasingly poor chromatic dispersion performance.

The last important consideration in the design and use of the spectrograph is the input

focusing lens that directs the light from the experiment onto the spectrograph input slit. As with all spectrographs, the numerical aperature of the input focusing lens should, ideally, be matched to the acceptance angle of the collimating lens in the spectrograph. This will ensure maximum collection efficiency in the overall system. This input focusing lens should also be chromatically corrected in the wavelength range of interest. However, while mirror-based spectrographs are fairly tolerant to over/under illumination of the collimating mirror, there is a noticeable decrease in collimation performance with the DSLR lenses with significantly off-axis light, leading to decreased spectral sensitivity. To correct for this issue, under the specific illumination conditions of *any given experiment*, the focusing adjustments on first the spectrograph collimating lens and then the spectrograph focusing lens should be tuned to ensure the best possible spectral resolution. This is typically done with a calibration lamp or other similarly narrow-width spectral line source.

Overall, the significant increase in efficiency afforded by this spectrograph design comes at the cost of increased complexity in the configuration and use of the system. The specific requirements of any given application should dictate whether or not this type of custom spectrograph, versus a more complete and likely easier to use commercial option, is warranted.

APPENDIX B
TIME-RESOLVED SPECTROSCOPY SETUP - CALIBRATION AND DATA CORRECTION

The complete time-resolved spectroscopy setup used in this work is a relatively complex piece of precision scientific equipment, and much care must go into its setup, operation, and calibration. A complete discussion of these topics can not be undertaken here as it is fairly specific to a particular configuration and instruments. In general, however, there are several critical steps that must be performed to obtain accurate time-resolved spectroscopy data: static distortion correction of the streak image data, intensity uniformity correction for the entire system, and spectral calibration of the entire system. Each of these topics is discussed separately below.

B.1 Static Distortion Correction

As was described in Section 3.1.2, each streak "image" is captured by actually imaging the surface of the streak camera's phosphor screen after the excitation electrons are swept across it. As the phosphor screen itself is curved, the resulting streak image has curvature or static distortion. In photography terminology, it has barrel distortion. Figure B.1 shows an example streak image of a pulsed laser diode illuminating a line-pattern spatial grid in front of the streak camera input slit. When operating the streak camera in sweep mode, this will produce a dot-array pattern. The pattern is clearly non-uniform due to static distortion.

Unfortunately, correcting this distortion is not as simple as applying a uniform distortion correction algorithm, as each streak tube, phosphor screen, and imaging camera add their own subtle distortions to various parts of the image. As such, the streak camera manufacturer typically provides a utility and/or parameters to perform static distortion correction. However, in this work it was determined that the manufacturer provided utility was

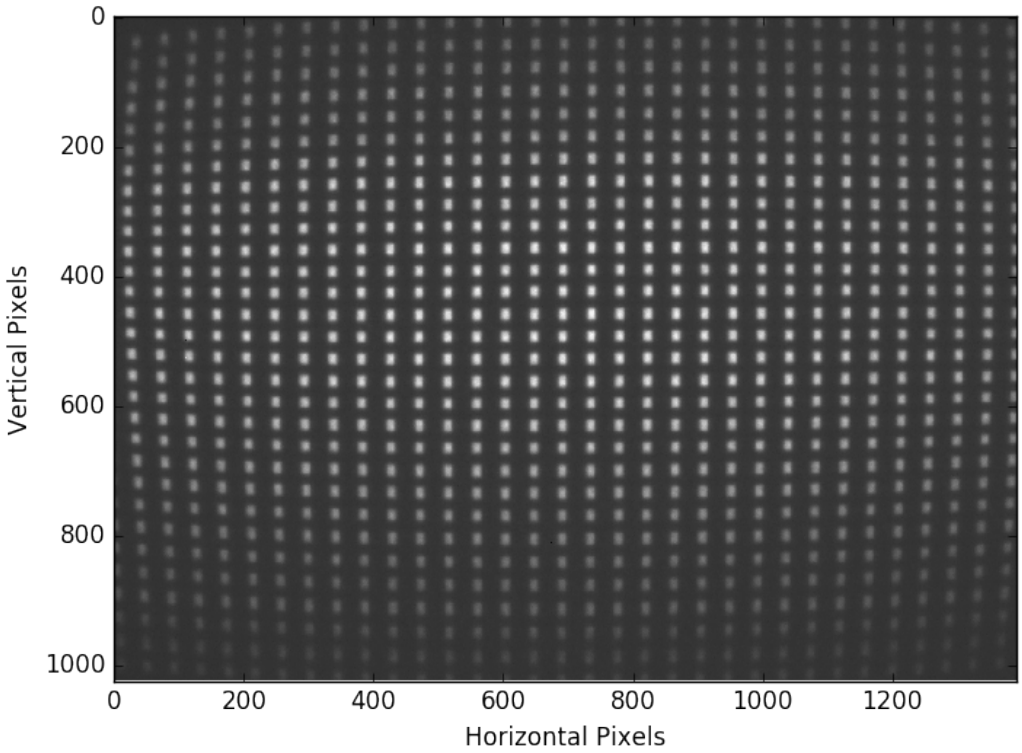

Figure B.1: Example *uncorrected* streak image showing a dot-array generated with a spatial grid template and a pulsed laser diode. The static distortion in both x and y dimensions is clear, especially near the edges of the image. The horizontal (columns) axis corresponds to the temporal axis of the streak camera, and the vertical (rows) axis corresponds to the spatial axis of the streak camera. In the time-resolved spectroscopy configuration, the spatial axis is the spectral axis.

not adequately removing the static distortion, and thus a custom, high-precision distortion-correction process was independently developed. It is composed of the following steps:

1. A reference image of a dot-array pattern is taken, using a known spatial separation of the dots (dx and dy) as references. If the spatial separation and pulse separation cannot be measured with sufficient accuracy, the middle row and column of the streak image can be used as references, as the static distortion of the image is minimal at these positions and axes.

2. The pixel locations of each dot in the pattern is extracted (many different methods are equally effective), and these are used to create a two mapping arrays for the

x and y axes: where the width and height of the arrays (in pixels) are defined as $dx(\mathrm{n}_{xdots} - 1)$ and $dy(\mathrm{n}_{ydots} - 1)$, and the values at each point are pixel coordinates in the original streak image that are mapped to that position in the corrected array. In this work, Lanczos interpolation over an 8x8 neighborhood is used to identify mappings at locations between the dots in the reference dot-array image, but other interpolation approaches are likely equally effective.

Figure B.2 shows the dot array streak image from Figure B.1 after applying the static distortion correction process. The dots are now clearly regular and uniform across the image, although the corrected image is slightly smaller as some information was lost around the edges where the dot pattern was incomplete.

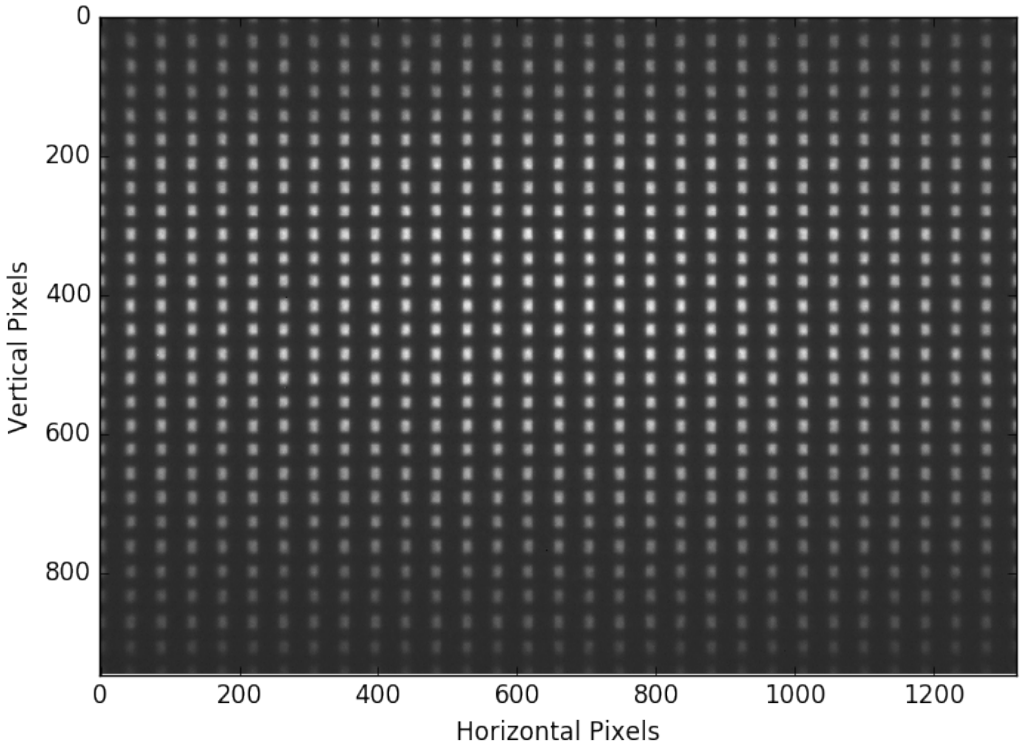

Figure B.2: Example of the dot array image shown in Figure B.1 after the static distortion correction process.

B.2 Intensity Uniformity Correction

As the final streak image data is captured from the luminescent response of the phosphor screen as it is struck by the swept electrons, the overall spatial uniformity of the output data is dependent on the specific response of each unique phosphor screen and streak tube used in every camera. While ideally the entire system would have a completely uniform intensity response, in practice this is not the case. Figure B.3 below shows an example streak image of a broadband QTH (quartz tungsten halogen) lamp incident on the streak camera input slit through several pieces of clean, white printer paper acting as a diffuse filter.

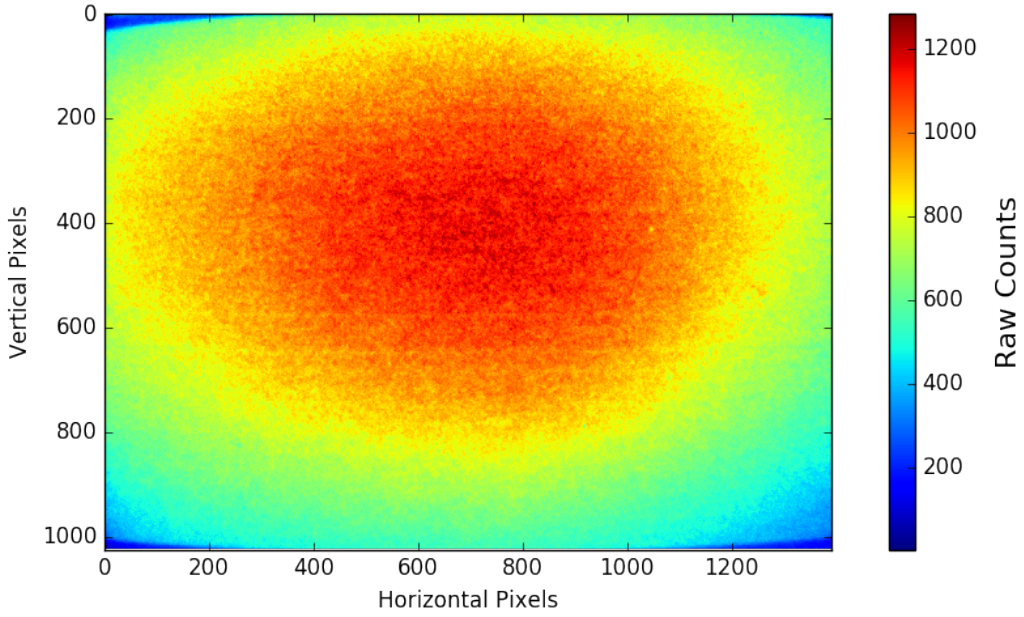

Figure B.3: Example uncorrected streak image with uniform illumination of the input slit. The raw intensity counts vary substantially (up to ~25%) over the image due to the non-uniformity of the streak tube, phosphor screen, and imaging camera.

This reference output of the streak image should approach uniformity in this configuration, but clearly it does not. As such, this non-uniformity can be corrected in two ways:

1. Dividing each captured streak image by the normalized reference just described

2. Dividing each captured streak image by a normalized reference image captured through the entire time-resolved spectroscopy setup

For this work the second option was chosen, as the many different optical elements in the entire setup also affect the intensity uniformity of the final streak image, and a single-step correction process was desired. For the AOMC multilayers, this reference image was captured by simply replacing the multilayer sample with a commercial high-reflectivity (>99.9%) mirror in the appropriate wavelength range. For the DBR multilayers, a reference fused silica substrate with no deposited layers was mounted in the standard laser-driven sample package described in Chapter 3. This reference image captured all of the spectral influence of the Xenon flash tube, lenses, filters, and spectrograph dispersion grating for each experiment. By then dividing any future data by these reference images, the "flat" (power/nm) spectral response of the multilayers could be obtained. While the reference images were captured before every set of experiments and every effort was made to ensure repeatability, the inherent shot-to-shot variance in the xenon flash lamp and streak camera prevented this correction method from produced a true, completely un-biased spectra. More work is needed to improve this aspect of the data correction process.

B.3 Spectral Calibration

Spectral calibration of the time-resolved spectroscopy setup was accomplished with a pencil-style Hg(Ar) calibration lamp. This particular model was chosen as it had the best selection of emissions peaks in the spectral range of interest (450-600 nm). It was placed in front of the microscope objective lens (i.e., where a multilayer sample would be in an actual experiment), and the streak camera was run in "focus" mode, which allows continuous acquisition of relatively low-intensity light signals. The adjustments of the spectrograph collimating and focusing lenses were used to obtain the sharpest possible peaks in the streak image, ensuring that the maximum spectral sensitivity of the entire system was obtained. The streak camera was then set to single acquisition mode, and swept at the fastest possible speed

that maintained usable signal-to-noise with the calibration lamp. Figure B.4 below shows an example streak image of the data taken at this stage, with four visible spectral peaks (435.84, 546.07, 576.96, and 579.07 nm).

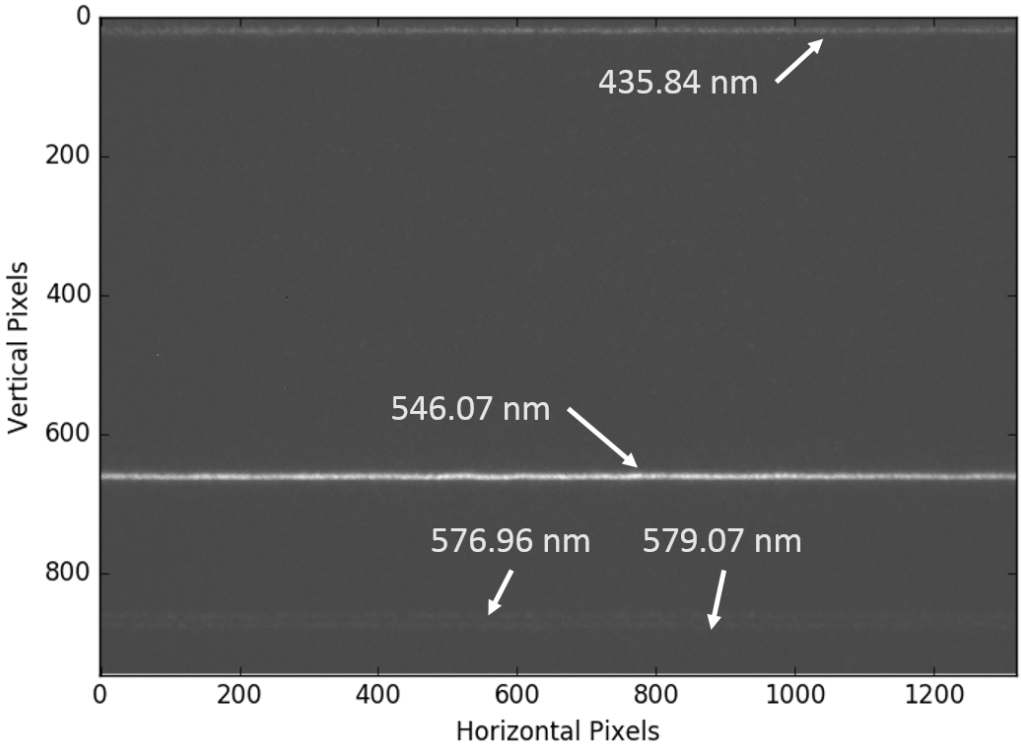

Figure B.4: Example static-distortion corrected streak image showing spectral calibration lines from a Hg(Ar) calibration lamp. Four lines are visible, corresponding to the 435.84, 546.07, 576.96, and 579.07 nm emission lines of the calibration lamp.

With this calibration image, a linear or multi-linear spectral calibration could be performed depending on whether just two or all four peaks were utilized. The large gap between the 435.85 and 546.07 nm peaks increases the potential for spectral calibration error, but no other suitable calibration lamp was found that was compatible with the experimental setup in the present work. It is most likely that any such error is significantly smaller than any of the other sources of error described in Chapter 5.

REFERENCES

[1] G. Crabtree, J. Sarrao, P. Alivisatos, W. Barletta, F. Bates, G. Brown, R. French, L. Greene, J. Hemminger, M. Kastner, B. Kay, J. Lewis, M. Ratner, R. Anthony, G. Rubloff, J. Spence, D. Tobias, J. Tranquada, and Basic Energy Sciences Advisory Committee (BESAC), "From Quanta to the Continuum: Opportunities for Mesoscale Science," Tech. Rep. 1183982, Sep. 2012.

[2] Marc Meyers, *Dynamic Behavior of Materials*. John Wiley and Sons, 1994.

[3] Jerry W. Forbes, *Shock Wave Compression of Condensed Matter: A Primer*. Springer-Verlag Berlin Heidelberg, 2012.

[4] L. M. Barker and R. E. Hollenbach, "Shock wave study of the phase transition in iron," *Journal of Applied Physics*, vol. 45, no. 11, pp. 4872–4887, Nov. 1974.

[5] P. J. Hazell, G. J. Appleby-Thomas, E. Wielewski, C. Stennett, and C. Siviour, "The influence of microstructure on the shock and spall behaviour of the magnesium alloy, Elektron 675," *Acta Materialia*, vol. 60, no. 17, pp. 6042–6050, Oct. 2012.

[6] Nesterenko, *Dynamics of Heterogeneous Materials*. New York: Springer, 2001.

[7] S. P. Marsh, *LASL Shock Hugoniot Data*. University of California Press, 1980.

[8] M. A. Meyers, "A model for elastic precursor waves in the shock loading of polycrystalline metals," *Materials Science and Engineering*, vol. 30, no. 2, pp. 99–111, Oct. 1977.

[9] S. Case and Y. Horie, "Discrete element simulation of shock wave propagation in polycrystalline copper," *Journal of the Mechanics and Physics of Solids*, vol. 55, no. 3, pp. 589–614, Mar. 2007.

[10] S. K. Dwivedi, J. R. Asay, and Y. M. Gupta, "Two-dimensional mesoscale simulations of quasielastic reloading and unloading in shock compressed aluminum," *Journal of Applied Physics*, vol. 100, no. 8, p. 083 509, Oct. 2006.

[11] L. Farbaniec, C. L. Williams, L. Kecskes, K. T. Ramesh, and R. Becker, "Microstructural effects on the spall properties of ECAE-processed AZ31b magnesium alloy," *International Journal of Impact Engineering*, vol. 98, no. Supplement C, pp. 34–41, Dec. 2016.

[12] R. W. Minich, J. U. Cazamias, M. Kumar, and A. J. Schwartz, "Effect of Microstructural Length Scales on Spall Behavior of Copper," *Metallurgical and Materials Transactions: Physical Metallurgy and Materials Science, A; New York*, vol. 35A, no. 9, pp. 2663–2673, Sep. 2004.

[13] R. L. Whelchel, G. B. Kennedy, S. K. Dwivedi, T. H. Sanders, and N. N. Thadhani, "Spall behavior of rolled aluminum 5083-H116 plate," *Journal of Applied Physics*, vol. 113, no. 23, p. 233 506, Jun. 2013.

[14] X. Chen and N. Chandra, "The effect of heterogeneity on plane wave propagation through layered composites," *Composites Science and Technology*, vol. 64, no. 1011, pp. 1477–1493, Aug. 2004.

[15] P. E. Specht, N. N. Thadhani, and T. P. Weihs, "Configurational effects on shock wave propagation in Ni-Al multilayer composites," *Journal of Applied Physics*, vol. 111, no. 7, p. 073 527, Apr. 2012.

[16] W. Riedel, M. Wicklein, and K. Thoma, "Shock properties of conventional and high strength concrete: Experimental and mesomechanical analysis," *International Journal of Impact Engineering*, vol. 35, no. 3, pp. 155–171, Mar. 2008.

[17] F. Bowden, *Initiation and Growth of Explosion in Liquids and Solids*. Cambridge University Press, 1985.

[18] Ralph Menikoff, "Pore Collapse and Hot Spots in HMX," Tech. Rep. LA-UR-03-3113, May 2003.

[19] A. Barua, S. Kim, Y. Horie, and M. Zhou, "Ignition criterion for heterogeneous energetic materials based on hotspot size-temperature threshold," *Journal of Applied Physics*, vol. 113, no. 6, p. 064 906, Feb. 2013.

[20] H. K. Springer, K. S. Vandersall, C. M. Tarver, and P. S. Souers, "Investigating Shock Initiation and Detonation in Powder Hmx with Reactive Mesoscale Simulations," Lawrence Livermore National Laboratory (LLNL), Livermore, CA, Tech. Rep. LLNL-CONF-656184, Jun. 2014.

[21] W. P. Bassett, B. P. Johnson, N. K. Neelakantan, K. S. Suslick, and D. D. Dlott, "Shock initiation of explosives: High temperature hot spots explained," *Applied Physics Letters*, vol. 111, no. 6, p. 061 902, Aug. 2017.

[22] T. S. Majmudar and R. P. Behringer, "Contact force measurements and stress-induced anisotropy in granular materials," *Nature*, vol. 435, no. 7045, pp. 1079–1082, Jun. 2005.

[23] S. K. Dwivedi, R. D. Teeter, C. W. Felice, and Y. M. Gupta, "Two dimensional mesoscale simulations of projectile instability during penetration in dry sand," *Journal of Applied Physics*, vol. 104, no. 8, pp. 083 502–083502–10, Oct. 2008.

[24] J. Borg, M. Morrissey, C. Perich, T. Vogler, and L. Chhabildas, "In situ velocity and stress characterization of a projectile penetrating a sand target: Experimental measurements and continuum simulations," *International Journal of Impact Engineering*, vol. 51, pp. 23–35, Jan. 2013.

[25] C. Daraio, V. F. Nesterenko, E. B. Herbold, and S. Jin, "Energy Trapping and Shock Disintegration in a Composite Granular Medium," *Physical Review Letters*, vol. 96, no. 5, p. 058 002, Feb. 2006.

[26] D. Eakins and N. N. Thadhani, "Discrete particle simulation of shock wave propagation in a binary Ni+Al powder mixture," *Journal of Applied Physics*, vol. 101, no. 4, p. 043 508, Feb. 2007.

[27] B. B. Aydelotte and N. N. Thadhani, "Mechanistic aspects of impact initiated reactions in explosively consolidated metal+aluminum powder mixtures," *Materials Science and Engineering: A*, vol. 570, pp. 164–171, May 2013.

[28] J. LaJeunesse, S. T. Stewart, G. Kennedy, N. Thadhani, and J. P. Borg, "Investigating velocity spectra at the Hugoniot state of shock loaded heterogenous materials," *AIP Conference Proceedings*, vol. 1793, no. 1, p. 120 007, Jan. 2017.

[29] J. E. Field, S. M. Walley, W. G. Proud, H. T. Goldrein, and C. R. Siviour, "Review of experimental techniques for high rate deformation and shock studies," *International Journal of Impact Engineering*, Fifth International Symposium on Impact Engineering, vol. 30, no. 7, pp. 725–775, Aug. 2004.

[30] S. N. Luo, B. J. Jensen, D. E. Hooks, K. Fezzaa, K. J. Ramos, J. D. Yeager, K. Kwiatkowski, and T. Shimada, "Gas gun shock experiments with single-pulse x-ray phase contrast imaging and diffraction at the Advanced Photon Source," *Review of Scientific Instruments*, vol. 83, no. 7, p. 073 903, Jul. 2012.

[31] L. M. Barker and R. E. Hollenbach, "Laser interferometer for measuring high velocities of any reflecting surface," *Journal of Applied Physics*, vol. 43, no. 11, pp. 4669–4675, Nov. 1972.

[32] O. T. Strand, D. R. Goosman, C. Martinez, T. L. Whitworth, and W. W. Kuhlow, "Compact system for high-speed velocimetry using heterodyne techniques," *Review of Scientific Instruments*, vol. 77, no. 8, p. 083 108, Aug. 2006.

[33] E. Daykin and C. Perez, "Techniques and Tools for PDV Applications: A Work In Progress," 2008.

[34] D. H. Dolan, "Accuracy and precision in photonic Doppler velocimetry," *Review of Scientific Instruments*, vol. 81, no. 5, p. 053 905, May 2010.

[35] D. D. Bloomquist and S. A. Sheffield, "Optically recording interferometer for velocity measurements with subnanosecond resolution," *Journal of Applied Physics*, vol. 54, no. 4, pp. 1717–1722, Apr. 1983.

[36] T. J. Vogler, W. M. Trott, W. D. Reinhart, C. S. Alexander, M. D. Furnish, M. D. Knudson, and L. C. Chhabildas, "Using the line-VISAR to study multi-dimensional and mesoscale impact phenomena," *International Journal of Impact Engineering*, Hypervelocity Impact Proceedings of the 2007 SymposiumHVIS 2007, vol. 35, no. 12, pp. 1844–1852, Dec. 2008.

[37] E. Daykin, M. Burk, D. Holtkamp, E. K. Miller, A. Rutkowski, O. T. Strand, M. Pena, C. Perez, and C. Gallegos, "Multiplexed photonic Doppler velocimetry for large channel count experiments," *AIP Conference Proceedings*, vol. 1793, no. 1, p. 160 004, Jan. 2017.

[38] R. A. Graham, F. W. Neilson, and W. B. Benedick, "Piezoelectric Current from ShockLoaded QuartzA Submicrosecond Stress Gauge," *Journal of Applied Physics*, vol. 36, no. 5, pp. 1775–1783, May 1965.

[39] H. Vantine, J. Chan, L. Erickson, J. Janzen, R. Weingart, and R. Lee, "Precision stress measurements in severe shockwave environments with lowimpedance manganin gauges," *Review of Scientific Instruments*, vol. 51, no. 1, pp. 116–122, Jan. 1980.

[40] F. Bauer, "Behavior of ferroelectric ceramics and PVF2 polymers under shock loading," in *AIP Conference Proceedings*, vol. 78, AIP Publishing, Apr. 1982, pp. 251–267.

[41] V. A. Borisenok, V. G. Simakov, V. A. Bragunets, V. G. Kuropatkin, V. A. Kruchinin, and V. N. Romaev, "Polyvinylidene Fluoride Dynamic Pressure Gauge: Physical Model and Experimental Results," *Combustion, Explosion and Shock Waves*, vol. 39, no. 5, pp. 585–590, Sep. 2003.

[42] M. Gonzales, A. Gurumurthy, G. B. Kennedy, A. M. Gokhale, and N. N. Thadhani, "Shock compression response of Ti+B reactive powder mixtures," *Journal of Physics: Conference Series*, vol. 500, no. 5, p. 052 013, 2014.

[43] H. J. Kostkowski and R. D. Lee, *Theory and Methods of Optical Pyrometry*, Report, Mar. 1962.

[44] J. E. Miller, T. R. Boehly, A. Melchior, D. D. Meyerhofer, P. M. Celliers, J. H. Eggert, D. G. Hicks, C. M. Sorce, J. A. Oertel, and P. M. Emmel, "Streaked optical

pyrometer system for laser-driven shock-wave experiments on OMEGA," *Review of Scientific Instruments*, vol. 78, no. 3, p. 034 903, Mar. 2007.

[45] W. P. Bassett and D. D. Dlott, "Multichannel emission spectrometer for high dynamic range optical pyrometry of shock-driven materials," *Review of Scientific Instruments*, vol. 87, pp. 103 107–, Oct. 2016.

[46] D. D. Bloomquist and S. A. Sheffield, "Thermocouple temperature measurements in shockcompressed solids," *Journal of Applied Physics*, vol. 51, no. 10, pp. 5260–5266, Oct. 1980.

[47] D. E. Hare, J. Franken, and D. D. Dlott, "Coherent Raman measurements of polymer thinfilm pressure and temperature during picosecond laser ablation," *Journal of Applied Physics*, vol. 77, no. 11, pp. 5950–5960, Jun. 1995.

[48] Y. Ping, F. Coppari, D. G. Hicks, B. Yaakobi, D. E. Fratanduono, S. Hamel, J. H. Eggert, J. R. Rygg, R. F. Smith, D. C. Swift, D. G. Braun, T. R. Boehly, and G. W. Collins, "Solid Iron Compressed Up to 560 GPa," *Physical Review Letters*, vol. 111, no. 6, p. 065 501, Aug. 2013.

[49] D. H. Dolan, C. T. Seagle, and T. Ao, "Dynamic Temperature Measurements with Embedded Optical Sensors.," Sandia National Laboratories (SNL-NM), Albuquerque, NM (United States), Tech. Rep. SAND2013-8203, Oct. 2013.

[50] P. H. Lissberger, "Optical applications of dielectric thin films," *Reports on Progress in Physics*, vol. 33, no. 1, p. 197, 1970.

[51] S. Wang, "Principles of distributed feedback and distributed Bragg-reflector lasers," *IEEE Journal of Quantum Electronics*, vol. 10, no. 4, pp. 413–427, Apr. 1974.

[52] S. Wang, R. F. Cordero, and C.-C. Tseng, "Analysis of distributedfeedback and distributedBraggreflector laser structures by method of multiple reflections," *Journal of Applied Physics*, vol. 45, no. 9, pp. 3975–3977, Sep. 1974.

[53] N. Bloembergen and A. J. Sievers, "NONLINEAR OPTICAL PROPERTIES OF PERIODIC LAMINAR STRUCTURES," *Applied Physics Letters*, vol. 17, no. 11, pp. 483–486, Dec. 1970.

[54] M. Kimura, K. Okahara, and T. Miyamoto, "Tunable multilayerfilm distributed-Braggreflector filter," *Journal of Applied Physics*, vol. 50, no. 3, pp. 1222–1225, Mar. 1979.

[55] J. P. van der Ziel and M. Ilegems, "Multilayer GaAs-Al_03ga_07as dielectric quarter wave stacks grown by molecular beam epitaxy," *Applied Optics*, vol. 14, no. 11, p. 2627, Nov. 1975.

[56] S. Larouche and L. Martinu, "OpenFilters: open-source software for the design, optimization, and synthesis of optical filters," *Applied Optics*, vol. 47, no. 13, pp. C219–C230, May 2008.

[57] I. H. Malitson, "Interspecimen Comparison of the Refractive Index of Fused Silica*,," *JOSA*, vol. 55, no. 10, pp. 1205–1209, Oct. 1965.

[58] R. Boidin, T. Halenkovi, V. Nazabal, L. Bene, and P. Nmec, "Pulsed laser deposited alumina thin films," *Ceramics International*, vol. 42, no. 1, Part B, pp. 1177–1182, Jan. 2016.

[59] G. Lee, D. A. Scripka, B. Wagner, N. N. Thadhani, Z. Kang, and C. J. Summers, "Design and fabrication of distributed Bragg reflector multilayers for dynamic pressure sensing," *Optics Express*, vol. 25, no. 22, pp. 27 067–27 076, Oct. 2017.

[60] C. Fabry and A. Perot, "Sur les franges des lames minces argentées et leur application à la mesure de petites épaisseurs dair," *Ann. Chim. Phys*, vol. 12, pp. 459–501, 1897.

[61] K. J. Vahala, "Optical microcavities," *Nature*, vol. 424, no. 6950, pp. 839–846, Aug. 2003.

[62] F. Ma and X. Liu, "Phase shift and penetration depth of metal mirrors in a microcavity structure," *Applied Optics*, vol. 46, no. 25, p. 6247, 2007.

[63] M. Kolle, B. Zheng, N. Gibbons, J. J. Baumberg, and U. Steiner, "Stretch-tuneable dielectric mirrors and optical microcavities," *Optics Express*, vol. 18, no. 5, p. 4356, Mar. 2010.

[64] G. Kamita, M. Kolle, F. Huang, J. J. Baumberg, and U. Steiner, "Multilayer mirrored bubbles with spatially-chirped and elastically-tuneable optical bandgaps," *Optics Express*, vol. 20, no. 6, pp. 6421–6428, Mar. 2012.

[65] L. Dongwen, M. Yang, C. Huang, and J. Dai, "Optical fiber high-temperature sensor based on dielectric films extrinsic fabry-perot cavity," *IEEE Photonics Technology Letters*, vol. Early Access Online, 2014.

[66] S. Kitagawa, H. Yamazaki, A. Hosoki, M. Nishiyama, and K. Watanabe, "Development of SPR temperature sensor using Au/TiO2 on hetero-core optical fiber," vol. 9754, 2016, 97541B–97541B–7.

[67] P. Morris, A. Hurrell, A. Shaw, E. Zhang, and P. Beard, "A FabryProt fiber-optic ultrasonic hydrophone for the simultaneous measurement of temperature and acoustic pressure," *The Journal of the Acoustical Society of America*, vol. 125, no. 6, pp. 3611–3622, Jun. 2009.

[68] S. Y. Choi, M. Mamak, G. von Freymann, N. Chopra, and G. A. Ozin, "Mesoporous Bragg Stack Color Tunable Sensors," *Nano Letters*, vol. 6, no. 11, pp. 2456–2461, Nov. 2006.

[69] K.-S. Kim, Y. Mizuno, and K. Nakamura, "Fiber-optic ultrasonic hydrophone using short FabryPerot cavity with multilayer reflectors deposited on small stub," *Ultrasonics*, vol. 54, no. 4, pp. 1047–1051, Apr. 2014.

[70] ——, "High-Speed Measurement of Refractive Index Using Dielectric Multilayer Films Deposited on Optical Fiber End," *Japanese Journal of Applied Physics*, vol. 51, p. 080 202, Jul. 2012.

[71] G. A. Cranch, R. Lunsford, J. Grn, J. Weaver, S. Compton, M. May, and N. Kostinski, "Characterization of laser-driven shock waves in solids using a fiber optic pressure probe," *Applied Optics*, vol. 52, no. 32, pp. 7791–7796, Nov. 2013.

[72] S. J. Mihailov, "Fiber Bragg Grating Sensors for Harsh Environments," *Sensors*, vol. 12, no. 2, pp. 1898–1918, Feb. 2012.

[73] A. Cusano, A. Cutolo, and J. Albert, Eds., *Fiber Bragg Grating Sensors: Recent Advancements, Industrial Applications and Market Exploitation*. BENTHAM SCIENCE PUBLISHERS, Mar. 2012, ISBN: 978-1-60805-084-0.

[74] X. Deng, G. Chen, Q. Peng, Z. Li, J. Meng, and J. Liu, "Research on the fiber Bragg grating sensor for the shock stress measurement," *The Review of Scientific Instruments*, vol. 82, no. 10, p. 103 109, Oct. 2011.

[75] G. Rodriguez, R. L. Sandberg, S. I. Jackson, D. M. Dattelbaum, S. W. Vincent, Q. McCulloch, R. M. Martinez, S. M. Gilbertson, and E. Udd, "Fiber Bragg grating sensing of detonation and shock experiments at Los Alamos National Laboratory," pp. 872 204–872 204, May 2013.

[76] A. Ravid, E. Shafir, S. Zilberman, G. Berkovic, B. Glam, G. Appelbaum, and A. F. Gefen, "Fibre Bragg Grating sensor for shock wave diagnostics," *Journal of Physics: Conference Series*, vol. 500, no. 14, p. 142 029, May 2014.

[77] R. L. Sandberg, G. Rodriguez, L. L. Gibson, D. M. Dattelbaum, G. D. Stevens, M. Grover, B. M. Lalone, and E. Udd, "Embedded optical probes for simultaneous pressure and temperature measurement of materials in extreme conditions," *Journal of Physics: Conference Series*, vol. 500, no. 14, p. 142 031, May 2014.

[78] G. Rodriguez and S. M. Gilbertson, "Ultrafast Fiber Bragg Grating Interrogation for Sensing in Detonation and Shock Wave Experiments," *Sensors*, vol. 17, no. 2, p. 248, Jan. 2017.

[79] A. A. Banishev, W. L. Shaw, W. P. Bassett, and D. D. Dlott, "High-Speed Laser-Launched Flyer Impacts Studied with Ultrafast Photography and Velocimetry," *Journal of Dynamic Behavior of Materials*, pp. 1–13, Feb. 2016.

[80] D. L. Paisley, S.-N. Luo, S. R. Greenfield, and A. C. Koskelo, "Laser-launched flyer plate and confined laser ablation for shock wave loading: Validation and applications," *Review of Scientific Instruments*, vol. 79, no. 2, p. 023 902, Feb. 2008.

[81] R. Fabbro, J. Fournier, P. Ballard, D. Devaux, and J. Virmont, "Physical study of laserproduced plasma in confined geometry," *Journal of Applied Physics*, vol. 68, no. 2, pp. 775–784, Jul. 1990.

[82] S. C. Kelly, "Shock-compression of Ni-Al nanolayered foils using controlled laser-accelerated thin foil impact," PhD thesis, Georgia Institute of Technology, North Avenue, Atlanta GA, 30332, Aug. 2013.

[83] Y. Tsuchiya, "Advances in streak camera instrumentation for the study of biological and physical processes," *IEEE Journal of Quantum Electronics*, vol. 20, no. 12, pp. 1516–1528, Dec. 1984.

[84] K. E. Brown, Y. Fu, W. L. Shaw, and D. D. Dlott, "Time-resolved emission of dye probes in a shock-compressed polymer," *Journal of Applied Physics*, vol. 112, no. 10, p. 103 508, Nov. 2012.

[85] Hamamatsu Photonics K.K., *Guide to Streak Cameras*, 2008.

[86] A. A. Banishev and D. D. Dlott, "Ultrafast pressure-sensitive paint for shock compression spectroscopy," *Journal of Applied Physics*, vol. 115, no. 20, p. 203 515, May 2014.

[87] P. Xiao, Z. Kang, A. A. Bansihev, J. Breidenich, D. A. Scripka, J. M. Christensen, C. J. Summers, D. D. Dlott, N. N. Thadhani, and M. Zhou, "Laser-excited optical emission response of CdTe quantum dot/polymer nanocomposite under shock compression," *Applied Physics Letters*, vol. 108, no. 1, p. 011 908, Jan. 2016.

[88] Z. Kang, A. A. Banishev, G. Lee, D. A. Scripka, J. Breidenich, P. Xiao, J. Christensen, M. Zhou, C. J. Summers, D. D. Dlott, and N. N. Thadhani, "Exploration of CdTe quantum dots as mesoscale pressure sensors via time-resolved shock-compression photoluminescent emission spectroscopy," *Journal of Applied Physics*, vol. 120, no. 4, p. 043 107, Jul. 2016.

[89] L. Cohen, *Time-frequency Analysis: Theory and Applications*. Upper Saddle River, NJ, USA: Prentice-Hall, Inc., 1995, ISBN: 978-0-13-594532-2.

[90] H. Song, X. Wu, C. Huang, Y. Wei, and X. Wang, "Measurement of fast-changing low velocities by photonic Doppler velocimetry," *Review of Scientific Instruments*, vol. 83, no. 7, p. 073 301, Jul. 2012.

[91] R. Gustavsen, "Wavelet analysis of heterodyne velocimetry (pdv) signals," in *2nd Annual Photonic Doppler Velocimetry (PDV) Workshop*, 2007.

[92] D. E. Kittell, J. O. Mares, and S. F. Son, "Measuring time-resolved detonation velocity using wavelet analysis and microwave interferometry," Sandia National Laboratories, Tech. Rep. SAND2014-15332C, 2014.

[93] A. F. Oskooi, D. Roundy, M. Ibanescu, P. Bermel, J. D. Joannopoulos, and S. G. Johnson, "Meep: A flexible free-software package for electromagnetic simulations by the FDTD method," *Computer Physics Communications*, vol. 181, no. 3, pp. 687–702, Mar. 2010.

[94] D. L. Windt, "IMDSoftware for modeling the optical properties of multilayer films," *Computers in Physics*, vol. 12, no. 4, pp. 360–370, Jul. 1998.

[95] H. Sugiura, K. Kondo, and A. Sawaoka, "Dynamic response of fused quartz in the permanent densification region," *Journal of Applied Physics*, vol. 52, no. 5, pp. 3375–3382, May 1981.

[96] J. Wackerle, "ShockWave Compression of Quartz," *Journal of Applied Physics*, vol. 33, no. 3, pp. 922–937, Mar. 1962.

[97] L. M. Barker and R. E. Hollenbach, "ShockWave Studies of PMMA, Fused Silica, and Sapphire," *Journal of Applied Physics*, vol. 41, no. 10, pp. 4208–4226, Sep. 1970.

[98] R. E. Setchell, "Index of refraction of shockcompressed fused silica and sapphire," *Journal of Applied Physics*, vol. 50, no. 12, pp. 8186–8192, Dec. 1979.

[99] C.-s. Zha, R. J. Hemley, H.-k. Mao, T. S. Duffy, and C. Meade, "Acoustic velocities and refractive index of SiO2 glass to 57.5 GPa by Brillouin scattering," *Physical Review B*, vol. 50, no. 18, pp. 13 105–13 112, Nov. 1994.

[100] D. Erskine, "High pressure Hugoniot of sapphire," *AIP Conference Proceedings*, vol. 309, no. 1, pp. 141–143, Jul. 1994.

[101] R. A. Graham and W. P. Brooks, "Shock-wave compression of sapphire from 15 to 420 kbar. The effects of large anisotropic compressions," *Journal of Physics and Chemistry of Solids*, vol. 32, no. 10, pp. 2311–2330, Jan. 1971.

[102] R. E. Setchell, "Refractive index of sapphire at 532 nm under shock compression and release," *Journal of Applied Physics*, vol. 91, no. 5, pp. 2833–2841, Mar. 2002.

[103] X. Cao, J. Li, J. Li, X. Li, L. Xu, Y. Wang, W. Zhu, C. Meng, and X. Zhou, "Refractive index of r-cut sapphire under shock pressure range 5 to 65GPa," *Journal of Applied Physics*, vol. 116, no. 9, p. 093 516, Sep. 2014.

[104] X. Cao, Y. Wang, X. Li, L. Xu, L. Liu, Y. Yu, R. Qin, W. Zhu, S. Tang, L. He, C. Meng, B. Zhang, and X. Peng, "Refractive index and phase transformation of sapphire under shock pressures up to 210GPa," *Journal of Applied Physics*, vol. 121, no. 11, p. 115 903, Mar. 2017.

[105] C. T. Seagle, J.-P. Davis, and M. D. Knudson, "Mechanical response of lithium fluoride under off-principal dynamic shock-ramp loading," *Journal of Applied Physics*, vol. 120, no. 16, p. 165 902, Oct. 2016.

[106] D. Fratanduono, "The Index of refraction of lithium fluoride at pressures in excess of 100 GPa," 2010.

[107] D. E. Fratanduono, T. R. Boehly, M. A. Barrios, D. D. Meyerhofer, J. H. Eggert, R. F. Smith, D. G. Hicks, P. M. Celliers, D. G. Braun, and G. W. Collins, "Refractive index of lithium fluoride ramp compressed to 800 GPa," *Journal of Applied Physics*, vol. 109, no. 12, p. 123 521, Jun. 2011.

[108] P. A. Rigg, M. D. Knudson, R. J. Scharff, and R. S. Hixson, "Determining the refractive index of shocked [100] lithium fluoride to the limit of transmissibility," *Journal of Applied Physics*, vol. 116, no. 3, p. 033 515, Jul. 2014.

[109] D. M. Dattelbaum, J. D. Jensen, A. M. Schwendt, E. M. Kober, M. W. Lewis, and R. Menikoff, "A novel method for static equation-of state-development: Equation of state of a cross-linked poly(dimethylsiloxane) (PDMS) network to 10 GPa," *The Journal of Chemical Physics*, vol. 122, no. 14, p. 144 903, Apr. 2005.

[110] C. A. Bolme, "Ultrafast dynamic ellipsometry of laser driven shock waves," Thesis, Massachusetts Institute of Technology, 2008.

[111] D. M. Dattelbaum, D. L. Robbins, S. A. Sheffield, E. B. Orler, R. L. Gustavsen, R. R. Alcon, J. M. Lloyd, and P. J. Chavez, "QuasiStatic and Shock Compressive Response of Fluorinated Polymers: KelF 800," *AIP Conference Proceedings*, vol. 845, no. 1, pp. 69–72, Jul. 2006.

[112] M.-S. Jeong, J. H. Kim, J.-H. Ko, Y. H. Ko, and K. J. Kim, "Pressure dependence of acoustic behaviors and refractive index of amorphous Kel F-800 copolymer studied by Brillouin spectroscopy," *Current Applied Physics*, vol. 13, no. 8, pp. 1774–1777, Oct. 2013.

[113] W. J. Carter and S. P. Marsh, "Hugoniot equation of state of polymers," Los Alamos National Laboratories, Tech. Rep. LA-13006-MS, 1995.

[114] D. J. Chapman, D. E. Eakins, D. M. Williamson, and W. Proud, "Index of refraction measurements and window corrections for PMMA under shock compression," in *AIP Conference Proceedings*, vol. 1426, AIP Publishing, Mar. 2012, pp. 442–445.

[115] D. V. Nazarov, A. L. Mikhaylov, A. V. Fedorov, S. F. Manachkin, V. D. Urlin, A. V. Menshikh, S. A. Finyushin, V. A. Davydov, and E. V. Filinov, "Characterization of Optically Transparent Window Materials for IsentropicCompression Studies," in *AIP Conference Proceedings*, vol. 706, AIP Publishing, Jul. 2004, pp. 1221–1224.

[116] R. G. McQueen and S. P. Marsh, "Equation of State for Nineteen Metallic Elements from ShockWave Measurements to Two Megabars," *Journal of Applied Physics*, vol. 31, no. 7, pp. 1253–1269, Jul. 1960.

[117] J. D. J. Stanford P. Lyon, "Sesame: the los alamos national laboratory equation of state database," Los Alamos National Laboratories, Tech. Rep. LA-UR-92-3407, 1992.

[118] P. J. Martin, H. A. Macleod, R. P. Netterfield, C. G. Pacey, and W. G. Sainty, "Ion-beam-assisted deposition of thin films," *Applied Optics*, vol. 22, no. 1, p. 178, Jan. 1983.

[119] R. S. Sennett and G. D. Scott, "The Structure of Evaporated Metal Films and Their Optical Properties," *Journal of the Optical Society of America*, vol. 40, no. 4, p. 203, Apr. 1950.

[120] D. B. Hall, P. Underhill, and J. M. Torkelson, "Spin coating of thin and ultrathin polymer films," *Polymer Engineering & Science*, vol. 38, no. 12, pp. 2039–2045, Dec. 1998.

[121] G. Lee, "Design and Fabrication of Multilayer Structures in Dynamic Sensing and Transparent Nanocomposite Scintillators for High Energy Detection," PhD thesis, Georgia Institute of Technology, North Avenue, Atlanta GA, 30332, Apr. 2017.

[122] J. Pivot, "Mechanical properties of SiOx thin films," *Thin Solid Films*, vol. 89, no. 2, pp. 175–190, Mar. 1982.

[123] W. D. Nix, "Mechanical properties of thin films," *Metallurgical Transactions A*, vol. 20, no. 11, pp. 2217–2245, Nov. 1989.

[124] H. Ni, X. Li, and H. Gao, "Elastic modulus of amorphous SiO2 nanowires," *Applied Physics Letters*, vol. 88, no. 4, p. 043 108, Jan. 2006.

[125] H. Li and J. J. Vlassak, "Determining the elastic modulus and hardness of an ultra-thin film on a substrate using nanoindentation," *Journal of Materials Research*, vol. 24, no. 03, pp. 1114–1126, Mar. 2009.

[126] Z. Ao and S. Li, "Temperature- and thickness-dependent elastic moduli of polymer thin films," *Nanoscale Research Letters*, vol. 6, no. 1, pp. 1–6, Mar. 2011.

[127] D. J. Funk, D. S. Moore, S. D. McGrane, K. T. Gahagan, J. H. Reho, S. J. Buelow, J. Nicholson, G. L. Fisher, and R. L. Rabie, "Ultrafast studies of shock waves using interferometric methods and transient infrared absorption spectroscopy," *Thin Solid Films*, Proceedings of Symposium H on Photonic Processing of Surfaces, Thin Films and Devices, of the E-MRS 2003 Spring Conference, vol. 453454, pp. 542–549, Apr. 2004.

[128] S. D. McGrane, D. S. Moore, and D. J. Funk, "Measurement of Shocked Thin Polymer Film Hugoniot Properties with Ultrafast Dynamic Ellipsometry," in *AIP Conference Proceedings*, vol. 706, AIP Publishing, Jul. 2004, pp. 1181–1186.

[129] S. I. Ashitkov, M. B. Agranat, G. I. Kanel, P. S. Komarov, and V. E. Fortov, "Behavior of aluminum near an ultimate theoretical strength in experiments with femtosecond laser pulses," *JETP Letters*, vol. 92, no. 8, pp. 516–520, Dec. 2010.

[130] R. Evans, A. D. Badger, F. Fallis, M. Mahdieh, T. A. Hall, P. Audebert, J.-P. Geindre, J.-C. Gauthier, A. Mysyrowicz, G. Grillon, and A. Antonetti, "Time- and Space-Resolved Optical Probing of Femtosecond-Laser-Driven Shock Waves in Aluminum," *Physical Review Letters*, vol. 77, no. 16, pp. 3359–3362, Oct. 1996.

[131] N. W. Ashcroft and K. Sturm, "Interband Absorption and the Optical Properties of Polyvalent Metals," *Physical Review B*, vol. 3, no. 6, pp. 1898–1910, Mar. 1971.

[132] S. B. Kormer, "OPTICAL STUDY OF THE CHARACTERISTICS OF SHOCK-COMPRESSED CONDENSED DIELECTRICS," *Soviet Physics Uspekhi*, vol. 11, no. 2, p. 229, Feb. 1968.

[133] J. H. Gladstone and T. P. Dale, "XIV. Researches on the refraction, dispersion, and sensitiveness of liquids," *Philosophical Transactions of the Royal Society of London*, vol. 153, pp. 317–343, Jan. 1863.

[134] *Behaviour of Dense Media Under High Dynamic Pressures: Symposium H.D.P. : IUTAM : Paris, September 1967*. Gordon and Breach, 1968.

[135] B. J. Jensen, D. B. Holtkamp, P. A. Rigg, and D. H. Dolan, "Accuracy limits and window corrections for photon Doppler velocimetry," *Journal of Applied Physics*, vol. 101, no. 1, p. 013 523, Jan. 2007.

[136] N. Nissim, S. Eliezer, L. Bakshi, L. Perelmutter, and M. P. Pasternak, "High pressure ellipsometry: A novel method for measuring the optical properties and electronic structure of materials in diamond anvil cells," *Review of Scientific Instruments*, vol. 82, no. 3, p. 033 905, Mar. 2011.

[137] C. T. Seagle, D. L. Heinz, Z. Liu, and R. J. Hemley, "Synchrotron infrared reflectivity measurements of iron at high pressures," *Applied Optics*, vol. 48, no. 3, p. 545, Jan. 2009.

[138] S. Grant, A. Bernstein, J. Lin, T. Ao, J. Davis, D. Dolan, C. Seagle, "Development of Dynamic Ellipsometry for Measurements or Iron Conductivity at Earths Core Conditions," Sandia, Tech. Rep. SAND2017-2349R, 2017.

[139] S. J. Ali, C. A. Bolme, G. W. Collins, and R. Jeanloz, "Development of a broadband reflectivity diagnostic for laser driven shock compression experiments," *Review of Scientific Instruments*, vol. 86, no. 4, p. 043 112, Apr. 2015.

[140] J. R. Asay and D. B. Hayes, "Shockcompression and release behavior near melt states in aluminum," *Journal of Applied Physics*, vol. 46, no. 11, pp. 4789–4800, Nov. 1975.

[141] J. L. Plissier and D. Partouche-Sebban, "Pyrometry measurements on shock-heated bismuth using PMMA and sapphire windows," *Physica B: Condensed Matter*, vol. 364, no. 14, pp. 14–28, Jul. 2005.

[142] D. D. Bloomquist and S. A. Sheffield, "Shockcompression temperature rise in polymethyl methacrylate determined from resistivity of embedded copper foils," *Applied Physics Letters*, vol. 38, no. 3, pp. 185–187, Feb. 1981.

[143] A. D. Raki, A. B. Djurii, J. M. Elazar, and M. L. Majewski, "Optical properties of metallic films for vertical-cavity optoelectronic devices," *Applied Optics*, vol. 37, no. 22, pp. 5271–5283, Aug. 1998.

[144] G. Hass and C. D. Salzberg, "Optical Properties of Silicon Monoxide in the Wavelength Region from 0.24 to 14.0 Microns*," *JOSA*, vol. 44, no. 3, pp. 181–187, Mar. 1954.

[145] A. A. Banishev, W. L. Shaw, and D. D. Dlott, "Dynamics of polymer response to nanosecond shock compression," *Applied Physics Letters*, vol. 104, no. 10, p. 101 914, Mar. 2014.